

Physical modelling of DMFC performance heterogeneities and the recovery of reversible cathode degradation

A thesis submitted to the Faculty of Energy-, Process- and Bio-Engineering of the
University of Stuttgart in partial fulfilment of the requirements for the degree of
Doctor of Engineering Sciences (Dr.-Ing.)

by

Marie-Dominique Fischer (née Baum)

born in Gießen

Committee chair: Prof. Dr. K. Andreas Friedrich

Committee members: Prof. Dr. Arnulf Latz

...

Date of defence: -tbd-

Institute for Building Energetics, Thermotechnology and Energy Storage
University of Stuttgart

2021

Acronyms

ACL	anode catalyst layer
BPP	bipolar plate
CCL	cathode catalyst layer
CFD	computational fluid dynamics
CL	catalyst layer
DMFC	direct methanol fuel cell
ECSA	electrochemically active surface area
EIS	electrochemical impedance spectra
EW	equivalent weight
FE	finite-element
FV	finite-volume
GDL	gas diffusion layer
HER	hydrogen evolution reaction
HOR	hydrogen oxidation reaction
MEA	membrane electrode assembly
MOR	methanol oxidation reaction
MPL	micro-porous layer
NCP	nonlinear complementarity problem
OCV	open circuit voltage
ORR	oxygen reduction reaction
PEM	polymer electrolyte membrane
PEMFC	polymer electrolyte membrane fuel cell
PFSA	poly-fluorinated sulfonic acid
PTFE	polytetrafluoroethylene
REV	representative elementary volume

Symbols

Symbol	Unit	Description
a_κ		activity of component κ
A_{cell}	m^2	cell area
A_{ch}	m^2	channel area
C_{DL}	F m^{-3}	double layer capacity
c_α^κ	mol m^{-3}	molar concentration of component κ in phase α
$C_{H_2O}^m$	mol m^{-3}	molar water concentration in the membrane
c_p	$\text{J kg}^{-1} \text{K}^{-1}$	specific heat capacity
\mathbf{d}_α^κ	$\text{mol m}^{-2} \text{s}^{-1}$	diffusive flux of component κ in phase α
D_α^κ	$\text{m}^2 \text{s}^{-1}$	diffusion coefficient of component κ in phase α
$D_{Kn,g}^\kappa$	$\text{m}^2 \text{s}^{-1}$	<i>Knudsen</i> diffusion coefficient of component κ
$D_{ion}^{\text{O}_2}$	$\text{m}^2 \text{s}^{-1}$	oxygen diffusion coefficient in the ionomer
d_{cell}	m	cell depth
d_{ch}	m	channel depth
d_{rib}	m	rib depth
E_a	J mol^{-1}	activation energy
$ECSA$	$\text{m}^2 \text{m}^{-3}$	electrochemically active surface area
E_i^0	V	equilibrium voltage of reaction i
EW	kg mol^{-1}	membrane equivalent weight
f_α^κ	Pa	fugacity of component κ in phase α
F	C mol^{-1}	<i>Faraday's</i> constant
f_V		water volume fraction
g	J mol^{-1}	<i>Gibbs</i> free energy
h	J mol^{-1}	molar enthalpy
h_α	J kg^{-1}	mass specific enthalpy of phase α
h_α^κ	J kg^{-1}	specific enthalpy of component κ in phase α
$H_{H_2O}^\kappa$	Pa	<i>Henry</i> coefficient of component κ in water
i	A m^{-2}	current density
i_{nom}	A m^{-2}	nominal current density: 0.25 A cm^{-2}
j	A m^{-3}	volumetric current density
j_0	A m^{-2}	exchange current density
\mathbf{K}	m^2	intrinsic permeability
k_{abs}, k_{des}	m s^{-1}	water absorption / desorption mass transfer coefficient
k_{ORR}	A m^{-3}	ORR rate constant
k_p	m^2	hydraulic permeability
$k_{r\alpha}$		relative permeability of phase α
l_{ch}	m	channel length

l_{in}	m	inlet length
l_{out}	m	outlet length
l_{tube}	m	tube length
M_{κ}	kg mol ⁻¹	molar mass of component κ
n		number of electrons transferred in the reaction
p	Pa	pressure
p_{α}	Pa	pressure of phase α
p_c	Pa	capillary pressure
p_{cb}	Pa	break through pressure
p_{sat}	Pa	vapour pressure
q		source term
q^{heat}	J m ⁻³ s ⁻¹	energy source term
q_{H^+} / q_{e^-}	A m ⁻³	charge source term
q_{κ}	mol m ⁻³ s ⁻¹	source term of component κ
R	J mol ⁻¹ K ⁻¹	ideal gas constant
RH		relative gas humidity
r_i	A m ⁻³	reaction rate of reaction i
R_n		resistance term
r_{pore}	m	pore radius
S_{α}		saturation of phase α
s	J mol ⁻¹ K ⁻¹	molar entropy
T	K	temperature
u_{α}	J kg ⁻¹	specific internal energy of phase α
\mathbf{v}_{α}	m s ⁻¹	velocity of phase α
V_i	m ³ mol ⁻¹	partial molar volume of species i
w_{ACL}	m	ACL thickness
w_{CCL}	m	CCL thickness
w_{ch}	m	channel width
w_{GDL}	m	GDL thickness
w_{MPL}	m	MPL thickness
w_{PEM}	m	PEM thickness
x_{α}^{κ}	mol mol ⁻¹	mole fraction of component κ in phase α

Greek Symbols

Symbol	Unit	Description
α		charge transfer coefficient
δ_{ion}	m	ionomer film thickness
ϵ		ratio between channel depth d_{ch} and cell depth d_{cell}
κ_i		electro-osmotic drag coefficient of species i
λ		reactant stoichiometry in anode or cathode feed
λ_{pm}	$\text{W m}^{-1} \text{K}^{-1}$	heat conductivity of the porous medium
$\lambda_{\text{H}_2\text{O}}$	mol mol^{-1}	moles of water per mol sulfonic acid in the membrane
μ_α	Pa s	dynamic viscosity of phase α
ϕ		porosity
φ	V	potential
Φ_α^κ		fugacity coefficient of component κ in phase α
Φ_{el}	V	electric potential
Φ_{ion}	V	ionic potential
Π^i	V	Peltier coefficient of reaction i
η_i	V	overpotential of reaction i
Ψ		flux term
Ψ_κ	$\text{mol m}^{-2} \text{s}^{-1}$	molar flux density of component κ
ρ_α	kg m^{-3}	density of phase α
ρ_α^n	mol m^{-3}	molar density of phase α
σ	S m^{-1}	conductivity
σ_T	$\text{W m}^{-1} \text{K}^{-1}$	thermal conductivity
ν_i		stoichiometry coefficient of species i
θ_κ		catalyst surface coverage with $\kappa = \text{PtO/PtOH}$
ξ		storage term

Subscripts and Superscripts

α	phase
κ	component
A	anode
<i>abs</i>	absorption
<i>ads</i>	adsorption
<i>c</i>	capillary
C	cathode
<i>ch</i>	channel
<i>diff</i>	diffusive
<i>des</i>	desorption
<i>Ed.</i>	educt
<i>eff</i>	effective
<i>el</i>	electrode
<i>elec</i>	electric
e^-	electron / electronic
<i>eq</i>	equilibrium
<i>g</i>	gas
H^+	proton / protonic
<i>i</i>	reaction index
<i>int</i>	interface
<i>i, j, k</i>	component index
<i>ion</i>	ionic
<i>l</i>	liquid
<i>liq</i>	liquid
<i>m</i> (subscript)	molar
<i>n</i> (subscript)	non-wetting phase
<i>n</i> (superscript)	molar
<i>nom</i>	nominal
<i>pm</i>	porous medium
<i>Prod.</i>	product
<i>s</i>	solid phase
<i>T</i>	thermal
<i>w</i>	wetting phase

Contents

1	Introduction	15
2	Background	17
2.1	DMFC working principle and characteristics	17
2.2	DMFC performance losses and degradation	19
2.2.1	Irreversible degradation mechanisms	19
2.2.2	Reversible degradation mechanisms	20
2.2.3	Hydrogen evolution in the DMFC anode	22
2.3	Physical Fuel Cell Modelling	22
3	State of the Art	27
3.1	DMFC Models in 1D	27
3.2	DMFC Models in 2D and 3D	30
3.3	Summary: DMFC models on the continuum scale	35
4	Scope of this work	39
5	Model Structure	41
5.1	Software	41
5.2	Modelling Domain	41
5.3	Model Geometry	41
5.3.1	Cell Area	42
5.3.2	Channel Area	44
5.3.3	Channel Length	44
5.4	Numerical Discretisation	45
5.5	Grid Structure	45
5.6	Primary Variables and Boundary Conditions	47
5.6.1	Anode Sub-Domain	47
5.6.2	Cathode Sub-Domain	49
5.6.3	PEM Sub-Domain	50
5.7	Coupling Conditions	50
5.8	Initial Conditions	51
6	Physical DMFC Model	53
6.1	Anode and Cathode Subdomain	54
6.1.1	Mass Conservation	54
6.1.2	Vapour-Liquid Equilibrium	56
6.1.3	Phase Transitions	57
6.1.4	Energy Conservation	57
6.1.5	Charge Conservation	58

6.2	PEM Subdomain	59
6.2.1	Membrane Water Content	59
6.2.2	Sorption Kinetics	60
6.2.3	Conservation Equations	61
6.3	Reaction Kinetics	64
6.3.1	Oxygen reduction reaction	64
6.3.2	Methanol oxidation reaction on Pt-Ru-surfaces	64
6.3.3	Methanol oxidation reaction on Pt-surfaces	64
6.3.4	Equilibrium potential	65
6.3.5	Reaction rates	67
6.3.6	Overpotentials	68
6.3.7	ECSA	69
6.3.8	Heat source from reaction	69
6.3.9	Sinks and sources	69
6.3.10	Ionomer film model	70
6.3.11	Platinum oxide formation	71
7	Model Validation and DMFC Performance Simulation	73
7.1	Transport Processes in the Membrane	74
7.1.1	Water Transport	74
7.1.2	Sorption Processes at the PEM/CL Interfaces	81
7.1.3	Local Water Transport	83
7.1.4	Proton Transport	85
7.1.5	Methanol Transport	87
7.1.6	Conclusion: PEM Transport Processes	90
7.2	Performance Heterogeneities	92
7.2.1	Resistances in the Cathode Catalyst Layer	93
7.2.2	Reference Model	100
7.2.3	Performance simulation with varying stoichiometry	102
7.2.4	Impact of the Operating Mode	105
7.2.5	Impact of the BPP Segmentation	108
7.2.6	Conclusion: Performance Heterogeneities	109
8	Recovery of Reversible DMFC Performance Losses	111
8.1	Formation of Platinum Oxides in the CCL	112
8.2	Boundary Conditions for the Simulation of Refresh Cycles	114
8.3	Refresh Simulation with the 2D Model	115
8.4	Model Convergence during Refresh Simulation	119
8.5	Local Conditions inside the DMFC during the Refresh Cycle	120
8.5.1	Oxygen Partial Pressure	120
8.5.2	Methanol Partial Pressure	122
8.5.3	Reactions in the CCL	123
8.5.4	Local Cathode Potential and Reduction of Platinum Oxides in the CCL	126
8.5.5	Local Potential and Hydrogen Evolution in the ACL	128

8.5.6	Water Activity and Liquid Water Distribution in the CCL	132
8.5.7	Impact of the Secondary MOR in the CCL	133
8.5.8	Variation: Secondary MOR with increased reaction rate	136
8.5.9	Impact of the BPP Segmentation	137
8.5.10	Conclusion: Local Conditions inside the DMFC during the Refresh Cycle	142
8.6	Variation of Air Stop Scenarios during the Refresh Cycle	143
8.6.1	Variation 1: Extended Air Stop	143
8.6.2	Variation 2: Incomplete Refresh	146
8.6.3	Variation 3: Optimised Air Stop Boundary Conditions	150
8.6.4	Variation 4: Nitrogen Flush	154
8.6.5	Conclusion: Variation of Air Stop Scenarios	158
9	Summary	161
	List of Tables	165
	List of Figures	167
	Bibliography	177

1 Introduction

The reduction of greenhouse gas emissions is a fundamental aspect in limiting the global heating and mitigating the worldwide climate change. Hereby, the decarbonisation of the energy sector is a primary goal, which includes the transition from power sources based on fossil fuels towards renewable energy sources and more efficient energy storage and conversion technologies. Fuel cells are an alternative power source in different fields of applications, such as transportation, stationary power supply or portable devices. The technology, which is based on the conversion of chemical energy to electrical energy, has the potential to replace internal combustion engines and thus contribute to the transformation of the energy sector.

In applications with a low power request up to a few kW, the direct methanol fuel cell (DMFC) can be used as a substitute for batteries or diesel engines. DMFCs are polymer electrolyte fuel cells, typically operating at temperatures below 100 °C with air as oxidant and a liquid mixture of methanol and water as fuel.

Methanol (CH_3OH) is a liquid at room temperature and miscible with water in any ratio, which makes its handling and storage easy. Due to its high energy density of 6.1 kWh kg^{-1} it is attractive as a fuel [4]. Methanol is a basic chemical and gets produced and used in large scales by the chemical industry for a wide range of products. Thus, methanol has a high availability worldwide at low costs. Today, CH_3OH is mostly generated conventionally from fossil resources such as natural gas or coal, but new power-to-liquid processes [16, 120, 64, 9, 137] enable the synthesis of 'green methanol' from CO_2 and H_2 in a sustainable way.

The direct methanol fuel cell provides a way for efficient energy conversion with the benefit of fast charging and an uninterrupted power supply for a long operating time [69, 86]. By using liquid methanol as a fuel, the DMFC system does not require advanced storage- or supply techniques, which makes it smaller and easier to install and handle compared to a hydrogen-based polymer electrolyte fuel cell (PEMFC) system. Providing these features, the DMFC becomes an alternative to diesel generators and batteries. Until now, DMFCs have been commercialised in several specific areas, which range from off-grid and backup power supply or auxiliary power units in stationary applications to on-board power supply in caravans and the use as power source for forklift trucks [46, 130].

Despite the successful market entry of DMFCs in several fields of applications, scientific research on the technology is ongoing in order to improve the DMFC's efficiency and durability while lowering its costs. In comparison with the structurally similar PEMFC, which runs on hydrogen and is the favoured solution for mobile applications, the DMFC

shows a lower performance and power density. This is rooted in the complex and slow methanol oxidation reaction in the DMFC anode, the formation of a mixed potential in the DMFC cathode and the development of mass transport limitations during operation due to the complicated two-phase flow in the cell. The DMFC also shows specific degradation phenomena over time, which need to be understood and mastered.

In order to achieve better performances and longer lifetimes with the DMFC, progress in the fields of materials, catalysis and the general fuel cell design is needed in combination with developments regarding the operating strategy.

2 Background

2.1 DMFC working principle and characteristics

The fuel cell converts chemical energy into electrical energy via an electrochemical reaction. It consists of two half cells where individual reactions take place: the anode, where a fuel gets oxidized, and the cathode, where an oxidant gets reduced. The two electrodes are separated by an electrolyte and connected by an outer electric circuit, which means that positive and negative charges (protons and electrons) flow in separate pathways.

Direct methanol fuel cells are low-temperature fuel cells which work with an acidic polymer electrolyte membrane (PEM) at an operating temperature $< 100^{\circ}\text{C}$. The DMFC anode and cathode typically consist of a flow field with a channel structure for the fluid supply, a gas diffusion layer (GDL), a micro-porous layer (MPL) and a catalyst layer (CL), respectively. The anode and cathode catalyst layer are separated by the PEM. Figure 2.1 shows a schematic of the DMFC structure and its working principle for a single cell.

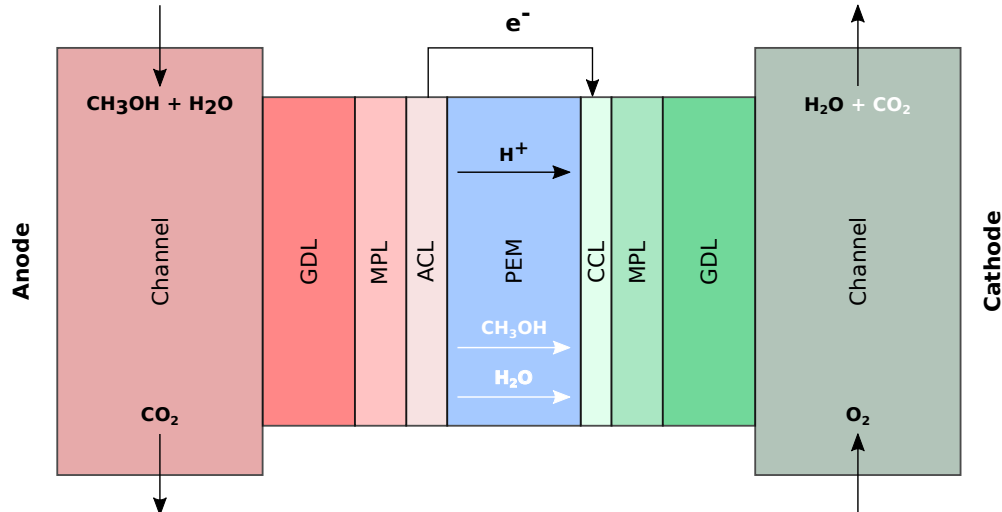
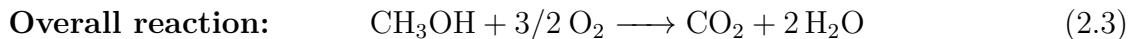
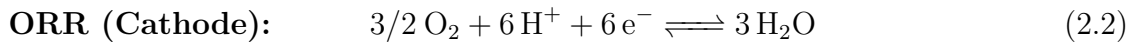


Figure 2.1: Schematic of the DMFC.

The fuel supplied to the DMFC anode is an aqueous methanol solution, whereas the cathode is supplied with air. During the methanol oxidation reaction (MOR) in the anode catalyst layer, methanol and water react to carbon dioxide under the release of protons and electrons. The protons are transported through the polymer electrolyte membrane to the DMFC cathode, whereas the electrons move there via an external electric circuit. In the CCL, protons and electrons react with oxygen in the oxygen

reduction reaction (ORR) under the formation of water.



In the DMFC, platinum and binary platinum-ruthenium catalysts are used to enable the electrochemical reactions [69]. Both half cell reactions, MOR and ORR, comprise multiple steps with several possible reaction paths. The oxidation of methanol is especially complex [65, 49]. During the dissociation and dehydrogenation of methanol on platinum, several intermediate species such as carbon monoxide but also formaldehyde and formic acid are formed [57, 65]. CO is a very stable adsorbate on platinum, which does not easily get oxidised, and thus can deactivate the catalyst (CO-poisoning) [74]. The removal of carbon monoxide in the DMFC anode is enabled by ruthenium, which is added to the platinum catalyst: On ruthenium surfaces, water dissociates easily, providing hydroxyl-species for the oxidation of CO to CO₂ [145, 50, 91, 144]. Due to these rather complicated reaction steps, the MOR kinetics are slow, especially in comparison with the oxidation of H₂ in PEMFCs, and the anode overpotential in the DMFC is non-negligible.

The polymer electrolyte membrane, which separates anode and cathode, is not only permeable for protons, but also for water and methanol molecules [117, 25]. Both species, H₂O and CH₃OH, get transferred through the membrane from anode to cathode during cell operation. As a consequence of the methanol crossover, a methanol oxidation reaction also takes place in the cathode catalyst, in addition to the ORR. The reaction mechanism for the MOR in the cathode is different to the one in the anode, since in the CCL no ruthenium is present to enhance the oxidation of intermediate carbon monoxide species. Instead, dissociated oxygen from the ORR can react with the CO-adsorbates and oxidise them to CO₂ [66]. This side reaction leads to a mixed potential in the DMFC cathode, which in consequence lowers the cell performance [37, 109, 87, 158].

Due to the complicated and slow reaction kinetics in the anode and the parallel reactions in the cathode, high platinum loadings are required in the DMFC. In order to minimise the methanol crossover, aqueous solutions with a low methanol molarity are supplied to the DMFC anode and membranes with a much higher thickness than in PEMFC are used. The development of polymer electrolyte membranes with a lower permeability for methanol is an ongoing field of research.

Water crossover from anode to cathode is another important phenomenon in DMFCs. The liquid anode feed, consisting of an aqueous methanol solution, on the one hand facilitates the hydration of the polymer electrolyte membrane and lowers the membrane's resistance to proton transport. On the other hand, the crossover of H₂O molecules through the PEM also enhances the risk of flooding in the DMFC cathode, where water is also formed as reaction product of the ORR.

The co-existence of gas phase and liquid phase in both electrodes is a characteristic feature of DMFCs: In the anode, where the feed is a liquid methanol solution and the MOR reaction product is gaseous CO_2 , and in the cathode, with air as gaseous feed, H_2O as reaction product of the ORR and H_2O and CH_3OH as crossover species with the possibility of condensation inside the electrode structure. Understanding the transient two-phase flow behaviour in the DMFC and its impact on the fuel cell properties is key to effective fluid management and thus stable and efficient fuel cell operation.

The physical and chemical processes inside the DMFC are complex, as they include a multiphase and multicomponent fluid transport with changing compositions inside the different layers of the cell, in combination with electrochemical reactions and charge and heat transfer. All these processes happen on different scales, through-plane and in-plane, and with varying dynamics in dependence on the actual operating conditions and material properties.

The DMFC thus exhibits a risk for internal heterogeneities with variances in the distribution of phases, species, humidity as well as temperature and charges along and across the cell. Differences in the local operating parameters lead to an inhomogeneous potential and current distribution and thus cell performance [80, 123, 124, 5, 111] and can furthermore result in a heterogeneous cell ageing [36, 17, 111].

2.2 DMFC performance losses and degradation

Apart from the challenges regarding efficient and optimal cell operation, the durability of DMFCs is a key aspect for the success of the technology. Like other types of fuel cells, the DMFC suffers from permanent as well as temporary degradation phenomena [24, 103, 18, 39], and the degradation rates reported for DMFCs are higher than for PEMFCs [2].

Even though the lifetime targets for DMFCs are moderate compared to PEMFCs [69, 92], as the use cases for DMFCs are primarily for portable and stationary applications, the avoidance and mitigation of degradation effects is a major field of research and further efforts need to be made to achieve reliable and durable systems.

2.2.1 Irreversible degradation mechanisms

Structural changes in the different layers of the fuel cell are the major cause for permanent DMFC degradation. The most important irreversible degradation mechanisms concern the integrity of the catalyst layers: As the function of a catalyst is highly dependent on its available surface area, the dispersion of catalytic nano-particles in the catalyst layers is a fundamental concern for the long-term stability of low-temperature fuel cells.

For platinum catalyst particles in the DMFC, the same degradation mechanisms apply as in PEMFCs: The active catalytic area can get reduced by platinum particle detachment, particle growth or particle dissolution [131]. Once dissolved, platinum ions can

re-deposit on other particles (Ostwald-ripening) or precipitate on the carbon support [131, 141]. Also a migration of dissolved platinum ions into and through the membrane can occur [31].

The dissolution of ruthenium particles in the anode catalyst and crossover through the membrane is another relevant factor for the DMFC durability [107, 31, 2, 36, 17, 71]. The loss of ruthenium not only decreases the catalytic activity in the DMFC anode, but its precipitation on the cathode catalyst also blocks catalyst sites for the ORR [107, 45, 121, 27, 36]. Furthermore, the dissolution of ruthenium has been reported to enhance the process of platinum dissolution in the ACL [71].

An additional mechanism which leads to a decrease of the electrochemically active surface area (ECSA) in the DMFC is the agglomeration of catalyst particles, which has been reported for Pt catalysts as well as for PtRu catalysts [27, 28, 68, 121, 41].

The cathode catalyst layer in the DMFC is furthermore prone to carbon corrosion, i.e. an erosion of the catalyst porous structure by oxidation of the carbon support to CO_2 [118, 29], which can occur at potentials $> 0.85 \text{ V}$.

Other irreversible degradation mechanisms in the DMFC concern the ionomer phases, specifically their chemical and mechanical properties [28]. On the one hand, the loss of ionomer in the catalyst layer has been reported [17, 110], which lowers the efficiency of the catalyst. On the other hand, an ageing of the PEM with effects like membrane thinning and membrane delamination can occur [27, 102], which deteriorate the membrane stability and lead to an increase of interface resistances between PEM and electrodes. Moreover, the formation of pinholes in the membrane is possible [102].

In the DMFC porous layers, i.e. GDL and MPL, structural changes affecting the porosity and permeability and alterations in the internal surface properties, e.g. a loss of hydrophobicity [24, 104], can occur, rendering permanently increased resistances to the reaction species' mass transport.

2.2.2 Reversible degradation mechanisms

Also reversible degradation mechanisms play a significant role for DMFCs: When operated in steady-state mode, the DMFC exhibits a tremendous voltage decay rate, which makes a continuous operation without additional measures inefficient and rather impossible [103, 18]. A great share of these observed performance loss is of temporary nature, that is why a periodic interruption of the fuel cell operation is necessary for performance recovery [104, 18].

One factor contributing to the recoverable part of the performance decay in the DMFC is a shift in the two-phase flow balance inside the cell over time in anode and cathode, which can induce mass transport limitations in the catalyst layers and change the gas/liquid transport properties of the porous media [104, 19, 20, 73].

The transport and distribution of CO₂ gas bubbles in the DMFC anode has been widely studied (cf. for example to [150] or [156]) and undoubtedly the removal of CO₂ from the ACL is important for maintaining an optimal supply of the catalyst with methanol [150, 19]. It should be noted that for DMFCs with serpentine channel flow-fields it is rather unlikely that the formation of gas slugs in the anode diffusion layer and channel completely block the transport path for methanol to the ACL [150, 73]. The accumulation of CO₂ in the anode porous media, however, might result in a dehydration of the ACL ionomer phase [19].

Also in the DMFC cathode changes in the two-phase flow balance can cause reversible degradation effects. On the one hand, the accumulation of liquid water in the cathode porous media (also termed as “flooding”) hinders oxygen molecules from reaching the active sites of the CCL and thus deactivates the respective area of the cell [104, 26]. On the other hand, an imbalance in the cathode humidification can render dry areas in the cell, which leads to increased resistances to the proton transport in catalyst layer and membrane [20].

A periodic interruption of the DMFC operation while continuing the media flow in anode and cathode can help to drive out accumulated reaction product species (gaseous CO₂ in the anode and liquid H₂O in the cathode), restore the reactant availability in the catalyst layers and balance out the cell humidification and thus recover the performance losses introduced by mass-transport related processes [39, 104, 18].

Another important reversible degradation mechanism in the DMFC is the formation of platinum and ruthenium oxide species in the catalyst layers, which do not promote the ongoing electrochemical reactions, but instead block active catalytic surface sites. The forming of catalyst surface oxides/hydroxides is very pronounced in the DMFC, due to the high potentials in anode (approx. $0.25\text{ V} \leq \Delta\Phi_{\text{Anode}} \leq 0.5\text{ V}$) and cathode (approx. $0.7\text{ V} \leq \Delta\Phi_{\text{Cathode}} \leq 0.9\text{ V}$) under load.

The role of ruthenium oxide species in the DMFC anode is still under investigation, since beneficial (hydrous) as well as harmful (anhydrous) forms of ruthenium oxides exist [57, 119, 65, 88, 36, 2]. The formation of *anhydrous* RuO₂/RuO₃ can lead to a deactivation of the catalytic activity [119, 65] and has been identified as a reversible catalyst degradation mechanism in the ACL. It can be recovered by applying a potential step to a lower potential [61, 62].

Platinum oxides and -hydroxides occur as intermediate species during the ORR in the cathode catalyst, where they get quickly reduced. In the presence of water, however, also the formation of platinum oxides/hydroxides due to the oxidization of H₂O on the platinum surfaces has been reported. These species do not participate in the ORR but block active surface sites of the catalyst [39, 148]. The mechanism for [PtO] and [PtOH] formation at potentials between 0.75 V to 0.85 V vs. RHE is a relevant degradation mechanism in the DMFC cathode catalyst layer, as shown by Eickes et al. [39]. The

development of these surface species is logarithmic over time and fully recoverable when the cathode potential is brought below 0.5 V, where the platinum oxides and -hydroxides get reduced. This state can be evoked with an “air break” strategy for the DMFC cathode, which has been proven to be a suitable performance recovery procedure [39, 104, 26, 18, 20].

2.2.3 Hydrogen evolution in the DMFC anode

An interesting phenomenon which occurs under oxygen-depleted condition in the DMFC cathode is the evolution of hydrogen in the DMFC anode [154, 153, 122]. The effect has first been observed under OCV-conditions with a low cathode flow rate by Ye and co-workers [154]. Later, the formation of H_2 in the DMFC anode has also been confirmed during recovery procedures with intentional cathode air starvation [20].

The mechanism can be explained as follows: When the oxygen content in the cathode falls below a certain threshold (typically at the outlet position), the oxygen reduction reaction comes to a halt and the methanol oxidation reaction due to methanol crossover becomes the dominant reaction in this part of the cathode catalyst layer. At the same time, the cathode inlet area of the cell maintains its regular operation with the ORR, since sufficient O_2 is available there. Essentially, the cell splits into two different operating zones, with the part including the cathode inlet area operating normally on anode and cathode (“galvanic region”), while the other part (including the cathode outlet area) reverses its behaviour (“electrolytic region”) [154]. The protons produced in the cathode MOR in the oxygen-depleted area move through the PEM to the anode (opposite to the regular cell operation, where the protons are transferred from anode to cathode), while the electrons produced in the MOR migrate *in-plane* in the CCL towards the ORR zone. On the anode side of the “electrolytic” region, the protons transferred through the membrane from the cathode side form H_2 together with electrons from the “galvanic” region of the anode.

2.3 Physical Fuel Cell Modelling

Physical modelling of low-temperature fuel cells can help to generate a deeper understanding of the cell behaviour and experimentally observed phenomena.

Depending on the scope and purpose, different types of fuel cell models exist, which differ with regards to their scale (nano-, micro-, meso- or macro-scale) as well as their dimension (1D to 3D) and their degree of detailing the physicochemical processes inside the fuel cell.

Describing the processes inside the fuel cell in a model is not trivial: The challenges include portraying the multiphase and multicomponent fluid transport through the cell, with changing transport properties inside the different layers, in combination with complicated electrochemical reactions as well as charge and heat transfer. These processes happen through-plane and in-plane and on different scales, i.e. the micro-, meso- and

macroscale, with varying dynamics in dependence on the actual operating conditions.

1D continuum models allow an investigation of the overall cell behaviour as well as individual effects like reaction kinetics with a high degree of detailing in dependence on specific boundary conditions. The missing spatial resolution along or across the channel, however, limits the ability to study interactions between different processes and parameters within the fuel cell structure, which are highly coupled to each other.

A detailed analysis of individual structural effects and morphologies and their impact on parameters like the wetting-behaviour in a layer can be achieved with 3D microstructure models. Microstructure models are also used to predict volume-averaged transport coefficients for a specific material, which then can be used in macroscopic fuel cell models [147]. Models focussing on the microstructure and the transport phenomena within are limited to a narrow modelling domain due to the high computational costs and thus not suitable for portraying the entire cell behaviour regarding the interactions of species, charge and heat transfer.

In order to study the overall cell behaviour in dependence of the internal conditions as well as local heterogeneities across the cell, multidimensional, i.e. 2D or 3D, models on the continuum-scale can be used. These macroscopic fuel cell models build the link between detailed micro- or mesoscale models on the one hand, which often focus on single phenomena like water transport, and stack models, which do not resolve the detailed physical processes inside the cell, but phenomenologically describe the overall fuel cell behaviour. With a multidimensional fuel cell model, the simulation of the complex interplay between fluid transport in combination with heat and charge transfer as well as electrochemical reactions within a single cell is possible.

A continuum-scale fuel cell model requires a mass and momentum balance, a charge balance and an energy balance. These governing equations have to be solved for every conservation species at every point in the cell or rather the modelling domain. Due to the multiphase and multicomponent problem in low-temperature fuel cells (and especially the DMFC), also phase transitions and the thermodynamic relation between the species have to be considered.

The mass transport in the fuel cell is strongly determined by the properties of the materials used in the fuel cell structure. The different layers of the fuel cell, i.e. the gas channels, gas diffusion layers, microporous layers, catalyst layers and the membrane vary substantially regarding their morphology and surface characteristics and consequently exhibit individual resistances to mass transport.

In the channels of the fuel cell's flow fields, species transport can be described by classical fluid dynamics. Within the GDLs, MPLs and CLs with their heterogeneous and porous structure, however, the porous media theory has to be applied.

GDL and MPL mostly consist of PTFE-coated carbon fibres, which create a solid ma-

trix with pores in the nano- and micrometer range. Every material has a distinct pore size distribution, porosity, permeability and (internal) wettability. The resistance to fluid transport in these materials is furthermore determined by their capillary properties, which differ depending on whether the material is in contact with a gas or a liquid phase (or rather “wetting” and “non-wetting” phase). The correlation between capillary pressure and saturation is of great importance for the two-phase flow behaviour in the fuel cell. For models on the continuum scale, effective transport properties and capillary pressure-saturation relations have to be derived for each layer of the fuel cell. These properties could either be determined by experiments or from suitable microstructure models.

The catalyst layer consists of ionomer and catalyst particles dispersed on a porous carbon matrix, creating an even more heterogeneous microstructure compared to MPL and GDL, with special resistances towards gas and liquid transport. The ionomer phase enables the transport of protons to and from the catalyst surface, where the electrochemical reactions take place and thus the sinks and sources for charges and species have to be considered. The electrochemical reactions can be either portrayed with elementary kinetics, which include the individual reaction steps on the molecular scale, or with global reaction kinetics, which phenomenologically describe the electrochemical reactions. The resulting sinks and sources for mass, charges and heat are derived from the reaction rates.

The transport inside the membrane is fundamentally different from the transport in the porous media: While the morphology of the solid porous media and their characteristics regarding mass transport are more or less stable, the properties and the structure of the polymer electrolyte membrane strongly depend on its degree of hydration. The uptake of water into the membrane is a characteristic feature which determines the transport of species as well as of protons through the ionomer [82]. A two-phase flow regime with a distinction between a gas and a liquid phase does not exist in the membrane, instead species transport happens rather coupled to or dissolved in the very ionomer structure [78].

At the interface between membrane and catalyst layers, mass, heat and charge transfer occurs between layers with significant differences in their structural and physicochemical properties. In addition to that, non-equilibrium processes like phase-dependent water sorption or membrane swelling take place, which influence the behaviour of the polymer electrolyte [52, 89]. The description of these interface processes and the coupling between the different domains (in case a multi-domain approach has been chosen for the model) in the fuel cell is a major challenge for physical modelling. Most macroscopic models assume the catalyst layer as infinitesimally small and thus do not discretize them spatially. When it comes to local effects and the transfer of charge, heat and species over the PEM/CL interfaces, however, the conditions *inside* the CL are of fundamental importance and must not be neglected [147, 44].

Not only mass transport is essential for describing the fuel cell function, but also charge transport. In the electrochemical reactions in anode and cathode catalyst layer protons as well as electrons are produced or consumed. The fuel cell’s working principle is based

on the separation between positive and negative charges. While the carbon structure in CL, MPL and GDL is electronically conductive and enables electron transport between catalyst layer and current collector at the channel wall, the protons are only able to move within the ionomer phases, i.e. catalyst layer ionomer and polymer electrolyte membrane, which do not conduct negative charges. This requires the formulation of two individual charge balances for H^+ and e^- , which render the distribution of the ionic as well as the electric potential within the cell.

The heat transfer is another important aspect in fuel cells, which are usually operated with a temperature control. The heat generated in the electrochemical reactions and due to ohmic losses in the membrane has to be transported through the cell. All materials in the fuel cell exhibit a certain heat capacity and thermal conductivity and thus enable the heat transfer from the cell towards the current collector.

Considering all these aspects, i.e. the electrochemical reactions as well as mass, charge and heat transport in dependence of their individual resistances per layer, the fuel cell performance can be simulated.

A great number of effective parameters and correlations has to be derived or approximated from experiments for a fuel cell model on the continuum scale. Many transport parameters in the fuel cell not only depend on one variable like the temperature, but on several others, like the humidity or the compression of the structure, too. This imposes a challenge for parameter derivation, since individual properties can easily get over- or underestimated.

For any model, a sound validation against experimental data is thus recommended in order to prove the meaningfulness of the simulation and the validity of the model description. Given the complexity of the processes inside the fuel cell, the comparison of a simulation result to a single experimental polarisation curve, which relates the cell voltage to the current density as a result of charge and species transport and temperature combined, is strictly speaking not sufficient to verify a model. Instead, it would be desirable to also scrutinize the mass, charge and heat transport individually, if experimental measurements are available.

3 State of the Art

The exploration of the DMFC as a power source started in the 1950s, and research activities on the topic have accelerated since the 1990s [4]. Today, plenty of experimental studies on materials and catalysis as well as on DMFC performance and degradation exist, while modelling studies on the behaviour of DMFCs are less common.

The first DMFC models date back to the late 1990s and were mostly steady-state mathematical models in 0D or 1D. They were used to address fundamental topics for the functioning of the DMFC like methanol crossover [32, 136, 128, 37], the effect of the mixed potential in the DMFC cathode [136, 37] and the impact of the two-phase phenomena in the DMFC [136, 128]. Over the years, also modelling studies on dynamic phenomena inside the DMFC arose [135, 126], as well as transient models with a focus on performance degradation [54, 66].

Numerical models with a spatial resolution in 2D and 3D using computational fluid dynamics occurred shortly after the year 2000 [35, 143, 151, 149]. The mass transport within the cell, two-phase flow phenomena and the overall cell performance in dependence on different structural cell parameters and operating conditions are the leading topics in these studies [151, 73, 48, 139]. In some cases, multidimensional models are also used for investigating specific operating conditions like the starvation of reactants or the cell behaviour during start/stop scenarios [155, 152].

In the following sections, an overview of selected DMFC models on the continuum scale is given and relevant multidimensional modelling studies are discussed in detail.

3.1 DMFC Models in 1D

The first DMFC models with a spatial resolution in 1D were used to study the sensitivity of mass transport and performance to the layer thickness [14, 37], the thermal behaviour of a DMFC stack [3] as well as to analyse the distribution of reaction species and mass transport limitations [129, 128]. The works of Scott, Sundmacher, Cruickshank and Dohle include a model validation with experimental cell performance data under various methanol feed concentrations and/or temperatures [32, 128, 136, 37] and water and methanol crossover rates [32, 37].

In 2002, Meyers and Newmann presented a detailed thermodynamic framework for the transport of protons, water and methanol within the DMFC membrane [94, 95]. The authors formulated their conservation equations in dependence of the chemical potential, respectively, and considered sorption processes into the membrane for water as well as for methanol. The 1D steady-state model included species transport through the gas

diffusion layers, the catalyst layers and the membrane and considered elementary reaction kinetics in anode and cathode. The model formulated the electrodes as single phase problems with a liquid phase in the anode and a gas phase in the cathode. It was used to study the performance of the DMFC in dependence on the membrane thickness as well as the methanol concentration [96]. The methanol crossover through the membrane was validated for various feed concentrations in the DMFC anode.

Siebke et al. [132] developed a DMFC model in 1D in order to study the limiting processes for the DMFC performance. In the model the gas/liquid interactions in the DMFC were considered with the formation of liquid water in the porous media, a phase-dependent membrane humidification and the effect of water film formation in the cathode catalyst layer. The study incorporated an extensive experimental validation of the model with polarisation curves with varying O_2 -concentration, temperatures, cathode humidification levels and air flow rates. The model was able to phenomenologically depict the described variations without any parameter fitting and the study highlighted the impact of the cathode potential on the DMFC performance.

Casalegno et al. [23] developed an isothermal steady-state 1D+1D model of the DMFC, considering two phase flow in the anode and one single phase in the cathode. The study focused on the effect of temperature and methanol stoichiometry on the cell performance. A model validation was performed against experimental polarisation curves as well as the methanol crossover rate at different temperature levels. In a later publication, the model was used to study the effect of methanol crossover in the DMFC in combination with experiments [22].

Zago [159] extended the 1D+1D model presented by Casalegno et al. by including water transport through the membrane and a two-phase flow in the DMFC cathode. A cathode flooding model was further added and integrated in the framework. The model was validated against experimental data for the water crossover and polarisation curves for a DMFC operated at two different methanol stoichiometries. Later, Zago's model was used to study the effect of an anode MPL on the transport and distribution of water and methanol within the DMFC [157].

Ko et al. [76] presented an isothermal two-phase model for the DMFC in 1D with five layers in the MEA. The membrane was assumed to be fully hydrated and methanol and water crossover through the membrane were considered in the model. No individual charge balances were solved, instead the cell voltage was derived in dependence on the current, the overpotentials and membrane and contact resistances. Water flooding in the DMFC cathode was considered by correlating the effective oxygen diffusion coefficient to the liquid saturation of the porous medium. With their DMFC model, the authors studied the sensitivity of the cell performance with respect to methanol feed concentration and temperature as well as the influence of these parameters on the methanol crossover. The simulation results were compared to experimental performance data for twelve different temperature/concentration combinations and a good agreement between model and experiments was achieved with one single set of parameters, i.e. the model

was not adjusted for the different cases. Moreover, the methanol crossover rates were validated against experimental data with a variation in temperature, membrane thickness and methanol feed concentration.

Also dynamic DMFC models have been developed since the early 2000s: Sundmacher et al. [135] and Zhou et al. [162], for example, presented mathematical models including elementary kinetics for the electrochemical reactions in the anode and cathode catalyst. In combination with experiments, the effect of dynamically changing methanol feed concentrations on the cell performance was studied.

Schultz and Sundmacher further developed a 1D model for studying multicomponent mass transport phenomena and cell performance of the DMFC [127]. The non-isothermal model incorporated a spatial resolution of the catalyst layers and assumed Butler-Volmer kinetics in both electrodes. The model was experimentally validated in terms of water and methanol crossover rates as well as cell performance for different temperature levels. In a following publication [126], the authors extended their model with two variants of more detailed anode and cathode reaction kinetics and used it to study the dynamic cell response to changes in the methanol feed concentration in the DMFC anode. Again, the model verification was performed against own experimental performance data.

Gerteisen presented a detailed transient model for the DMFC membrane electrode assembly in 1D and studied the formation of mixed potentials in the DMFC anode and cathode as well as the effect of catalyst poisoning [54]. The work focussed on electrochemical phenomena, so the catalyst layers were spatially resolved in the model and the formation of intermediate species on the Pt- and Ru-catalyst were considered in the reaction kinetics. The model accounted for the crossover of methanol from anode to cathode as well as oxygen crossover in the opposite direction.

With his model, Gerteisen studied the development of the local potentials, the methanol distribution within the cell and the impact of the MOR in the cathode catalyst. The model was further used to simulate a dynamic relaxation of the DMFC anode potential in dependence on methanol stoichiometry and current loads, which had been previously experimentally observed by the author. The phenomenon could be explained by the formation of a mixed potential and CO-poisoning in the DMFC anode catalyst. Additionally, the local distribution of species as well as catalyst surface coverages and reaction rates within the MEA were presented.

Jahnke et al. [66] developed a transient 1D model for the DMFC with a detailed description of the electrochemical reactions as well as the individual potentials in the membrane and the electrodes. The model considered the two-phase transport in the DMFC anode and water and methanol crossover through the membrane. The membrane's transport parameters included a dependency on the membrane's water content. Elementary kinetics for MOR and ORR in the DMFC anode and cathode were implemented. The authors presented a thorough validation of their model against a set of experimental performance data, methanol crossover rates and impedance spectra. The model was used to simulate

the steady-state performance, the cell's impedance as well as the transient DMFC behaviour under load jumps and load cycles, and a special focus was brought to the effect of methanol crossover and CO-poisoning.

3.2 DMFC Models in 2D and 3D

Divisek et al. [35] presented a detailed numerical model for the DMFC membrane electrode assembly in 2D, considering two-phase flow in the porous media and elementary kinetics in the spatially resolved catalyst layers. The gas and liquid flow in the MEA was described according to the porous media theory, with a simplified approach for the DMFC membrane. The model was verified against performance data with different methanol feed concentrations. With their non-isothermal model, the authors investigated the distribution of methanol, liquid saturation and temperature within the cell for different operating conditions and the corresponding cell performance.

Ge and Liu [51] published a 3D two-phase model for the DMFC with a single domain continuum approach, including anode and cathode channels, GDLs and CLs as well as the membrane. The isothermal steady-state model followed the multiphase mixture theory. No individual charge balances were solved, i.e. the cell voltage was calculated as function of overpotentials and resistances. The reaction kinetics were described via Tafel equations. Methanol crossover due to electro-osmotic drag and diffusion was considered, but no MOR in the CCL was solved and water crossover through the membrane was neglected in the study. The model was used to analyse the species distribution along the channel and across the cell on the anode side of the DMFC, with a focus on the liquid saturation and carbon dioxide dispersal. The simulated cell performance was compared to experimental data for one stoichiometry-temperature-condition.

Yan and Jen [149] developed an isothermal two-phase DMFC model in 2D and followed a single domain approach including MEA and channels (the catalyst layers were not spatially resolved) with a multiphase mixture model. A capillary pressure-saturation relation was not considered in the porous media and the model did not account for individual charge balances. The membrane was assumed to be fully humidified. A validation of the model against experimental performance data at two temperatures was shown. With their model, the authors studied the sensitivity of the DMFC performance on its operating parameters, i.e. methanol feed concentration, temperature, pressure and stoichiometry as well as the membrane thickness.

Yang and Zhao [151] presented an isothermal two-phase model of a DMFC in 2D in order to study the mass transport within the cell. The model provided a spatial resolution of the catalyst layers in anode and cathode and considered methanol as well as water crossover through the membrane. The membrane was assumed to be fully hydrated, diffusive water transport in the PEM was thus neglected in the model. The model contained individual layer domains, which were coupled through interface continuity conditions. The electro-chemistry was described via global reaction kinetics and

an agglomerate model was considered for oxygen transport in the CCL, incorporating among others the effect of a liquid film resistance in the catalyst. Methanol oxidation in the CCL was considered in form of a parasitic current density, but not solved with individual kinetics. Also the potential within the cell was not solved individually, but calculated as a boundary condition from overpotentials and resistances in the cell. The study provided a model validation against polarisation curves for different methanol feed concentrations from literature. With their model, the authors studied the distribution of species and phases across the cell and the effect of the anode flow rate and the porosity of the individual layers on the overall cell performance and the methanol crossover rate.

Jung [72] presented a non-isothermal 3D DMFC model considering the two-phase flow in the cell for studying the effect of the micro-porous layer in anode and cathode on the phase distribution and the crossover of water and methanol. The multiphase mixture model integrated a “saturation jump” model for the liquid saturation at the interface between the different porous layers. Water as well as methanol crossover through the membrane were considered, with the membrane assumed to be fully fully hydrated. The model did not account for individual charge balances, instead, a simplified approach for calculating the cell voltage was used. The model considered a “heat pipe” effect in the energy balance. Two different cell set-ups (parallel flow-field and serpentine flow-field) were looked at in the study.

The author presented current density distributions along the cell and liquid saturation distributions through the MEA. The impact of an MPL in the anode and cathode electrode was studied in detail with respect to the saturation distribution in each layer for various MEA configurations (with and without MPL). Also temperature distributions were shown and phase changes and thermal diffusion effects indicated. Moreover, the methanol concentration distribution in the anode catalyst layer as well as the “crossover current density” and overall current density in the cell were given for varying stoichiometries. Unfortunately, Jung’s study did not provide any model verification.

Ye et al. [155] developed a steady-state 2D DMFC cell model for studying the evolution of hydrogen in the DMFC anode during OCV under oxygen depleted conditions in the DMFC cathode. Their non-isothermal along-the-channel model considered a single phase in anode and cathode and was set up in one single domain. The transport of methanol and water through the membrane were described by diffusion and electro-osmotic drag. Water sorption was considered at the PEM/CL interfaces and the membrane’s transport parameters were expressed as functions of the membrane’s water content. The charge balances were expressed individually for protons and electrons.

The authors showed the oxygen concentration in the CCL along the channel for various air flow rates at the cathode channel inlet and the corresponding local ionic potential and current density in the ACL over the channel length. The formation of two reaction zones in anode and cathode with galvanic and electrolytic operation was identified in dependence on the local oxygen availability in the cathode catalyst layer. The authors correlated the hydrogen evolution rate in the ACL to the the air flow rate in the cath-

ode upstream (with its corresponding oxygen-depleted area in the CCL). Not only the effect of variations in the air flow rate in the cathode at OCV was analysed, but also the impact of flooding in the cathode catalyst on the development of heterogeneous DMFC operation due to oxygen depletion in the CCL was studied.

No direct model validation was given by Ye and co-workers, however, their modelling study was grounded on their own previous experimental findings on the development of hydrogen in the DMFC anode at OCV at a critical air flow rate [153]. Moreover, their simulation results for an assumed flooding induced air starvation in the DMFC cathode at OCV and consequential development of a galvanic and electrolytic region in the cell showed a good agreement with experimental results of Kulikovsky et al. [80], who found an inhomogeneous current distribution along the channel in case a critical minimum air flow rate was applied to the cell.

The steady-state model was later extended with a two-phase flow description in the DMFC cathode and the option for a hydrogen evolution reaction in the cathode by Yang et al. [152], who studied the effect of oxygen depletion in the DMFC cathode under load both experimentally and numerically. Severe inhomogeneities in the local current density along the channel were observed for the studied cases with a low air stoichiometry, with local current densities one order of magnitude higher than the overall output current density. The authors identified this effect as a possible cause for ruthenium dissolution in the DMFC anode catalyst layer. As a further consequence under even more extreme conditions for the mal-distribution of air, a local reversal of the cell potential and a hydrogen evolution in the DMFC cathode was mentioned.

García-Salaberri et al. [48] presented a steady-state 2D+1D model across-the-channel for a liquid fed DMFC, based on the work of Vera [140], with a spatially resolved anode GDL. The aim of their work was to study inhomogeneities due to compression of the flow-field in the distribution of species in the anode GDL. The isothermal model put a focus on the effective material properties of the GDL and the two-phase flow in the DMFC anode within the porous medium and at the GDL interface to the flow-field with its channel-rib-structure.

While the model's description of the anode GDL included a multiphase approach resolved in 2D, the remaining layer of the DMFC, i.e. anode channel and catalyst layer, membrane and cathode catalyst layer, GDL and channel were presented as single-phase 1D models. The model assumed the membrane to be fully hydrated and accounted for water transport through the membrane by electro-osmotic drag only, while for methanol, also diffusion was considered. Only one charge balance rendering the electric cell voltage in dependence of resistances and overpotentials was taken into account, i.e. the ionic potential in the membrane and catalyst layers' ionomer phase were not reflected by the model.

The authors incorporated the *van Genuchten* approach for the anode GDL's capillary pressure-saturation relation with GDL-specific parameters from the experimental work of

Gostick et al. [55] and compared the resulting flow velocities and distribution of the gas phase to simulation results obtained with the commonly used *Leverett* function. They found substantial differences in the resulting predictions of the gas/liquid distribution in the porous medium and stated that a description of the capillary transport with the *Leverett* function renders physically inconsistent results.

The model of García-Salaberri was not validated against experimental data, while the basic model of Vera was verified on experimental DMFC polarization curves for different methanol concentrations in the anode feed. With their model, the authors studied the effect of compression on the GDL from the channel-rib-structure of the flow-field regarding the distribution of gas and liquid phase within the DMFC anode.

The model was later extended with a 2D description of the cathode GDL [47], while the fuel cell channels, the catalyst layers and the membrane remained as 1D models. With their extended model considering two-phase flow in anode and cathode GDL, the authors portrayed the effect of oxygen starvation in the DMFC cathode and the evolution of hydrogen in the DMFC anode under the oxygen-depleted conditions, as described by Yang et al. [152]. The model was verified against experimental and numerical data from other groups with polarization curves and limiting current densities for different methanol feed concentrations.

Wang and Sauer [142] developed a transient single-phase model of a DMFC with a spatial resolution in 2D which was coupled with a DMFC system model. The model covered the fundamental aspects of mass transport through the different structures of the DMFC but neglected two-phase flow effects. It included a simplified modelling approach for the cell voltage, without solving charge balances individually. The model considered a fully hydrated membrane and omitted the water crossover in the DMFC. The non-isothermal FEM model in co-flow mode was validated against a global polarization curve.

The authors studied the dynamic response of the DMFC in the system to a load jump with regard to the reactant supply across the membrane electrode assembly and along the channel. They found the methanol concentration profile in the anode channel to differ from the concentration profile in the anode catalyst layer, with an concentration undershoot and potential overshoot in the ACL during a load jump. The extend and dynamics of the methanol crossover through the DMFC membrane were found to directly follow the methanol concentration in the anode catalyst layer. The authors further showed the variations in the local current density in dependence of the position along the channel.

The performance heterogeneities along the channel determined in this study arose merely from the reactant availability and were not linked to local inhomogeneities in the material properties in the cell, e.g. in dependence on the humidification, which are known to affects charge- as well as species transport, especially in membrane and catalyst layers.

Vasile et al. [138] presented a 3D model for a DMFC single cell with 7 individual domains, comprising the flow field, the GDLs, the CLs and the membrane. In each layer,

an individual set of governing equations was solved and the domains were sequentially coupled. The model could be solved for steady-state conditions as well as dynamic conditions. Methanol and water crossover through the membrane was considered, and a differentiation between the electric potential in the solid structure and the ionic potential in the ionomer phase of the fuel cell was made, i.e. individual charge balances for H^+ and e^- were solved.

The model was non-isothermal and considered a two-phase flow in the porous media. The capillary-pressure saturation relation in the porous layers was expressed with the *Leverett* function. The membrane was assumed to be fully hydrated and water crossover was expressed only via electro-osmotic drag, while for the methanol crossover, diffusion and electro-osmotic drag were considered as transport mechanisms. The methanol oxidation in the cathode catalyst was described individually via an oxygen-activated reaction path. The description of the ohmic resistance or rather the transport of protons through the membrane was not further specified in the publication.

The authors fitted the model's electrochemical parameters to experimental polarisation curves of a commercial DMFC for different combinations of methanol feed concentration and operating temperature. A major draw-back of this model is that for every set of concentration- and temperature-boundary conditions a different parameter set of charge transfer coefficients for MOR and ORR was applied in the model. This procedure questions whether the physical description of mass and charge transfer in the model covered all relevant dependencies and thus the models predictiveness.

With their model, Vasile et al. studied the local methanol distribution, the local current density and the local temperature within the DMFC single cell at different operating temperature and methanol concentration combinations. The authors presented the modelling results for several catalyst loading configurations, starting from a uniform anode catalyst distribution to an optimized, inhomogeneous catalyst loading within the cell.

Later, the model was used in combination with experiments to investigate the impact of the flow field design and membrane type on the methanol crossover and the DMFC performance [139]. Experimental results for membrane diffusion coefficients of H_2O and CH_3OH at different temperatures and methanol feed concentrations were shown for several membrane types. These parameters were incorporated in the model. Like in their first publication, the model's electrochemical parameters were fitted for every set of boundary conditions, rendering a high agreement between the simulated polarisation curves with the experimental data on the one hand, but raising doubts about the physical description and model predictiveness.

The authors presented the methanol consumption rates, the gas flow velocity in the channels as well as the local current density distribution within the cell as modelling results for different flow field patterns and membrane types in 2D. Moreover, crossover rates for water and methanol and the anodic overpotential resulting from the simulations were shown.

3.3 Summary: DMFC models on the continuum scale

In the past two decades, a range of DMFC models on the continuum scale have been developed for studying the behaviour and performance of the direct methanol fuel cell and its sensitivity to operating parameters as well as cell design. While the core description of mass, charge and heat transport in the cell is similar, the models reviewed in this chapter vary strongly with regard to their detailing and formulation of the physics inside the cell.

The variances range from the model structure itself (single-domain or multi-domain, transient or steady-state, 1D or higher dimensional, amount of layers depicted in the modelling domain), to the description of the electrochemical reactions and the cell potential, the coverage of the gas/liquid interplay in the different layers and the coupling between processes in the porous domains and the membrane, and the ionomer's very properties.

Many models, especially those in 2D and 3D, put a strong focus on the description of the two-phase flow within the DMFC with a variety of modelling approaches. Often, a multi-fluid [8] approach with *Darcy's* law is included for accounting for the species transport within the porous domains and, in most cases, the *Leverett* function is used to formulate the capillary pressure-saturation relation in the porous media. Experimental studies on commercial GDL materials, however, suggest that other phenomenological relations like the *van Genuchten* or the *Brooks-Corey* law better represent the wetting properties of the porous layers in the fuel cell [55, 160].

Surprisingly, even though a great number of models describe the gas/liquid interactions and the distribution of gas and liquid phase in the DMFC in detail, a direct correlation between the two-phase flow conditions in the cell and the actual cell performance is hardly discussed.

Numerous DMFC models work with a strongly simplified description of the membrane behaviour and its properties, even though it is known (cf. for example Kusoglu et al. [82] or Kreuer et al. [78]) that the polymer electrolyte membrane is highly sensitive to the humidity and phase conditions in the cell and its properties regarding mass transport as well as ion transport significantly change with the degree of humidification.

In most cases, the DMFC membrane is assumed to be “fully hydrated” and the membrane's transport parameters for species and protons are formulated independent of the actual humidity, despite this property could be derived from the elaborate two-phase flow descriptions, which many models offer, with little effort.

The water crossover through the DMFC membrane is then either completely omitted or, implied by the assumption of a fully hydrated membrane without a concentration gradient for water, solely attributed to hydraulic permeation and electro-osmotic drag.

With such a strong simplification in the model's membrane description, an announced studying of two-phase flow effects in the cell then in reality is restricted to the porous domains and channels of the DMFC, but does not truly cover the gas/liquid interplay in the entire membrane electrode assembly.

The methanol crossover in the DMFC, on the other hand, has been always considered in the models reviewed here and is usually described by mass transport through the membrane via diffusion and electro-osmotic drag. The reaction of crossover methanol in the CCL, however, is often not accounted for as an individual reaction, instead, a "parasitic current" is considered in a simplified electrochemical model.

Individual charge balances in electrodes and membrane, which would render the electric and ionic potential distributions across the cell in the different layers, are frequently not considered in DMFC performance models, especially not in the 2D and 3D models. The electrochemical performance of the cell is then described solely in form of a relation for the electric cell voltage as function of current density, overpotentials and resistance terms.

This simplified approach limits a model's possibility to study a relevant characteristic of the cell, namely the local cell potential and performance behaviour, which cannot easily be measured experimentally. On the other hand, those modelling studies which focussed on the individual potential distributions within the cell rendered new insights and explanations that supported or complemented experimental observations.

Most of the higher-dimensional models use global reaction kinetics to formulate the electrochemical reactions instead of elementary kinetics, mainly due to the computational costs, while in several one-dimensional studies, elementary kinetics are looked at.

An interesting aspect is whether or not the catalyst layers are spatially resolved in the continuum models. Frequently, the catalyst layers are only considered as infinitesimally small layers between membrane and GDL, despite an otherwise complete spatial resolution of the cell. With this approach, one of the most challenging aspects of modelling polymer electrolyte membrane fuel cells [147] is neglected, and relevant interactions and dependencies for mass and charge transport in the cell get overlooked.

Also outstanding is the fact that degradation phenomena in the DMFC have so far scarcely been investigated theoretically (especially not with multidimensional models). This finding, on the other hand, is consistent with the low number of DMFC models which consider details in the catalyst layers and resolve them spatially.

Lastly it should be noted that among the higher-dimensional DMFC models which have emerged over the past two decades, a surprising amount of works lacks a verification of the theoretical results, while detailed studies on the cell performance behaviour and mass transport phenomena with spatially resolved simulation results are presented.

A careful model validation should be imperative for these works, due to the complex

matter of the cell's physics and the strong coupling between individual effects. To cover this, one should not only focus on the overall cell performance, but also address the mass, heat and charge transfer through the MEA, which is so fundamental for the functioning of the DMFC.

The 1D DMFC models discussed here provide a broader and more detailed model verification against experimental data in many cases, including the mass transport of water and methanol through the MEA as well as the cell performance under varying operating conditions and even electrochemical characteristics via impedance spectra.

4 Scope of this work

In this thesis, a transient, physics-based model of a DMFC single cell in 2D is presented, which exhibits a comprehensive description of the complex and highly coupled processes inside the direct methanol fuel cell.

The model is used to study the local conditions in the DMFC and their impact on the cell performance, especially with a focus on humidity-related phenomena. Performance heterogeneities within the cell, which have been experimentally observed, are examined in detail with the model, and important influence factors and processes for the observed cell behaviour are identified.

The macroscopic model features a spatial resolution of the fuel cell's catalyst layers, in contrast to the majority of DMFC models reported in literature. This trait allows to study the development and effect of heterogeneities inside the DMFC catalyst layers with regard to the local cell performance and later with respect to the recovery of temporary performance losses.

The model aims to enable a better understanding of the effect of the two-phase flow conditions inside the DMFC on the cell performance, and focuses not only on the gas/liquid interactions in the cell's porous media, but also on its effect to species transport within the DMFC membrane. The impact of the local humidity distribution on surface processes in the catalyst as well as interface processes between membrane and catalyst layers is carefully examined. These features distinguish this work from the majority of DMFC models published in literature, which assume the membrane to be fully humidified and neglect the humidity-dependence of the membrane's transport processes and interactions at the interface to the catalyst layers.

This work includes an extensive model verification for mass and charge transport as well as performance. Local performance data from a macro-segmented cell under varying humidity conditions from the experimental work of Rabissi et al. [111] is used for validating the 2D continuum model *locally*. The modelled mass transport of methanol and water through the DMFC membrane is verified against experimentally obtained crossover rates. In addition to that, the membrane's resistances to charge transport are confirmed with locally resolved impedance spectra. This distinguishes the presented work from many other modelling studies on DMFC, which rarely offer such a thorough and detailed validation approach.

The model predictions about the DMFC behaviour are later tested against experimental performance- and mass transport data for varying stoichiometry conditions in the cell, which have not been part of the data set for model calibration.

The validated cell model is then used to study the transient processes in the DMFC during the recovery of reversible cathode degradation. The formation and reduction of surface oxide species on the cathode catalyst in dependence on the actual reactant distribution and electrochemical reactions along the channel is explored in transient simulations and analysed with respect to the spatial distribution within the cathode catalyst layer. Moreover, the frequently observed production of hydrogen in the DMFC anode under oxygen-depleted conditions in the DMFC cathode is reproduced.

With the 2D model presented here, the impact of different influence parameters and chemical reactions on the recovery of the DMFC cathode's catalyst surface area during a refresh procedure can be distinguished. Moreover, several variations of possible refresh procedure are compared with regard to their efficiency to reduce platinum oxide surface species and thus recover the electrochemical activity of the catalyst.

Overall, this modelling study shall render insights into local conditions and processes within the DMFC which are experimentally not or not directly accessible.

5 Model Structure

A two-dimensional, transient DMFC model was implemented in the modelling framework NEOPARD-X [43, 44], which allows the physical modelling of fuel cells and electrolyzers on the continuum-level. NEOPARD-X is based on the porous media flow simulator DuMu^x [42], which in turn depends on DUNE [10, 11].

The model uses the continuum approach for porous media [7] with effective transport properties based on a representative elementary volume (REV).

5.1 Software

In this work, DuMu^x version 2.7 and DUNE version 2.3.1 are used. Required software packages are Dune PDE-Lab [13] (version 2.0.0), DUNE-Multidomain [98] (version 2.0) and DUNE-Multidomaingrid [99] (version 2.3.0), UG [12] (version 3.11.0) and SuperLU [34] (version 4.3).

5.2 Modelling Domain

The 2D model represents a nine-layer DMFC single cell 'along the channel' in counter-flow mode, as depicted in figure 5.1. A straight flow channel is assumed in anode and cathode, respectively. All nine layers of the cell model are spatially resolved, including the anode and cathode catalyst layer.

The modelling domain is divided into three sub-domains for anode, cathode and PEM. The anode and cathode sub-domains comprise four layers each, namely channel, GDL, MPL and CL, while the membrane is a sub-domain on its own. The balance equations solved in each sub-domain differ from each other, that is why coupling conditions apply at the interface between two sub-domains (cf. sections 5.6 and 5.7).

5.3 Model Geometry

The model's geometrical parameters are derived from the 25 cm² DMFC single cell used in the experimental work of Rabissi et al. [111]. The experimental cell has a triple-serpentine flow-field on anode and cathode, while the 2D model only comprises one single channel in anode and cathode and does not depict the perpendicular channel-rib-structure of the flow-fields. That is why several abstractions regarding the model geometry have to be made in order to obtain representative model dimensions.

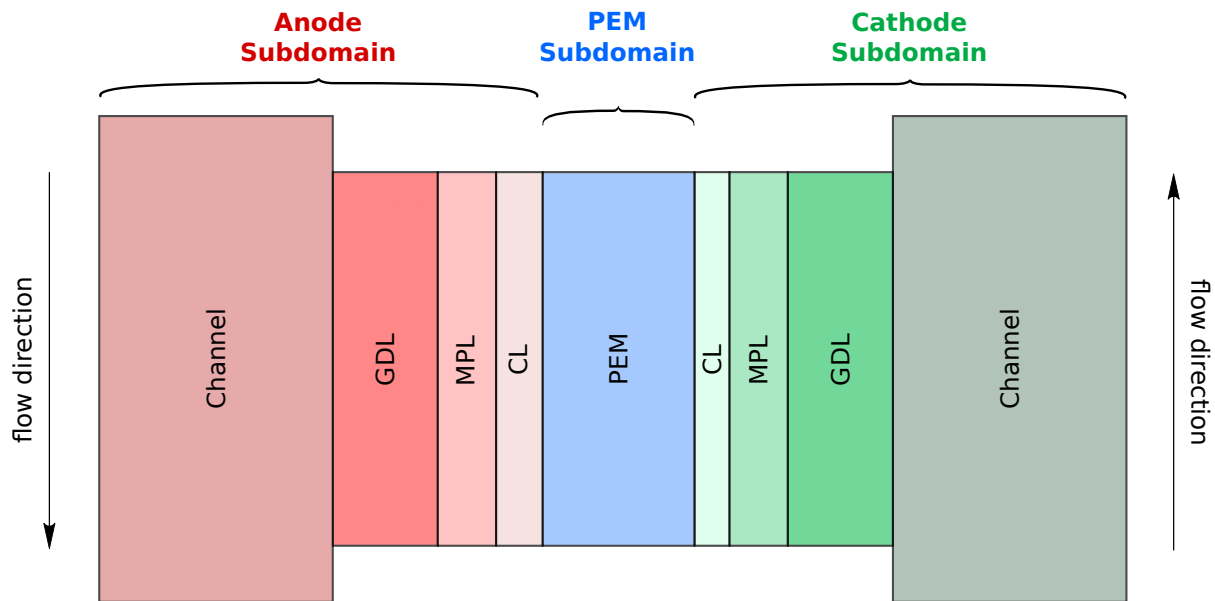


Figure 5.1: The modelling domain.

The model geometry comprises further elements in addition to the mere fuel cell geometry, namely an inlet and outlet section in the channels as well as a tube after the channel outlet element on both sides, anode and cathode (cf. figure 5.2).

The additional tube length ensures homogeneous flow conditions at the model boundary in outflow direction, which is necessary for the chosen outflow boundary condition (cf. [43] and section 5.6). The boundary conditions for the anode or cathode “outlet” as specified in section 5.6 are, more precisely, applied at the tube outlet positions, which mark the outer boundary of the modelling domain.

The model’s geometrical parameters are given in table 5.1.

5.3.1 Cell Area

The area projected by the 2D model in x- and y-direction is not the cell area, but the cross-section through the MEA (x-direction) for one idealised straight channel in anode and cathode (y-direction). Properties like the current density i or the crossover fluxes \dot{N}_κ^{cross} are typically specified in units per cell area, that is why the model’s cell area A_{cell} needs to be determined. A_{cell} is the product of the channel length l_{ch} in y-direction and the cell depth d_{cell} in z-direction (eq. 5.1).

$$A_{cell} = l_{ch} \cdot d_{cell} \quad (5.1)$$

The DMFC model does not cover the third spatial dimension, so the cell depth d_{cell} , which represents the sum of the flow-field’s channel depth d_{ch} and its rib depth d_{rib} in z-direction, is a virtual quantity.

$$d_{cell} = d_{ch} + d_{rib} \quad (5.2)$$

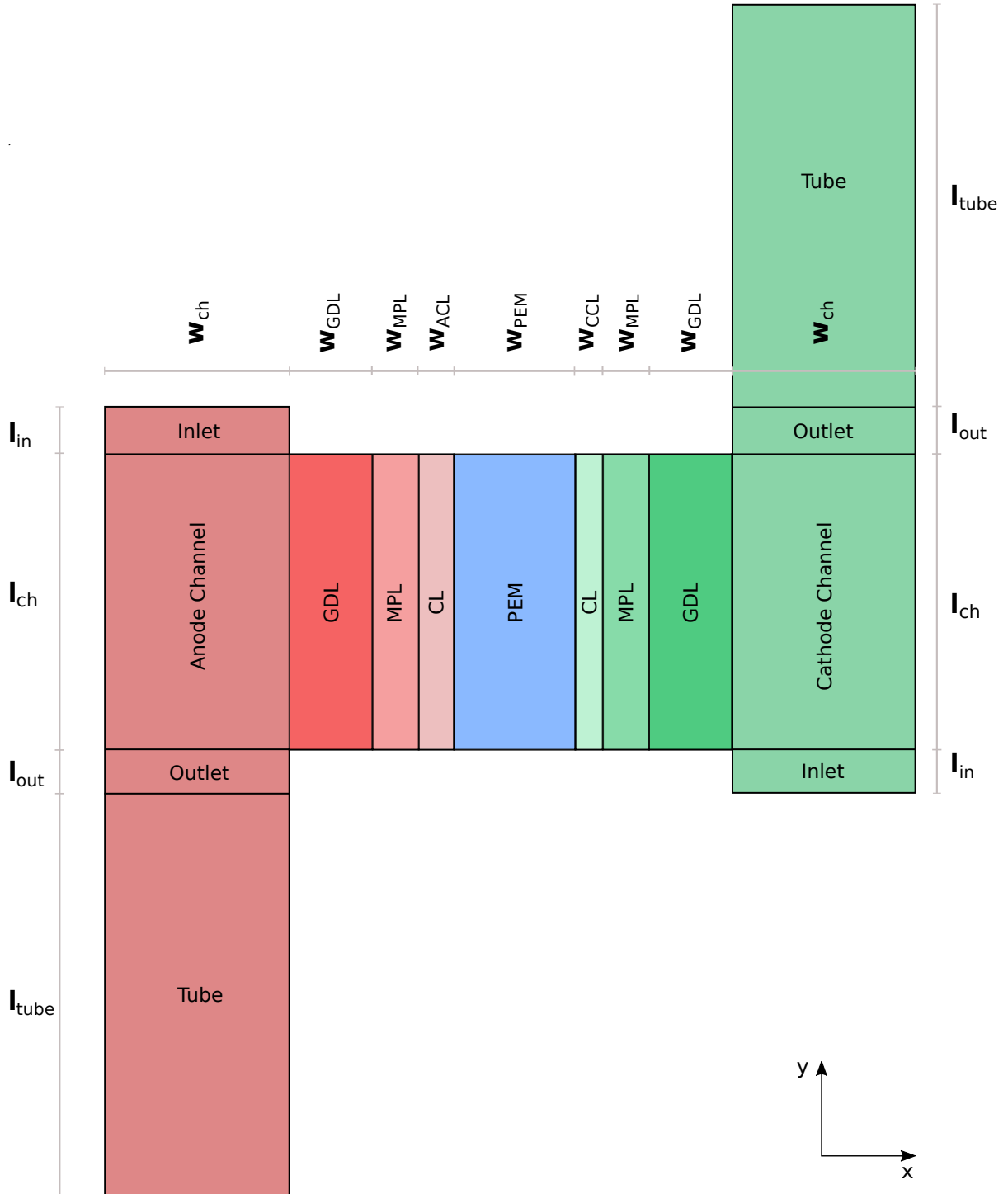


Figure 5.2: Model Geometry (not drawn to scale). The layers of the anode sub-domain are shown in red, the layers of the cathode sub-domain in green, and the PEM sub-domain is coloured in blue. The measures for the individual lengths and widths are given in table 5.1. The grid structure can be found in section 5.5.

Table 5.1: Geometrical model parameters (z-direction not part of modelling domain). Measures of the experimental cell [111, 114] are marked with an asterisk *.

Parameter	Symbol	Value	Unit	Direction	Reference
GDL Thickness	w_{GDL}	3.5×10^{-4}	m	x	MEA spec.
MPL Thickness	w_{MPL}	4.5×10^{-5}	m	x	estimated
Anode CL Thickness	w_{ACL}	4.0×10^{-5}	m	x	MEA spec.
Cathode CL Thickness	w_{CCL}	3.0×10^{-5}	m	x	MEA spec.
PEM Thickness	w_{PEM}	1.27×10^{-4}	m	x	MEA spec.
Channel Width	w_{ch}^*	8.0×10^{-4}	m	x	measured [114]
Channel Depth	d_{ch}^*	8.0×10^{-4}	m	z	measured [114]
Rib Depth	d_{rib}^*	8.5×10^{-4}	m	z	measured [114]
Cell Area	A_{cell}^*	25×10^{-4}	m ²	yz	measured [114]
Inlet and Outlet Length	l_{in}/l_{out}	0.1	m	y	defined
Tube Length	l_{tube}	1.0	m	y	defined
Channel Length	l_{ch}	0.505	m	y	calculated (eq. 5.8)
Cell Depth	d_{cell}	1.0	m	z	defined

The model's channel length l_{ch} has to be derived from the real cell geometry (cf. equations 5.4 to 5.8). The virtual cell depth d_{cell} is set to 1 m.

5.3.2 Channel Area

The model's component fluxes in the channels (e.g. inflow and outflow in anode and cathode) are averaged over the channel area A_{ch} . The channel area, again, is a virtual quantity, as the 2D modelling domain only comprises the channel width in x-direction (w_{ch}), but not the channel depth d_{ch} , which would extend in z-direction (not part of the model). The channel depth d_{ch} must not be confused with the cell depth d_{cell} (cf. eq. 5.2). The channel area A_{ch} is the product of channel width and channel depth:

$$A_{ch} = w_{ch} \cdot d_{ch} \quad (5.3)$$

5.3.3 Channel Length

The model's channel length is derived by the relation of model geometry to the geometry of the experimental DMFC flow-field. Note that the model only portrays one third of the real cell, as one single channel is simulated in the anode and cathode sub-domain, whereas the real DMFC flow-field includes three channels.

$$\frac{A_{cell}}{A_{ch}} \equiv \frac{1}{3} \cdot \frac{A_{cell}^*}{A_{ch}^*} \quad (5.4)$$

$$\frac{l_{ch} \cdot d_{cell}}{w_{ch} \cdot d_{ch}} = \frac{1}{3} \cdot \frac{A_{cell}^*}{w_{ch}^* \cdot d_{ch}^*} \quad (5.5)$$

$$l_{ch} = \frac{1}{3} \cdot \frac{d_{ch}}{d_{cell}} \cdot \frac{w_{ch} \cdot A_{cell}^*}{w_{ch}^* \cdot d_{ch}^*} \quad (5.6)$$

with the dimensionless number ϵ

$$\epsilon = \frac{d_{ch}}{d_{cell}} = \frac{d_{ch}}{d_{ch} + d_{rib}} \equiv \frac{d_{ch}^*}{d_{ch}^* + d_{rib}^*} \quad (5.7)$$

and $w_{ch} = w_{ch}^*$ follows the model's channel length

$$l_{ch} = \frac{\epsilon}{3} \cdot \frac{A_{cell}^*}{d_{ch}^*} \quad (5.8)$$

5.4 Numerical Discretisation

The model's spatial discretisation is achieved with the so-called 'box method' [63, 60], which combines the features of the finite-volume and the finite-element discretisation: The technique is locally mass conservative and supports the application of unstructured grids.

A description of the box method can be found in [6] and [63] and also the the DuMu^x handbook [38]. The time discretisation is achieved with a fully implicit Euler scheme.

5.5 Grid Structure

The mesh for the modelling domain is generated as described in [43] based on the geometrical parameters of table 5.1. The discretisation was chosen individually for each layer (see tab. 5.2 and fig. 5.3), depending on the layer's impact on the model convergence (cf. [43]).

Table 5.2: Grid Parameters: Number of cells per layer.

	Channel	GDL	MPL	ACL	CCL	PEM	Inlet	Outlet	Tube
n_{cells}^x	3	6	6	6	10	4	3	3	3
n_{cells}^y	20	20	20	20	20	20	3	3	3

NEOPARD-X's 'grid creator' is capable of generating graded grids with which the mesh can be locally refined or coarsened. The model's spatial resolution is increased in anode and cathode CL in x-direction towards the CL/PEM-interfaces in this study. Furthermore, the grid of the cathode MPL is refined towards the CL-interface in x-direction. All other layers in the modelling domain were meshed uniformly in x- and y-direction.

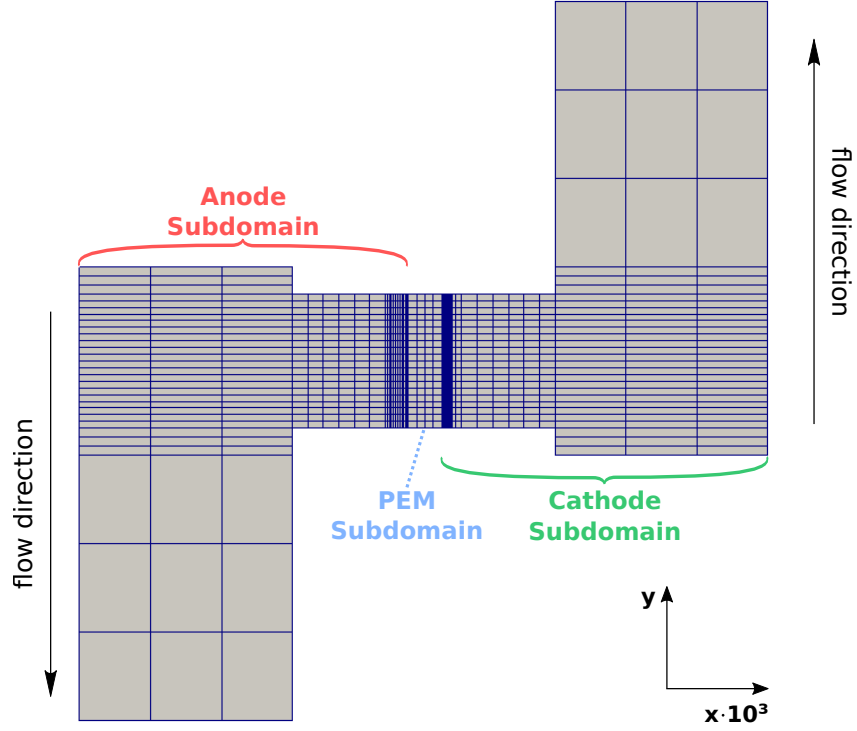


Figure 5.3: Grid structure of the 2D DMFC model.

Table 5.3: Grading Factors used in NEOPARD-X's grid creator (cf. [43])

Position	Direction	f_{grad}
Anode CL	x	-1.1
Cathode CL	x	1.15
Cathode MPL	x	2.0

5.6 Primary Variables and Boundary Conditions

In every sub-domain of the model an individual set of primary variables exists, for which conservation equations have to be solved (cf. section 6.1 and 6.2). Suitable boundary conditions need to be specified for every primary variable at all boundaries of a sub-domain. At the interfaces between two sub-domains, coupling conditions apply for those primary variables which are present in both sub-domains.

The position of the model's boundaries and coupling interfaces in the modelling domain are depicted in figure 5.4 and figure 5.5. The primary variables and boundary conditions for each subdomain are described in the following, while the coupling conditions at the interfaces between the sub-domains are described in section 5.7.

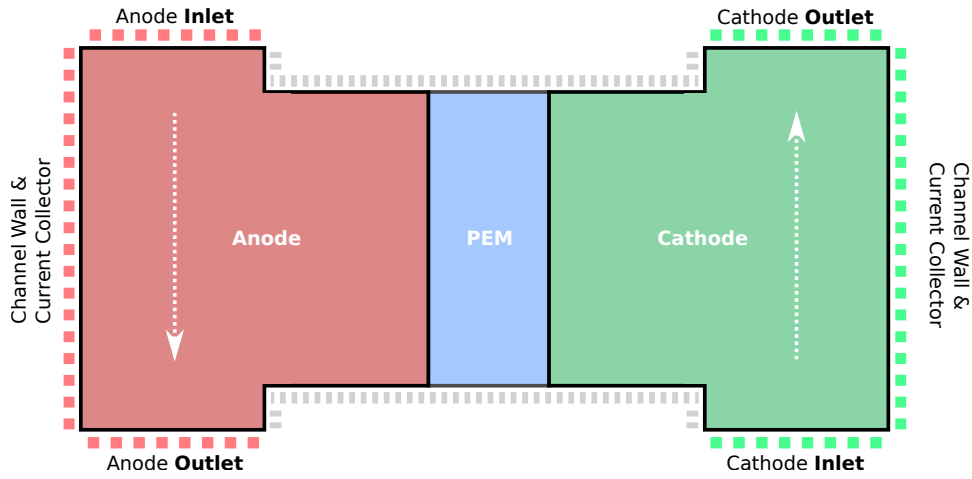


Figure 5.4: The model boundaries. The boundary conditions applied at the anode boundaries (red dashes) and cathode boundaries (green dashes) are described in section 5.6. No-flow Neumann conditions apply at the boundaries marked with the narrowly dashed lines in grey for all variables.

The model's boundary conditions are chosen according to the experimental operating conditions in the work of Rabissi et al. [111]. There, the cell is operated in counterflow mode at $T = 75^\circ\text{C}$ with constant flow rates on anode and cathode equivalent to a stoichiometry of $\lambda_A = 6$ and $\lambda_C = 3$ at $i = 0.25 \text{ A cm}^{-2}$. The anode feed consists of a liquid 1 M methanol solution, while the cathode is fed with humidified air (RH = 10 % or RH = 50 %). The experiments were performed unpressurised, i.e. $p_g^{\text{out}} = 1 \text{ atm}$.

5.6.1 Anode Sub-Domain

The primary variables in the anode sub-domain are the liquid pressure p_l , the liquid saturation S_l , the temperature T , the electric and ionic potential, Φ_{el} and Φ_{ion} , and further the mole fractions of CH_3OH , H_2O , CO_2 and H_2 .

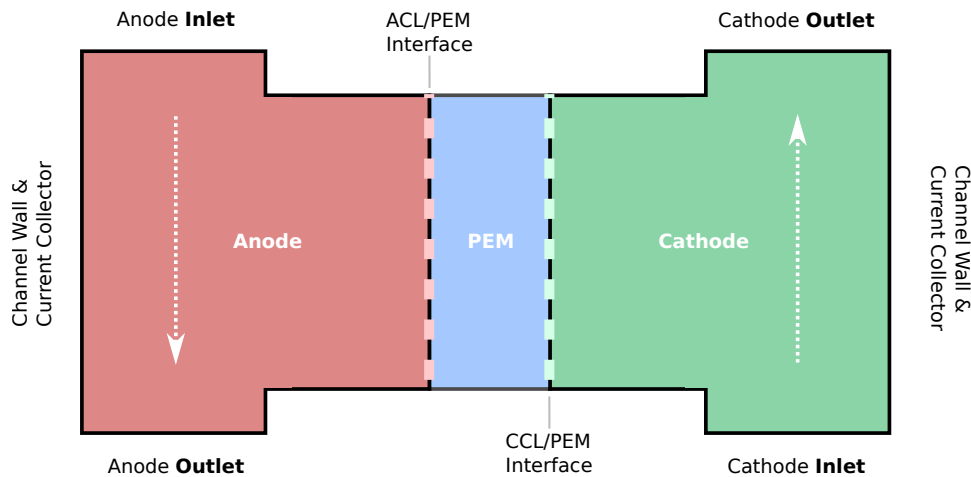


Figure 5.5: Coupling interfaces between the model sub-domains. The respective coupling conditions are described in section 5.7.

At the anode channel wall, which corresponds to the current collector position, Dirichlet conditions are set for the temperature ($T = 348.15 \text{ K}$) and the electric potential ($\Phi_{el} = 0 \text{ V}$).

At the anode channel inlet, Dirichlet conditions are set for the liquid mole fractions of H_2O , CO_2 and H_2 as well as for the liquid saturation, while a Neumann condition is set for CH_3OH .

The composition of the anode feed in the experiments is known: there, a liquid 1 M methanol solution is used. For numerical reasons, a two-phase flow with a gas saturation of $S_g = 1 \%$ is set in the model at the anode inlet boundary (instead of a pure liquid flow). The gas phase is assumed to consist of H_2O , CO_2 and CH_3OH . With this assumption and the fix value for the liquid methanol mole fraction $x_{\text{CH}_3\text{OH}}^l$, the composition of gas and liquid phase at anode inlet can be calculated for a vapour-liquid equilibrium (cf. section 6.1.2). The parameters $x_{\text{CO}_2}^l$ and $x_{\text{H}_2\text{O}}^l$ are determined as follows:

$$x_{\text{H}_2\text{O}}^l|_{init} = 1.0 - x_{\text{CH}_3\text{OH}}^l \quad (5.9)$$

$$x_{\text{CO}_2}^g = 1.0 - x_{\text{CH}_3\text{OH},eq}^g - x_{\text{H}_2\text{O},eq}^g|_{init} \quad (5.10)$$

$$x_{\text{CO}_2}^l = x_{\text{CO}_2}^g \cdot p_g / H_{\text{H}_2\text{O}}^{\text{CO}_2} \quad (5.11)$$

$$x_{\text{H}_2\text{O}}^l = 1.0 - x_{\text{CH}_3\text{OH}}^l - x_{\text{CO}_2,eq}^l \quad (5.12)$$

For methanol, a Neumann condition describing the methanol inflow is set at the anode channel inlet. The molar flux density of methanol at the anode channel inlet $\Psi_{\text{CH}_3\text{OH}}^{A,in}$ is calculated with eq. 5.13:

$$\Psi_{\text{CH}_3\text{OH}}^{A,in} = \frac{\lambda_{\text{CH}_3\text{OH}} \cdot i_{nom}}{6 F} \cdot \frac{A_{cell}}{A_{ch}} \quad (5.13)$$

At the anode outlet (or, more specific, the anode tube end, cf. figure 5.2), an outflow condition is set for all fluid components but H_2O . Since the equation system is overdetermined, the boundary condition for the water mole fraction can be replaced by a boundary condition for the liquid pressure (cf. [43]). At anode channel outlet, a Dirichlet condition is thus set for the liquid pressure p_l .

At the anode interface to the membrane, coupling conditions describe the interaction of temperature T , ionic potential Φ_{ion} , H_2O and CH_3OH between the two sub-domains. The coupling conditions are specified in section 5.7.

For all remaining boundary/primary variable combinations in the anode sub-domain, no-flow Neumann conditions apply.

5.6.2 Cathode Sub-Domain

In the cathode sub-domain, O_2 and N_2 , CH_3OH , H_2O and CO_2 can be present as mobile species in gas and liquid phase. The component's mole fractions in the gas phase are primary variables in the model. Furthermore, PtO and PtOH are included as adsorbed, immobile species on the catalyst surface in the cathode sub-domain. The catalyst surface coverages Θ_{PtO} and Θ_{PtOH} are the primary variables in the model. The remaining primary variables in the cathode sub-domain are temperature T , electric and ionic potential, Φ_{el} and Φ_{ion} , as well as the pressure and saturation of the gas phase, p_g and S_g .

Just like in the anode sub-domain, a Dirichlet condition for the temperature ($T = 348.15 \text{ K}$) is set at the cathode channel wall.

Depending on the operating mode of the fuel cell, the boundary condition for the electric potential Φ_{el} at the current collector (located on the cathode channel wall) is either a Dirichlet condition or a Neumann condition: In case of a potentiostatic fuel cell operation, the cell voltage is set as Dirichlet boundary condition for Φ_{el} at the cathode current collector, whereas in case of galvanostatic cell operation, the current density i is set as a Neumann condition at the current collector.

In the experiments, humidified air is used as cathode feed gas. The cathode in-stream is assumed to consist of N_2 , O_2 and H_2O . The humidification degree of the cathode air can vary, consequently the gas composition at the cathode channel inlet boundary needs to be calculated in dependence of the relative cathode gas humidity RH:

$$x_{\text{H}_2\text{O}}^g = \text{RH} \cdot p_{\text{H}_2\text{O}}^{\text{sat}} / p_g \quad (5.14)$$

$$x_{\text{O}_2}^g = 0.21 \cdot (1 - x_{\text{H}_2\text{O}}^g) \quad (5.15)$$

$$x_{\text{N}_2}^g = 0.79 \cdot (1 - x_{\text{H}_2\text{O}}^g) \quad (5.16)$$

A Dirichlet condition is set for the gas mole fractions of O_2 , H_2O , CH_3OH and CO_2 at the cathode channel inlet boundary. Since methanol and carbon dioxide are assumed not to be present in the cathode feed gas, their mole fractions at cathode inlet are zero.

For nitrogen, a Neumann condition with the nitrogen inflow into the cathode channel is set at the cathode inlet boundary. The molar flux density of N_2 at cathode channel inlet is calculated with eq. 5.17:

$$\Psi_{N_2}^{C,in} = \frac{x_{N_2}^g}{x_{O_2}^g} \cdot \frac{\lambda_{O_2} \cdot i_{nom}}{4F} \cdot \frac{A_{cell}}{A_{ch}} \quad (5.17)$$

Another Dirichlet condition at cathode channel inlet is set for the gas saturation S_g .

Outflow conditions at cathode outlet are set for the components O_2 , CH_3OH , H_2O , and CO_2 . The corresponding boundary condition for N_2 is substituted by a Dirichlet condition for the gas pressure p_g [43].

No-flow Neumann conditions are set for all other boundary/primary variable combinations.

At the coupling interface to the PEM sub-domain, coupling conditions apply for the ionic potential Φ_{ion} , the temperature T , and the species CH_3OH and H_2O . The coupling between the sub-domains is detailed in section 5.7.

5.6.3 PEM Sub-Domain

The primary variables in the membrane are the ionic potential Φ_{ion} , the temperature T , and the molar concentrations of CH_3OH and H_2O . In contrast to the electrodes, where a two-phase flow is considered, only a single (liquid) mobile phase is assumed to be present in the membrane sub-domain. Gas crossover over the membrane is neglected in the model.

The PEM sub-domain has two internal coupling interfaces to the anode and cathode sub-domain, as well as two external boundaries (cf. figures 5.4 and 5.5). At the external boundaries, no-flow conditions apply for all primary variables, while at the internal boundaries, coupling conditions have to be specified. The coupling conditions can be either of a Dirichlet type or a Neumann type (cf. [43]) and depend on the current model solution.

5.7 Coupling Conditions

Local thermodynamic equilibrium is assumed at the coupling interfaces between the membrane and the anode and cathode sub-domain. Consequently, the temperature T and the electrolyte potential Φ_{ion} are continuous over the interfaces. Dirichlet type coupling conditions are thus specified at the ACL/PEM interface and PEM/CCL interface with the values of T and Φ_{ion} of the respective position in the electrode sub-domains.

Also the concentration of methanol is assumed to be continuous over both PEM/CL interfaces. While in the electrodes the mole fraction $x_{CH_3OH}^\alpha$ are the primary variables

for methanol, in the membrane sub-domain the molar concentration $C_{\text{CH}_3\text{OH}}^m$ is considered as a primary variable. Dirichlet type conditions are set at both membrane coupling interfaces and the liquid molar concentration of methanol $C_{\text{CH}_3\text{OH}}^m$, determined from the vapour-liquid equilibrium in the catalyst layer (cf. section 6.1.2), is used as coupling parameter.

The essential parameter for coupling the water between the membrane and electrodes is the membrane water content $\lambda_{\text{H}_2\text{O}}$. At the membrane interfaces, the value for $\lambda_{\text{H}_2\text{O}}$ in equilibrium is determined via a sorption isotherm (cf. section 6.2.1) under consideration of the local two-phase conditions in the catalyst layers (eq. 6.29).

The model considers water sorption as non-equilibrium process at the membrane interfaces to anode and cathode, therefore Neumann type coupling conditions apply at both PEM/CL interfaces for the molar flux density of water $\Psi_{\text{H}_2\text{O}}^{\text{abs/des}}$. The sorption kinetics rendering $\Psi_{\text{H}_2\text{O}}^{\text{abs/des}}$ over the membrane interfaces are described in section 6.2.2.

In section 7.1.2, a case where the H_2O sorption kinetics at the membrane interfaces are neglected is studied with the model. In that particular simulation, an equilibrium between the water content in the catalyst layers and the membrane is assumed and Dirichlet type condition for $\lambda_{\text{H}_2\text{O}}$ is set at both PEM/CL interfaces instead of the usual Neumann type coupling conditions.

5.8 Initial Conditions

The initial conditions for the anode and cathode sub-domain in the model are listed in table 5.4. For most of the primary variables, the initial conditions are equal to the Dirichlet boundary conditions at the respective positions. For the primary variables which occur solely in the catalyst layers, i.e. Φ_{ion} , Θ_{PtO} and Θ_{PtOH} , only initial conditions are specified, as the catalyst layer has no external boundaries in the modelling domain except at the top and bottom of the MEA, where no-flow boundary conditions apply.

The relative humidity RH in the cathode feed is an input parameter with which $x_{\text{H}_2\text{O}}^g$ and consequently $x_{\text{O}_2}^g$ and $x_{\text{N}_2}^g$ at cathode inlet can be calculated (cf. eq. 5.14 - 5.16).

The initial conditions for the PEM sub-domain at the coupling interfaces are listed in table 5.5. Note that the values are no input parameters but result from the initial model solution at the coupling interfaces. The initial values *within* the PEM sub-domain result from a linear interpolation in through-plane (x) direction between the values at the coupling interfaces.

Table 5.4: Initial Conditions (IC) and Boundary Conditions (BC) in the electrodes.

Variable	Anode ($\alpha = l$)	Cathode ($\alpha = g$)	Position	IC/BC
T	348.15 K	348.15 K	Channel Wall	IC & BC
Φ_{ion}	0.0 V	0.0 V	Catalyst Layer	IC
Φ_{el}	0.0 V	Φ_{el}^{BC}	Current Collector	IC & BC
p_α	101 325 Pa	101 325 Pa	Outlet	IC & BC
S_l	0.99	0.0	Inlet	IC & BC
$x_{CO_2}^\alpha$	$x_{CO_2}^{eq,l}$ (cf. eq. 5.10)	0.0	Inlet	IC & BC
$x_{CH_3OH}^\alpha$	0.0193	0.0	Inlet	IC & BC
$x_{H_2O}^\alpha$	$1 - x_{CH_3OH}^l$	$RH \cdot p_{H_2O}^{sat}/p_g$	Inlet	IC & BC
$x_{O_2}^\alpha$	-	$0.21 \cdot (1 - x_{H_2O}^g)$	Inlet	IC & BC
$x_{N_2}^\alpha$	-	$0.79 \cdot (1 - x_{H_2O}^g)$	Inlet	IC & BC
$x_{H_2}^\alpha$	0.0	-	Inlet	IC & BC
Θ_{PtO}	-	0.0	Catalyst Layer	IC
Θ_{PtOH}	-	0.0	Catalyst Layer	IC

Table 5.5: Initial Conditions (IC) and Coupling Conditions (CC) in the PEM.

Variable	Anode/PEM Interface	Cathode/PEM Interface	CC/BC
$\lambda_{H_2O}^{PEM}$	$\lambda_{H_2O}^{ACL}$	$\lambda_{H_2O}^{CCL}$	IC
$C_{CH_3OH}^{PEM}$	$C_{CH_3OH,l}^{ACL}$	$C_{CH_3OH,l}^{CCL}$	IC, CC
T^{PEM}	T_{ACL}	T_{CCL}	IC, CC
Φ_{ion}^{PEM}	$\Phi_{ion,ACL}$	$\Phi_{ion,CCL}$	IC, CC

6 Physical DMFC Model

The processes inside a DMFC are complex, including multiphase, multicomponent fluid transport inside porous media combined with electrochemical reactions as well as charge and energy transfer. In order to describe the fuel cell behaviour, a macroscopic model using the continuum approach [7] is set up. The transport of species is described by means of effective transport properties, based on representative elementary volumes (REV).

Both, anode and cathode sub-domain, comprise a two-phase, multicomponent system in a heterogeneous, porous matrix. In the PEM sub-domain, the system is reduced to a single-phase, multicomponent problem. The model is non-isothermal and considers ionic and electronic charge transport.

For each modelling domain, the following assumptions are made:

1. local thermodynamic equilibrium holds
2. gases and mixtures are ideal
3. solid phases are rigid
4. gravitational effects can be neglected

Any energy, charge and mass conservation in the model is described by a balance equation of the form

$$\frac{\partial \xi}{\partial t} + \nabla \cdot \Psi - q = 0 \quad (6.1)$$

with a storage term ξ , a flux term Ψ and a source term q for the conservation variable. For every subdomain, an individual physical formulation for mass, energy and charge transfer is required.

Material Properties The experimental cells [111], which were used for model validation, consisted of a Nafion[®] 115 membrane with a GDL of the type Sigracet[®] SGL35 DC with 20 wt% PTFE and a microporous layer. The anode catalyst had a loading of 1.8 mg/cm² PtRu and the cathode catalyst contained 1.2 mg/cm² Pt.

The effective material properties of these substrates were not directly available. Instead, the structural properties of GDL, MPL and CLs were estimated based on the findings of Rashapov et al. [116, 115], El-kharouf et al. [75] and Andisheh-Tadbir et al. [1] (cf. table 6.1).

6.1 Anode and Cathode Subdomain

In the anode and cathode subdomain, a gas and a liquid phase are assumed to be in equilibrium inside the porous matrix. The components CH_3OH , H_2O , CO_2 and H_2 are included in the anode subdomain, whereas the cathode subdomain accounts for O_2 , N_2 , H_2O , CH_3OH and CO_2 as fluid components. Additionally, two platinum oxide species are considered as adsorbates in the CCL. Since these adsorbates are immobile, the flux term in their balance equations becomes zero.

6.1.1 Mass Conservation

The mass balance for a component κ in a two-phase system reads

$$\frac{\partial (\phi \sum_{\alpha} \rho_{\alpha}^n x_{\alpha}^{\kappa} S_{\alpha})}{\partial t} - \nabla \cdot \sum_{\alpha=1}^2 (\rho_{\alpha}^n x_{\alpha}^{\kappa} \mathbf{v}_{\alpha} + \mathbf{d}_{\alpha}^{\kappa}) - q^{\kappa} = 0 \quad (6.2)$$

The velocity of phase α is described with the extended Darcy law [60] for multiphase systems:

$$\mathbf{v}_{\alpha} = -\frac{k_{r\alpha}}{\mu_{\alpha}} \mathbf{K} \nabla p_{\alpha} \quad (6.3)$$

In the liquid phase, the components are treated as solutes in water and Fick's law is used for the description of the diffusive flux of component κ [79]

$$\mathbf{d}_l^{\kappa} = -D_{pm,l}^{\kappa} \rho_l^n \nabla x_l^{\kappa}. \quad (6.4)$$

The diffusion coefficient $D_{pm,\alpha}^{\kappa}$ accounts for the tortuosity of the porous medium with a Bruggeman correlation

$$D_{pm,\alpha}^{\kappa} = (\phi S_{\alpha})^{1.5} D_{\alpha}^{\kappa}. \quad (6.5)$$

In the gas phase, Knudsen diffusion is considered as an additional process, since the pore sizes of the MPL and catalyst layer are in the same order of magnitude as the mean diffusion length of the gas molecules [40, 101]. The Knudsen diffusion coefficient is

$$D_{Kn,g}^{\kappa} = \frac{2}{3} r_{pore} \sqrt{\frac{8RT}{\pi M^{\kappa}}}. \quad (6.6)$$

The effective diffusion coefficient for component κ in the gas phase is described with the Bosanquet formulation [44] and reads

$$D_{eff,g}^{\kappa} = \left(\frac{1}{D_{pm,g}^{\kappa}} + \frac{1}{D_{Kn,g}^{\kappa}} \right)^{-1}. \quad (6.7)$$

The diffusive flux \mathbf{d}_g^{κ} of component κ in the gas phase is derived with the approach of Stefan-Maxwell [79, 108], which describes the interaction of two components i and j in an N -component system:

$$\nabla x_g^i = \sum_{j=1}^N \frac{c_g^i c_g^j}{c_g^2 D_{eff,g}^i} \left(\frac{\mathbf{d}_g^j}{c_g^j} - \frac{\mathbf{d}_g^i}{c_g^i} \right). \quad (6.8)$$

Table 6.1: Spatial parameters of the porous layers (estimated based on [116, 115, 75, 1]).

	Permeability \mathbf{K} / m^2	Porosity $\phi / -$	Pore Radius r_{pore} / m
ACL	5×10^{-14}	0.35	70×10^{-9}
CCL	5×10^{-14}	0.35	70×10^{-9}
MPL	1×10^{-13}	0.5	90×10^{-9}
GDL	4×10^{-11}	0.82	22×10^{-6}
Channel	1.23×10^{-8}	1.0	1×10^{-3}

The parameters \mathbf{K} , ϕ and r_{pore} are given in tab. 6.1 for each layer in the anode and cathode sub-domain.

The phase pressures p_α in the porous medium are related by the capillary pressure, which is a function of wetting phase saturation S_w . Here the gas is defined as the wetting phase and the liquid is defined as the non-wetting phase.

$$p_c(S_w) = p_n - p_w = p_l - p_g \quad (6.9)$$

The *van Genuchten* model [53] is used in order to describe the capillary pressure-saturation relation and the relative permeabilities of the two phases in the porous media of the DMFC [160]:

$$S_w = \left(1 + \left(\frac{p_c}{p_{cb}} \right)^n \right)^{-m} \quad p_c > 0; \quad m = 1 - \frac{1}{n} \quad (6.10)$$

$$k_{rw} = S_w^{1/2} \left(1 - \left(1 - S_w^{1/m} \right)^m \right)^{1/2} \quad (6.11)$$

$$k_{rn} = (1 - S_w)^{1/3} \left(1 - S_w^{1/m} \right)^{2m} \quad (6.12)$$

Several studies on commercial fuel cell materials found this approach superior to the correlation of *Leverett* and *Udell*, which is commonly used in fuel cell modelling (cf. [160, 56]).

Each layer in the model's anode and cathode sub-domain has an individual set of parameters for the $p_c S_w$ -relation (cf. tab. 6.2) in order to account for the different material characteristics. As no experimental data on the capillary pressure/saturation-relations of the materials used in the study of Rabissi et al. [111] were available, the values for n and p_{cb} in eq. 6.10 had to be estimated (cf. section 7.2.1).

The resulting $p_c S_w$ -correlations for GDL, MPL and anode and cathode CL are shown in figure 6.1.

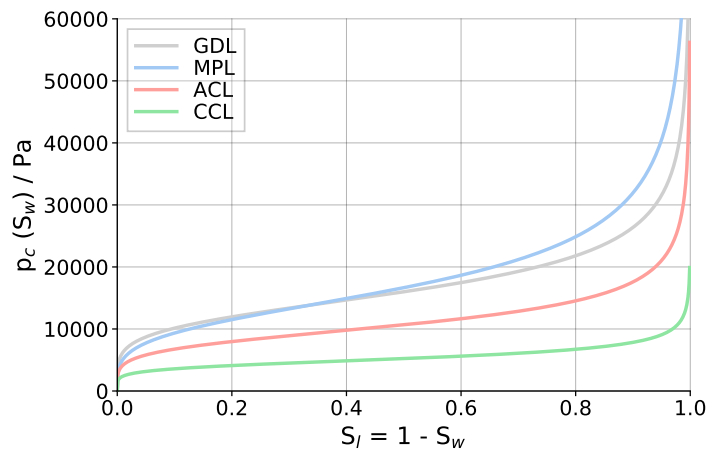


Figure 6.1: Capillary pressure-saturation relations for the different porous layers in the DMFC model obtained with eq. 6.10 and the parameters of tab. 6.2.

Table 6.2: Parameters for the $p_c S_w$ -relation (eq. 6.10).

	ACL	CCL	AMPL	CMPL	GDL	Channel
n	5.0	6.0	4.0	4.0	5.0	5.0
p_{cb} / Pa	10000	5000	15000	15000	15000	15000

6.1.2 Vapour-Liquid Equilibrium

The vapour-liquid equilibrium of multicomponent mixtures is characterised by the equality of the component's fugacity f^κ in the gas and in the liquid phase [108]

$$f^\kappa = f_g^\kappa = f_l^\kappa \quad (6.13)$$

with

$$f^\kappa = \Phi_\alpha^\kappa x_\alpha^\kappa p_\alpha. \quad (6.14)$$

Gases are assumed to be ideal with $\Phi_\alpha^\kappa = 1$, thus

$$f_g^\kappa = x_g^\kappa p_g. \quad (6.15)$$

In the liquid phase, the dissolved components in water are very dilute with $x_l^\kappa < 0.05$. Henry's law is applied in order to describe the fugacity of these components $\kappa \neq \text{H}_2\text{O}$ the liquid phase:

$$f_l^\kappa = x_l^\kappa H_{\text{H}_2\text{O}}^\kappa. \quad (6.16)$$

For water, which has a concentration $x_{\text{H}_2\text{O}} \rightarrow 1$ in the liquid phase, Raoult's law is used in order to describe the phase equilibrium with

$$f_l^{\text{H}_2\text{O}} = x_l^{\text{H}_2\text{O}} p_{\text{sat}}^{\text{H}_2\text{O}}. \quad (6.17)$$

6.1.3 Phase Transitions

Phase transitions in the porous media are calculated with the approach of Lauser et al. [85]: a nonlinear complementary function f^{NCP} is formulated out of a set of complementary conditions which describe the existence of a phase α . Together with the balance equations of the system, f^{NCP} can be solved with a semi-smooth Newton method.

The sum of all phase saturations in the system must be 1, with $M = 2$ for the two-phase problem in the DMFC.

$$\sum_{\alpha=1}^M S_{\alpha} = 1 \quad (6.18)$$

The following conditions describe the local presence of a phase α :

If a phase α is present, the sum of its mole fractions must be 1.

$$\forall \alpha : \sum_{\kappa=1}^N x_{\alpha}^{\kappa} = 1 \rightarrow S_{\alpha} > 0 \quad (6.19)$$

If a phase α is not present (i.e. $S_{\alpha} = 0$), the sum of its mole fractions in the N -component system may be lower than 1.

$$\forall \alpha : S_{\alpha} = 0 \rightarrow \sum_{\kappa=1}^N x_{\alpha}^{\kappa} \leq 1 \quad (6.20)$$

As a result follows

$$\forall \alpha : S_{\alpha} \left(1 - \sum_{\kappa=1}^N x_{\alpha}^{\kappa} \right) = 0. \quad (6.21)$$

Equations 6.19 - 6.21 can be re-written as nonlinear complementary function f^{NCP}

$$f^{NCP}(a, b) = \min \left\{ S_{\alpha}, 1 - \sum_{\kappa=1}^N x_{\alpha}^{\kappa} \right\} \quad (6.22)$$

with the constraints $f^{NCP}(a, b) = 0$ and $a \geq 0 \wedge b \geq 0 \wedge a \cdot b = 0$ [43].

6.1.4 Energy Conservation

The conservation of energy is described in form of equation 6.1. Since thermal equilibrium is assumed in the model, only one energy balance per subdomain has to be solved. The energy balance accounts for the thermal properties of gas and liquid phase as well as for the solid phase of the porous medium.

$$\begin{aligned} & \frac{\partial \left(\phi \sum_{\alpha=1}^M \rho_{\alpha} u_{\alpha} S_{\alpha} + (1 - \phi) \rho_s c_{p,s} \right)}{\partial t} \\ & + \nabla \cdot \left(- \sum_{\alpha=1}^M \frac{k_{r\alpha}}{\mu_{\alpha}} \rho_{\alpha} h_{\alpha} \mathbf{K} \nabla p_{\alpha} - \sum_{\kappa=1}^N \sum_{\alpha=1}^M h_{\alpha}^{\kappa} M^{\kappa} \mathbf{d}_{\alpha}^{\kappa} - \lambda_{pm} \nabla T \right) \\ & - q^{heat} = 0. \end{aligned} \quad (6.23)$$

An empirical relation based on measurements of the GDL's thermal conductivity in dependence on the liquid saturation (cf. [15]) is used to describe the effective thermal conductivity of the porous media:

$$\lambda_{pm} = 1.3067 S_l^3 - 3.5474 S_l^2 + 3.3638 S_l + 0.8763. \quad [\text{W m}^{-1} \text{K}^{-1}] \quad (6.24)$$

Heat is generated in the catalyst layers due to the electrochemical reactions. The calculation of the respective source term q^{heat} is based on the description of Lampinen and Fomino [84] and can be found in section 6.3.8.

6.1.5 Charge Conservation

As electro-neutrality applies to the fuel cell, two charge balances for electrons and protons are included in the model in the anode and cathode subdomain. While electron transport occurs exclusively in the solid matrix, the protons only move in the ionomer phase of catalyst layers and membrane.

In both cases, the charge flux is described by Ohm's law, with the gradient in the respective potential as driving force. In the catalyst layers, the electrical double layer enables the storage of H^+ and e^- . The sinks and sources for electrons and protons are the electrochemical reactions (cf. section 6.3.9). The balance equations for the charges in the anode and cathode subdomain then read

$$\frac{\partial (-C_{DL} (\Phi_{el} - \Phi_{ion}))}{\partial t} - \nabla \cdot (\sigma_{eff}^{e^-} \nabla \Phi_{el}) - q^{e^-} = 0. \quad (6.25)$$

$$\frac{\partial (-C_{DL} (\Phi_{el} - \Phi_{ion}))}{\partial t} - \nabla \cdot (-\sigma_{eff}^{H^+} \nabla \Phi_{ion}) - q^{H^+} = 0. \quad (6.26)$$

The flux terms in equations 6.25 and 6.26 have an opposite sign, due to the opposite charges of H^+ and e^- .

The double layer capacities used in the model are $C_{DL}^A = 4 \times 10^7 \text{ F m}^{-3}$ and $C_{DL}^C = 5 \times 10^7 \text{ F m}^{-3}$. Both values are fitted.

The ionic conductivity in the DMFC catalyst layers is described with an empirical function in dependence of the water activity (eq. 6.27). The parameters $A = 0.015$ and $B = 6.0$ are fitting values (cf. section 7.2.1 for details).

$$\sigma_{ion}^{CL} = A \cdot \exp(B \cdot a_{\text{H}_2\text{O}}) \quad [\text{S m}^{-1}] \quad (6.27)$$

6.2 PEM Subdomain

The membrane forms an own modelling domain with the conservation species H_2O , CH_3OH , H^+ and the temperature T . Any gas transport in the PEM is neglected, only the interaction between components in the liquid phase and the ionomer are taken into account. The PEM sub-domain is coupled with the anode and cathode sub-domain via coupling conditions at the PEM/CL-interfaces (cf. section 5.7).

6.2.1 Membrane Water Content

The properties of the polymer electrolyte membrane are highly dependent on its water content. The water content is described with the quantity $\lambda_{\text{H}_2\text{O}}$, which relates the number of water molecules to the number of sulfonic acid groups in the polymer:

$$\lambda_{\text{H}_2\text{O}} = \frac{[\text{H}_2\text{O}]}{[\text{SO}_3^-]} \quad (6.28)$$

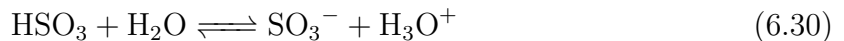
The membrane water content, $\lambda_{\text{H}_2\text{O}}$, is strongly determined by the conditions at the membrane's interfaces to the catalyst layers. It is influenced by the local temperature as well as the water activity in the gas phase and whether or not the membrane surface is in contact with a liquid phase [90, 82]. The water uptake from a liquid phase results in higher values of $\lambda_{\text{H}_2\text{O}}$ than the water uptake from a vapour phase, even if the gas phase is fully saturated. The latter phenomenon is commonly observed in experiments (for Nafion[®] 115 membranes cf. Maldonado et al. [90]) and is called a *Schröder's Paradox* [125]. The mechanism leading to the difference in membrane water uptake in dependence of the phase, however, is still not fully understood (cf. Kreuer [77] and Kusoglu et al. [82]).

The model accounts for the varying humidity and phase conditions at the PEM/CL interfaces and the resulting differences in the membrane's water uptake by the following expression of $\lambda_{\text{H}_2\text{O}}$:

$$\lambda_{\text{H}_2\text{O}} = S_l \cdot \lambda_{\text{H}_2\text{O}}^l + S_g \cdot \lambda_{\text{H}_2\text{O}}^g \quad (6.29)$$

For a fully liquid-equilibrated PEM/CL interface, the membrane's water content is assumed to be constant with $\lambda_{\text{H}_2\text{O}}^l = 22$.

The water content of the gas-equilibrated ionomer, $\lambda_{\text{H}_2\text{O}}^g$, is described by a sorption isotherm [94]. The ionomer's sulfonic acid groups are assumed to be in chemical equilibrium with water, i. e.



Equation 6.31 describes the sulfonic acid's chemical equilibrium with water, while equation 6.32 describes the equilibrium between water molecules in the gas phase and in the ionomer.

$$\frac{\lambda_{\text{H}_3\text{O}^+}}{(1 - \lambda_{\text{H}_3\text{O}^+})(\lambda_{\text{H}_2\text{O}} - \lambda_{\text{H}_3\text{O}^+})} \exp(\phi_1 \lambda_{\text{H}_3\text{O}^+}) \exp(\phi_2 \lambda_{\text{H}_2\text{O}}) = K_1 \quad (6.31)$$

$$\frac{p_{\text{H}_2\text{O}}}{p_{\text{sat}}} = K_2 (\lambda_{\text{H}_2\text{O}} - \lambda_{\text{H}_3\text{O}^+}) \exp(\phi_2 \lambda_{\text{H}_3\text{O}^+}) \exp(\phi_3 \lambda_{\text{H}_2\text{O}}) \quad (6.32)$$

The parameters ϕ_{1-3} are described in eq. 6.33 to 6.35 in dependence on the membrane's equivalent weight EW and the binary interaction coefficients E_{ij}^* .

$$\phi_1 = 2(E_{\text{H}_2\text{O}, \text{H}_2\text{O}}^* - 2E_{\text{H}_3\text{O}^+, \text{H}^+}^* - 2E_{\text{H}_2\text{O}, \text{H}_3\text{O}^+}^*) / EW \quad (6.33)$$

$$\phi_2 = 2(E_{\text{H}_3\text{O}^+, \text{H}_2\text{O}}^* - E_{\text{H}_2\text{O}, \text{H}_2\text{O}}^*) / EW \quad (6.34)$$

$$\phi_3 = 2E_{\text{H}_2\text{O}, \text{H}_2\text{O}}^* / EW \quad (6.35)$$

Table 6.3 lists the parameters K_1 and K_2 and the coefficients E_{ij}^* used in the sorption isotherm of gaseous H_2O .

Table 6.3: Water sorption isotherm parameters.

Parameter	Unit	Value	Reference
K_1	-	100	[94]
K_2	-	$0.217 \exp\left[\frac{1000}{R} \left(\frac{1}{303.15} - \frac{1}{T}\right)\right]$	[146]
$E_{\text{H}_2\text{O}, \text{H}_2\text{O}}^*$	kg / mol	-4.17×10^{-2}	[94]
$E_{\text{H}_3\text{O}^+, \text{H}_2\text{O}}^*$	kg / mol	-5.2×10^{-2}	[94]
$E_{\text{H}_3\text{O}^+, \text{H}^+}^*$	kg / mol	3.7216	[94]

In some cases, not the water content $\lambda_{\text{H}_2\text{O}}$ but its volumetric fraction in relation to the ionomer are considered for the description of humidity-dependent PEM parameters (cf. [146]). This water volume fraction f_V is defined as

$$f_V = \frac{\lambda_{\text{H}_2\text{O}} \cdot V_{\text{H}_2\text{O}}}{(V_m + \lambda_{\text{H}_2\text{O}} \cdot V_{\text{H}_2\text{O}})}. \quad (6.36)$$

6.2.2 Sorption Kinetics

The sorption of water into polymer electrolyte membranes is a transient process and the water uptake from a gas phase appears to be significantly slower than from a liquid phase [52, 161]. In addition to that, the process of absorption is slower than the process of desorption [89, 52, 161]. The local phase and humidity conditions at the PEM/CL

interface therefore not only influence the amount of water in the membrane, $\lambda_{\text{H}_2\text{O}}$, but also the process of water uptake itself.

Sorption kinetics for the water transfer to and from the membrane are thus included in the coupling conditions at the PEM/CL interfaces of the DMFC model in dependence of the temperature and the local distribution of gas and liquid phase in the catalyst layers (cf. Ge et al. [52]):

Absorption (if $C_{\text{H}_2\text{O}}^m < C_{\text{H}_2\text{O}}^{eq}$):

$$\Psi_{\text{H}_2\text{O}}^{abs} = k_{abs}^l \cdot S_l \cdot (C_{\text{H}_2\text{O}}^m - C_{\text{H}_2\text{O}}^{eq,l}) + k_{abs}^g \cdot S_g \cdot (C_{\text{H}_2\text{O}}^m - C_{\text{H}_2\text{O}}^{eq,g}) \quad (6.37)$$

$$k_{abs}^\alpha = k_{abs}^{\alpha,*} \cdot f_V \cdot \left(2416 \cdot \left(\frac{1}{303.15} - \frac{1}{T} \right) \right) \quad (6.38)$$

Desorption (if $C_{\text{H}_2\text{O}}^m > C_{\text{H}_2\text{O}}^{eq}$):

$$\Psi_{\text{H}_2\text{O}}^{des} = k_{des}^l \cdot S_l \cdot (C_{\text{H}_2\text{O}}^m - C_{\text{H}_2\text{O}}^{eq,l}) + k_{des}^g \cdot S_g \cdot (C_{\text{H}_2\text{O}}^m - C_{\text{H}_2\text{O}}^{eq,g}) \quad (6.39)$$

$$k_{des}^\alpha = k_{des}^{\alpha,*} \cdot f_V \cdot \left(2416 \cdot \left(\frac{1}{303.15} - \frac{1}{T} \right) \right) \quad (6.40)$$

The molar water concentration $C_{\text{H}_2\text{O}}^m$ in the membrane is

$$C_{\text{H}_2\text{O}}^m = \lambda_{\text{H}_2\text{O}} \cdot \frac{\rho^{PEM}}{EW} \quad (6.41)$$

with $\lambda_{\text{H}_2\text{O}}$ according to eq. 6.29.

The parameter $C_{\text{H}_2\text{O}}^{eq}$ describes the membrane's molar water concentration in equilibrium (cf. section 6.2.1). The parameters for the calculation of the water sorption kinetics (eq. 6.37 to 6.40) are given in table 6.4.

Table 6.4: Water sorption kinetic parameters.

Parameter	Value	Reference
$k_{abs}^{g,*}$	$1.14 \times 10^{-5} \text{ m s}^{-1}$	[52]
$k_{des}^{g,*}$	$4.59 \times 10^{-5} \text{ m s}^{-1}$	[52]
$k_{abs}^{l,*}$	$1.14 \times 10^{-2} \text{ m s}^{-1}$	estimated (cf. sec. 7.1.2)
$k_{des}^{l,*}$	$4.59 \times 10^{-2} \text{ m s}^{-1}$	estimated (cf. sec. 7.1.2)

6.2.3 Conservation Equations

Just like in the anode and cathode subdomain, for every primary variable in the PEM subdomain (i.e. H^+ , T , and the species CH_3OH and H_2O) a balance equation of the general form

$$\frac{\partial \xi}{\partial t} + \nabla \cdot \Psi + q = 0 \quad (6.42)$$

is solved.

Note that the membrane does not exhibit any sinks or sources for the species CH_3OH , H_2O and H^+ , but for the temperature T .

6.2.3.1 Protons

The proton balance reduces to

$$\nabla \cdot (-\sigma_{ion} \nabla \varphi) = 0 \quad (6.43)$$

as for H^+ neither a storage term nor sinks or sources are present in the PEM. The proton conductivity in the membrane is expressed with an empirical function (cf. section 7.1.4) in dependence of the membrane's water volume fraction f_V and temperature:

$$\sigma_{ion}(f_V) = 0.077 \cdot \exp(11 \cdot f_V) \cdot \exp\left(\frac{15000}{R} \cdot \left(\frac{1}{303.15} - \frac{1}{T}\right)\right). \quad (6.44)$$

6.2.3.2 Water

The PEM model accounts for diffusion, convection and electro-osmotic drag as transport mechanisms for H_2O in the membrane. The water balance equation in the PEM reads

$$\frac{\partial \left(\lambda_{\text{H}_2\text{O}} \cdot \frac{\rho^{PEM}}{EW} \right)}{\partial t} + \nabla \cdot \left(-D_{\text{H}_2\text{O}}^{PEM} \nabla \lambda_{\text{H}_2\text{O}} - \frac{\sigma_{ion} \cdot \kappa_{\text{H}_2\text{O}}}{F} \nabla \varphi - K_{\text{H}_2\text{O}}^{PEM} \nabla p \right) = 0. \quad (6.45)$$

The water diffusion coefficient $D_{\text{H}_2\text{O}}^{PEM}$ in Nafion depends on the temperature as well as on the membrane's water content. The formulation of $D_{\text{H}_2\text{O}}^{PEM}$ follows the approach of Weber and Newman [146], who relate the diffusion coefficient to the water volume fraction f_V :

$$D_{\text{H}_2\text{O}}^{PEM} = D_{\text{H}_2\text{O}}^0 \cdot f_V \cdot \frac{\rho^{PEM}}{EW} \cdot \exp\left(2416 \cdot \left(\frac{1}{303} - \frac{1}{T}\right)\right) \quad (6.46)$$

The pre-factor $D_{\text{H}_2\text{O}}^0 = 2.652 \times 10^{-10} \text{ m}^2 \text{ s}^{-1}$ is a fitted value. For the electro-osmotic drag coefficient, a constant value of $\kappa_{\text{H}_2\text{O}} = 0.35$ is used (cf. section 7.1.1) and the permeation coefficient $K_{\text{H}_2\text{O}}^{PEM}$ reads

$$K_{\text{H}_2\text{O}}^{PEM} = \frac{k_p}{\mu_{\text{H}_2\text{O}}} \cdot C_{\text{H}_2\text{O}}^m = \frac{k_p}{\mu_{\text{H}_2\text{O}}} \cdot \lambda_{\text{H}_2\text{O}} \cdot \frac{\rho^{PEM}}{EW}. \quad (6.47)$$

with an assumed hydraulic permeability of $k_p = 1 \times 10^{-20} \text{ m}^2$. As the pressure is not a primary variable in the PEM subdomain, the pressure gradient ∇p is derived by linear interpolation between the liquid pressures at the PEM/CL interfaces from anode to cathode.

6.2.3.3 Methanol

Diffusion and electro-osmotic drag are also considered as transport mechanisms for CH_3OH through the membrane, whereas hydraulic permeation is not taken into account for this species. Consequently, the balance for methanol in the membrane is

$$\frac{\partial C_{\text{CH}_3\text{OH}}^n}{\partial t} + \nabla \cdot \left(-D_{\text{CH}_3\text{OH}}^{\text{PEM}} \nabla C_{\text{CH}_3\text{OH}}^n - \frac{\sigma_{\text{ion}} \cdot \kappa_{\text{CH}_3\text{OH}}}{F} \nabla \varphi \right) = 0 \quad (6.48)$$

with the diffusion coefficient

$$D_{\text{CH}_3\text{OH}}^{\text{PEM}} = D_{\text{CH}_3\text{OH}}^0 \cdot \exp \left(2416 \cdot \left(\frac{1}{303} - \frac{1}{T} \right) \right) \quad (6.49)$$

with the fit parameter $D_{\text{CH}_3\text{OH}}^0 = 1.35 \times 10^{-10} \text{ m}^2 \text{ s}^{-1}$.

The electro-osmotic drag coefficient for methanol is defined as

$$\kappa_{\text{CH}_3\text{OH}} = \kappa_{\text{H}_2\text{O}} \cdot x_{\text{CH}_3\text{OH}}. \quad (6.50)$$

At the PEM/CL coupling interfaces (cf. section 5.7), the molar concentration of methanol in the membrane is assumed to be in equilibrium and equal to the liquid molar concentration of methanol in the catalyst layer.

6.2.3.4 Temperature

Ohmic heating due to the proton flux is considered as a source term for the temperature in the membrane. The thermal properties of the membrane are assumed to be determined by the ionomer substrate and its water content. The contribution of methanol on the membrane's energy balance is neglected.

The energy balance thus includes the following expressions for the storage, flux and source terms:

$$\xi_T = f_V \rho_{\text{H}_2\text{O}} h_{\text{H}_2\text{O}} + (1 - f_V) \rho_{\text{PTFE}} c_{p,\text{PTFE}} T \quad (6.51)$$

$$\Psi_T = -\sigma_T \nabla T + \Psi_{\text{H}_2\text{O}} M_{\text{H}_2\text{O}} h_{\text{H}_2\text{O}} \quad (6.52)$$

$$q_T = -i \nabla \varphi = -\sigma_{\text{ion}} \nabla \varphi \nabla \varphi. \quad (6.53)$$

The thermal conductivity of the Nafion membrane is described as a function of $\lambda_{\text{H}_2\text{O}}$ according to [21]:

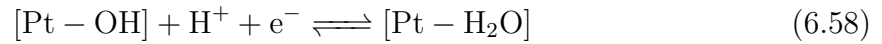
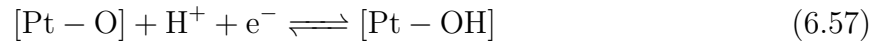
$$\sigma_T = 0.177 + 3.7 \cdot 10^{-3} \lambda_{\text{H}_2\text{O}}. \quad (6.54)$$

6.3 Reaction Kinetics

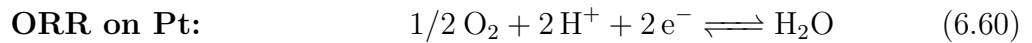
The electrochemical reactions in the DMFC catalyst layers, i.e. the oxygen reduction on the Pt-catalyst (cathode) and the methanol oxidation on the Pt-Ru-catalyst (anode), are multi-step reactions, respectively. In the model, global kinetics are used instead of elementary kinetics, due to the computational costs.

6.3.1 Oxygen reduction reaction

The dissociative oxygen reduction on platinum can be described as a five-step mechanism [66] where oxygen adsorbs on a free platinum site, dissociates and then reacts with protons and electrons under the formation of water:

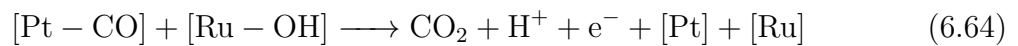
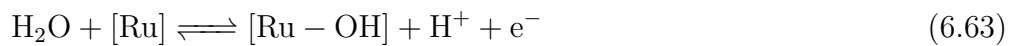
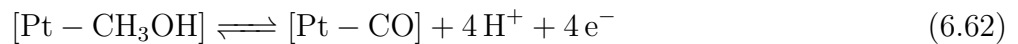


The global reaction equation for oxygen on the cathode is:



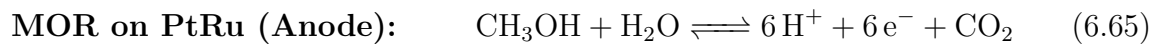
6.3.2 Methanol oxidation reaction on Pt-Ru-surfaces

The oxidation of methanol on a platinum-ruthenium catalyst can be divided into four main reaction steps, as described in [54]:



The dissociation of H_2O on Pt-surfaces is also possible, but this reaction is much slower than the dissociation of H_2O on Ru-surfaces (eq. 6.63) and thus not the favourable reaction path in a mixed Pt-Ru-catalyst.

The single reactions (6.61 - 6.64) can be summed to a global reaction equation:

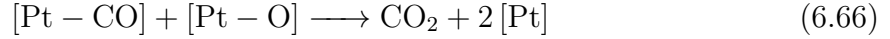


6.3.3 Methanol oxidation reaction on Pt-surfaces

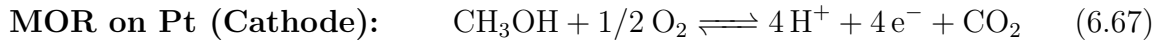
Due to methanol crossover through the membrane, CH_3OH is also present at the PEM/CCL-interface. There, it reacts on the CCL's Pt-catalyst.

In pure Pt-catalysts, the methanol oxidation takes a different pathway than in the mixed Pt-Ru-catalyst, as no ruthenium is present. However, the dissociation steps of methanol on Pt (eq. 6.61 and 6.62) are the same as in the ACL.

The primary reaction in the cathode CL is the ORR, which provides [Pt–O]-species on the catalyst surface (cf. equation 6.56). The [Pt–CO]-species from methanol dissociation on platinum (equation 6.62) can react with these oxygen species as follows [66, 54]:

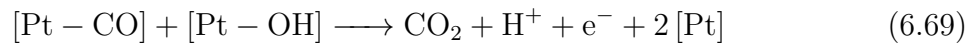
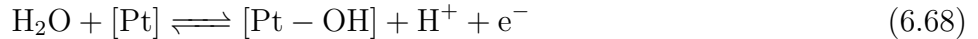


The global reaction equation for methanol oxidation on platinum reads:



As long as oxygen is present in the CCL, reaction 6.67 will proceed and is the main reaction path for the MOR on the cathode.

Another reaction path for the MOR in the cathode catalyst is possible in case adsorbed water species are available on the Pt-surface (either through direct dissociation of H_2O [30] or via other reactions, compare eq. 6.57). However, this reaction is slow compared to reaction 6.66.



In this case, the global reaction on [Pt] equals reaction 6.65:



Reaction 6.69 plays a role under oxygen depleted conditions, e.g. during the air stop phase in the DMFC refresh procedure (cf. section 8).

6.3.4 Equilibrium potential

The equilibrium potential for each half-cell reaction at reference conditions ($T_0 = 298.15 \text{ K}$, $p_0 = 101\,325 \text{ Pa}$) can be determined from the Gibbs free energy Δg_i^0 [81]:

$$E_i^0 = -\frac{\Delta g_i^0}{n F} \quad [\text{V}] \quad (6.71)$$

with

$$\Delta g^0 = \Delta h^0 - T^0 \Delta s^0 \quad [\text{kJ mol}^{-1}] \quad (6.72)$$

and

$$\Delta g_i^0 = \sum_k^{Prod.} \nu_k \cdot g_k^0 - \sum_j^{Ed.} \nu_j \cdot g_j^0 \quad (6.73)$$

Table 6.5: Thermodynamic properties of reactants at reference condition (T^0, p^0) [100]

	$\text{H}_2\text{O}(\text{l})$	$\text{O}_2(\text{g})$	$\text{CO}_2(\text{g})$	$\text{CH}_3\text{OH}(\text{l})$	$\text{H}_2(\text{g})$
g^0 [kJ mol^{-1}]	-306.69	-61.12	-457.25	-276.37	-38.96
s^0 [$\text{J mol}^{-1} \text{K}^{-1}$]	69.95	205.00	213.79	127.19	130.68

As the half-cell reactions include charged species (H^+ and e^-), those species have to be accounted for in the calculation of the equilibrium potential. The Gibbs free energy of H^+ and e^- can be derived from the hydrogen oxidation reaction [84]:



With

$$\Delta g_{HOR}^0 = 0 \text{ kJ mol}^{-1}$$

follows

$$(g_{\text{H}^+}^0 + g_{\text{e}^-}^0) = 1/2 g_{\text{H}_2}^0 = -19.48 \text{ kJ mol}^{-1} \quad (6.75)$$

With the knowledge of the Gibbs free energy of one proton and one electron (from eq. 6.75) and the thermodynamic data given in table 6.5, one can compute the Gibbs energy per reaction g_i^0 for each half-cell reaction with eq. 6.73:

$$\Delta g_{MOR,A}^0 = -8.87 \text{ kJ mol}^{-1} \quad (6.76)$$

$$\Delta g_{ORR}^0 = -474.34 \text{ kJ mol}^{-1} \quad (6.77)$$

$$\Delta g_{MOR,C}^0 = +228.3 \text{ kJ mol}^{-1} \quad (6.78)$$

The equilibrium potentials at reference condition (T^0, p^0) then are:

$$E_{MOR,A}^0 = -\frac{\Delta g_{MOR,A}^0}{6F} = +0.015 \text{ V} \quad (6.79)$$

$$E_{ORR}^0 = -\frac{\Delta g_{ORR}^0}{2F} = +1.229 \text{ V} \quad (6.80)$$

$$E_{MOR,C}^0 = -\frac{\Delta g_{MOR,C}^0}{4F} = -0.592 \text{ V} \quad (6.81)$$

For any temperature T different to T_0 , the equilibrium potential is

$$E^0(T) = E^0 + \frac{\Delta s}{nF}(T - T^0) \quad (6.82)$$

The reaction entropy is assumed to be independent of temperature, i.e. $\Delta s \approx \Delta s^0$. Besides its temperature dependence, the equilibrium potential also changes with reactant

activity. This relation is known as Nernst-Equation [100]. The temperature and activity dependent equilibrium potential then reads:

$$E^0(T, a_i) = E^0 + \frac{\Delta s^0}{n F} (T - T^0) - \frac{R T}{n F} \ln \frac{\prod a_{Prod,i}^{\nu_i}}{\prod a_{Ed,i}^{\nu_i}} \quad (6.83)$$

In order to determine the reaction entropies s^0 at reference conditions for the half cell reactions, the entropies of H^+ and e^- on a Platinum catalyst have to be known. Here, the theory of Lampinen and Fomino [84] is adapted, who derived a formulation for the partial entropies of charged species:

$$s_{H^+}^0 = 0 \text{ J mol}^{-1} \text{ K}^{-1} \quad (6.84)$$

$$s_{e^-}^0 = 65.29 \text{ J mol}^{-1} \text{ K}^{-1}. \quad (6.85)$$

With

$$\Delta s^0 = \sum_k^{Prod.} \nu_k \cdot s_k^0 - \sum_j^{Ed.} \nu_j \cdot s_j^0 \quad (6.86)$$

the reaction entropies Δs_i^0 at standard conditions can then be determined:

$$\Delta s_{MOR,A}^0 = -408.39 \text{ J mol}^{-1} \text{ K}^{-1} \quad (6.87)$$

$$\Delta s_{ORR}^0 = -326.26 \text{ J mol}^{-1} \text{ K}^{-1} \quad (6.88)$$

$$\Delta s_{MOR,C}^0 = -245.26 \text{ J mol}^{-1} \text{ K}^{-1} \quad (6.89)$$

Activities of protons and electrons are assumed to be 1. The equilibrium potentials for the half-cell reactions are therefore

$$E_{ORR}^0(T, a_i) = 1.229 \text{ V} + \frac{\Delta s_{ORR}^0}{2 F} (T - T^0) - \frac{R T}{2 F} \cdot \ln \left(\frac{a_{H_2O}}{\sqrt{a_{O_2}}} \right) \quad (6.90)$$

$$E_{MOR,A}^0(T, a_i) = 0.015 \text{ V} + \frac{\Delta s_{MOR,A}^0}{6 F} (T - T^0) - \frac{R T}{6 F} \cdot \ln \left(\frac{a_{H_2O} \cdot a_{CH_3OH}}{a_{CO_2}} \right) \quad (6.91)$$

$$E_{MOR,C}^0(T, a_i) = -0.592 \text{ V} + \frac{\Delta s_{MOR,C}^0}{4 F} (T - T^0) - \frac{R T}{4 F} \cdot \ln \left(\frac{\sqrt{a_{O_2}} \cdot a_{CH_3OH}}{a_{CO_2}} \right) \quad (6.92)$$

6.3.5 Reaction rates

The global ORR is expressed as Butler-Volmer kinetics, while the MORs are expressed as Tafel type kinetics.

$$r^{BV} = j \cdot \left[\exp \left(\frac{\alpha n F}{R T} \eta \right) - \exp \left(\frac{(1 - \alpha) n F}{R T} \eta \right) \right] \quad [\text{A m}^{-3}] \quad (6.93)$$

$$r^{Tafel} = j \cdot \exp \left(\frac{\alpha n F}{R T} \eta \right) \quad [\text{A m}^{-3}] \quad (6.94)$$

The current densities j account for the local reactant concentration and stoichiometry, the local available electrochemical surface area (cf. sec. 6.3.7), and the temperature:

$$j = j_0 \cdot ECSA \cdot \Pi_k^{Ed.} \bar{a}_k^{\nu_k} \cdot \exp \left(\frac{E_a}{R} \cdot \left(\frac{1}{T_{ref}} - \frac{1}{T} \right) \right) \quad [\text{A m}^{-3}] \quad (6.95)$$

As a measure for the species concentration in equation 6.95, the following activities a are used:

$$\begin{aligned} \bar{a}_{\text{CH}_3\text{OH},l} &= \frac{c_{\text{CH}_3\text{OH}}^l}{c_{\text{CH}_3\text{OH}}^{ref}} & \bar{a}_{\text{CH}_3\text{OH},g} &= \frac{p_{\text{CH}_3\text{OH}}}{p_{ref}} \\ \bar{a}_{\text{O}_2} &= \frac{p_{\text{O}_2}}{p_{ref}} & \bar{a}_{\text{H}_2\text{O}} &= 1.0 \end{aligned}$$

For methanol, the overall activity in eq. 6.95 is implemented as follows:

$$\bar{a}_{\text{CH}_3\text{OH}} = S_l \cdot \bar{a}_{\text{CH}_3\text{OH},l} + S_g \cdot \bar{a}_{\text{CH}_3\text{OH},g} \quad (6.96)$$

The kinetic parameters for MOR and ORR on anode and cathode are given in table 6.6.

Table 6.6: Kinetic parameters for reaction rate calculation. Values are either taken from [132] or assumed. Note that j_0 is a fit parameter in the model.

Parameter	Unit	MOR (A)	ORR	MOR (C) O ₂ -activated	MOR (C) H ₂ O-activated
j_0	A m ⁻²	6.0×10^{-5}	6.0×10^{-3}	9.5×10^{-13}	5.0×10^{-7}
α	-	0.15	0.5	0.25	0.15
n	-	6	2	4	6
E_a	kJ mol ⁻¹	35 [132]	72 [132]	30 [132]	35 [132]
T_{ref}	K	333.15 [132]	353.15 [132]	296.15 [132]	333.15 [132]
p_{ref}	Pa	101325	5×10^5 [132]	101325	101325
$c_{\text{CH}_3\text{OH}}^{ref}$	mol m ⁻³	1000		1000 [132]	1000
ν_j	-	$\nu_{\text{CH}_3\text{OH}} = 1.0$ $\nu_{\text{H}_2\text{O}} = 1.0$	$\nu_{\text{O}_2} = 0.5$	$\nu_{\text{CH}_3\text{OH}} = 1.0$ $\nu_{\text{O}_2} = 0.5$	$\nu_{\text{CH}_3\text{OH}} = 1.0$ $\nu_{\text{H}_2\text{O}} = 1.0$

6.3.6 Overpotentials

The overpotential is the potential difference between electrode potential and ionic potential. For any specific half-cell reaction i , the reaction's equilibrium potential E_i^0 has to be accounted for. The overpotential is then calculated as follows:

$$\eta_i = \varphi_{el} - \varphi_{ion} - E_i^0 \quad [\text{V}] \quad (6.97)$$

6.3.7 ECSA

The electrochemical surface area (ECSA) is calculated as suggested by Harvey et al. [59]:

$$ECSA = \frac{\epsilon_L \cdot 3.0 \cdot mPt}{rPt \cdot \rho Pt \cdot t_{cat}} \left[\frac{\text{m}^2}{\text{m}^3} \right] \quad (6.98)$$

with the platinum density $\rho Pt = 21\,450 \text{ kg m}^{-3}$ and the effective platinum surface ratio ϵ_L , the Pt loading of the catalyst mPt , the Pt particle radius rPt and the catalyst layer thickness $tCat$. The parameters for equation 6.98 are given in table 6.7.

In the cathode CL, also the formation of platinum oxide surface species is considered (cf. section 6.3.11). The effective ECSA for the cathode kinetics, depending on the actual local conditions inside the cathode CL, is described in equation 6.120.

Table 6.7: Parameters for ECSA calculation.

Parameter	Unit	ACL	CCL	Reference
ϵ_L	-	0.75	0.75	[59]
mPt	kg m^{-2}	1.8×10^{-2}	1.2×10^{-2}	MEA specification
rPt	m	7.867×10^{-9}	3.439×10^{-9}	MEA specification
$tCat$	m	4.0×10^{-5}	3.0×10^{-5}	MEA specification

6.3.8 Heat source from reaction

The heat produced by an electrochemical reaction is dependent on the reaction entropy, the reaction rate and the overpotential [84]

$$q_{Heat} = -|r_i| \cdot (\Pi^i - |\eta_i|) \left[\frac{\text{J}}{\text{m}^3 \text{s}} \right] \quad (6.99)$$

The reaction's Peltier coefficient Π^i is calculated as follows [147]

$$\Pi^i = \frac{T \Delta s^i}{n F} \quad [\text{V}] \quad (6.100)$$

6.3.9 Sinks and sources

The electrochemical reactions result in sinks and sources for the reactant species κ . The species' stoichiometry coefficient in the reaction, $\nu_{\kappa,i}$, has to be taken into account.

$$q_{\kappa,i} = \nu_{\kappa,i} \cdot \frac{r_i}{n F} \left[\frac{\text{mol}}{\text{m}^3 \text{s}} \right] \quad (6.101)$$

For protons and electrons, the source or sink equals the reactions rate r_i in the respective electrode:

$$q_{H^+} = q_{e^-} = r_i \left[\frac{\text{A}}{\text{m}^3} \right] \quad (6.102)$$

6.3.10 Ionomer film model

The heterogeneous structure of the catalyst layer can impose resistances to the reactant transport. For the ORR in the cathode CL, an ionomer film model was integrated, as described by Futter et al. [44] on the base of models by Hao [58] and Jomori [70].

The ionomer film model considers three resistance mechanisms which hinder the transport of O₂ from the gas phase to the Pt-sites of the catalyst:

$$\sum_n R_n = R_{liq} + R_{diff} + R_{int} \quad (6.103)$$

The first term, R_{liq} , describes the transport resistance due to liquid water blocking the pore space in the catalyst with

$$R_{liq} = C_1 \sqrt[3]{S_l} \quad (6.104)$$

The second term, R_{diff} , describes the resistance to oxygen diffusion through the ionomer phase of the catalyst

$$R_{diff} = \frac{\delta_{ion}}{D_{ion}^{O_2}} \quad (6.105)$$

The third term, R_{int} , accounts for a combination of interface resistances with the transition of O₂ from gas phase into the ionomer and from the ionomer to the Pt surface under consideration of the local humidity

$$R_{int} = C_2 \exp(C_3 a^{H_2O}) \quad (6.106)$$

The parameters for equations 6.104 - 6.106 are given in table 6.8.

Table 6.8: Parameters for ionomer film model.

Parameter	Value	Unit	Reference
C_1	1.1×10^4	$s\ m^{-1}$	fitted
C_2	1.0×10^4	$s\ m^{-1}$	fitted
C_3	-2.5		fitted
δ_{ion}	7.0×10^{-9}	m	[97]

According to [134], the effective diffusion coefficient $D_{ion}^{O_2}$ for oxygen in Nafion[®] can be described as

$$D_{ion}^{O_2} = 4.38 \times 10^{-6} \exp\left(\frac{-2.5 \times 10^4}{RT}\right) \left[\frac{m^2}{s}\right] \quad (6.107)$$

The reaction rate r_{ORR} is then:

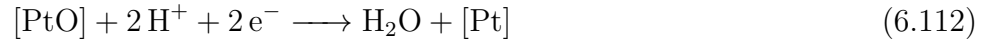
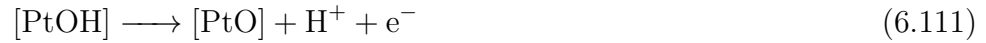
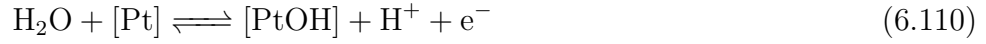
$$r_{ORR}^{IF} = \frac{k_{ORR} \cdot \left(-\sum_n R_n k_{ORR} + \sqrt{4 EC SA^2 c_{O_2}^g n^2 F^2 + (\sum_n R_n)^2 k_{ORR}^2}\right)}{2nF EC SA \sqrt{c_{O_2}^{ref}}} \quad (6.108)$$

with

$$k_{ORR} = j_0 \cdot \exp\left(\frac{E_a^{ORR}}{R} \cdot \left(\frac{1}{T_{ref}} - \frac{1}{T}\right)\right) \cdot \left[\exp\left(\frac{\alpha n F}{R T} \eta_{ORR}\right) - \exp\left(\frac{(1 - \alpha_{ORR}) n F}{R T} \eta_{ORR}\right) \right] \quad \left[\frac{\text{A}}{\text{m}^3} \right] \quad (6.109)$$

6.3.11 Platinum oxide formation

In the cathode CL, where oxygen and water is present, platinum oxide species (PtOx) form on the platinum catalyst surface at potentials above 0.6 V [33, 147]. Those species block active Pt-sites, leading to a loss in ECSA and thus performance. The semi-empirical model accounts for the formation of the species PtOH and PtO as described by Jahnke et al. [67] and assumes the following reaction mechanisms:



In the model, PtOH and PtO are considered as additional primary variables in the cathode CL. As these surface species are immobile, their balance equations read

$$\frac{\partial \theta_{\text{PtOH}}}{\partial t} - q_{\text{PtOH}} = 0 \quad (6.113)$$

$$\frac{\partial \theta_{\text{PtO}}}{\partial t} - q_{\text{PtO}} = 0 \quad (6.114)$$

The reaction rates for the formation of PtOH and PtO are (cf. [67]):

$$r_{\text{PtOH}} = 50 \cdot (1 - \theta_{\text{PtOH}}) \cdot a_{\text{H}_2\text{O}}^g \cdot \exp\left(\frac{-1.1 \times 10^4}{R T} \theta_{\text{PtOH}}\right) \cdot \exp\left(\frac{0.5 F}{R T} \eta^{\text{PtOH}}\right) - \theta_{\text{PtOH}} \cdot \exp\left(\frac{-0.5 F}{R T} \eta^{\text{PtOH}}\right) \quad [\text{s}^{-1}] \quad (6.115)$$

$$r_{\text{PtO}}^{FW} = 8 \times 10^{-2} \cdot \theta_{\text{PtOH}} \cdot \exp\left(\frac{-1.3 \times 10^5}{R T} \theta_{\text{PtO}}\right) \cdot \exp\left(\frac{0.25 F}{R T} \eta^{\text{PtO}}\right) \quad [\text{s}^{-1}] \quad (6.116)$$

$$r_{\text{PtO}}^{BW} = 2.8054 \times 10^{18} \cdot \theta_{\text{PtO}} \cdot \exp\left(\frac{-2 F}{R T} (\varphi_{el} - \varphi_{ion})\right) \quad [\text{s}^{-1}] \quad (6.117)$$

With the overpotentials

$$\eta^{\text{PtOH}} = \varphi_{el} - \varphi_{ion} - E_{\text{PtOH}}^0 \quad [\text{V}] \quad (6.118)$$

$$\eta^{\text{PtO}} = \varphi_{el} - \varphi_{ion} - E_{\text{PtO}}^0 \quad [\text{V}] \quad (6.119)$$

and $E_{\text{PtOH}}^0 = 0.75 \text{ V}$ and $E_{\text{PtO}}^0 = 0.83 \text{ V}$.

With this formulation, the model is able of describing the logarithmic increase of the platinum oxide coverage in the CCL (cf. [67]), which is important for the simulation of the reversible cathode degradation and refresh procedure in the DMFC (section 8).

The effect of the platinum oxide coverages on the ORR kinetics is expressed by the empirical ECSA reduction in the CCL (with $ECSA_0$ from eq. 6.98):

$$ECSA = ECSA_0 \cdot (1 - 0.2 \cdot \theta_{\text{PtOH}} - 3 \cdot \theta_{\text{PtO}}) \quad \left[\frac{\text{m}^2}{\text{m}^3} \right] \quad (6.120)$$

When considering the formation of the PtOx-species, additional source and sink terms have to be formulated for water and protons in addition to the source terms of PtOH and PtO:

$$q_{\text{PtOH}} = r_{\text{PtOH}} - r_{\text{PtO}}^{FW} \quad \left[\text{s}^{-1} \right] \quad (6.121)$$

$$q_{\text{PtO}} = r_{\text{PtO}}^{FW} - r_{\text{PtO}}^{BW} \quad \left[\text{s}^{-1} \right] \quad (6.122)$$

$$q_{\text{H}_2\text{O}} = 2.1 \frac{C}{\text{m}^2} \cdot \frac{ECSA}{F} \cdot (r_{\text{PtO}}^{BW} - r_{\text{PtOH}}) \quad \left[\frac{\text{mol}}{\text{m}^3 \text{ s}} \right] \quad (6.123)$$

$$q_{\text{H}^+} = q_{\text{e}^-} = ECSA \cdot 2.1 \frac{C}{\text{m}^2} \cdot (r_{\text{PtOH}} + r_{\text{PtO}}^{FW} - 2 \cdot r_{\text{PtO}}^{BW}) \quad \left[\frac{\text{A}}{\text{m}^3} \right] \quad (6.124)$$

6.3.11.1 Hydrogen evolution

Under oxygen depleted conditions (cf. section 8), spontaneous hydrogen evolution at the DMFC anode can occur. The model accounts for the hydrogen evolution reaction (HER) in the anode:



The HER kinetics are expressed as a with a Butler-Volmer equation:

$$r_{\text{HER}} = j_{\text{HER}} \cdot ECSA \cdot \left[\exp \left(\frac{-(1-\alpha) n F}{R T} \eta \right) - \frac{p_{\text{H}_2}}{p_{\text{ref}}} \exp \left(\frac{\alpha n F}{R T} \eta \right) \right] \quad \left[\frac{\text{A}}{\text{m}^3} \right] \quad (6.126)$$

with the parameters $j_{\text{HER}} = 3 \times 10^{-5} \text{ A m}^{-2}$ (fitted value), $\alpha = 0.5$ and $n = 2$.

The reaction's overpotential, η_{HER} , is

$$\eta_{\text{HER}} = \varphi_{\text{el}} - \varphi_{\text{ion}} - E_{\text{HER}}^0 \quad [\text{V}] \quad (6.127)$$

with $E_{\text{HER}}^0 = 0.0 \text{ V}$.

The resulting sinks and sources for H_2 , H^+ and e^- are

$$q_{\text{H}_2} = \frac{r_{\text{HER}}}{2F} \quad \left[\frac{\text{mol}}{\text{m}^3 \text{ s}} \right] \quad (6.128)$$

$$q_{\text{H}^+} = q_{\text{e}^-} = -r_{\text{HER}} \quad \left[\frac{\text{A}}{\text{m}^3} \right] \quad (6.129)$$

7 Model Validation and DMFC Performance Simulation

In this section, the results of the DMFC performance simulation and the different steps towards model validation are presented. Along with this model verification, the local conditions, which lead to performance heterogeneities within the DMFC, are analysed.

For model validation, experimental data from the work of Rabissi et al. [111] was used. The provided data from three DMFC single cells of the same type contained performance measurements from a macro-segmented cell set-up as well as locally resolved impedance spectra. Furthermore, the experimentally determined methanol and water flux rate at cathode outlet was available.

In order to mimic the experimental set-up and thus be directly comparable to the experimental data, the model's cathode BPP is divided into four segments. These segments were chosen in agreement with the corresponding areas of the macro-segmented cell of [111]. The segmentation scheme of the modelling domain is shown in figure 7.1. The current flow over the segment boundaries (in y-direction) is disabled in the model.

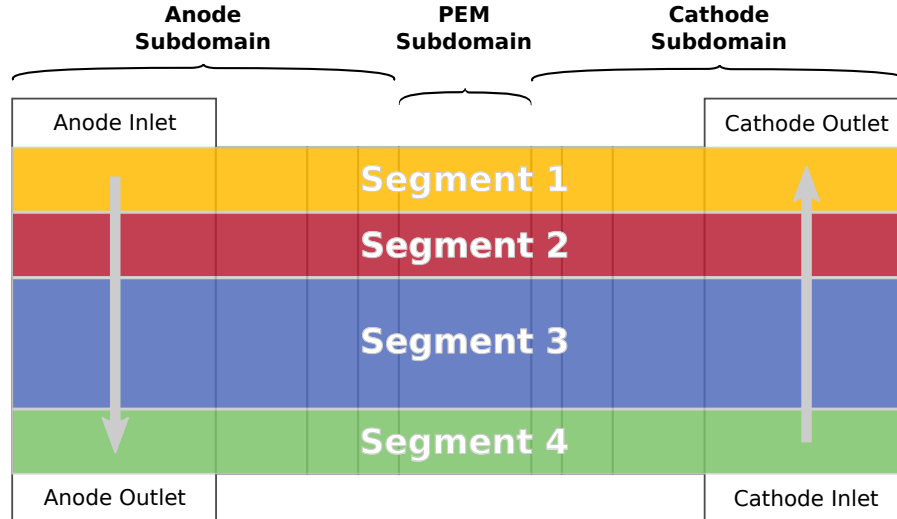


Figure 7.1: Segmentation scheme of the modelling domain.

If not stated differently, simulations with the DMFC model were carried out in the potentiostatic mode and the data is plotted against the *total* current density. The simulation results were evaluated per cell as well as per segment area. Data analysis is performed for the entire cell as well as for the cathode inlet segment (S4) and cathode outlet segment (S1).

With the model described in sections 5 and 6, simulations at RH 10 % and RH 50 % were performed. The corresponding boundary conditions are specified in section 5.7. These simulations are referred to as *reference simulations* (cf. sec. 7.2.2).

Alterations in the model description were only performed when necessary for studying individual effects on the local cell performance. These cases, where changes in the model compared to the reference were made, are explicitly mentioned.

7.1 Transport Processes in the Membrane

In order to understand the performance heterogeneities inside the DMFC as observed in the work of Rabissi et al. [111], it is essential to correctly describe the transport of water, methanol and protons in the polymer electrolyte membrane.

In the following sections, the validation of the PEM sub-model is described step by step and the local conditions within the DMFC membrane are examined in detail. Note that the membrane's properties are highly coupled with the conditions in the catalyst layers, which are discussed later in section 7.2.

7.1.1 Water Transport

Experimental data on the DMFC's total water flux rate at cathode outlet was available for the two cathode humidity levels, RH 10 % and RH 50 % over the entire operating range. For comparison with the simulation, these data were transferred into water flux rates *per channel area* (fig. 7.2), as the model only represents one out of three channels in the cell's flow-field. The respective calculation procedures can be found in section 5.3.

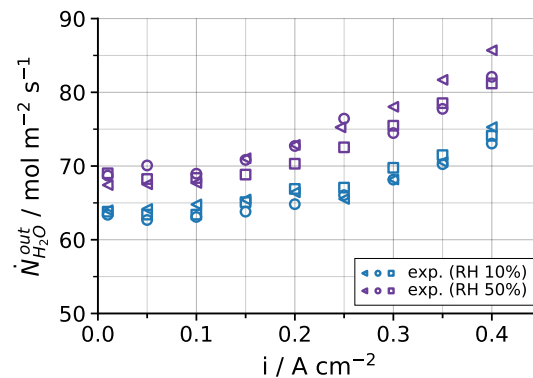


Figure 7.2: Experimental data: Water flux rate $\dot{N}_{H_2O}^{out}$ measured at the cathode outlet of the cell (given per channel area) for RH 10 % and RH 50 %.

The water flux rates $\dot{N}_{H_2O}^{out}$, however, do not directly describe the water transport in the membrane. Instead, the total amount of water at cathode outlet is the sum of three contributions: the amount of water in the air stream at cathode inlet $\dot{N}_{H_2O}^{in}$, the water

source in the cathode CL, $\dot{N}_{\text{H}_2\text{O}}^{\text{source}}$, and the net water crossover through the membrane, $\dot{N}_{\text{H}_2\text{O}}^{\text{cross}}$.

The amount of water supplied to the cell, $\dot{N}_{\text{H}_2\text{O}}^{\text{in}}$, results directly from the inlet boundary conditions for the cathode RH. For the cell examined, $\dot{N}_{\text{H}_2\text{O}}^{\text{in}}$ is constant for each humidity level, because the air feed to the cathode is not λ -controlled. The water source from reaction $\dot{N}_{\text{H}_2\text{O}}^{\text{source}}$, on the other hand, scales proportionally with the current density. The remaining unknown is the crossover rate through the PEM $\dot{N}_{\text{H}_2\text{O}}^{\text{cross}}$, which could be computed with eq. 7.1:

$$\dot{N}_{\text{H}_2\text{O}}^{\text{cross}} = \dot{N}_{\text{H}_2\text{O}}^{\text{out}} - \dot{N}_{\text{H}_2\text{O}}^{\text{in}} - \dot{N}_{\text{H}_2\text{O}}^{\text{source}} \quad (7.1)$$

The resulting H_2O crossover rates for RH 10 % and RH 50 %, calculated with equation 7.1, are shown in figure 7.3. The values are given *per cell area* (cf. sec. 5.3) and still called “experimental”, as the values were directly converted from the experimental data.

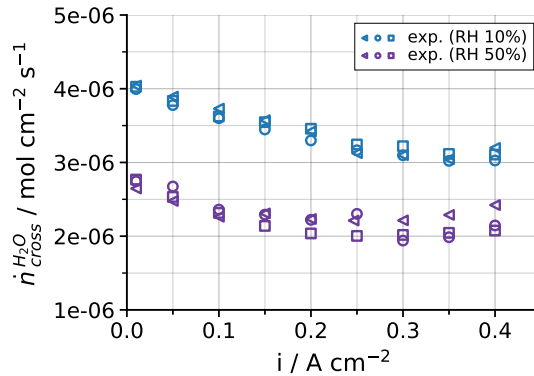


Figure 7.3: Water crossover fluxes per cell area $\dot{n}_{\text{H}_2\text{O}}^{\text{cross}}$ for RH 10 % and RH 50 %, determined from the experimental data on $\dot{N}_{\text{H}_2\text{O}}^{\text{out}}$.

Note that other than the total water flux rates at cathode outlet, $\dot{N}_{\text{H}_2\text{O}}^{\text{out}}$, the H_2O crossover through the membrane at higher cathode humidity, i.e. RH 50 %, is significantly lower compared to the crossover rate at RH 10 %.

The water crossover in the membrane itself is determined by a combination of three transport mechanisms: diffusion, permeation and electro-osmotic drag. The impact of each process on $\dot{n}_{\text{H}_2\text{O}}^{\text{cross}}$ is discussed in the following paragraphs.

7.1.1.1 Membrane Water Content

The membrane’s water content $\lambda_{\text{H}_2\text{O}}$ plays a major role for the transport processes inside the PEM. It is dependent on the the local water activity in the gas phase and the saturation of the liquid phase at the PEM/CL interfaces in anode and cathode, as described in sections 6.2.1 and 6.2.2. The humidity conditions at the CL/PEM interfaces, in turn, are influenced by the fluid compositions, the reactions in the CLs, the capillary properties

of CLs, MPLs and GDLs but also the water crossover itself (see section 7.2.1).

$\lambda_{\text{H}_2\text{O}}$ is thus a highly coupled quantity which represents the complex interactions in fluid transport between the different domains of the fuel cell.

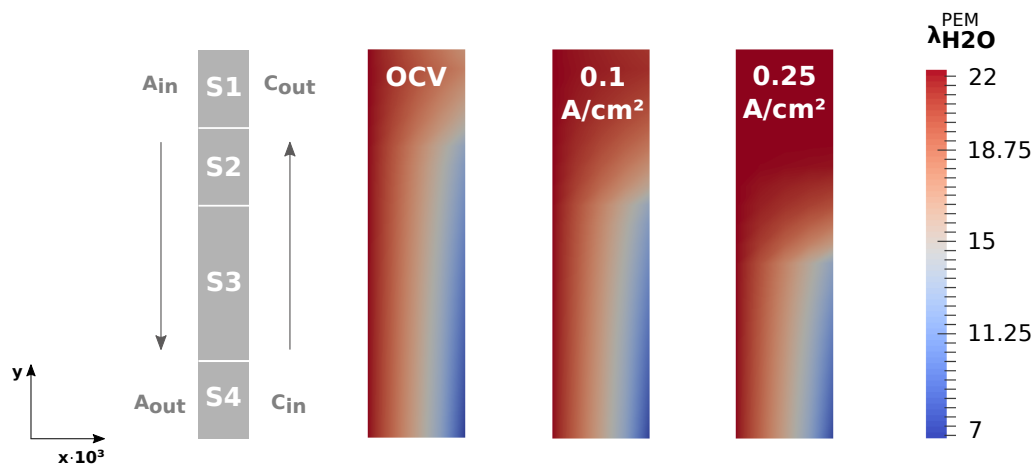


Figure 7.4: Membrane water content $\lambda_{\text{H}_2\text{O}}$ at operation with RH 10 % at OCV, 0.1 A/cm² and 0.25 A/cm² (reference simulation). The 2D plot shows the PEM magnified by 10^3 in x-direction.

With the reference simulation at RH 10 %, the $\lambda_{\text{H}_2\text{O}}$ distributions shown in figure 7.4 were obtained. As can be seen the plots, at the ACL/PEM interface the water content in the membrane is high and its variation with current is negligible. At the PEM/CCL interface, however, great variations in $\lambda_{\text{H}_2\text{O}}$ can be observed: In the cathode inlet segment (S4), $\lambda_{\text{H}_2\text{O}}$ remains at a low level over the entire current range. At cathode outlet (S1) in contrast, the membrane's water content rises strongly with increasing current. This behaviour is to a great extent coupled to the presence of liquid water in the CCL at the respective position, which is discussed in section 7.2.1.

With the higher cathode humidity of RH 50 %, the water content in the membrane and its resulting gradient from anode to cathode look different compared to the case with RH 10 % (cf. figure 7.5). At the ACL/PEM interface, $\lambda_{\text{H}_2\text{O}}$ remains at approx. 22 since the anode boundary conditions did not change in the simulation. In contrast, the membrane shows a strong gradient of $\lambda_{\text{H}_2\text{O}}$ along the channel at the PEM/CCL interface already at OCV for the operation with high cathode humidity. At a current density of 0.1 A/cm² and more, the gradient in $\lambda_{\text{H}_2\text{O}}$ across the membrane (x-direction) is negligible in the cathode outlet area (S1 and S2), while it persists in S4 (cathode inlet).

Overall, the distribution of $\lambda_{\text{H}_2\text{O}}$ in the DMFC membrane is heterogeneous and shows strong gradients not only from anode to cathode, but also along the channel at the PEM/cathode interface.

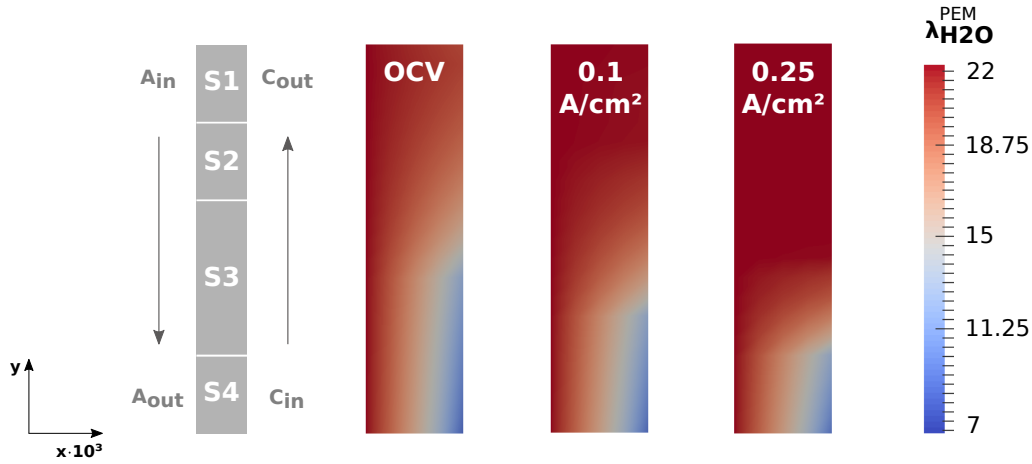


Figure 7.5: Membrane water content $\lambda_{\text{H}_2\text{O}}$ at operation with RH 50 % at OCV, 0.1 A/cm² and 0.25 A/cm² (reference simulation). The 2D plot shows the PEM magnified by 10³ in x-direction.

7.1.1.2 Diffusion

The gradient in the membrane's water content $\lambda_{\text{H}_2\text{O}}$ is the driving force for water diffusion through the PEM. At low current densities and low humidity levels in the DMFC cathode, the gradients in $\lambda_{\text{H}_2\text{O}}$ across the membrane are strongest, which lets deduce that diffusion plays a dominant role under these conditions.

In order to confirm this hypothesis, a simulation with diffusion as the only transport mechanism for H₂O in the membrane was performed and compared to the water crossover data determined from experiments. The simulation result for RH 10 % plotted in figure 7.6 shows that diffusive transport alone describes the water crossover up to a current density of 0.15 A/cm² sufficiently well. At higher current densities, the diffusion-only approach underestimates the water crossover, indicating the relevance of additional mechanisms for the water transport at this point.

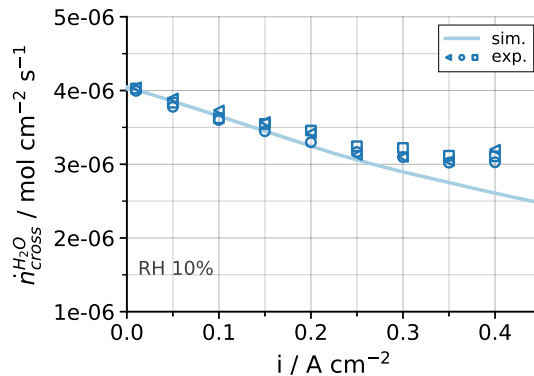


Figure 7.6: Simulated water crossover flux $\dot{n}_{\text{H}_2\text{O}}^{\text{cross}}$ by diffusion only in comparison to the experimental data (RH 10 %).

7.1.1.3 Electro-osmotic drag

Another transport mechanism for water within the polymer electrolyte membrane is the so-called electro-osmotic drag. It describes the transport of water molecules induced by the transport of protons through the membrane.

The transport of protons can occur by two different processes: the vehicular mechanism, which describes the diffusive transport of hydronium ions, H_3O^+ , and the Grotthuss mechanisms, which describes the transport of protons by the formation and breaking of hydrogen bonds [78, 106, 82]. For membranes with a low hydration level, the vehicular mechanism is the prevalent proton transport mechanism, while the Grotthuss mechanism dominates in fully hydrated (i.e. liquid-equilibrated) membranes. Only the vehicular proton transport mechanism is coupled to a net flow of H_2O -molecules.

A majority of PEMFC and DMFC models published use a drag coefficient based on the vehicular mechanism in order to describe the electro-osmotic effect in the membrane. These models mostly incorporate the relation of Springer et al. [133] for the electro-osmotic drag coefficient $\kappa_{drag}^{\text{H}_2\text{O}}$, which reads

$$\kappa_{drag}^{\text{H}_2\text{O}} = 2.5 \frac{\lambda_{\text{H}_2\text{O}}}{22} \quad (7.2)$$

According to this relation, the electro-osmotic drag coefficient increases linearly with the membrane's water content $\lambda_{\text{H}_2\text{O}}$. A simulation with the $\kappa_{drag}^{\text{H}_2\text{O}}$ description of eq. 7.2 was performed in order to test the respective correlation. Note that also diffusion and permeation were included as mechanisms for H_2O transport in the model for this simulation.

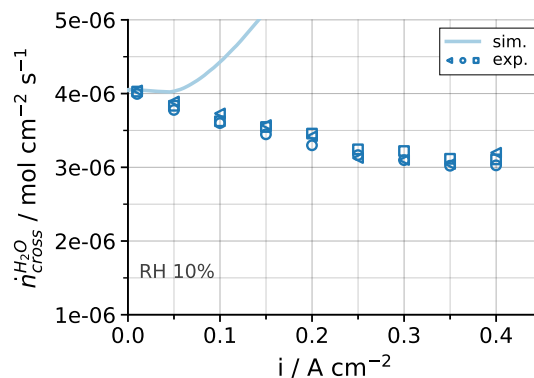


Figure 7.7: Simulated water crossover flux $\dot{n}_{\text{H}_2\text{O}}^{\text{cross}}$ by diffusion and electro-osmotic drag with a drag coefficient of $\kappa_{drag} = 2.5 \cdot \lambda_{\text{H}_2\text{O}}/22$ in comparison to the experimental data.

The simulation result with $\kappa_{drag}^{\text{H}_2\text{O}}$ described by the Springer relation (eq. 7.2) is shown in figure 7.7.

As can be seen in the comparison of simulated and experimental water flow over current density, the water crossover gets strongly over-estimated with this correlation for $\kappa_{drag}^{H_2O}$, even at low current densities. The respective simulation had to be aborted due to convergence problems at $i \approx 0.2 \text{ A/cm}^2$.

Since a water flux through the membrane described with $\kappa_{drag}^{H_2O} = 2.5 \cdot \lambda_{H_2O}/22$ could not be verified against the experimental data, a closer look was taken on the work of Peng et al. [106]. The group performed experiments with Nafion membranes of $50 \mu\text{m}$ thickness and varying temperatures up to 80°C with a novel experimental technique, and found the electro-osmotic drag coefficient in Nafion to be *decreasing* with increasing λ_{H_2O} and $\kappa_{drag}^{H_2O} \leq 1$. This finding, which stands in contrast to a majority of measurements and the common approach in PEMFC modelling, was carefully verified with different experimental approaches by the group. The authors argue that with increasing membrane water content, the Grotthuss mechanism is favoured for proton transport over the vehicular mechanism, i.e. the higher the membrane's water content, the lower the link between proton transport and water transport in the PEM.

As the water content in the DMFC membrane is significantly higher compared to a typical PEMFC, the hypothesis of Peng et al. was considered and tested: In the DMFC model, the electro-osmotic drag coefficient then was assumed to be constant (i.e. independent from λ_{H_2O}) with $\kappa_{drag}^{H_2O} = 0.325$, since a concise correlation the electro-osmotic drag coefficient and the membrane water content was not known.

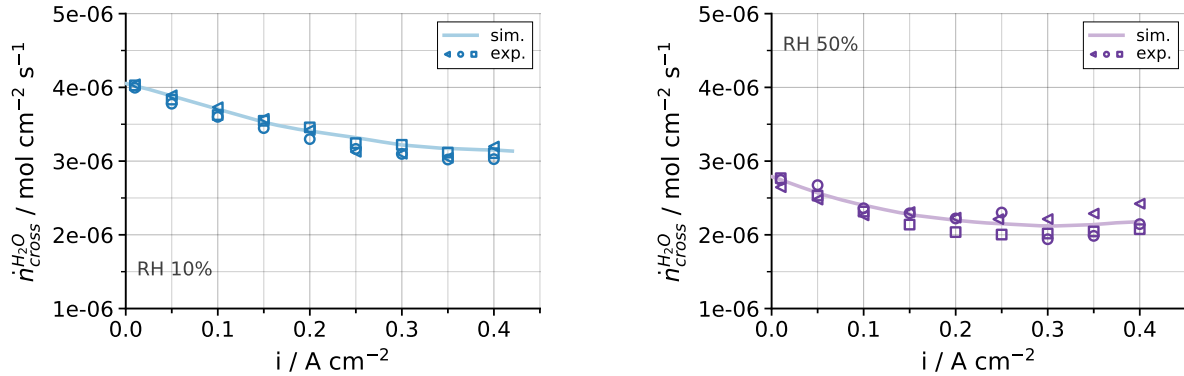


Figure 7.8: Simulated water crossover $\dot{n}_{cross}^{H_2O}$ for RH 10 % and RH 50 % by diffusion and electro-osmotic drag with a drag coefficient of $\kappa_{drag}^{H_2O} = 0.325$ in comparison to the experimental data (reference simulation).

With the low and constant value for $\kappa_{drag}^{H_2O}$, very good results for the water crossover through the membrane could be obtained in the simulation for both humidity levels, RH 10 % and RH 50 %, as figure 7.8 shows.

7.1.1.4 Permeation

Hydraulic permeation of H_2O molecules due to a pressure gradient across the membrane is another possible transport mechanism for water in low-temperature fuel cells. An according correlation was implemented in the DMFC model (cf. section 6.2.3 eq. 6.45).

In the model's PEM sub-domain the pressure is not a primary variable, that is why the liquid pressure at the PEM/CL coupling interfaces was interpolated between anode and cathode side. Note that p_l at these interfaces depends on the catalyst layer's capillary pressure p_c . A hydraulic permeation coefficient of $k_p = 1 \times 10^{-20} \text{ m}^2$ in the membrane was assumed, which is low but in the order of magnitude as reported in literature [93, 82].

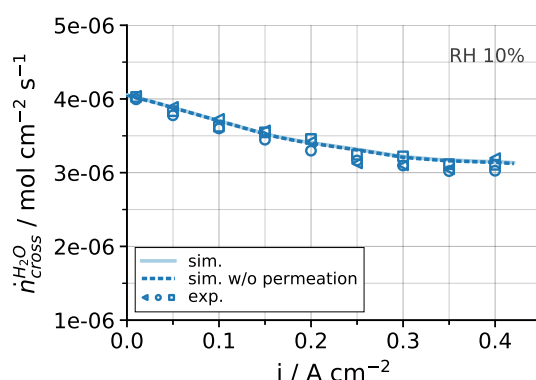


Figure 7.9: Simulated water crossover flux $\dot{n}_{\text{H}_2\text{O}_{\text{cross}}}$ with and without permeative water transport included in the PEM model in comparison to the experimental data.

A comparison of the simulated water crossover with and without permeation as transport mechanism in the PEM and the experimental data shows that the impact of hydraulic permeation is negligible in this set-up with an unpressurised system and the chosen model parameters (cf. plot 7.9). It should be noted that it could well be that the fitted value for the membrane water diffusion coefficient in the model includes a permeative share. Qualitatively, it is expected that the effect of permeative and diffusive water transport overlap for the given scenario, as the gradient in the driving force for both mechanisms is directly coupled to the liquid water saturation at the PEM/CL interfaces in anode and cathode.

Since the experimental data did not include a pressure variation, the effect of permeation could not be further quantified. As the uncertainty regarding the CL's capillary pressures and consequently the exact pressure conditions at the CL/PEM interfaces is high, the impact of hydraulic permeation on the water crossover in the DMFC was not further studied here.

For the given experimental scenario, the H_2O -crossover through the membrane could be satisfactorily described with water transport via to diffusion and electro-osmotic drag.

7.1.2 Sorption Processes at the PEM/CL Interfaces

The sorption of water to and from the polymer electrolyte membrane is a complex and dynamic process, so that the equilibrium membrane water content of the sorption isotherm is not instantly reached [89]. The time it takes until the membrane water content is in equilibrium depends on the local temperature and humidity conditions at the membrane interface. The water sorption from a gas phase into the membrane is considerably slower than the sorption of water from a liquid phase, which could be a rate-limiting step for the water transfer inside the fuel cell [52, 161].

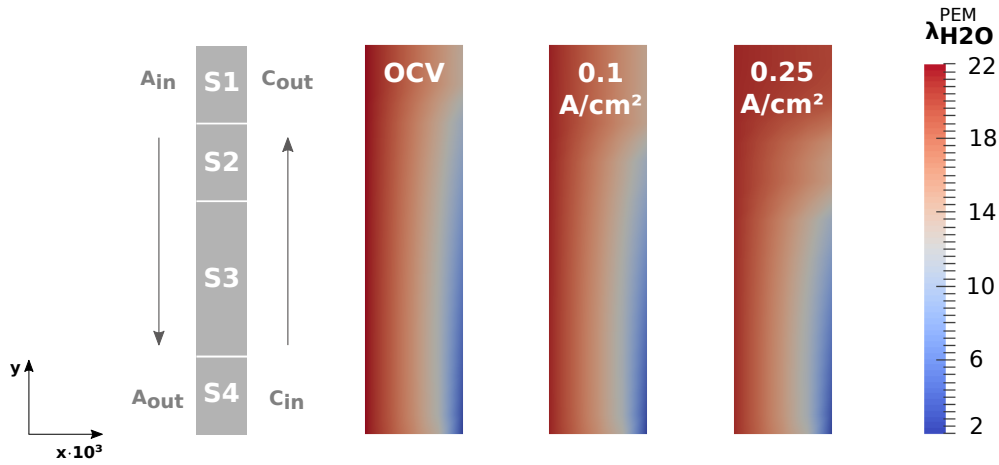


Figure 7.10: Membrane water content $\lambda_{\text{H}_2\text{O}}$ in a simulation *without* sorption kinetics at the PEM/CL interfaces for RH 10 % at OCV, 0.1 A/cm² and 0.25 A/cm² (compare with fig. 7.4 for the reference simulation *with* sorption kinetics). The 2D plot shows the PEM magnified by 10³ in x-direction.

For the DMFC with its dynamic phase transitions in anode and cathode, it is expected that the different rate constants for water sorption to and from the membrane in dependence of its state have a large impact on the water balance and the two-phase flow behaviour in the cell. In order to correctly describe the interactions between the membrane and the electrodes, H₂O sorption kinetics based on the study of Ge et al. [52] were included in the model's coupling conditions at the PEM interfaces to the anode and cathode sub-domain (cf. section 6.2.2).

With the DMFC model, the effect of sorption kinetics at the membrane/electrode interfaces could be studied by varying the coupling conditions for the water transfer: Simulations *without* sorption kinetics at the coupling interfaces were carried out for RH 10 % and RH 50 %. In this case, the PEM/CL interfaces are assumed to be always in equilibrium and the transfer of H₂O from and to a gas phase is equally fast than the transfer from and to a liquid phase.

The neglect of sorption kinetics at the PEM/CL interfaces has a great effect on the

membrane water content $\lambda_{\text{H}_2\text{O}}$ and the water crossover, as a comparison between the simulation results of the variation with the reference simulation shows:

The model predicts a much lower membrane water content $\lambda_{\text{H}_2\text{O}}$ at the interface to the cathode catalyst layer in case no sorption kinetics are considered, as can be seen in figure 7.10. Compare figure 7.4 for the values obtained with the reference simulation *with* sorption kinetics, where the resulting $\lambda_{\text{H}_2\text{O}}$ is significantly higher at the PEM/CCL interface over the entire operating range. The effect that the mass transport resistance due to sorption at a membrane/vapour interface keeps the humidification of the membrane high has also been described by Zhao et al. in their experimental study on Nafion 1100 membranes [161].

In the simulation *without* sorption kinetics (figure 7.10), the gradient in $\lambda_{\text{H}_2\text{O}}$ across the membrane (x-direction) is higher compared to the reference (cf. figure 7.4). As a consequence, the overall water crossover through the PEM is accelerated, as the simulation results in figure 7.11 show. This behaviour can be observed for both humidity levels, RH 10 % and RH 50 %.

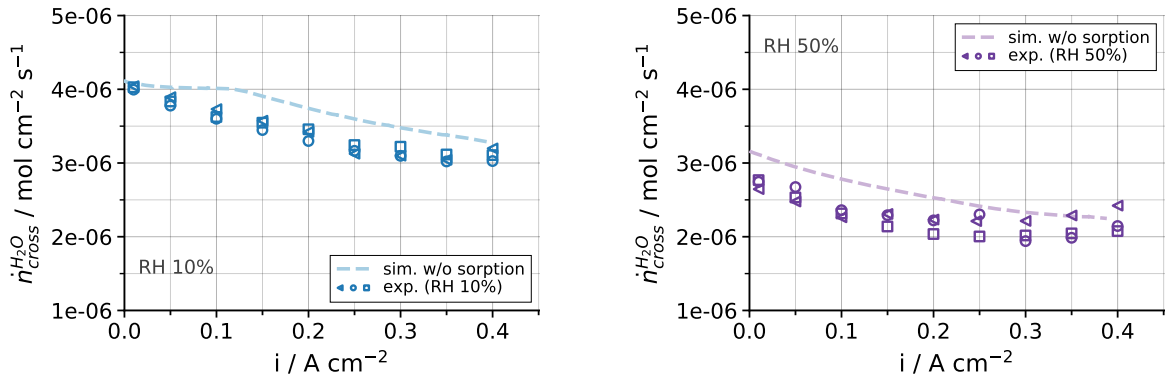


Figure 7.11: Water crossover through the membrane in the simulation *without* sorption kinetics at the PEM/CL interfaces for RH 10 % and RH 50 % in comparison to the experimental data.

Figure 7.11 also shows that in case the sorption kinetics are neglected in the model, the H_2O -crossover diverges from the experimental data for RH 10 %, despite starting at the correct level at OCV. The bend in the simulated water crossover rate at $i \approx 0.12 \text{ A/cm}^2$ correlates with the formation of liquid water in the CCL at cathode outlet and the instant rise of $\lambda_{\text{H}_2\text{O}}$ at the CCL interface. Figure 7.12 shows the water crossover rate and the profile of $\lambda_{\text{H}_2\text{O}}$ at the PEM/CCL interface in segment 1 (cathode outlet) in direct comparison.

The observed behaviour in $\dot{n}_{\text{H}_2\text{O, cross}}$ can be explained as follows: When sorption kinetics are neglected, humidity changes at the PEM interface instantly lead to a change of the membrane's water content in the model. In case a liquid phase emerges at the membrane

interface, $\lambda_{\text{H}_2\text{O}}$ increases proportionally (cf. eq. 6.29), just as observed for the PEM/CCL interface in S1, the cathode outlet segment, in the simulation. As a consequence, the gradient in $\nabla \lambda_{\text{H}_2\text{O}}$ between anode and cathode decreases and the diffusive water transport, which has been identified to be the leading transport mechanism through the membrane, sinks (cf. eq. 6.45).

For RH 50 %, the simulation *without* sorption kinetics renders an overall reasonable water crossover profile, however the crossover rate is too high and does not match the experimentally determined flux (figure 7.11).

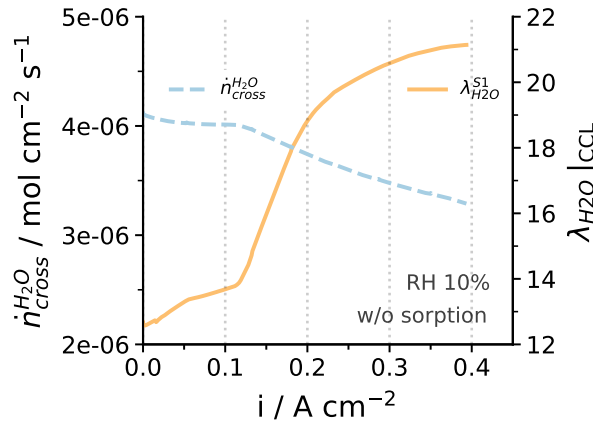


Figure 7.12: Overall water crossover through the membrane in blue and membrane water content $\lambda_{\text{H}_2\text{O}}$ at the PEM/CCL interface in S1 (cathode outlet) in orange in simulation *without* sorption kinetics (RH 10 %).

The simulation results show that the assumption that the water transfer at the membrane interfaces happens instantly and is equally fast for a gas-equilibrated as well as for a liquid-equilibrated membrane leads to an over-estimation of the water transport through the DMFC membrane. In contrast, when including the sorption kinetics in the model at the membrane interfaces (reference), the experimentally observed water crossover in the cell can be satisfactorily described for RH 10 % as well as for RH 50 % without any changes in the model and with just one single set of parameters (cf. figures 7.8 and 7.13b).

This result highlights the relevance of the mass transport resistance imposed by the sorption process at the membrane/CL interfaces for water transport under the heterogeneous and dynamically changing humidity conditions inside the DMFC.

7.1.3 Local Water Transport

After verifying the water transport processes in the membrane, the *local* crossover rates, which are experimentally not accessible, could be studied with the model. Figure 7.14 shows the local water crossover rates for the first and the last segment of the cell obtained with the reference simulation with RH 10 % and RH 50 %. Here, the data is plotted versus the segment's local current density and the overall crossover rate for the entire cell is

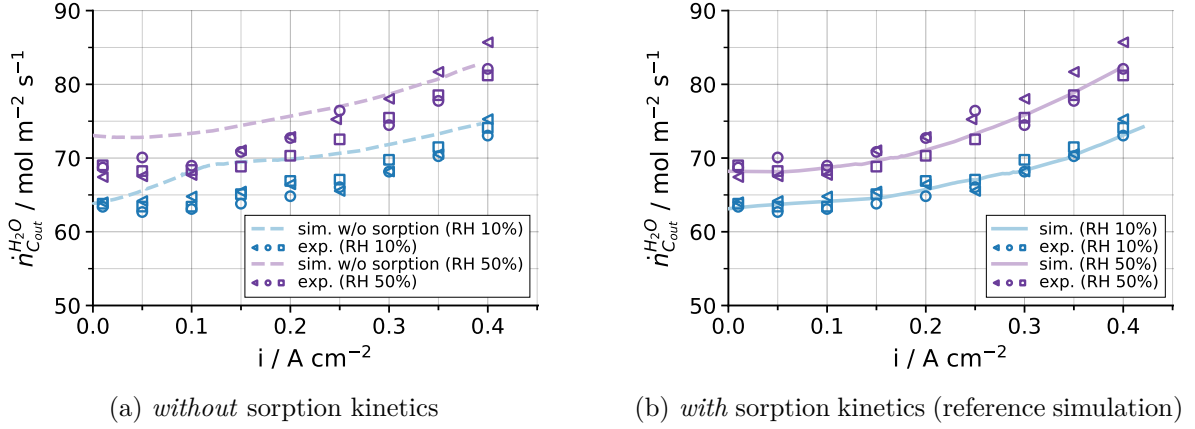


Figure 7.13: Simulation results for water flux at cathode outlet a) *without* sorption kinetics and b) *with* sorption kinetics (reference simulation) at the PEM/CL interfaces RH 10 % and RH 50 %) in comparison to the experimental data.

given as a reference.

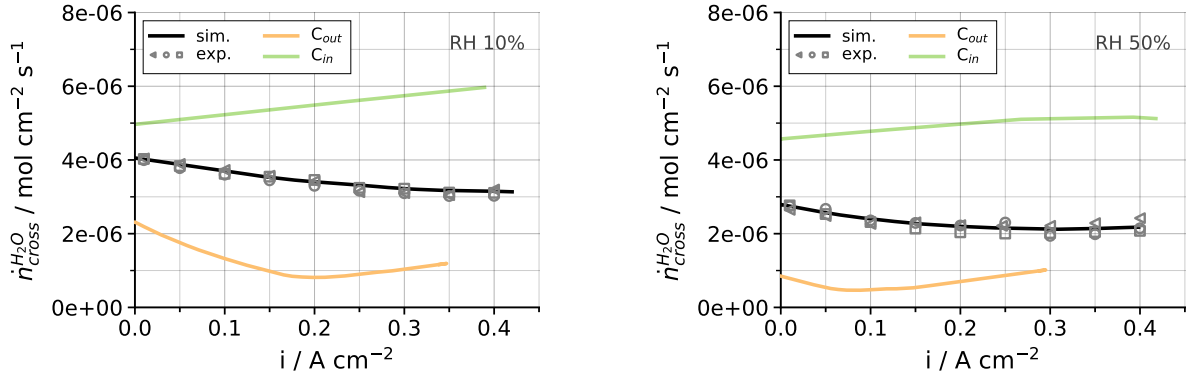


Figure 7.14: Total water crossover rate $\dot{n}_{\text{H}_2\text{O}}$ for RH 10 % (left) and RH 50 % (right) from experiment and simulation in comparison to the *local* water crossover rates in the first and last segment of the cell (reference simulation). Note that the local crossover rates are plotted against the local current density.

The local crossover rates show a similar behaviour for RH 10 % and RH 50 %: In S4 (cathode inlet/anode outlet), where the largest humidity gradient across the membrane occurs, the highest crossover rate can be observed. It rises continuously over current, for RH 10 % as well as for RH 50 %. In S1 (cathode outlet/anode inlet), the crossover rate is much lower, due to the comparably small gradient of $\lambda_{\text{H}_2\text{O}}$ in the membrane. At low current densities, the local H_2O crossover rate in this segment sinks down first, then rises again at higher current densities.

The rise in the local crossover rates, both for the cathode inlet as well as for the cathode outlet segment, can be attributed to the impact of the electro-osmotic drag, as a com-

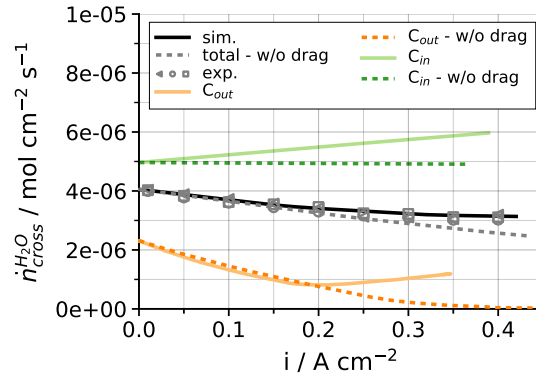


Figure 7.15: Total and local water crossover rates $\dot{n}_{\text{H}_2\text{O}_{\text{cross}}}$ of the reference simulation (solid lines) and a variation *without* electro-osmotic drag (“diffusion only”, dashed lines) in comparison to the experimental data (RH 10 %). Note that the local crossover rates are plotted against the local current density.

parison of the reference simulation at RH 10 % with the “diffusion only” variation shows in figure 7.15.

7.1.4 Proton Transport

The transport of protons through the membrane is a key factor for the performance of polymer electrolyte fuel cells and thus an essential part of the DMFC model. The proton conductivity σ_{ion} of the polymer is a function of the temperature and the membrane’s water content.

Locally resolved electrochemical impedance spectra (EIS) were available from the experiments for RH 10 % and RH 50 % in the cathode, each for a current density of $i = 0.1 \text{ A/cm}^2$ and $i = 0.25 \text{ A/cm}^2$. With these experimental data, it was possible to quantify the effect of the local humidity conditions in the cathode on the membrane resistance to proton transport.

A common approach in fuel cell modelling is the use of empirical relations, as for example derived by Weber et al. [146] or by Springer et al. [133], in order to describe the membrane’s ionic conductivity. These two relations were implemented and tested with the DMFC model, respectively.

Springer correlation [133]:

$$\sigma_{\text{ion}}^{\text{PEM}}(\lambda_{\text{H}_2\text{O}}) = (0.5139 \cdot \lambda_{\text{H}_2\text{O}} - 0.326) \cdot \exp\left(1268 \cdot \left(\frac{1}{303.15} - \frac{1}{T}\right)\right) \quad (7.3)$$

Weber correlation [146]:

$$\sigma_{\text{ion}}^{\text{PEM}}(f_V) = 0.05 + 0.5 \cdot (f_V - 0.06)^{1.5} \cdot \exp\left(\frac{15000}{R} \cdot \left(\frac{1}{303.15} - \frac{1}{T}\right)\right) \cdot 100 \quad (7.4)$$

The NEOPARD-X framework, in which the DMFC model was implemented, also includes an option to simulate impedance spectra [43]. EIS were simulated with the model for the different expressions of σ_{ion}^{PEM} and compared to the experimental data.

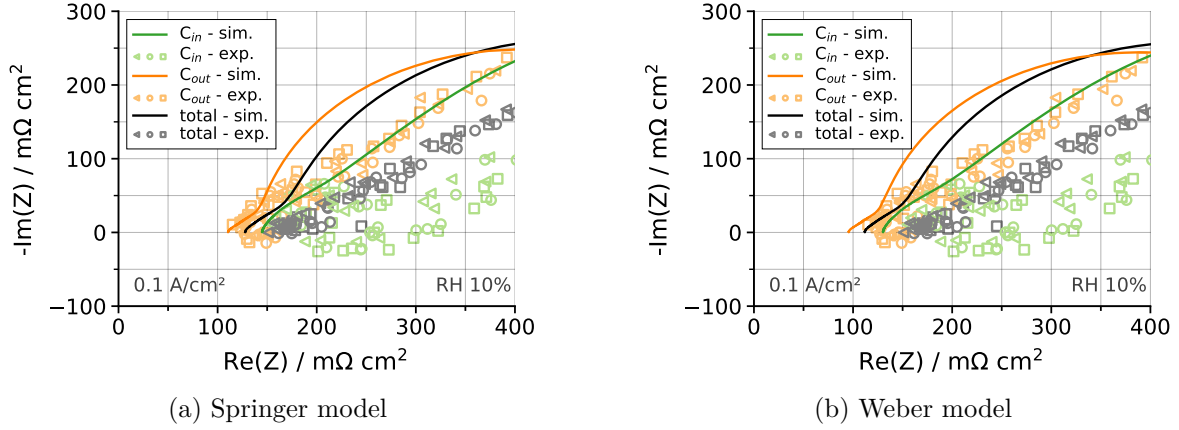


Figure 7.16: Nyquist plots obtained in simulations for $i = 0.1 \text{ A/cm}^2$ at RH 10 % with σ_{ion}^{PEM} described by (a) the Springer model [133] and (b) the Weber model [146] in comparison to the experimental data.

Figure 7.16 shows the Nyquist diagrams of the EIS simulations at $i = 0.1 \text{ A/cm}^2$ with the Springer expression (fig. 7.16a) and the Weber expression (fig. 7.16b) for σ_{ion}^{PEM} in comparison with the experimental data.

In the experiments, a large spread in the membrane resistance can be observed along the channel from cathode outlet to cathode inlet: The well-humidified membrane at cathode outlet (S1) shows the lowest ohmic resistance, while a strong increase in the membrane resistance can be observed for the dry conditions in S4, the cathode inlet segment.

Neither the Weber correlation 7.4 nor the Springer correlation 7.3 could satisfactorily describe the experimentally observed dependence of the membrane's proton conductivity on $\lambda_{\text{H}_2\text{O}}$ in the model. With both expressions for σ_{ion}^{PEM} , the ohmic resistance in the dry cathode inlet segment and also the average ohmic resistance of the cell get significantly underestimated (figure 7.16).

In order to correctly represent the correlation between the local membrane humidity and its resistance to proton transport, an own relation for σ_{ion}^{PEM} was developed (cf. section 6.2.3 equation 6.44). This empirical expression describes a stronger variation of the membrane's ionic conductivity with the membrane water content $\lambda_{\text{H}_2\text{O}}$ than the literature models, as a comparison of the three relations in plot 7.17 shows.

With the description of σ_{ion}^{PEM} by eq. 6.44, the local ohmic resistances in the membrane obtained with the 2D DMFC model are in good agreement with the experimental data,

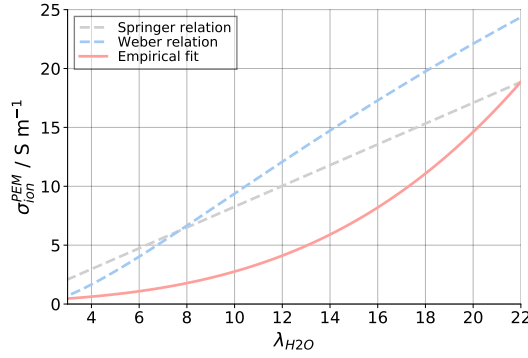


Figure 7.17: Comparison of the three discussed empirical relations for the membrane's ionic conductivity σ_{ion} as a function λ_{H_2O} at $T = 348.15$ K.

as the resulting Nyquist diagrams in figures 7.18 and 7.19 show. The predicted resistances match well locally for both humidities, RH 10 % and RH 50 %, and at both current densities, 0.1 A/cm^2 as well as 0.25 A/cm^2 .

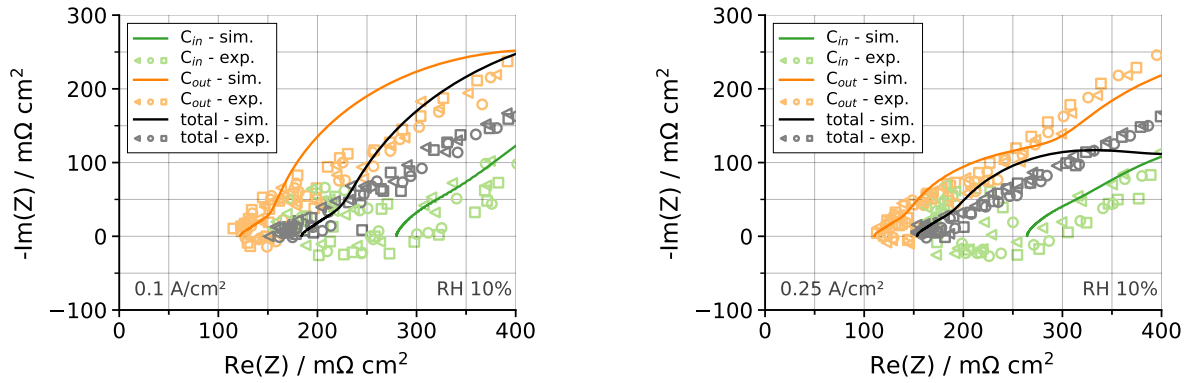


Figure 7.18: Nyquist plots obtained from the *reference simulation* with σ_{ion}^{PEM} described by eq. 6.44 for RH 10 % at 0.1 A/cm^2 (left) and 0.25 A/cm^2 (right) in comparison to the experimental data.

The reference DMFC model is thus able to correctly describe the membrane's resistance to proton transport in dependence on the heterogeneous humidity conditions along the channel.

7.1.5 Methanol Transport

The crossover of methanol through the membrane is determining the formation of a mixed potential in the DMFC cathode and thus another relevant transport mechanism in the PEM model. It is described in a similar manner to the water transport (cf. section 6.2.3): Diffusion and electro-osmotic drag are assumed to be the dominant transport processes for CH_3OH . Methanol permeation through the membrane, however, is neglected in the model. Moreover, the methanol concentration at the PEM/CL interfaces is assumed to

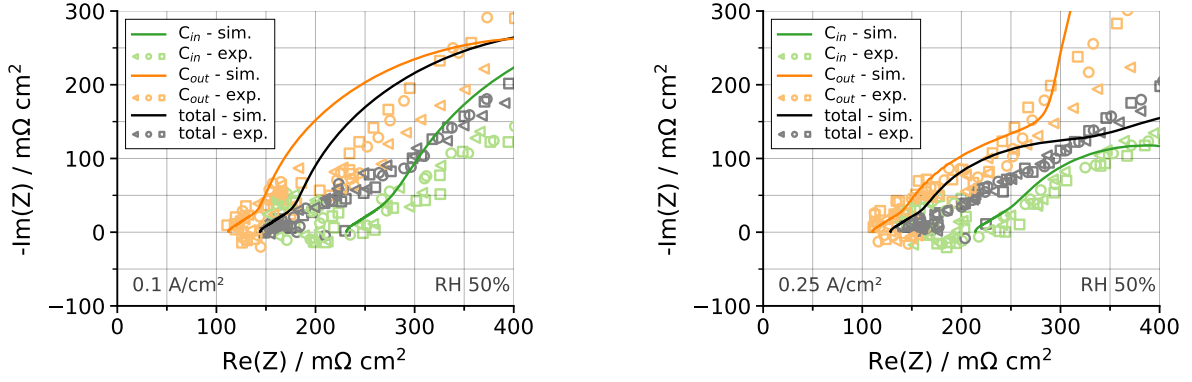


Figure 7.19: Nyquist plots obtained from the *reference simulation* with σ_{ion}^{PEM} described by eq. 6.44 for RH 50 % at 0.1 A/cm^2 (left) and 0.25 A/cm^2 (right) in comparison to the experimental data.

be in equilibrium, so no sorption kinetics are considered at the membrane's coupling interfaces to the anode and cathode sub-domain for methanol.

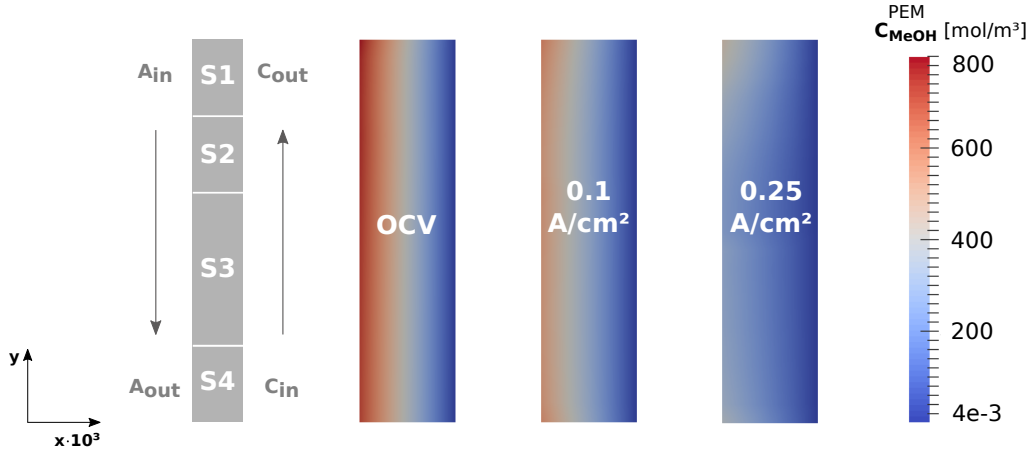


Figure 7.20: Methanol molar concentration C_{MeOH}^{PEM} in the membrane at operation with RH 10 % for OCV, 0.1 A/cm^2 and 0.25 A/cm^2 (reference simulation). The 2D plot shows the PEM magnified by 10^3 in x-direction.

Figure 7.20 shows the methanol concentration within the membrane at different operating points obtained with the reference simulation at RH 10 %. At OCV, there is a strong gradient from anode to cathode across the membrane, and the distribution is homogeneous along the channel on anode and cathode side. With $i = 0.1 \text{ A/cm}^2$, the gradient decreases since the methanol concentration at the PEM/ACL interface is reduced. At higher current densities, i. e. 0.25 A/cm^2 , the methanol concentration at the anode interface has notably decreased and a concentration gradient along the channel has formed along the ACL at the interface to the membrane. The concentration is highest in S1, the anode inlet/cathode outlet segment, followed by S4, the anode outlet area. The lowest concentration on the anode side can be observed at the transition area between S2 and S3 at this operating point. On the PEM/CCL interface, the methanol concentration

is steadily low over the entire operating range, since crossover methanol gets directly oxidised in the cathode catalyst layer.

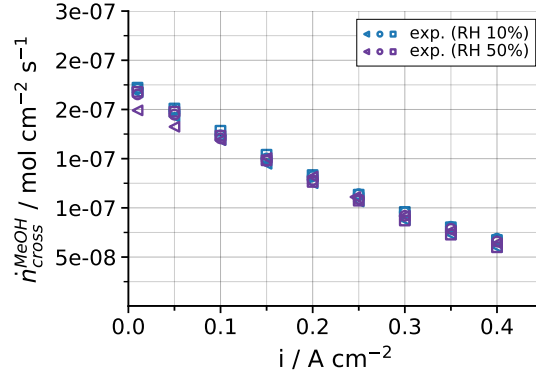


Figure 7.21: Experimental data: Methanol crossover rates for RH 10 % and RH 50 %.

The experimentally determined methanol crossover rates decreases continuously with increasing current and is independent from the cathode relative humidity, as can be seen in figure 7.21. With the chosen described formulation in the model (cf. eq. 6.48), the methanol transfer through the membrane could be reasonably described, as a comparison of the reference simulations for RH 10 % and RH 50 % with the experimental data shows (figure 7.22).

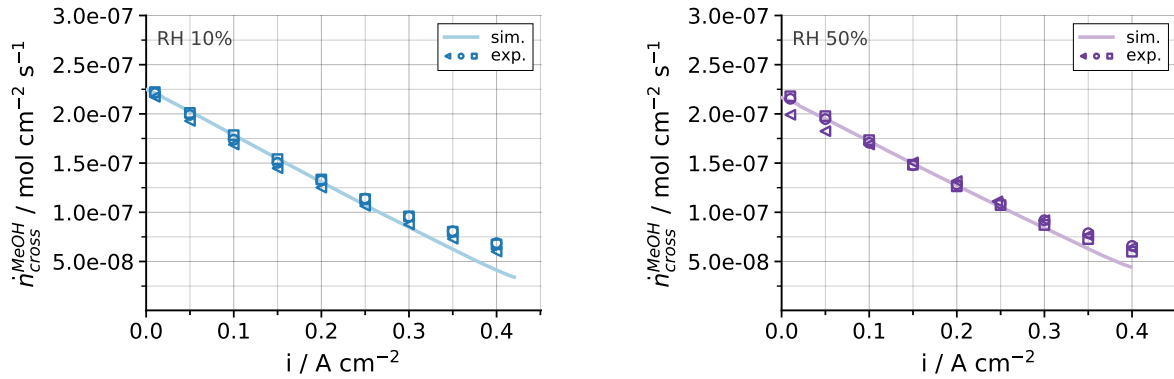


Figure 7.22: Simulated methanol crossover rates $\dot{n}_{\text{cross}}^{\text{MeOH}}$ for RH 10 % and RH 50 % (reference simulation) in comparison to the experimental data.

Only at high current densities ($i > 0.3 \text{ A/cm}^2$), the methanol flux gets slightly underestimated in the simulation. When repeating the simulation with a higher electro-osmotic drag coefficient for methanol, this behaviour did not change (simulation result not shown here), which indicates that the formulation of the methanol transport in the anode porous layers (GDL, MPL, CL) might be somewhat too slow in the model.

The local methanol crossover follows the ACL distribution of methanol along the channel, as figure 7.23 shows: The transfer of methanol is highest in the anode inlet/cathode outlet area and lowest in the anode outlet/cathode inlet area in both cases, RH 10 % and RH 50 %. At low current density, the differences along the channel are small, while at higher current densities, the evolving CH_3OH gradient from anode inlet (S1) to anode outlet (S4) is directly reflected by the methanol crossover rate across the membrane.

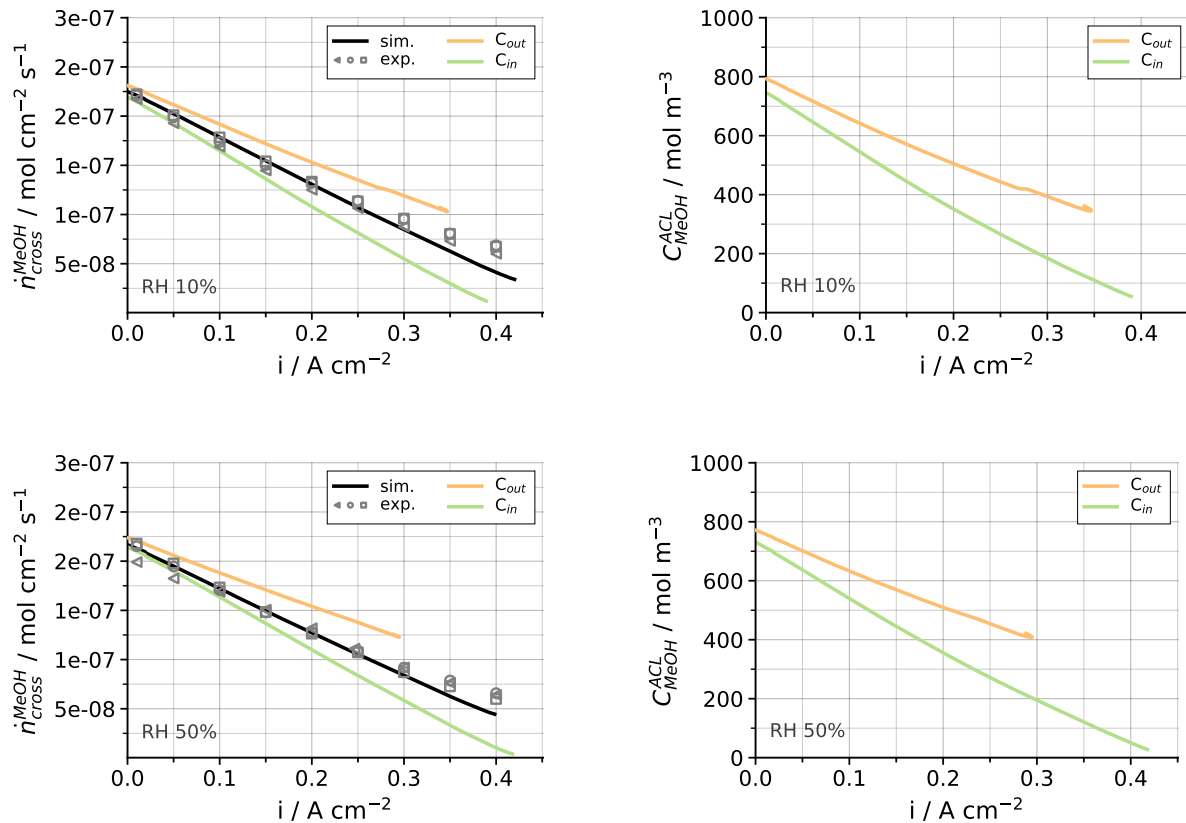


Figure 7.23: Total methanol crossover $\dot{n}_{\text{cross}}^{\text{MeOH}}$ for RH 10 % and RH 50 % from experiment and simulation in comparison to the *local* methanol crossover rates in the first and last segment of the cell (left) and corresponding local methanol concentrations $C_{\text{MeOH}}^{\text{ACL}}$ in the ACL (right). Note that the local properties are plotted against the local current density. Reference Simulation.

7.1.6 Conclusion: Transport Processes in the DMFC membrane

The transport of water, protons and methanol through the DMFC membrane has been analysed in detail with the 2D model and a verification of the model description with experimental data has been accomplished.

While a variation in the DMFC cathode humidity conditions had a strong impact on the transport of water and protons through the membrane, the crossover of methanol was

hardly affected. This indicates that the transport of methanol in the DMFC membrane is mainly determined by the conditions in the DMFC anode, namely the local distribution of CH_3OH at the ACL/PEM interface. As no experimental data on variations in the DMFC anode conditions was available, these effects on methanol transport were not studied in detail here. For the given set-up, methanol transport in the DMFC membrane could be satisfactorily described by diffusion and electro-osmotic drag.

Water and proton transport proved to be very sensitive to changes in the DMFC cathode humidity conditions. A much higher water crossover from anode to cathode could be observed for dry cathode conditions (RH 10 %) compared to the case air with RH 50 % was supplied to the cell. The model shows that also the local crossover rate of water is much higher in the dry cathode inlet area of the cell than in the cathode outlet area with a much higher local humidity.

Under the experimental conditions with an unpressurised system, diffusion and electro-osmotic drag could be identified as the relevant transport mechanisms for water through the DMFC membrane. The common approach in fuel cell modelling of describing the electro-osmotic drag by assuming proton transport via the vehicular mechanism failed for the DMFC studied here. In case of the liquid-fed DMFC with a comparatively well-humidified ionomer, the proton transport seemed to be best described assuming a Grotthuss-type mechanism, which leads to a decoupling between the movement of protons and the movement of H_2O -molecules. With this approach, convincing results for the water transport through the DMFC membrane could be achieved in the simulation.

The local water content in the ionomer phase is not merely determined by the local humidity conditions at the PEM/CL interfaces, but also by the interface resistances to water sorption depending on the state of water in the open pore space of ACL and CCL. With the model it could be shown that for the significant variance in gas and liquid distribution inside the DMFC anode and cathode, sorption kinetics must not be neglected when modelling the membrane water content and respective transport processes in the DMFC.

The ionic conductivity in the DMFC membrane proved to be very sensitive to the local humidity conditions at the PEM/CCL interface and consequently the local water content in the membrane. Significant variances in the membrane ionic conductivity, which could be observed experimentally for different cathode humidity levels, were depicted in the model by an empirical correlation, which proved valid for the cell provided with air with RH 10 % as well as RH 50 %.

With the thorough investigation of the individual humidity-dependent transport properties and mechanisms in the DMFC membrane and the successful verification against experimental data with varying humidity levels, the membrane model can be seen as validated.

7.2 Heterogeneities in the local DMFC performance

Validating the transport processes for water, methanol and protons in the membrane was a fundamental step towards simulating the DMFC performance. With the verified description of the local membrane properties and transport mechanisms under various humidity conditions in the cathode, the 2D model could be used to study performance heterogeneities on the cell level.

The experimental data of [111] show strong variations within the DMFC single cell: In figure 7.24, the performance data of three different cells (marked with different symbols) are portrayed for RH 10 % (left) and RH 50 % (right). Depicted are the overall cell voltage in grey, the voltage of the cathode inlet segment S4 in green and the voltage of the cathode outlet segment S1 in orange. As can be seen in figure 7.24, variations in the local cell performance occur over the entire current range for RH 10 % as well as for RH 50 %.

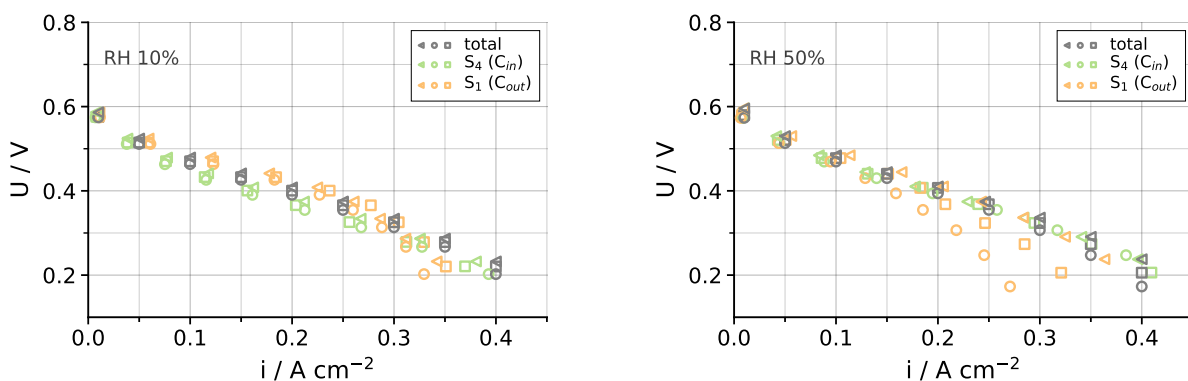


Figure 7.24: Experimental data: Total cell voltage and local cell voltage in S1 (cathode outlet/anode inlet) and S4 (cathode inlet/anode outlet) for RH 10 % and RH 50 %. Note that the local cell voltages are plotted against the local current densities in the respective segment.

In case of RH 10 % (left image), the performance of S4 (cathode inlet) is permanently lower than the overall cell voltage and the deviations are largest in the medium current density range. Segment 1 (cathode outlet) performs better than the overall cell voltage up to a current density of $i \approx 0.3 \text{ A/cm}^2$. In the high current density range, the performance of S1 gets drastically reduced and at $i = 0.35 \text{ A/cm}^2$, this segment of the cell performs worse than S4 and the cell in total.

For RH 50 % (right picture), the performance of S4 (green, cathode inlet) is more or less identical with the overall cell, whereas the voltage of segment 1 (orange, cathode outlet) diverges towards lower potentials, starting from a current density of $i \approx 0.15 \text{ A/cm}^2$. The data of the three different cells scatter strongly at this point.

Rabissi et al. [111] attribute the observed variations in the local cell performance to heterogeneities in the local DMFC cathode humidity, with drying effects in the cathode

inlet area and flooding effects at cathode outlet. With the 2D DMFC model, the conditions and mechanisms leading to the observed performance heterogeneities in the cell shall be further studied.

In section 7.1.4, one mechanism leading to the divergence in the local cell performance, namely the humidity-dependent resistance to proton transport in the DMFC membrane, has already been identified. In order to study the effect of the membrane's ohmic resistance on the cell performance exclusively, a simulation was carried out with the humidity-dependence of the catalyst's ionic conductivity (eq. 6.27) and the resistances in the CCL's ionomer film model (eqs. 6.104 and 6.106) disabled, i.e. $\sigma_{ion}^{CL} = \sigma_{ion}^{CL}(a_{H_2O} = 1)$ and $R_{liq} = 0$ and $R_{int} = 0$.

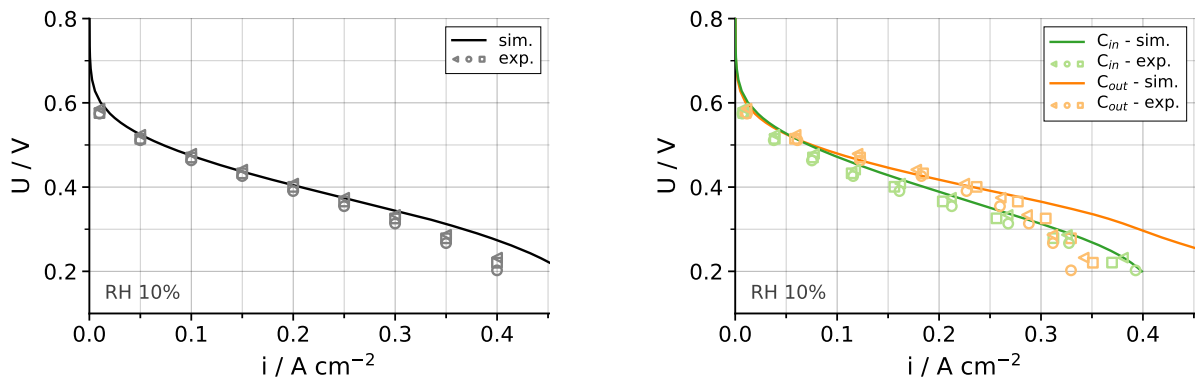


Figure 7.25: Simulation result for the total cell voltage (left) and the local cell voltages (right) at the cathode inlet and cathode outlet segment of the DMFC obtained with model including only the membrane-related resistances to charge and species transport as discussed in section 7.1 in comparison to the experimental data (RH 10 %).

Figure 7.25 shows the result of this simulation in comparison with the experimental data for RH 10 %. In the figure on the left, the overall DMFC performance is plotted and in the figure on the right the local cell performance of S1 and S4. The simulation makes clear that the humidity-dependence of the membrane ohmic resistance comes into effect at medium to high current densities. It renders a lower performance in the cathode inlet segment (S4) compared to the cathode outlet segment (S1) at current densities higher than 0.1 A/cm^2 . The poor performance of the cathode inlet segment at low current densities $i < 0.1 \text{ A/cm}^2$ and the decreasing cell voltage at high current densities $i > 0.25 \text{ A/cm}^2$, however, cannot be explained by the ohmic resistance of the PEM.

7.2.1 Resistances in the Cathode Catalyst Layer

The catalyst layer with its heterogeneous composition and complex structure also exhibits a great potential for resistances towards species and charge transport [83, 105]. On the one hand, its narrow pore sizes and varying internal surface properties strongly influence the interplay between gas and liquid phase. On the other hand, the ionomer

thin film in the catalyst layer imposes new resistances to proton and species transport. The transport processes are dominated by interface effects and much slower than in the bulk membrane. Again, the local water activity plays a crucial role for the characteristics of this layer in the fuel cell.

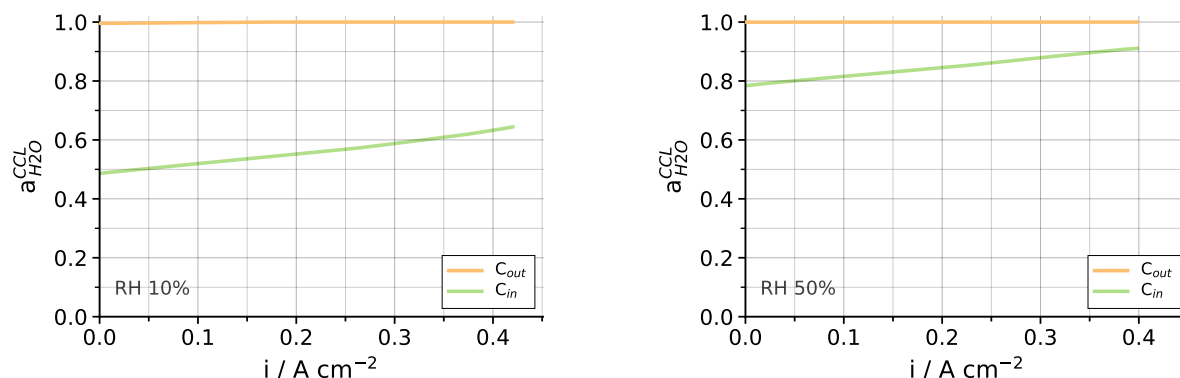


Figure 7.26: Local water activity a_{H_2O} in the cathode inlet and cathode outlet segment of the CCL during operation with RH 10 % and RH 50 % (reference simulation).

The reference simulation shows that the actual water activity in the cathode catalyst layer of the DMFC is much higher than the relative humidities in the cathode feed gas (cf. fig. 7.26).

For a RH of 10 % in the air feed at cathode inlet, the model predicts a water activity in the cathode inlet segment of the CCL (S4) of about 50 % at OCV. With increasing current density, a_{H_2O} linearly rises up to a mean value of $\approx 65\%$ in this segment (figure 7.26). In the cathode outlet area of the CCL (S1), on the other hand, the gas is fully saturated over the entire operating range.

The qualitatively same behaviour can be observed along the channel if the cell is operated with RH 50 % (fig. 7.26): in this case the gas is also partially saturated at cathode inlet and fully saturated at cathode outlet. At the cathode inlet segment of the CCL, the local water activity rises from about 80% at OCV up to over 90% at a current density of 0.4 A/cm² in this case.

The elevated humidity levels in the catalyst layer result from the material characteristics and transport properties of the different porous layers GDL, MPL and CL in combination with the water source from the electrochemical reaction and the water crossover through the membrane.

7.2.1.1 Resistances to proton transport in the CCL

The proton transport properties of thin film ionomers are even more sensitive to the humidity than the properties of bulk Nafion, as for example Paul et al. [105] showed. In their study, the authors found that σ_{ion} in ionomer thin films could vary in more

than four orders of magnitude within a humidity range of $0.2 \leq a_{\text{H}_2\text{O}} \leq 0.95$. The local relative humidities in the DMFC cathode catalyst layer fall well within this range. Even if in contact with a fully saturated gas phase, an ionomer thin film shows a much lower ionic conductivity than a typical polymer electrolyte membrane.

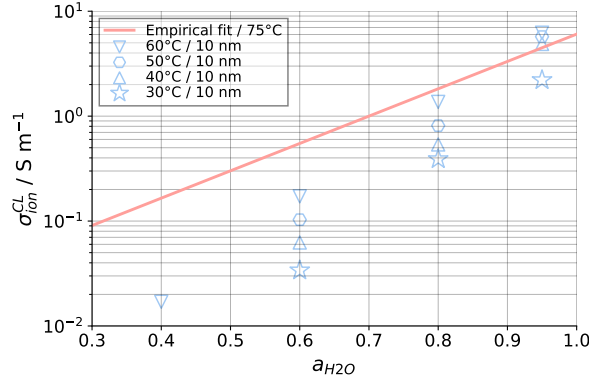


Figure 7.27: Ionic conductivity of Nafion thin-films as presented by Paul et al. [105] (blue symbols) and own empirical relation for $\sigma_{\text{ion}}^{\text{CL}}$ (eq. 6.27) (red line).

Following these findings, a correlation for $\sigma_{\text{ion}}^{\text{CL}}$ in the catalyst layers was derived as a function of the local water activity (cf. eq. 6.27). Figure 7.27 shows the resulting ionic conductivity of the CL in the model compared to data presented by Paul et. al. [105].

With this description of $\sigma_{\text{ion}}^{\text{CL}} = f(a_{\text{H}_2\text{O}})$ in the anode and cathode catalyst layer, the DMFC model renders the local performances shown in figure 7.28 for RH 10 % and RH 50 %. In these simulations, the resistances R_{liq} and R_{int} in the CCL's ionomer film model (eqs. 6.104 and 6.106) were disabled, while the ionic conductivities in membrane $\sigma_{\text{ion}}^{\text{PEM}}$ and catalyst layer $\sigma_{\text{ion}}^{\text{CL}}$ were implemented in dependence of the local humidity conditions, as described in eqs. 6.44 and 6.27.

The catalyst layer's humidity dependent resistance to proton transport contributes to the poor performance of the cell's cathode inlet area (S4) at low current densities, as the comparison between the simulation results in figure 7.25 ($\sigma_{\text{ion}}^{\text{CL}} = \text{const.}$) and figure 7.28 ($\sigma_{\text{ion}}^{\text{CL}} = f(a_{\text{H}_2\text{O}})$) for RH 10 % shows.

By considering the humidity-dependence of the membrane's and catalyst layer's ionic conductivity, the model is fit to describe the experimentally observed performance heterogeneities in the DMFC for the low to medium current regime at both humidity levels, RH 10 % and RH 50 % (cf. figure 7.28): Up to a current density of 0.2 A/cm^2 for RH 10 % and 0.15 A/cm^2 for RH 50 %, the local cell voltages predicted by the model now match well the with the experimental data.

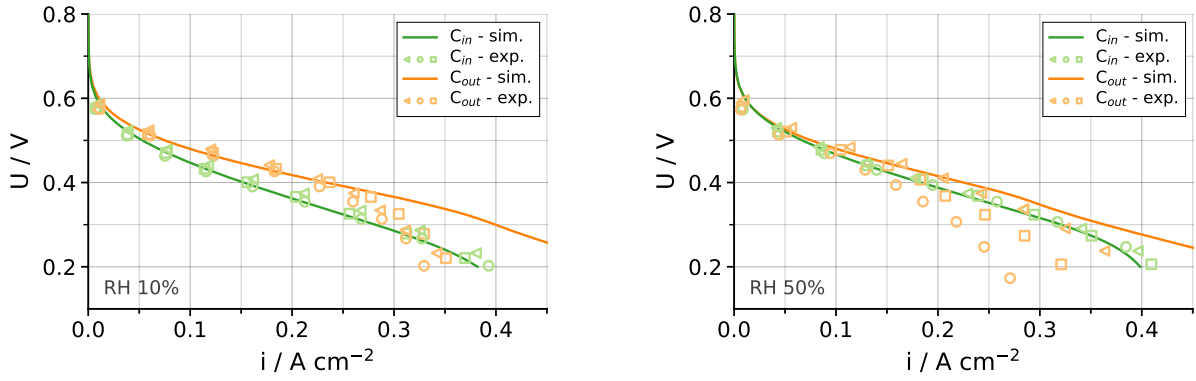


Figure 7.28: Simulation result for the local cell voltages at the cathode inlet and cathode outlet segment of the DMFC obtained with model including the membrane-resistances to charge and species transport as discussed in section 7.1 and the resistance to proton transport in the CCL with $\sigma_{ion}^{CL} = f(a_{H_2O})$ (cf. eq. 6.27) for RH 10 % and RH 50 % in comparison to the experimental data.

7.2.1.2 Resistances to species transport in the CCL

At higher current densities, the effect of mass transport limitations can be noticed in the local cell voltage of the cathode outlet segment in the experiments (cf. fig. 7.24). The observed performance decrease in this segment is stronger for RH 50 % than for RH 10 %, which lets assume that flooding is the relevant process here. Flooding describes the resistance to species transport due to accumulation of liquid water in the porous medium.

The formation of liquid water within the electrode is directly coupled with the internal surface properties and the morphology of the porous structures. The saturation, which describes the share of liquid and gas relative to the available pore volume, is coupled to the capillary pressure within the porous structure (cf. eq. 6.10).

Experimental studies on the capillary behaviour of GDL and CL materials show that residual saturations exist for the gas and for the liquid phase [83, 160] and a hysteresis in the $p_c S_w$ -relation occurs, depending on whether a liquid is injected or withdrawn from the porous medium [55, 83]. This model, however, omits hysteresis in the description of the capillary behaviour of the porous media in the fuel cell. Furthermore, the concept of a residual saturation in the porous media is neglected and both phases are assumed to be mobile over the entire saturation range. This procedure was chosen due to the high uncertainty of the actual wetting properties of the materials used in the experimental work of Rabissi et al. [111].

Following the findings of Kusoglu et al. [83], the $p_c S_w$ -relations were parametrised in a way that the catalyst layers show a more hydrophilic behaviour than GDL and MPL (cf. fig. 6.1 and tab. 6.2). With this description of the porous media capillary properties in the model, the liquid saturation profiles shown in figure 7.29 are obtained in the cathode catalyst layer with the reference simulation for a cathode inlet relative humidity of 10 %

and 50 %, respectively.

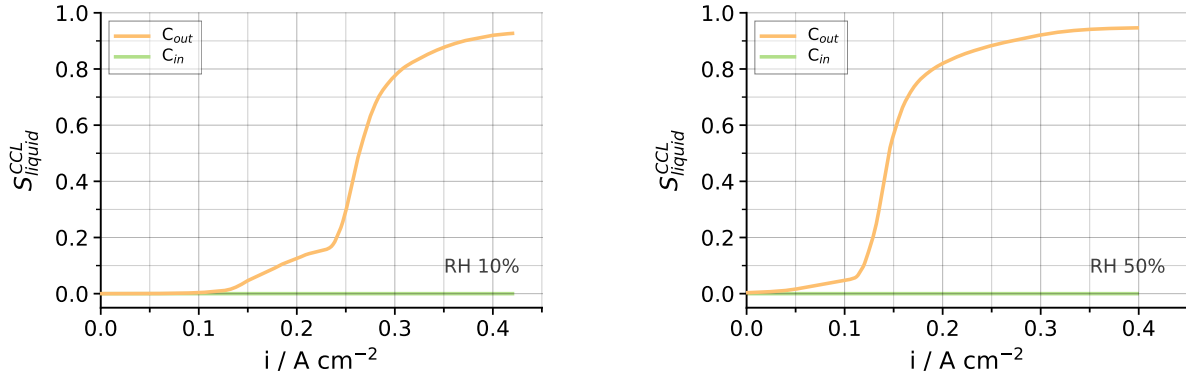


Figure 7.29: Liquid saturation in the cathode inlet and cathode outlet segment of the CCL during operation with RH 10 % and RH 50 % (reference simulation).

In case of RH 10 %, liquid emerges in the CCL’s cathode outlet segment (S1) starting at a current density of about 0.15 A/cm² (cf. plot 7.29). At $i = 0.25\ A/cm^2$, a steep increase in the liquid saturation can be observed and S_l rises up to a maximum of over 90% at $i = 0.4\ A/cm^2$. In the cathode inlet segment of the CCL (S4), on the other hand, no liquid emerges over the entire current range.

With a cathode inlet relative humidity of 50 %, the saturation in the CCL starts rising from OCV onwards in S1 (cathode outlet) and the simulation predicts liquid saturation values $S_l > 60\%$ already at a current density of $i \approx 0.15\ A/cm^2$. With rising current density, values of $S_l \approx 95\%$ are reached (cf. figure 7.29). The cathode inlet area of the CCL (S4) remains dry, just as in the case with lower cathode humidity.

These simulation results obtained for the liquid saturation in the CCL (fig. 7.29) phenomenologically match the experimentally determined flooding effects in the DMFC’s cathode outlet segment (S1) in terms of occurrence over current and also in terms of intensity (cf. fig. 7.24). Nevertheless, the mere presence of liquid water in the CCL does not result in a performance decrease in the simulation with $\sigma_{ion}^{CL} = f(a_{H_2O})$ and $\sigma_{ion}^{PEM} = f(\lambda_{H_2O})$, as the direct comparison of S_l^{CCL} with the local cell voltages in figure 7.30 shows (R_{liq} and R_{int} are disabled in the CCL’s ionomer film model).

The voltage in the cathode outlet area S1 (orange) at high current densities is over-estimated in the simulation compared with the experimental results, despite the CCL segment is nearly fully saturated with liquid. This result indicates that the oxygen transport towards the reaction sites in the CCL predicted by the model is too fast. The same behaviour can be noted for RH 50 %, where the cathode outlet segment gets filled with liquid even earlier, but no effect on the local performance in S1 can be detected.

The simplified description of the porous media behaviour in the model with the neglect of possibly limited phase mobilities and residual saturations in the porous layers could

be one factor contributing to the underestimation of mass transport resistances in the simulation. Apart from that, the transport of an oxygen molecule towards the active site of a catalyst particle in the CCL includes some more steps than solely diffusion through a fully or partially saturated porous matrix.

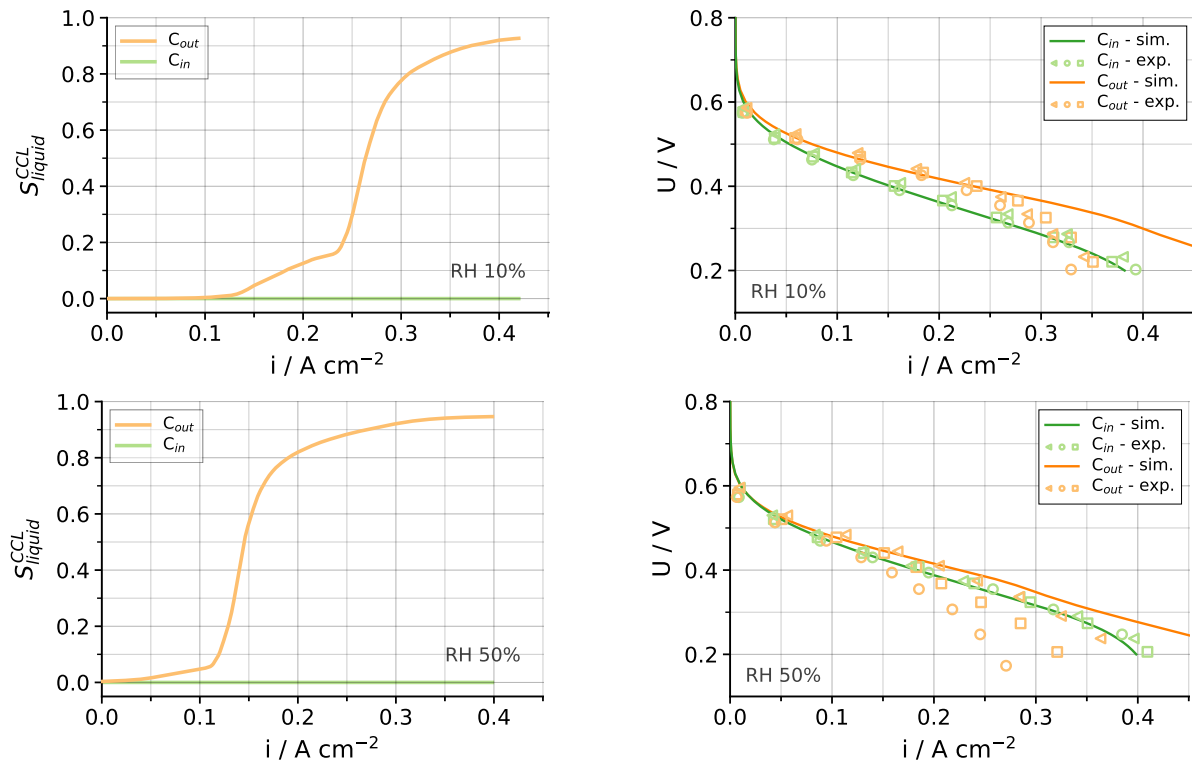


Figure 7.30: Liquid saturation in the cathode inlet and cathode outlet segment of the CCL (left) and resulting local cell performances (right) in the simulation in case the ionomer film model (sec. 6.3.10) is deactivated.

The catalyst structure is complex and heterogeneous, as it consists of a porous carbon structure with fine dispersed platinum particles and a dispersed hydrophilic ionomer phase, rendering narrow pore sizes and irregular conditions with a much larger spread in the local material properties compared to the other porous layer in the fuel cell, MPL and GDL. This behaviour can hardly be covered with the volume averaged modelling approach using effective material properties.

In order to reaching the catalyst's triple phase boundary, the relevant path for O_2 from the open pore space can not only involve the transport through very narrow pores (Knudsen diffusion, relevant when pore sizes are in the order of the mean diffusion length of the molecule itself, included in eq. 6.7), but also the transport to and through an ionomer thin film or through a liquid film covering the platinum particle surface. These mechanisms represent additional resistances for the transport of oxygen towards the active [Pt]-sites and its participation in the electrochemical reaction.

In order to capture these phenomena in the model, an ionomer film model was included in the description of the ORR kinetics (cf. section 6.3.10).

The ionomer film model adds three further resistance terms for oxygen transport in the catalyst layer: the diffusion resistance which the ionomer phase imposes to an O_2 -molecule before it can reach a [Pt]-surface, the resistance due to liquid water blocking the path from the open pore space to the Pt-particle surface and, moreover, the interface resistances to the transfer of oxygen from the gas to the ionomer phase and from the ionomer phase to the [Pt]-site. These terms correlate with the thickness of the ionomer film in the catalyst, the liquid saturation and the local water activity in the gas phase, respectively.

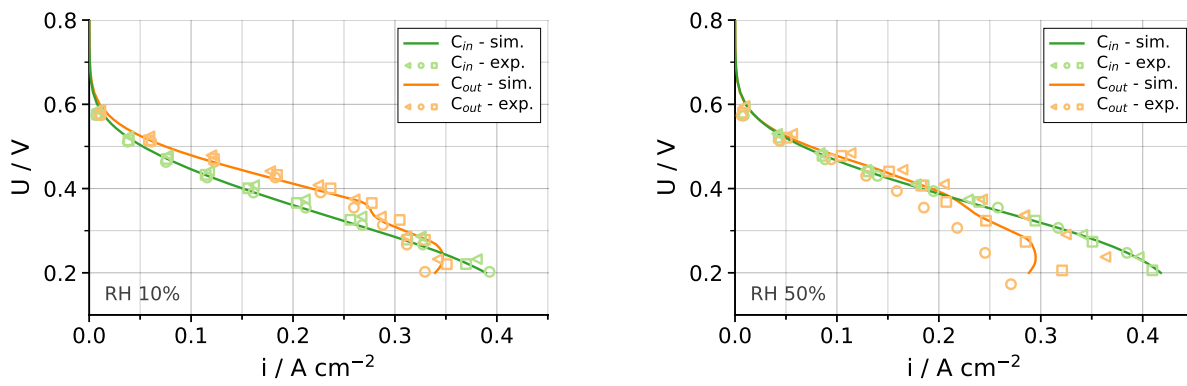


Figure 7.31: Simulation result for the local cell performance of the DMFC's cathode inlet (green) and cathode outlet (orange) segment obtained with the reference model (including the ionomer film model in the ORR kinetics) for RH 10 % and RH 50 % in comparison to the experimental data.

By including the ionomer film model, it is finally possible to portray the experimentally observed mass transport limitations in the cathode outlet area of the DMFC at high current densities with the model, as the reference simulation results for the cell performance at both humidity levels show in figure 7.31.

At voltages below 0.25 V, a minor deviation occurs when the model predicts a decrease in the local current density at cathode outlet in the potentiostatic simulation, which is not observable in the experiments. Apart from that, the model now very well describes the local performance of the cell over the entire current range for RH 10 % as well as for RH 50 %. It correctly captures the resistances to ion transport at low to medium current, which come into effect at the dry cathode inlet area of the cell, but also the resistances to mass transport in the cathode outlet segment at high current densities.

7.2.2 Reference Model

With the verification of local resistances in the CCL, the validation of the performance model was accomplished. The physical 2D model accurately describes the overall cell performance (cf. figure 7.32) as well as the heterogeneous local cell performance along the channel (figure 7.33). Simulations performed with the validated 2D DMFC model are referred to as “reference simulation” in this work.

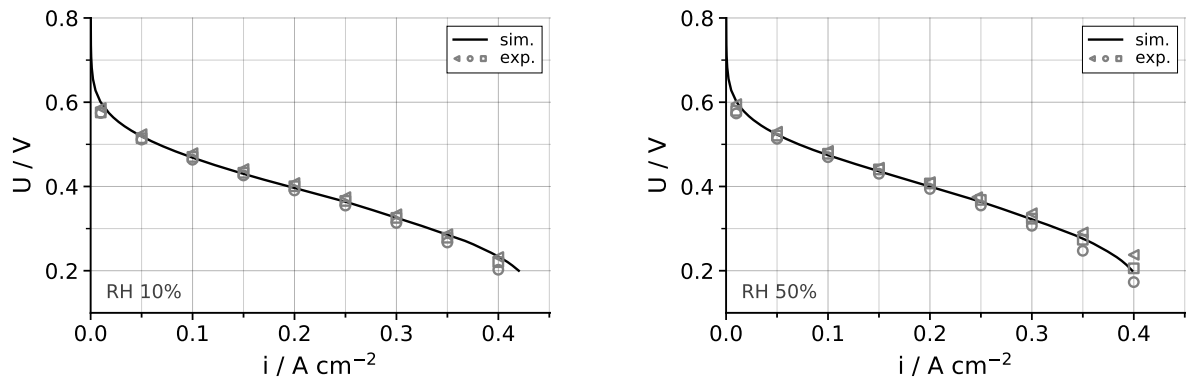


Figure 7.32: Simulation with the reference model: Cell performance during operation with RH 10 % (left) and RH 50 % (right) in comparison to the experimental data.

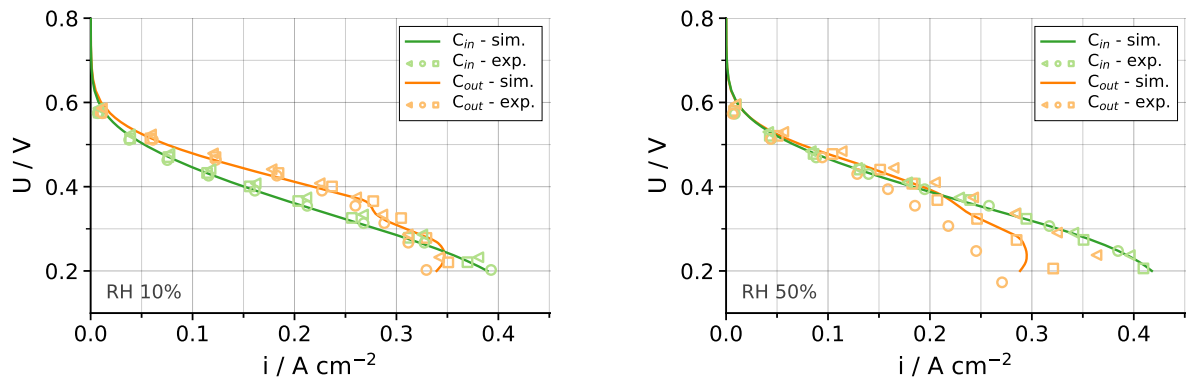


Figure 7.33: Simulation with the reference model: Local cell performance in the DMFC’s cathode inlet (green) and cathode outlet (orange) for RH 10 % (left) and RH 50 % (right) in comparison to the experimental data.

The corresponding conditions inside the DMFC membrane have been discussed in section 7.1. Figure 7.34 shows the water fluxes at cathode outlet for RH 10 % and RH 50 % obtained in the reference simulation in comparison with the experimental data.

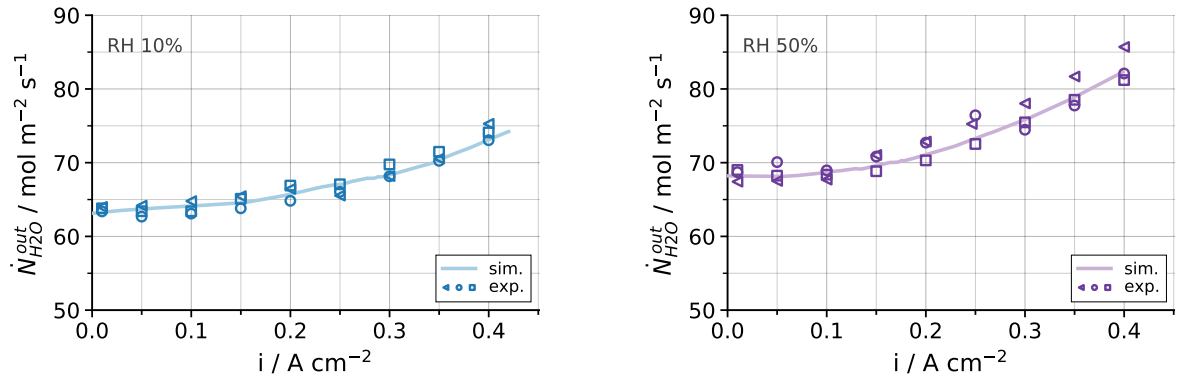


Figure 7.34: Simulation with the reference model: Water flux rate at cathode outlet during operation with RH 10 % (left) and RH 50 % (right) in comparison to the experimental data.

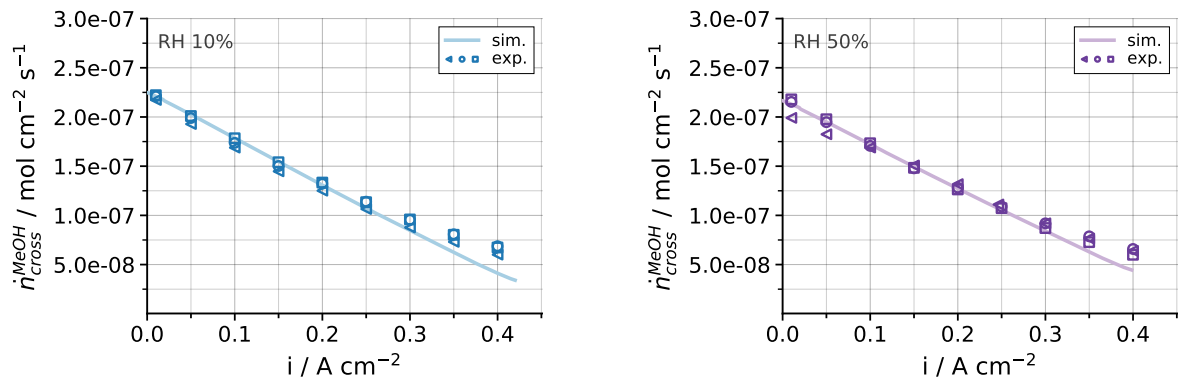


Figure 7.35: Simulation with the reference model: Methanol crossover rates \dot{n}_{cross}^{MeOH} for RH 10 % (left) and RH 50 % (right) in comparison to the experimental data.

7.2.3 Performance simulation with varying stoichiometry

The validated 2D DMFC model was further used to simulate the cell performance under different stoichiometry conditions. For these simulations, only the simulation boundary conditions at anode and cathode inlet were altered, but no changes were made in the model description or its parameters. The simulation results thus show the model prediction of the cell behaviour and can be directly compared to experimental data, which were not part of the data set used for fitting and model validation.

Performance data of segmented cell measurements and the corresponding methanol and water crossover fluxes were available for the stoichiometry combinations $\lambda_A = \lambda_C = 3$ at RH 10% and $\lambda_A = \lambda_C = 6$ at RH 10% and RH 50%. As with the standard case with $\lambda_A = 6$ and $\lambda_C = 3$, the cells were not λ -controlled in the experiments, but operated with a constant flow rate equivalent to the respective stoichiometry at a current of $0.25 \frac{A}{cm^2}$.

Figure 7.36 shows the predicted mass flow of water and methanol through the cell for the case with $\lambda_A = 3 = \lambda_C$, which match very well with the experimental data.

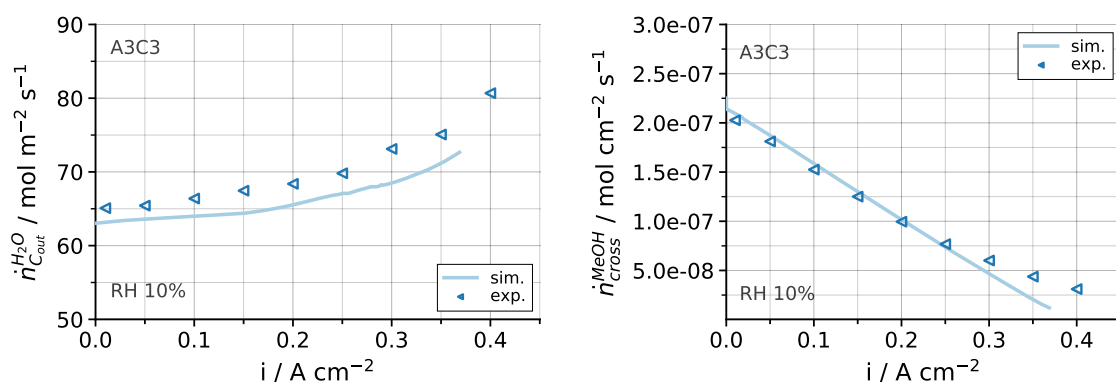


Figure 7.36: Simulation with the reference model: Water flux at cathode outlet (left) and methanol crossover rate (right) for $\lambda_A = \lambda_C = 3$ at RH 10%.

In figure 7.37, the corresponding overall and local cell performance for $\lambda_A = \lambda_C = 3$ at RH 10% predicted in the simulation vs. the experimental data is shown.

The simulation captures the effect of the reduced anode stoichiometry quite well, with mass transport limitations coming into effect in the anode outlet (cathode inlet) segment at higher current densities (opposite to what is observed in the reference case with $\lambda_A = 6$ and $\lambda_C = 3$, where the mass transport limitations occur at the cathode outlet / anode inlet area).

Also in case of $\lambda_A = \lambda_C = 6$, the simulated cell performance is in good agreement with the experimental data on the total as well as on the local scale, as figure 7.38 for RH 10% and figure 7.39 for RH 50% show.

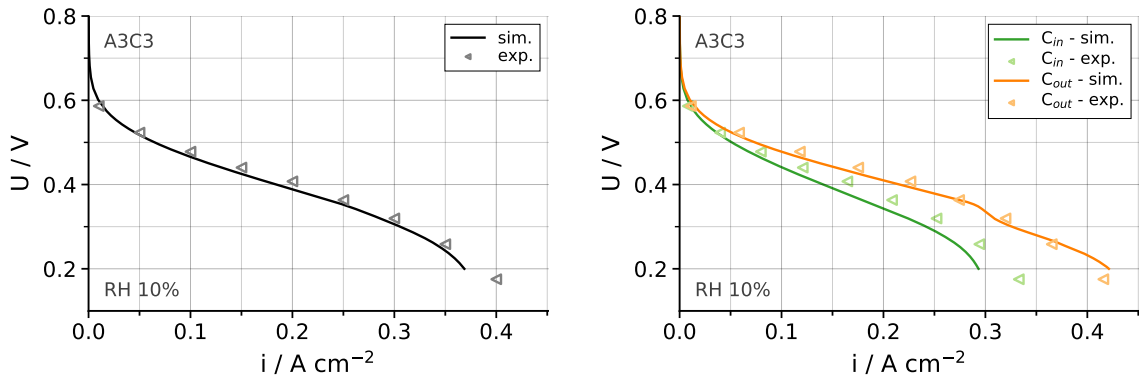


Figure 7.37: Simulation with the reference model: Overall cell performance (left) and local cell performance (right) for a stoichiometry of $\lambda_A = \lambda_C = 3$ at RH 10%.

The higher cathode stoichiometry leads to an increased flow rate in the cathode MEA and prevents the accumulation of water and consequently no flooding effects are visible in the cell performance at higher current densities. This result is valid for both humidity levels.

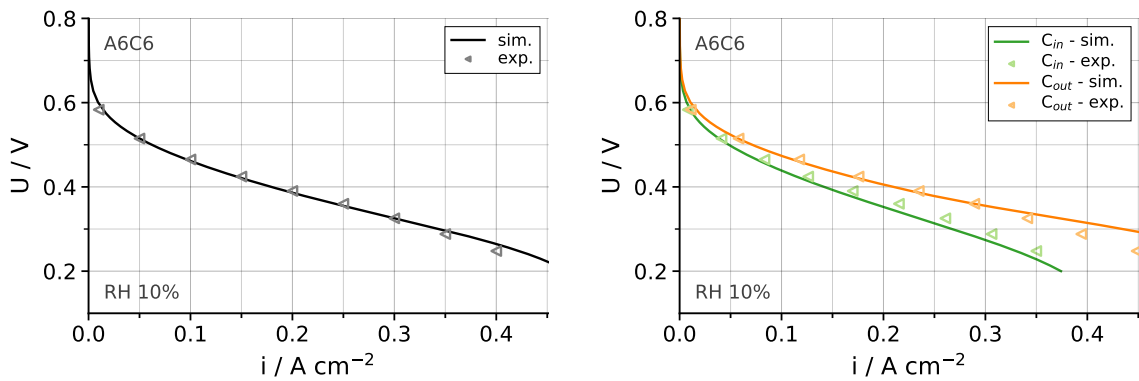


Figure 7.38: Simulation with the reference model: Overall cell performance (left) and local cell performance (right) for a stoichiometry of $\lambda_A = \lambda_C = 6$ at RH 10%.

Also the simulated water fluxes for the case $\lambda_A = \lambda_C = 6$ show a reasonable agreement with the experimental data for RH 10% and RH 50%, as shown in figures 7.40 and 7.41. Meanwhile, the methanol crossover rates get somewhat overestimated with the model.

The reason for this deviation between model prediction and experiment is not straight forward: on the one hand, the model accurately predicts the methanol crossover in the reference case with $\lambda_A = 6$ and $\lambda_C = 3$ as well as the case of operation with $\lambda_A = \lambda_C = 3$ for RH 10%, which shows that differences resulting from the changes in the anode stoichiometry and thus methanol availability at the PEM/ACL interface are satisfactorily covered by the model.

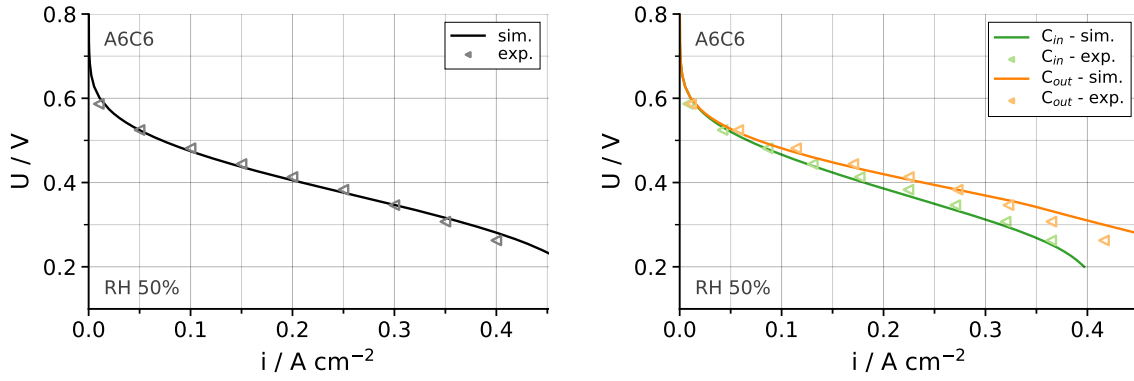


Figure 7.39: Simulation with the reference model: Overall cell performance (left) and local cell performance (right) for a stoichiometry of $\lambda_A = \lambda_C = 6$ at RH 50%.

The experimentally observed lower crossover rate for methanol in case of $\lambda_A = \lambda_C = 6$ (with an anode stoichiometry equivalent to the reference operating conditions) could then only result from the increased cathode flow rate. This conflicts, however, with the assumption that the crossover methanol fully reacts in the CCL under regular fuel cell operation.

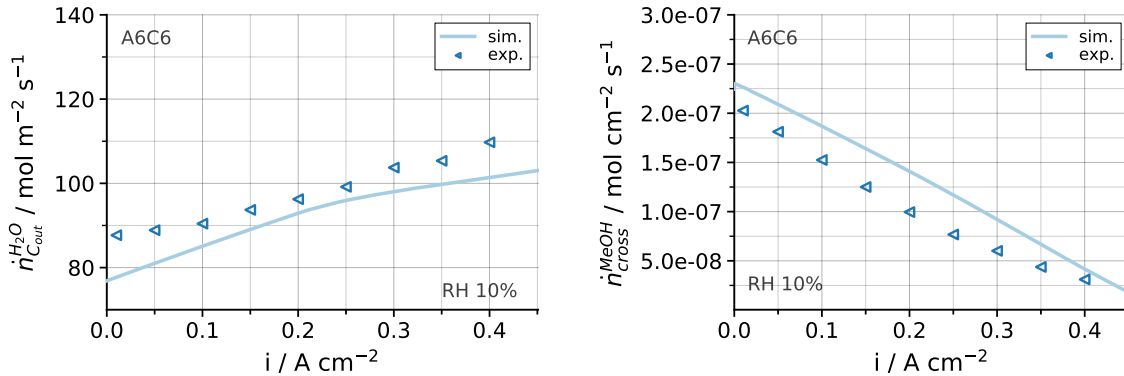


Figure 7.40: Simulation with the reference model: Water flux at cathode outlet (left) and methanol crossover rate (right) for $\lambda_A = \lambda_C = 6$ at RH 10%.

In order to better understand the deviation, the experimental data for the different stoichiometry cases were compared to each other (cf. figure 7.42). In direct comparison, it becomes obvious that the experimental methanol crossover rate is identically low in case of $\lambda_A = \lambda_C = 3$ and $\lambda_A = \lambda_C = 6$, while the reference case with $\lambda_A = 6$ and $\lambda_C = 3$ shows a higher methanol crossover. This invalidates the hypothesis that an increase in the cathode flow rate is responsible for the decrease of the methanol crossover.

The reason for the offset in the methanol crossover rate for the stoichiometry case $\lambda_A = \lambda_C = 6$ remains unknown and no physical explanation can be found for the observed experimental cell behaviour. As the experimental behaviour could not be further verified or investigated, the interpretation of the conflicting results remains an open point.

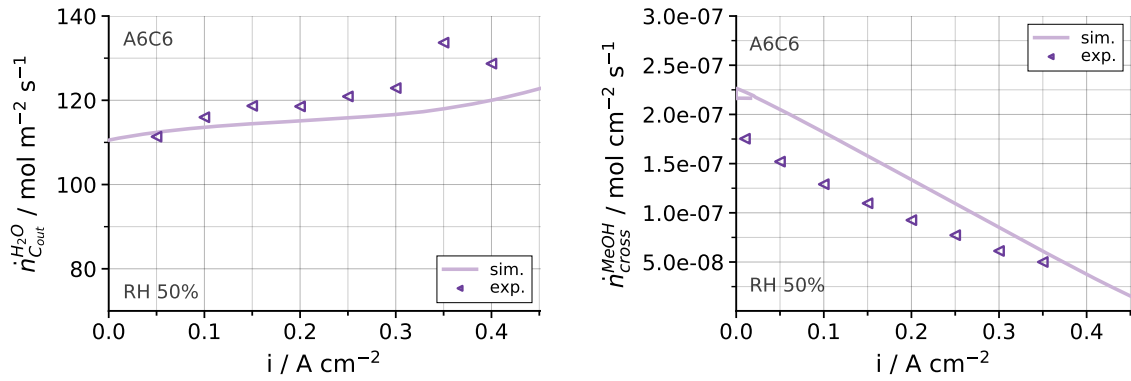


Figure 7.41: Simulation with the reference model: Water flux at cathode outlet (left) and methanol crossover rate (right) for $\lambda_A = \lambda_C = 6$ at RH 50%.

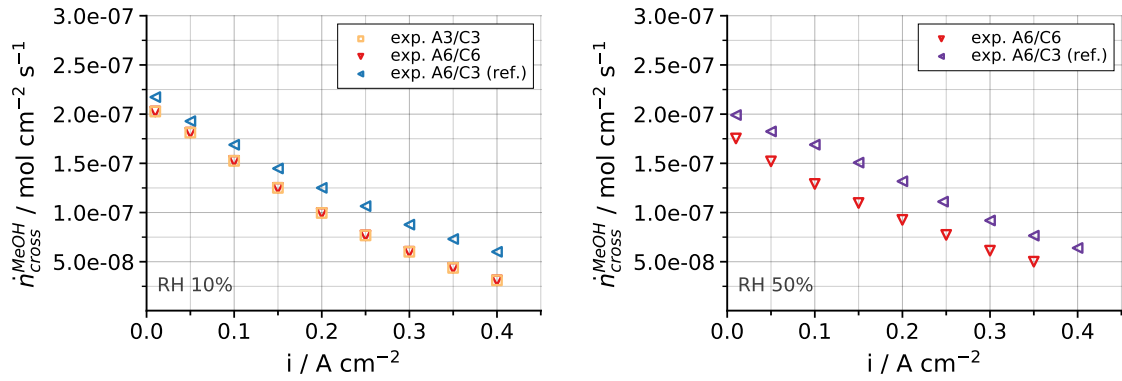


Figure 7.42: Comparison of the experimental methanol crossover rates for the different stoichiometry combinations for RH 10% (left) and RH 50% (right).

The good agreement of the simulation results obtained for this stoichiometry variation (without any modification in the model description) with the available experimental data on the overall cell performance as well as the local cell performance and the mass transport of methanol and water through the membrane underlines the model's capability to portray the relevant processes within the DMFC.

7.2.4 Impact of operating mode on the local cell performance

The reference simulations were performed in the potentiostatic mode, since the experimental data [111] used for model validation were obtained by potentiostatic cell operation. With the model, the impact of the operating mode on the local cell performance could be tested. The performance simulations for RH 10 % and RH 50 % were repeated with galvanostatic operation (cf. section 5.6) and compared to the results obtained with the simulation results with potentiostatic operation.

Figure 7.43 shows the total and local cell voltages over current during potentiostatic and galvanostatic operation in direct comparison for the cases RH 10 % and RH 50 %.

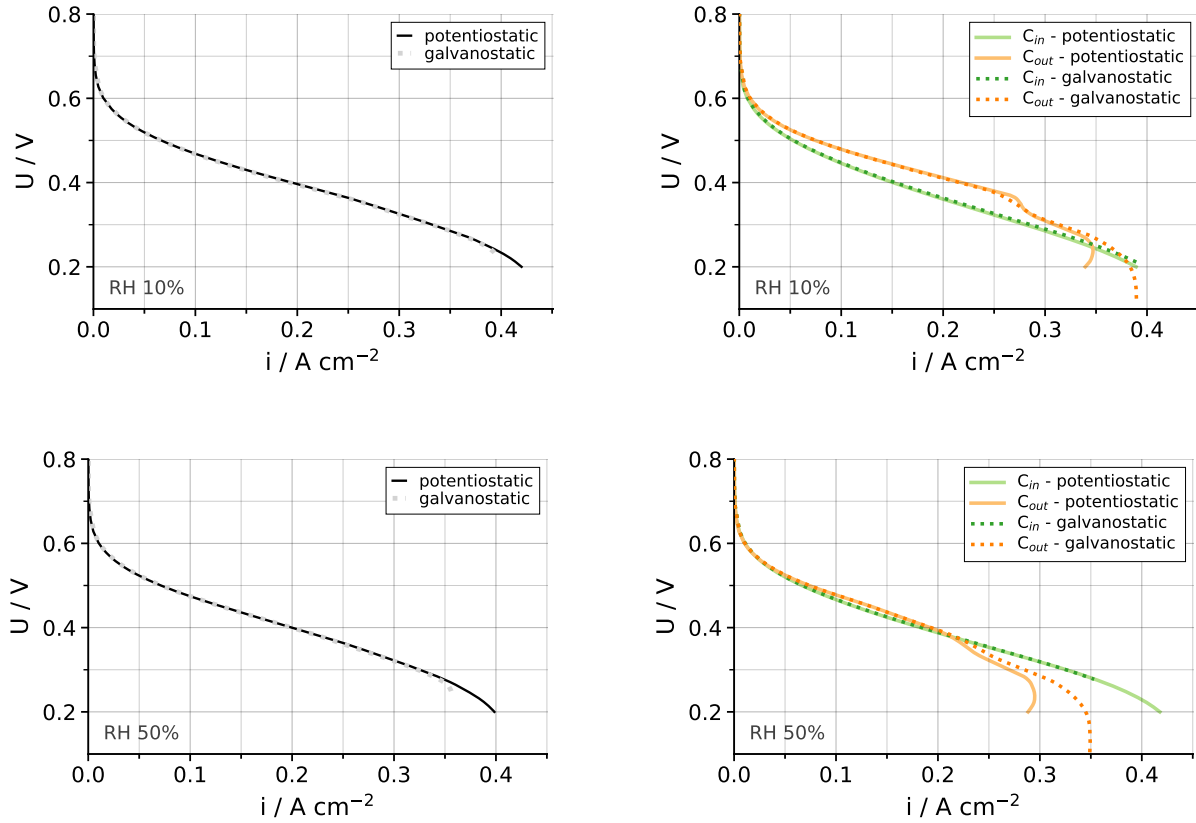


Figure 7.43: Simulation with the reference model: Impact of the operating mode (galvanostatic/potentiostatic) on the cell performance. Left: Total cell voltage. Right: Local cell voltages.

In the overall cell voltage (grey/black), no deviation is visible between the two operating modes, neither for dry (RH 10 %) nor for humid (RH 50 %) cell operation. The local voltages at cathode inlet (S4, green) and cathode outlet (S1, orange), however, show differences between the two operating modes show at high current densities ($i > 0.35$ A/cm² for RH 10 % and $i > 0.25$ A/cm² for RH 50 %).

In case of galvanostatic operation, the voltage drop at cathode outlet sets on later than in case of the potentiostatic mode, for RH 10 % as well as for RH 50 %, despite almost identical liquid saturation profiles (fig. 7.44).

When looking at the local cell voltages in all four segments (figure 7.45), it becomes clear that it is the potential distribution along the channel which varies significantly at high current densities, depending on whether the cell potential or the cell current is the leading operating parameter. The potentiostatic operating mode allows a stronger performance divergence along the channel.

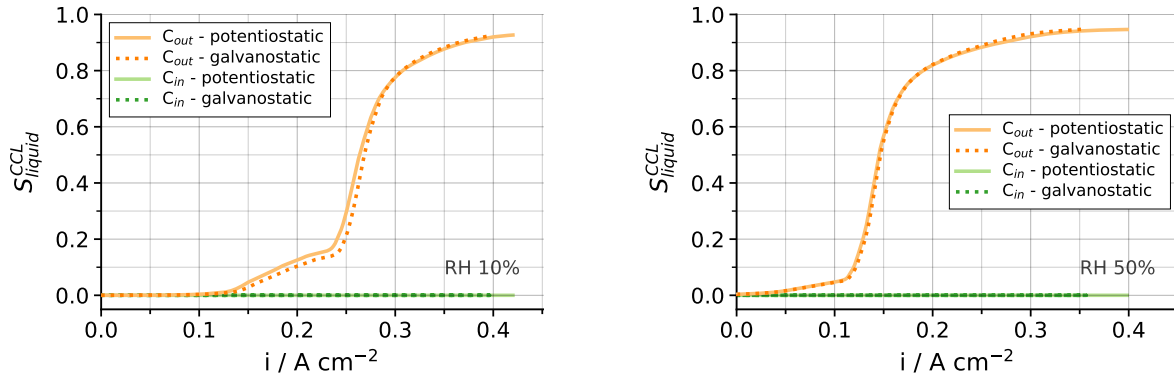


Figure 7.44: Simulation with the reference model: Impact of the operating mode (galvanostatic/potentiostatic) on the formation of liquid water in the CCL.

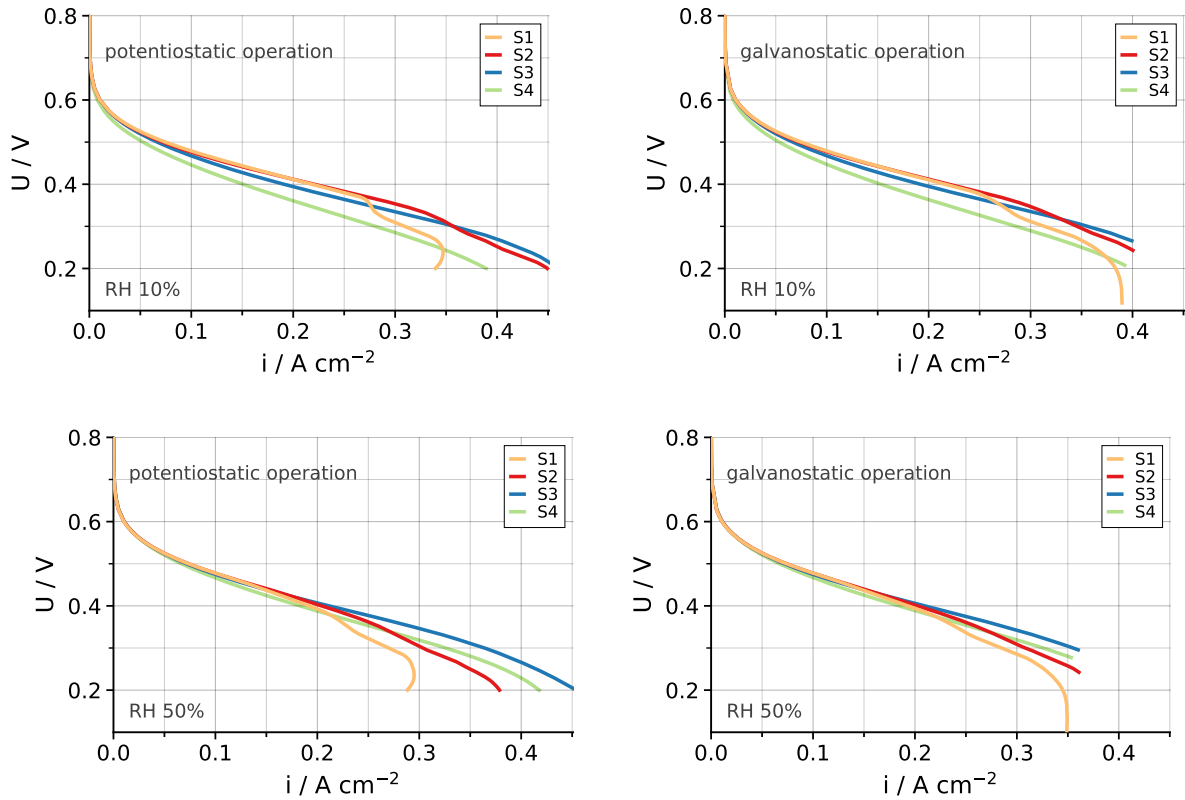


Figure 7.45: Simulation with the reference model: Impact of the operating mode (galvanostatic/potentiostatic) on the local cell performances.

7.2.5 Impact of BPP segmentation on the local cell performance

Also the effect of the bipolar plate's segmentation on the local cell performance could be tested with the model. In order to simulate the cell behaviour with a continuous, i.e. non-segmented BPP, the segmentation boundary condition in the DMFC model was disabled.

In figure 7.46, the simulated local cell performance in case of a galvanostatic and potentiostatic operation with and without segmentation is shown in direct comparison for RH 10 % and RH 50 %, respectively. In case of the potentiostatic simulation, the segmentation of the cell's bipolar plate has no impact on the local cell performance. For the galvanostatic operation, a minor deviation is visible in the flooded cathode outlet area, with the continuous cell performing slightly better than the segmented cell. The impact of the segmentation on the simulation results regarding performance heterogeneities is, however, negligible.

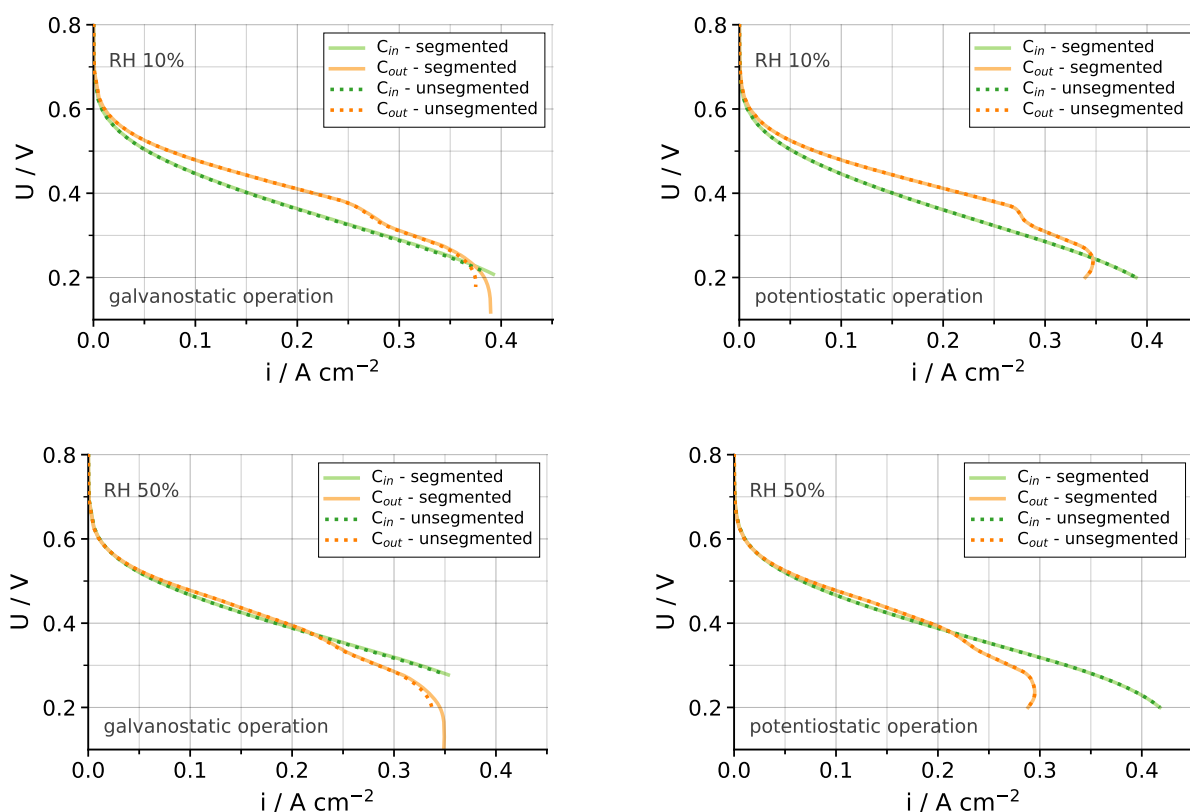


Figure 7.46: Simulation with the reference model: Impact of the BPP segmentation on the local cell performance.

Given the model is able to describe the local processes inside the DMFC with a sufficient accuracy, it can be concluded that observations made with a segmented cell set-up are directly transferable to a cell without segmentation.

7.2.6 Conclusion: Heterogeneities in the Local DMFC Performance

The 2D DMFC model has been thoroughly validated against experimental data, overall and on the local scale, and was used to study different humidity-related effects which lead to a heterogeneous performance across the cell. The conditions inside the DMFC run in counter-flow mode vary substantially along the channel, with the cathode inlet/anode outlet area being comparably dry, while the cathode outlet/anode inlet area of the cell is well-humidified and prone to liquid water formation. The DMFC shows a diverging local cell performance along the channel over the entire operating range.

The mass and proton transport inside the DMFC is highly complex due to phase changes and the resulting two-phase flow regime within the cell as well as the strong coupling between the different domains. This modelling study has highlighted the strong dependence of material properties and species transport on the local humidity and phase conditions within the DMFC and the importance of interface processes at the membrane interfaces as well as inside the composite structure of the catalyst layers.

Interface resistances are an important factor contributing to the local performance heterogeneities observed in the DMFC, which - in comparison to PEMFC - appears to have a good humidification level overall. As previously discussed, the two-phase flow conditions at the PEM/CL interfaces, namely the water activity and the presence or absence of a liquid phase, strongly influence the properties and processes within the cell.

The poor performance of the DMFC cathode inlet area in case the cell is run with RH 10 % originates from the comparably dry conditions in the CCL, which result in a high ohmic resistance of the membrane on the one hand, but also a significant resistance to proton transport in the CL's thin film ionomer. The physical description of the resistance terms for proton transport has been validated against the experimental data and was set in context with literature reports. A sound formulation was derived which accurately covers the cell behaviour for wet and for dry operation (RH 50 % and RH 10 %) equivalently.

The mass transport limitations in the cathode outlet area, which is visible for either operating mode at high current densities, result from liquid water blocking the transport of oxygen molecules towards the active sites of the catalyst. Even though this macroscopic model is not able to cover the local formation of liquid water inside the CL's particular micro- and nano-structure in detail, good results in describing the observed 'flooding phenomena' could be achieved by relating the liquid saturation in the CCL to an ionomer film resistance in the electrochemical reaction.

With the described effects the mechanisms leading local heterogeneities inside the DMFC could be well explained. The model proves fit to precisely portraying humidity-related effects within the DMFC and the resulting local and total cell performance for an operation with wet and dry conditions in the cathode path (RH 50 % and RH 10 %) with just one set of parameters.

Moreover, the quality of the model could be confirmed in simulations with varying stoichiometry conditions in the cell. Again, a good agreement between the prediction of the cell behaviour with the reference model (without any changes in equations or parameters) and the experimental findings was achieved, for the local cell performance as well as for the overall mass transport through the membrane.

The model could thus be seen as validated and is further used to study the conditions inside the DMFC during recovery procedures for reversible cathode degradation.

8 Recovery of Reversible DMFC Performance Losses

Under continuous operation, direct methanol fuel cells show a significant performance loss, which is linked to reversible degradation. The factors contributing to this performance decay are, on the one hand, the formation and accumulation of gaseous CO_2 in the DMFC anode, which lowers the content of the MOR reactants water and methanol in the ACL and thus leads to a diminished reaction rate. On the other hand, also cathode related phenomena like the accumulation of liquid water in the CCL as well as the formation of platinum oxides and hydroxides (PtOx-species) due to water dissociation on platinum and thus a reduction of the cathode ECSA have been identified as reversible degradation mechanisms [39]. Due to the high cathode potentials, the formation of PtOx-species in the CCL is a very relevant process in the DMFC. By applying a suitable recovery procedure (including an air break as well as an OCV phase), the reversible performance losses can be recovered [39, 104, 18, 20, 113].

Rabissi et al. [113] have described a *refresh cycle* for DMFC where a phase of continuous operation is followed by an OCV sequence and a subsequent stop of the air flow for a certain period, before resuming to normal operation again. The authors showed that the temporary performance loss in the DMFC could be almost fully recovered with this procedure. The suggested refresh cycle does not require any additional set-up or gas supply and thus could be easily integrated in the DMFC operation.

For the model verification in this work, experimental data on the described refresh procedure was available from the work of Rabissi et al. [111] in form of global U-t-profiles. A representative sequence including a refresh cycle is plotted in figure 8.1.

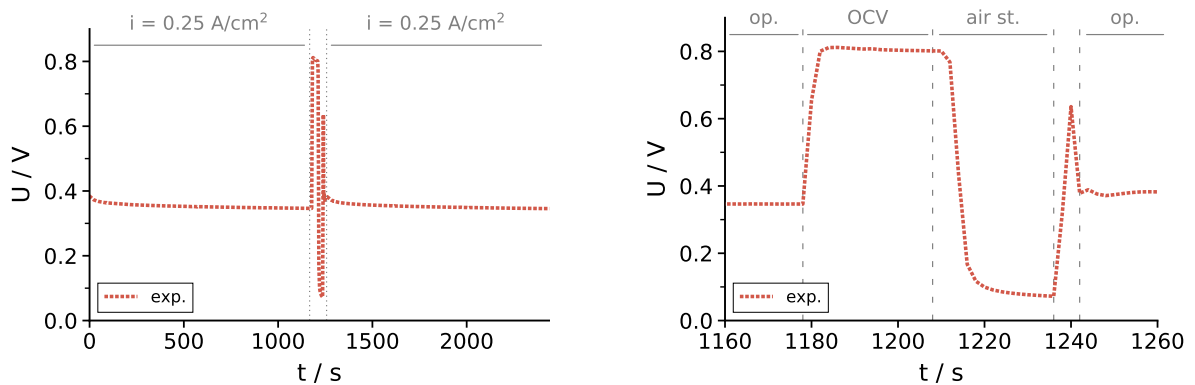


Figure 8.1: Experimental Data: Voltage profile during a sequence of continuous operation interrupted by a refresh cycle. The figure on the right shows the cell voltage during the different stages of the refresh cycle in detail.

The experimental data show a significant voltage decay of approximately 117 mV h^{-1} during continuous operation at $i = 0.25 \text{ A/cm}^2$. By carrying out a refresh cycle after every 20 min of operation, the performance loss could be fully recovered. During the air stop phase of the refresh cycle, the cell voltage drops down from OCV (ca. 0.8 V) to below 0.1 V . As soon as the air flow is resumed, the global cell voltage shoots up to $U > 0.6 \text{ V}$. When subsequently the current gets drawn again, a small voltage dip below 0.4 V can be observed, before the cell shows its regular behaviour for operation at $i = 0.25 \text{ A/cm}^2$ after a few seconds.

The validated DMFC model was used to simulate the refresh cycle in order to gain further insights into the local cell behaviour during this procedure.

8.1 Formation of Platinum Oxides in the CCL

With the transient model, the formation of platinum oxides in the cathode catalyst layer and their impact on the cell performance could be simulated. The model description for the formation of the PtOx-species can be found in section 6.3.11. Figure 8.2 shows the simulation result for the development of the cathode catalyst surface coverage with PtOH and PtO over time with the DMFC operated at $i = 0.25 \text{ A/cm}^2$ continuously.

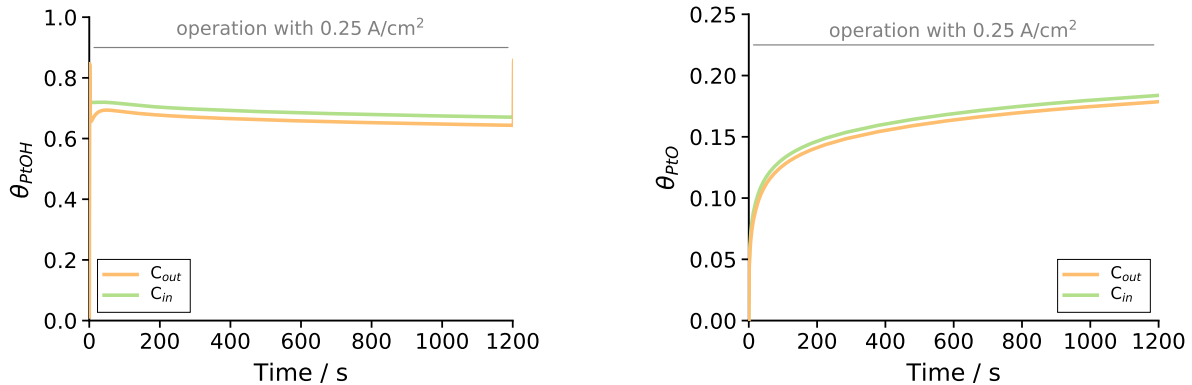


Figure 8.2: Development of the cathode catalyst surface coverage with PtOH (left) and PtO (right) at cathode inlet and cathode outlet during the period of continuous operation with $i = 0.25 \text{ A/cm}^2$.

During operation with $i = 0.25 \text{ A/cm}^2$, PtOH covers approximately 70 % of the catalyst surface right from the beginning. A mild variation between the coverage along the channel is predicted by the model, as figure 8.2 shows. θ_{PtOH} slightly reduces over time in the period under constant load. The surface coverage with PtO, on the other hand, increases with a logarithmic shape over time, as the simulation shows (fig. 8.2). After 20 minutes of operation with $i = 0.25 \text{ A/cm}^2$, a surface coverage of $\theta_{\text{PtO}} \approx 18 \%$ is reached.

Figure 8.3 shows the distribution of the two oxide species in the CCL at the end of the operation period. For both species, PtOH and PtO, the distribution is homogeneous

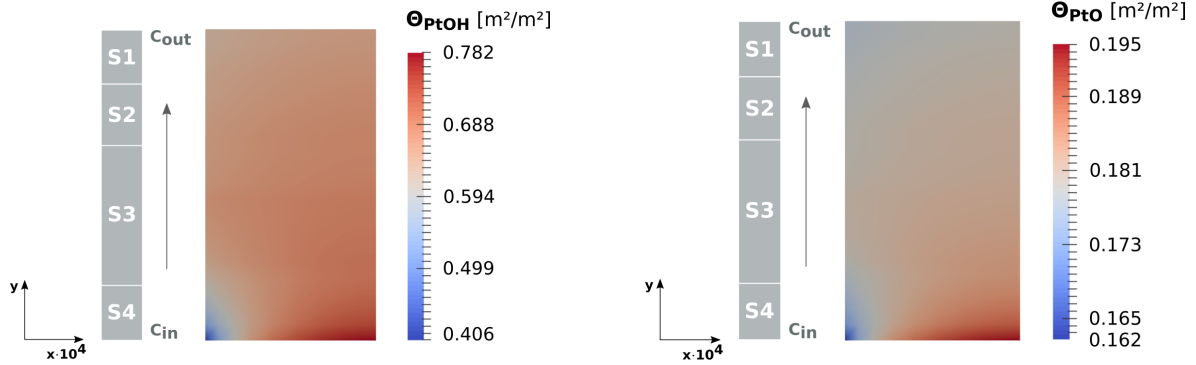


Figure 8.3: Distribution of surface coverage with PtOx-species in the CCL after 20 minutes of operation with $i = 0.25 \text{ A/cm}^2$ simulated with the transient DMFC model. The 2D plot shows the CCL magnified by 10^4 in x-direction.

for S1, S2 and S3 in x-direction and shows a mild gradient in y-direction. In the inlet segment, S4, however, strong gradients across the CCL occur in x-direction. The catalyst surface coverage is lowest at the PEM/CCL-interface and highest at the CCL/CMPL-interface with both species.

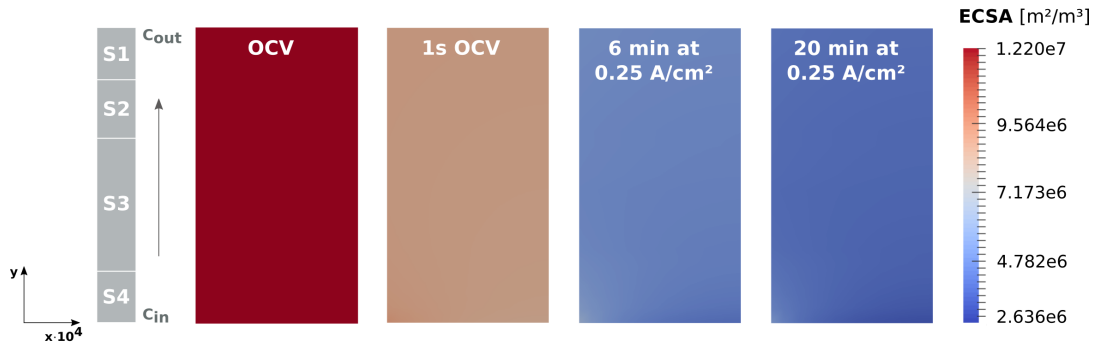


Figure 8.4: ECSA within the CCL at different stages of the continuous operation with $i = 0.25 \text{ A/cm}^2$ simulated with the transient DMFC model. The 2D plot shows the CCL magnified by 10^4 in x-direction.

The cathode ECSA gets considerably reduced by the developing PtO-coverage of the CCL during operation, which results in the discussed performance losses. The computed cathode ECSA at OCV, after 6 minutes and after 20 minutes of operation is shown in figure 8.4. As can be seen in the simulation result, the ECSA in the CCL has diminished by almost 4/5 after 20 minutes of regular operation.

8.2 Boundary Conditions for the Simulation of Refresh Cycles

In order to simulate the refresh procedure with the transient DMFC model, suitable boundary conditions and operating conditions for the refresh cycle had to be determined. In contrast to the performance simulations, which were primarily carried out in the potentiostatic mode, the refresh simulations had to be performed galvanostatically.

The period of continuous cell operation at 0.25 A/cm^2 as well as the OCV phase could be simulated by using the regular boundary conditions for galvanostatic operation. The cathode flow boundary conditions for the different stages of the refresh cycle, however, had to be chosen with care.

During the air stop phase, the cathode gas supply is stopped while the anode flow remains as usual, and no current is drawn from the cell. Experimentally, this can be easily achieved by closing the valves of the cathode air supply. As the valve is located outside the cell, residual air from the gas tubes can still diffuse towards the CCL and is available for reactions, despite there is no convective flow in the channel any more.

Reflecting these conditions in the model was challenging for several reasons: Firstly, the level of residual air in the tube and the dynamics of oxygen diffusion into the cell were unknown. As the gas tubes were not part of the modelling domain, both flow and concentration conditions at cathode inlet had to be assumed for the simulation. Secondly, it was not possible to set the convective gas flow in the cathode channel to zero in the model, as a simultaneous no-flow boundary condition at cathode inlet together with the outflow boundary condition at cathode outlet led to numerical problems.

Table 8.1: Operating scheme for standard refresh simulation.

Phase	Duration	Current	Air flow	x_{O_2}
Initialise simulation	2 s	$0.0 \rightarrow 0.25 \text{ A cm}^{-2}$	N_0	x_0
Regular operation	1200 s	0.25 A cm^{-2}	N_0	x_0
OCV	30 s	0.0 A cm^{-2}	N_0	x_0
Air stop (phase 1)	10 s	0.0 A cm^{-2}	$N_0 \rightarrow 0.03 \cdot N_0$	$x_0 \rightarrow 0.238 \cdot x_0$
Air stop (phase 2)	10 s	0.0 A cm^{-2}	$0.03 \cdot N_0$	$0.238 \cdot x_0$
Resume N and x	1 s	0.0 A cm^{-2}	$0.03 \cdot N_0 \rightarrow N_0$	$0.238 \cdot x_0 \rightarrow x_0$
Resume current	1 s	$0.0 \rightarrow 0.25 \text{ A cm}^{-2}$	N_0	x_0

In order to overcome this problem, the cathode inflow in the simulation was reduced to a minimum value > 0 (here: 3 % of its regular flow rate). With this very small flow velocity in the channel, the numerical stability of the air stop simulation could be ensured and the flux condition in the real cell approximated. Additionally, the oxygen concentration in the gas flow was gradually reduced, accounting for the limited amount of residual air in the gas tube.

In the simulation, the air stop period was divided into two phases: at first, flow and oxygen concentration were simultaneously reduced to their minimum values, and then kept constant at this low level for the rest of the air stop period. Note that the air stop duration in the standard simulation is 20 s, while it lasts 30 s in the experiments.

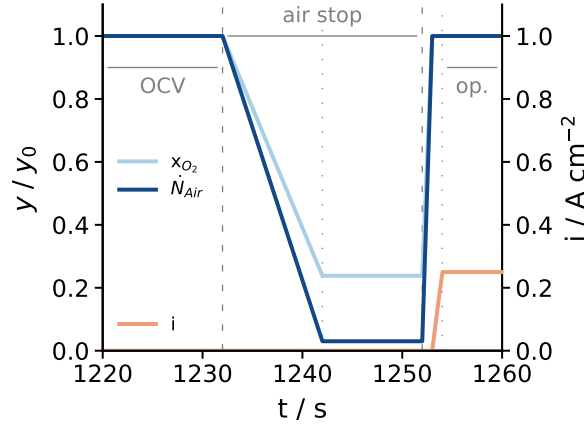


Figure 8.5: Cathode boundary conditions for the oxygen concentration x_{O_2} , the air flow \dot{N}_{Air} and the current density i in the standard refresh simulation (cf. tab. 8.1).

After the air stop, cathode gas flow and current are resumed in order to run the cell under its normal operating conditions at $i = 0.25 \text{ A/cm}^2$ again. For the modelling, this meant that flow, concentration and current density had to be ramped up to their nominal values at the respective cathode boundaries. This was achieved within two stages: firstly, the cathode inflow rate and simultaneously the oxygen concentration at cathode inlet were ramped to their target values within 1 s. Secondly, the current was brought back to $i = 0.25 \text{ A/cm}^2$ within 1 s. After 2 s in total, the regular operating conditions for the cell in galvanostatic mode were re-established.

The described simulation boundary conditions for the different phases of the refresh cycle are visualised in figure 8.5.

8.3 Refresh Simulation with the 2D Model

The standard refresh simulation was carried out with the validated cell model and the boundary conditions of table 8.1. Note that in all refresh simulations presented here, the ionomer film model in the 2D model's ORR kinetics (cf. section 6.3.10) is deactivated in order to overcome numerical issues in the simulation. This modification is discussed later in section 8.4.

Figure 8.6 shows the cell voltage profile during a sequence of operation at nominal current density including a refresh cycle obtained in the experiments (dashed lines) and the

reference refresh simulation with the 2D model (solid lines).

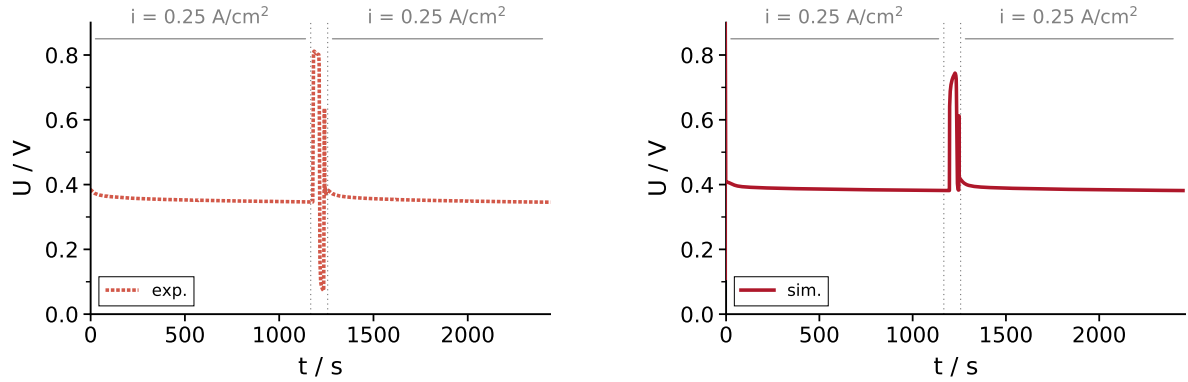


Figure 8.6: Experimental data (dashed lines) and simulation result (solid lines): Cell voltage profile in the course of a full sequence of continuous operation and refresh .

The comparison of the two profiles shows that the voltage decay during operation with the nominal current density is satisfactorily described with the DMFC model: in the simulation, a voltage drop of approximately 34 mV is predicted within 20 minutes, matching with the experimentally observed voltage drop of $\approx 39 \text{ mV}$ within this period.

A substantial rise in the cell voltage can be observed during the OCV phase subsequent to the cell operation at nominal current density (figure 8.7). The OCV phase is the first part of the refresh sequence. Experimentally, an OCV value of $> 0.8 \text{ V}$ is observed, however, the voltage in the simulation only rises to $\approx 0.75 \text{ V}$. The simulated OCV during the refresh sequence does not reach steady-state within the 30 s OCV-phase. Moreover, it is far lower than the OCV of $\approx 0.89 \text{ V}$ which is obtained with the model during the regular performance simulation (sec. 7).

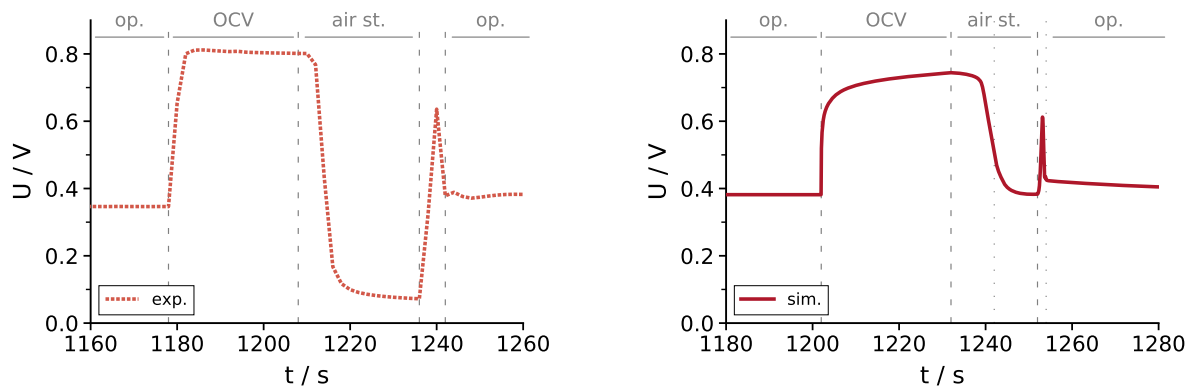


Figure 8.7: Experimental data (dashed lines, left) and simulation result (solid lines, right): Detailed cell voltage profile during the refresh cycle.

The deviation of the modelled cell behaviour during the OCV phase shall be briefly discussed here: When switching from operation at 0.25 A/cm^2 to OCV, the gas/liquid balance within the CCL changes significantly. The production of water in the CCL due to the electrochemical reaction is reduced to a minimum while the flow rate through the cathode remains equally high as under load. As a consequence, liquid water which has accumulated in the CCL, gets drained away (cf. fig. 8.8).

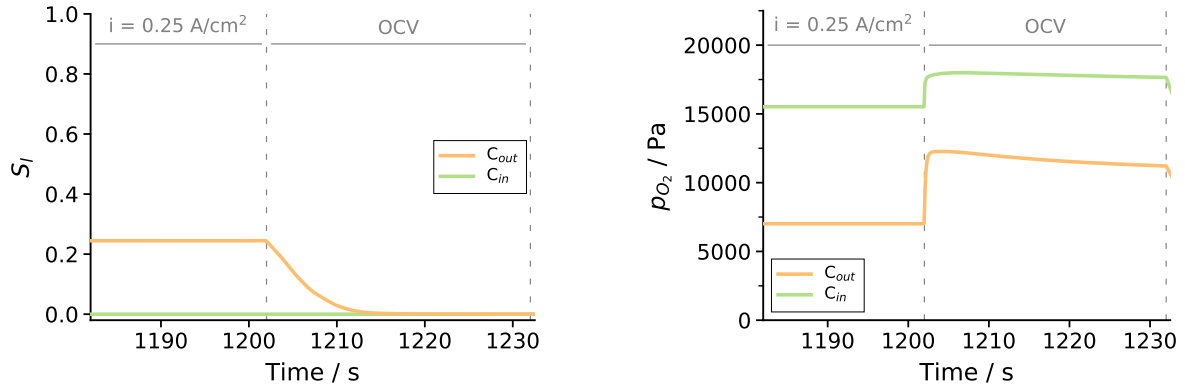


Figure 8.8: Refresh Simulation: Liquid saturation (left) and oxygen partial pressure (right) in the CCL during the transition from operation at 0.25 A/cm^2 to OCV.

In addition to the change in the liquid distribution, the availability of the reaction species within the MEA increases during the OCV phase, due to the much lower reaction rates in the anode and cathode catalyst layer. The oxygen partial pressure in the CCL shoots up instantly when the simulation switches from operation at 0.25 A/cm^2 to OCV, as figure 8.8 shows. The methanol concentration in the anode catalyst layer, however, rises much slower and steadily over the entire duration of the OCV phase in the simulation, as shown in figure 8.9. The MOR reaction rate in the anode catalyst layer directly scales with the methanol concentration according to eq. 6.95, and contributes to the resulting cell voltage.

The slow increase in the methanol concentration in the ACL is most likely the cause for the OCV continuously rising and not reaching a steady state within 30 s in the simulation, unlike the experimental cell voltage (cf. figure 8.7). This finding is another indication that the description of the methanol transport within the anode porous layers is somewhat too slow in the 2D model, a hypothesis that had already been issued in chapter 7.1.5 in the discussion and validation of the methanol crossover rate through the membrane.

The OCV phase in the refresh cycle is followed by the air stop phase. Experimentally, a sharp drop in the cell voltage can be observed during this sequence, and also the simulation qualitatively predicts this behaviour (cf. figure 8.10). The delay in the cell voltage drop in the simulation at the beginning of the air stop phase is caused by the chosen

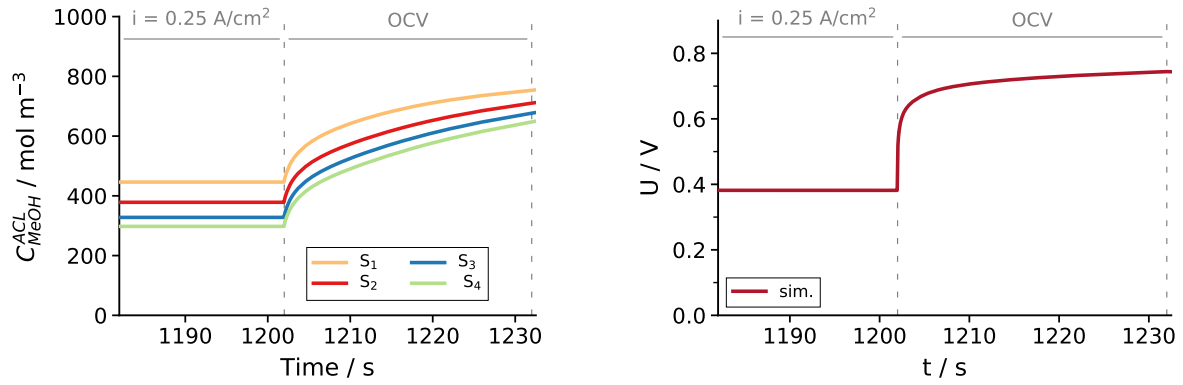


Figure 8.9: Refresh Simulation: Local methanol concentration in the ACL during the transition from operation at 0.25 A/cm^2 to OCV with 0.0 A/cm^2 (left) and development of the cell voltage (right).

simulation boundary conditions with the two steps in reduction of flow and oxygen concentration (cf. section 8.2 and figure 8.5). The experimental cell voltage approximates a minimum value $< 0.1 \text{ V}$ during this phase with oxygen-depleted conditions in the CCL, while the minimum cell voltage achieved with the model in the reference simulation is only in the range of $< 0.4 \text{ V}$.

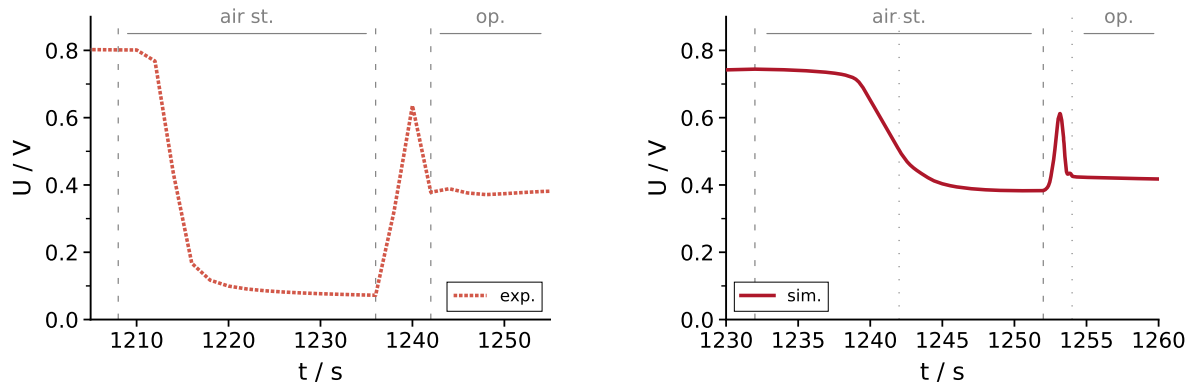


Figure 8.10: Refresh Simulation: Development of the cell voltage in simulation and experiment during the air stop phase.

Two influence factors for the quantitative deviation of the simulated minimum cell voltage during the air stop phase compared to the experiments shall be discussed here in short (note that a detailed analysis and evaluation of the conditions in the DMFC during the different stages of the refresh cycle will be provided in the following sections): The cell voltage drop during the air stop phase is caused by a drop in the cathode potential due to the depletion of oxygen at the cathode catalyst and a consequent shift in the electrochemical reactions. As will be later discussed in sections 8.5 and 8.6, the available amount of oxygen in the CCL during the air stop phase strongly determines the decline of the local cathode potential. The boundary conditions of the reference refresh simulation include a small percentage of oxygen at the cell's cathode channel inlet boundary (cf. fig.

8.5 and tab. 8.1). With these boundary conditions, an full oxygen depletion in the CCL is *not* achieved in the reference simulation (compare section 8.5). In the experiments, the oxygen concentration in the CCL is presumably lower. Another important influence for the decline of the local cathode potential during the air stop phase, as will be later discussed (cf. sections 8.5.3 and 8.5.7), is the mechanism of the secondary methanol oxidation reaction in the CCL under oxygen depleted conditions (eq. 6.69). The 2D model's parametrisation of the H₂O-activated MOR in CCL kinetics might be too slow compared to the actual reaction rates, leading to the observed mismatch between the simulated and experimentally observed minimum cell voltage during the air stop phase. This hypothesis will be elaborated in section 8.5.7.

The resumption of flow and current density after the air stop phase leads to a voltage overshoot in both, simulation and experiment (figure 8.10). When resuming to operation at $i = 0.25 \text{ A/cm}^2$, experimentally a small dip is visible in the cell voltage, before the voltage reaches its steady state value. This behaviour is not predicted in the reference refresh simulation with the boundary conditions of table 8.1, but will be later explained and depicted with the model during variations of air stop scenarios in sections 8.6.1 and 8.6.3.

Despite the discussed quantitative deviations, the standard refresh simulation qualitatively captures the individual stages of the refresh cycle in good accordance with the experiments.

8.4 Model Convergence during Refresh Simulation

The heterogeneous and dynamically changing conditions within the cathode catalyst layer during the refresh cycle were a challenge for the model's numerical stability. In order to ensure model convergence and enable the simulation of the entire refresh sequence, the simulation boundary conditions during the air stop were chosen a little milder compared to the experiments, as described previously in section 8.2.

The numerically most difficult point of the refresh cycle is the resumption of flow and current after the air stop period ($t = 1252 - 1254 \text{ s}$). During this transition, massive changes in the local species distribution and reactions in the CCL occur in a very short amount of time. Despite the moderate boundary conditions and a careful choice of the time-step size, simulations with the reference model initially failed at this point (cf. fig. 8.11).

It was found that the ionomer film model with its resistances in the ORR significantly contributed to the numerical problems at the transition from refresh procedure to normal operation. As a consequence, the model parameters R_{int} and R_{liq} in the ionomer film model (eqs. 6.103 and 6.109) were deactivated in the refresh simulations.

This measure improved the model convergence by all means and ensured that the entire refresh sequence could be simulated. The impact of the deactivated ionomer film model

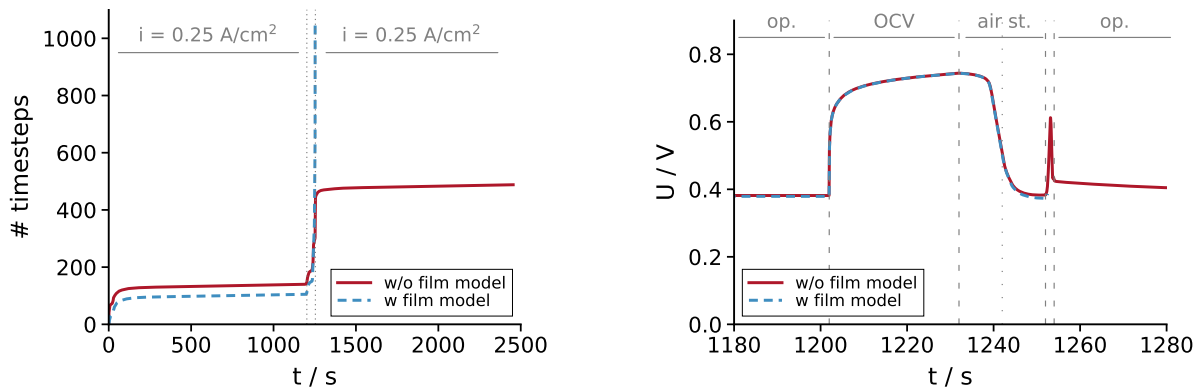


Figure 8.11: Model convergence (left) and corresponding cell voltage profile (right) during the refresh simulation *with* and *without* the ionomer film resistances included in the DMFC model (dashed blue line vs. red line).

on the simulation result is negligible, as the comparison of the cell voltage profile in the simulation with and without film resistances in figure 8.11 shows. All refresh simulation results discussed in this work were thus obtained with ionomer film resistances deactivated in the model, i.e. $R_{int} = 0$ and $R_{liq} = 0$. Apart from this, no alterations were made to the validated cell model.

8.5 Local Conditions inside the DMFC during the Refresh Cycle

The model is used to study the transient processes and local conditions inside the DMFC during the refresh cycle, which are not easily accessible in experiments. In the following, the distribution of reactants and PtOx-species in the CCL as well as individual reactions and local potentials in anode and cathode during the refresh procedure are presented and discussed.

All results were obtained with the standard refresh simulation as described in sections 8.2 to 8.4. After the analysis of the local conditions inside the DMFC, the role of the different methanol reaction paths in the CCL during the refresh cycle will be discussed, as well as the impact of the model's bipolar-plate segmentation on the simulation result.

8.5.1 Oxygen Partial Pressure

The local partial pressure of O_2 in the CCL during the refresh procedure is shown as a profile over time in figure 8.12.

Compared to the phase of operation with constant load, the oxygen partial pressure in the CCL jumps up during the OCV phase at cathode inlet as well as at cathode outlet, where the value almost doubles. When the air stop is initiated, p_{O_2} sinks down first at cathode outlet and later at cathode inlet. The logarithmic depiction reveals that at cathode outlet, values of $p_{O_2} < 1 \times 10^{-2} \text{ Pa}$ are reached during this period, while it only sinks to about 1 Pa in cathode inlet are of the CCL.

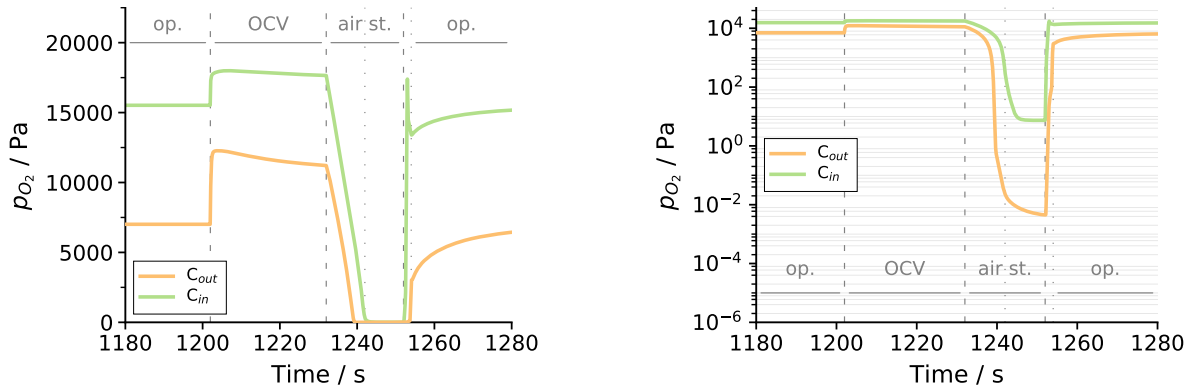


Figure 8.12: Oxygen partial pressure p_{O_2} in the CCL at cathode inlet and cathode outlet during the refresh cycle. The profiles are shown in a linear scale (left) and a logarithmic scale (right).

When the air flow in the channel is resumed, the oxygen concentration in the CCL shots up and approximates its steady state values during the following period of constant operation with $i = 0.25 \text{ A/cm}^2$. Note that at cathode inlet, a peak in p_{O_2} can be observed in the transition period between air stop and nominal operation.

The distribution of p_{O_2} across the entire CCL is shown in 2D in figure 8.13 for the different stages of the refresh procedure (after 30 s of OCV, after 10 and 20 s of air stop and after air flow and current density are established again).

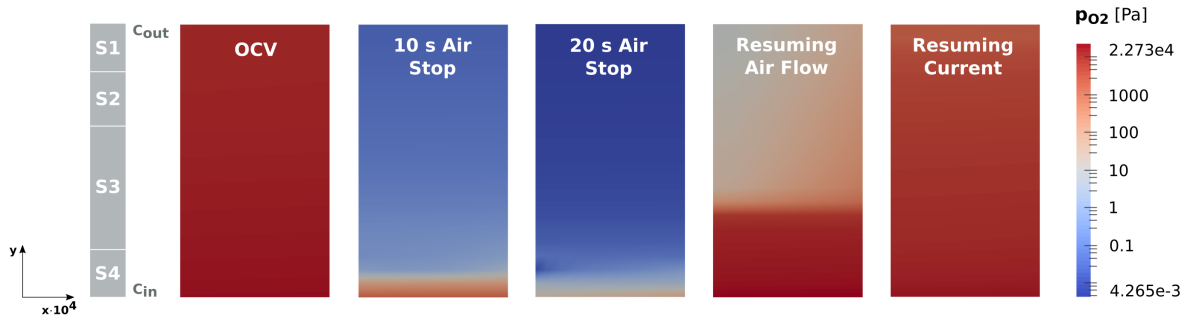


Figure 8.13: Oxygen partial pressure p_{O_2} within the CCL at different stages of the refresh cycle simulated with the transient DMFC model. The 2D plot shows the CCL magnified in x-direction by 10^4 and p_{O_2} on a logarithmic scale.

The 2D-plots show that gradients in p_{O_2} occur primarily along the channel, and not perpendicular from PEM/CCL-interface to CCL/MPL-interface. After 10 s of air stop, O_2 is still present in the cathode inlet segment, while it has been consumed in all other segments. After 20 s of air stop, also the amount of oxygen in the inlet area has diminished (cf. also fig. 8.12).

After the air flow in the channel has been resumed within 1 s, the oxygen front moving from inlet to outlet is visible. When the current density has been ramped up to its

nominal value 0.25 A/cm^2 in the following second, the entire CCL is filled with oxygen again.

8.5.2 Methanol Partial Pressure

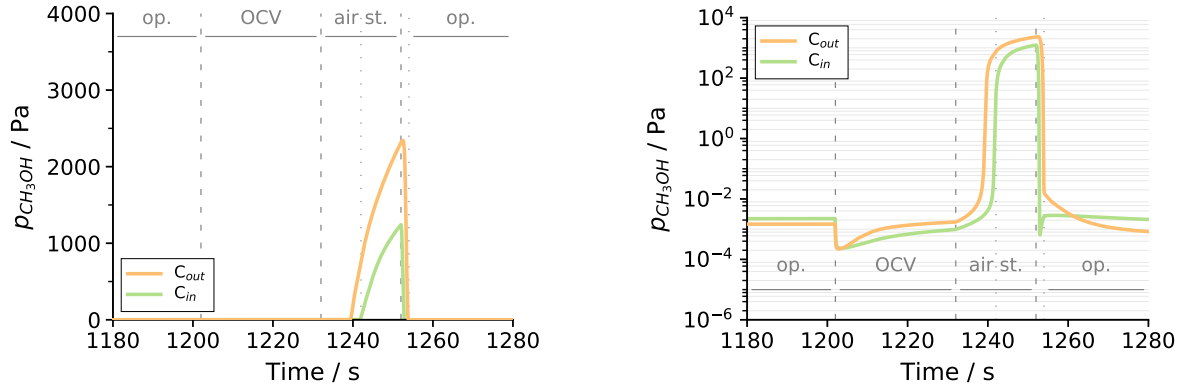


Figure 8.14: Methanol partial pressure $p_{\text{CH}_3\text{OH}}$ in the CCL at cathode inlet and cathode outlet during the refresh cycle. The profiles are shown in a linear scale (left) and in a logarithmic scale (right).

The crossover methanol gets consumed right at the PEM/CCL interface in a side reaction to the ORR during normal cell operation. During the air stop period in the refresh cycle, however, methanol accumulates in the CCL, as the simulation shows (figure 8.14). This happens first at cathode outlet as soon as oxygen is depleted there. A little later, CH_3OH also accumulates in the cathode inlet area of the CCL. When starting the air flow in the cathode again, the accumulated methanol gets instantly consumed in the reaction with the inflowing oxygen (oxygen-activated MOR, cf. eq. 6.67).

Looking at the local methanol partial pressure in a logarithmic plot (right picture in figure 8.14), one can clearly see that the methanol present in the CCL inversely correlates with the presence of oxygen there (cf. figure 8.12). This is evident for the OCV phase as well as for the transition phase between air stop and normal operation. Where a small oxygen peak at cathode inlet occurs, a dip in the local methanol concentration occurs at cathode inlet.

The spacial visualisation of the methanol distribution in the CCL for the different phases of the refresh cycle underlines this behaviour (figure 8.15): After 10 s of air stop, the methanol accumulation starts at cathode outlet and moves towards cathode inlet. After 20 s air stop, almost the entire cathode catalyst area is filled with a substantial amount of methanol. The accumulated methanol reacts with the inflowing air when the air flow in the cathode channel is re-established. The methanol front along the CCL can be clearly seen in the 2D plot. When the cell is under load again, no more methanol can be found in the CCL.

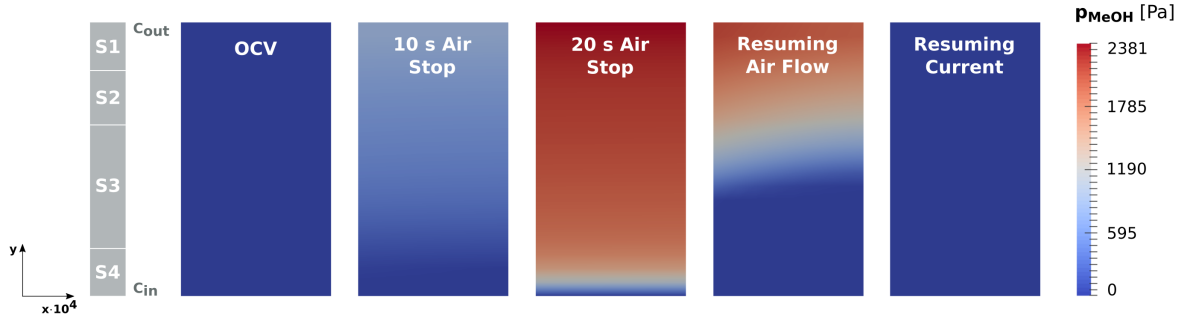


Figure 8.15: Methanol partial pressure $p_{\text{CH}_3\text{OH}}$ within the CCL at different stages of the refresh cycle simulated with the transient DMFC model. The 2D plot shows the CCL magnified by 10^4 in x-direction.

8.5.3 Reactions in the CCL

Not only the distribution of reactant species is of interest during the refresh cycle, but also the reactions themselves, especially in the CCL. The ORR reaction zone is depicted in figure 8.16. At all stages, gradients occur primarily along the channel and not in x-direction, following the presence of oxygen in the CCL. After 20 s of air stop, the reaction only takes place at cathode inlet (S4), where O_2 is still present. When the air flow is back on, there is a reaction peak (cf. fig. 8.15) in the middle segment of the (S3), where the oxygen front hits the accumulated methanol.

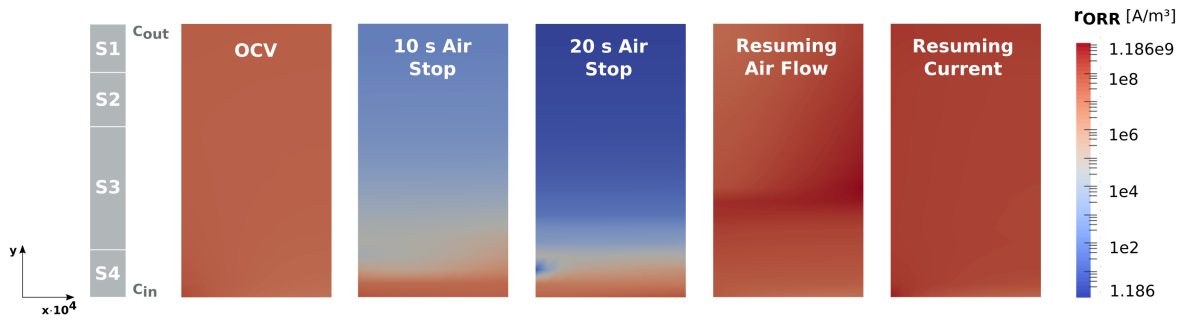


Figure 8.16: Oxygen reaction rate r_{ORR} within the CCL at different stages of the refresh cycle simulated with the transient DMFC model. The 2D plot shows the CCL magnified in x-direction by 10^4 and r_{ORR} on a logarithmic scale.

Methanol, on the other hand, reacts under two different mechanisms in the CCL (cf. section 6.3.3) and with the model it could be visualised where the discrete reactions for the MOR take place during refresh. Figures 8.17 and 8.18 show the reaction zones of the primary (i.e. O_2 -activated) and secondary (H_2O -activated) MOR at different stages of the refresh cycle.

As long as there is sufficient oxygen, the primary, oxygen consuming MOR basically oc-

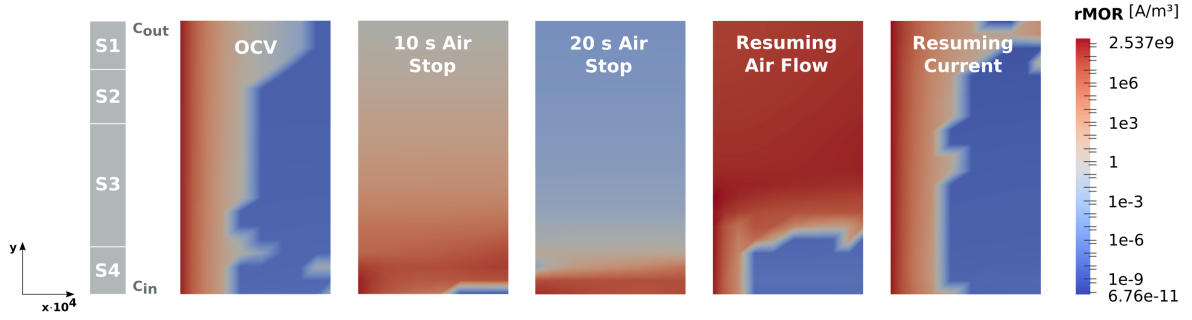


Figure 8.17: Primary methanol oxidation reaction rate r_{MOR} within the CCL at different stages of the refresh cycle simulated with the transient DMFC model. The 2D plot shows the CCL magnified in x-direction by 10^4 and r_{MOR} on a logarithmic scale.

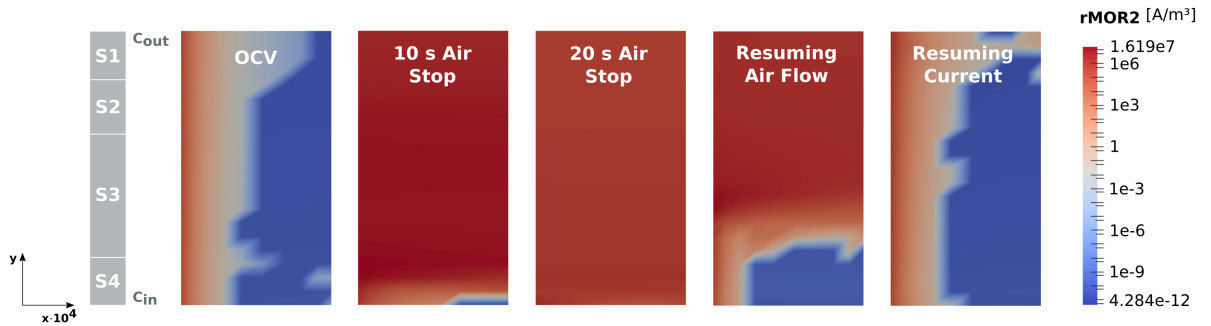


Figure 8.18: Secondary methanol oxidation reaction rate r_{MOR_2} within the CCL at different stages of the refresh cycle simulated with the transient DMFC model. The 2D plot shows the CCL magnified in x-direction by 10^4 and r_{MOR_2} on a logarithmic scale.

curs at the PEM/CCL interface, where crossover methanol arrives and is fully consumed by the reaction. Thus, there is a strong gradient in the reaction zone across the CCL in x-direction. When oxygen runs short at cathode outlet, the primary MOR comes to a halt and the reaction zone moves towards the inlet area, where O_2 is still available. After 20 s air stop, the primary MOR is only active in S4, while it is completely deactivated in S₁, S₂ and S₃, where no more oxygen is present (cf. fig. 8.17). As soon as the air flow is resumed, the primary MOR reaction zone moves towards the outlet again with a peak in S3, where then both methanol and oxygen are available in a substantial concentration. After the flow and current conditions are re-established, this reaction takes place at the PEM/CCL-interface again.

The secondary MOR, which is significantly slower than the primary MOR and has methanol and water as reactants, occurs just like the primary MOR at the PEM/CCL-interface during normal operation and OCV, since at this time CH_3OH is present only at this interface. During the air stop, this reaction becomes dominant over the entire CCL area (cf. fig. 8.18). At the same time the primary MOR and the ORR have come to a standstill due to the lack of oxygen in S₁ – S₃. When the air flow is resumed, the secondary MOR shows a peak where the oxygen front hits the accumulated methanol, just like the primary MOR.

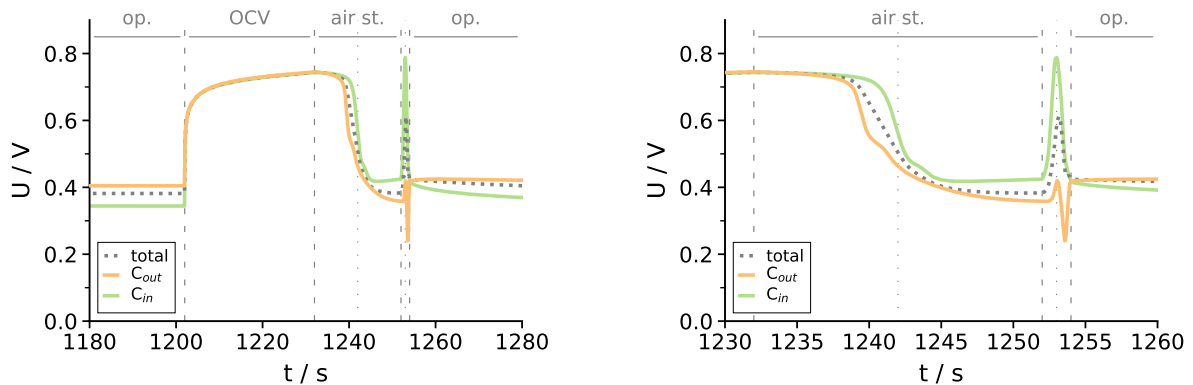


Figure 8.19: Development of the *local* cell voltage at cathode inlet and cathode outlet during the refresh cycle in comparison to the total cell voltage. Left: full refresh sequence, right: zoom to air stop and transition phase.

The transition and dominance of the three different reactions in the CCL also are reflected in the local cell voltage, as figure 8.19 shows. During the air stop phase, when oxygen gets depleted at cathode outlet, but persists at cathode inlet, the local potential is higher at cathode inlet (ORR dominant) than at cathode outlet (MOR dominant). A strong peak at cathode inlet segment can be observed when the oxygen flow restarts (between $t = 1252$ s and $t = 1253$ s) and also a (much smaller) peak at cathode outlet. In both segments, the ORR restarts then. Furthermore, when current is drawn from the cell, the voltage sinks down in all segments, forming a dip in the cathode outlet segment, where there is still a considerable amount of methanol present. When the current is back at

its nominal value of $i = 0.25 \text{ A/cm}^2$ at $t = 1254 \text{ s}$, the cell performs as usual with the performance gradient from cathode inlet to cathode outlet (cf. sec. 7.2).

8.5.4 Local Cathode Potential and Reduction of Platinum Oxides in the CCL

The local availability of oxygen during the air stop and the resulting variation of the electrochemical reactions in the CCL affect the electric and ionic potential. The course of the potential difference $\Delta\varphi = \varphi_{el} - \varphi_{ion}$ in the cathode catalyst layer is shown for the cathode inlet and cathode outlet segment in figure 8.20.

While $\Delta\varphi_{CCL}$ in the cathode is $> 0.8 \text{ V}$ in all segments during continuous operation with $i = 0.25 \text{ A/cm}^2$ and OCV, it sinks to $\approx 0.52 \text{ V}$ at cathode inlet and $\approx 0.43 \text{ V}$ at cathode outlet during the air stop. This result is qualitatively consistent with experimental measurements of the local cathode potential vs. RHE in the DMFC during the refresh cycle [113]. When the air flow starts again, $\Delta\varphi_{CCL}$ shows a small peak at cathode inlet, analogously to the oxygen concentration.

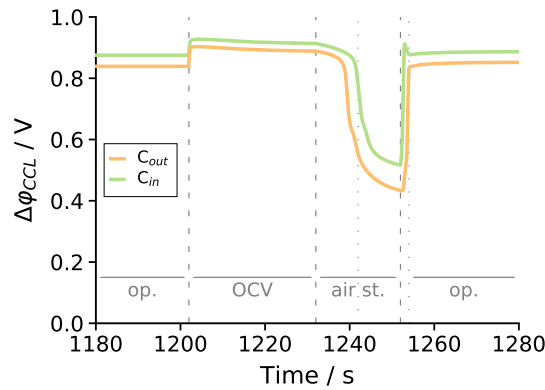


Figure 8.20: Local potential difference $\Delta\varphi_{CCL}$ in the CCL at cathode inlet and cathode outlet during the refresh cycle.

The changes in the local potential have an impact on the catalyst surface coverage: it leads to a reduction of the platinum oxide species and consequently a recovery of the cathode ECSA. Figure 8.21 shows the profiles of the surface species PtO and PtOH at cathode inlet and cathode outlet over time.

At the beginning of the OCV phase, the catalyst coverage with PtOH shoots up to $\theta_{\text{PtOH}} \approx 0.85$, and then decreases to $\theta_{\text{PtOH}} \approx 0.80$ during the 30 s of OCV. Meanwhile the coverage of the PtO remains unchanged at $\theta_{\text{PtO}} \approx 0.18$.

After ca. 10 s of air stop, when the local potential difference in the CCL drops below 0.6 V, the catalyst coverage with both PtOx-species sinks rapidly. In the outlet segments, S1 and S2, which are fully oxygen depleted, the oxide species get completely reduced.

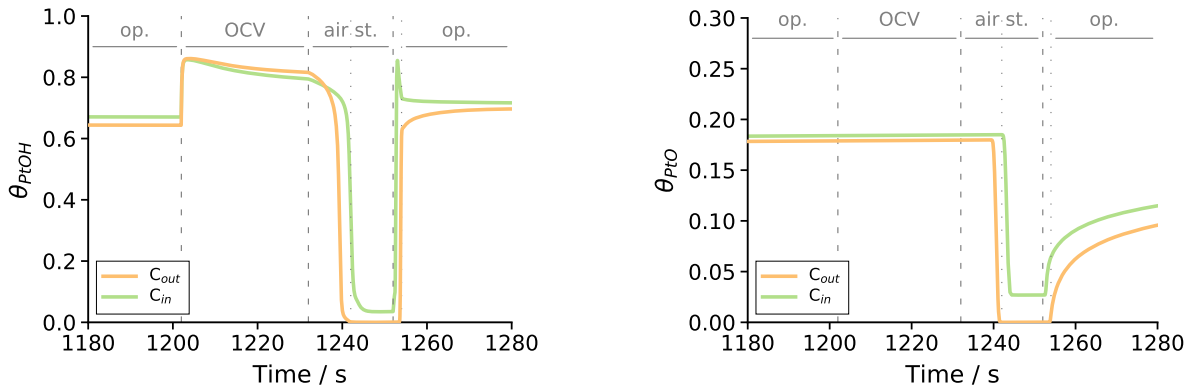


Figure 8.21: Cathode catalyst surface coverage with PtOH (left) and PtO (right) at cathode inlet and cathode outlet during the refresh cycle.

At cathode inlet (S4), where a residual amount of oxygen remains and $\Delta\varphi^{\text{CCL}}$ does not sink as low as in the other segments, the reduction of PtOx-species could only partially be achieved.

When flow and current are resumed, the local potential shoots up and so does the catalyst coverage with PtOH. In the following course of operation, it remains at a high level, just as before the refresh. The other oxide species, PtO, increases with a logarithmic shape over time, just as in the previous period of continuous operation. The gradient in the surface coverage with PtO along the channel is now more pronounced than in the previous phase of continuous operation. This results from the fact that this oxide species got only partially reduced during the air stop phase in the simulation.

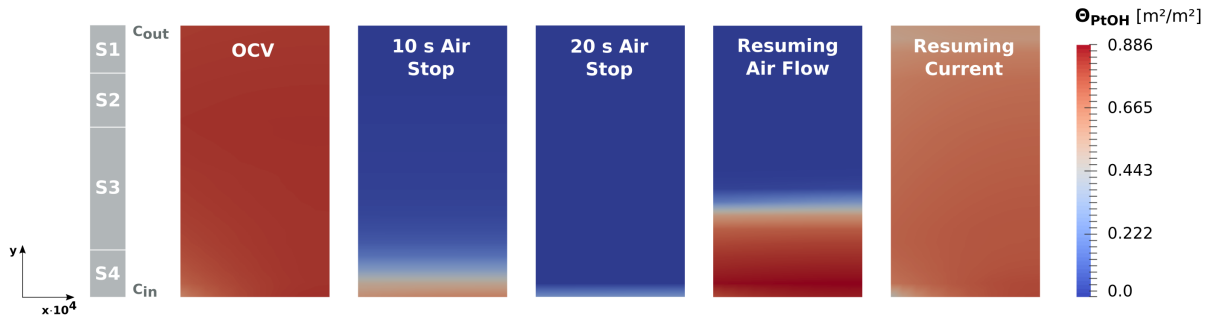


Figure 8.22: Catalyst surface coverage with PtOH in the CCL at different stages of the refresh cycle simulated with the transient DMFC model. The 2D plot shows the CCL magnified by 10^4 in x-direction.

The spatial distribution of θ_{PtOH} and θ_{PtO} in the CCL for the different stages of the refresh cycle is shown in figures 8.22 and 8.23. Both profiles are homogeneous across the CCL, gradients occur only along the channel. As already visible in the line plots, θ_{PtOH} is dynamic and follows the profile of p_{O_2} (cf. fig. 8.13) during the start up phase. In contrast, θ_{PtO} shows a slow and steady rise during the start up sequence, with impact

on the cathode ECSA.

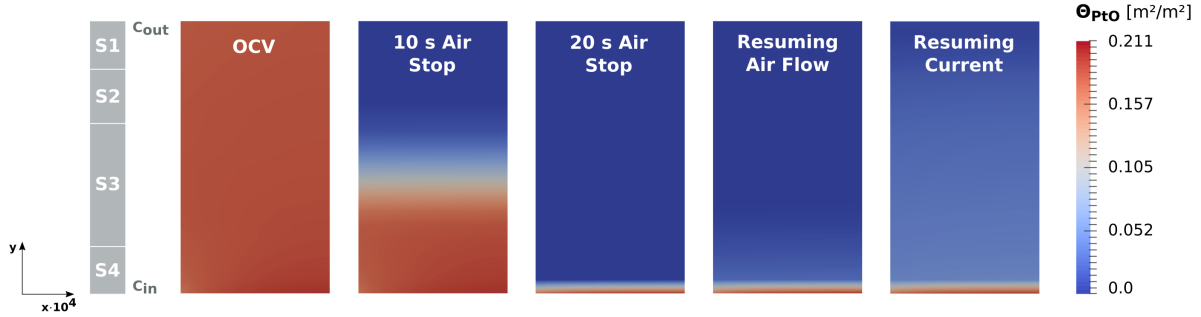


Figure 8.23: Catalyst surface coverage with PtO in the CCL at different stages of the refresh cycle simulated with the transient DMFC model. The 2D plot shows the CCL by 10^4 magnified in x-direction.

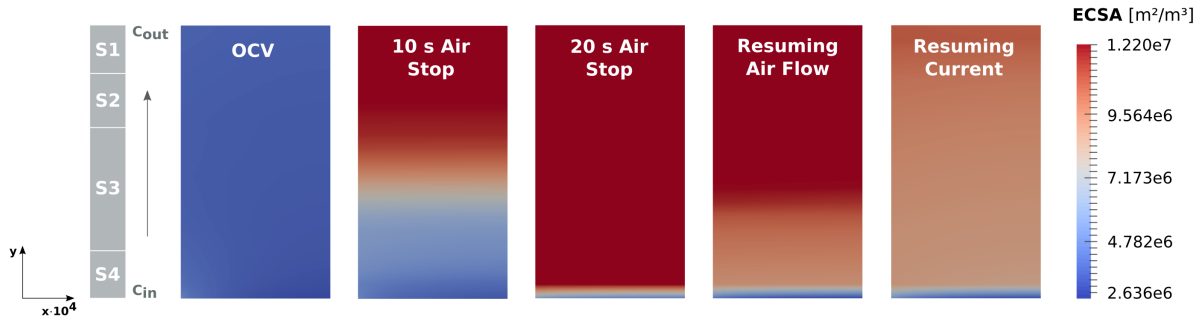


Figure 8.24: ECSA of the CCL at different stages of the refresh cycle simulated with the transient DMFC model. The 2D plot shows the CCL magnified by 10^4 in x-direction.

Since the ECSA in the CCL is determined by the presence of PtO-species, the distribution within the CCL over the refresh cycle inversely follows θ_{PtO} , as figure 8.24 shows. During the air stop period, it is fully recovered in all oxygen depleted areas. As soon as air flow and current are re-established, however, the active surface area instantly starts decreasing again, as the last two plots in figure 8.24 show.

8.5.5 Local Potential and Hydrogen Evolution in the ACL

The electrochemical reactions on the cathode side during the refresh cycle not only influence the local potential in the CCL, but also affect the anode local potential, as shown in figure 8.25: the potential difference in the anode, $\Delta\varphi = \varphi_{\text{el}} - \varphi_{\text{ion}}$, starts diverging during the air stop period, as soon as oxygen is depleted in the CCL at the cathode outlet area and the secondary MOR gains importance (compare figures 8.16 to 8.18).

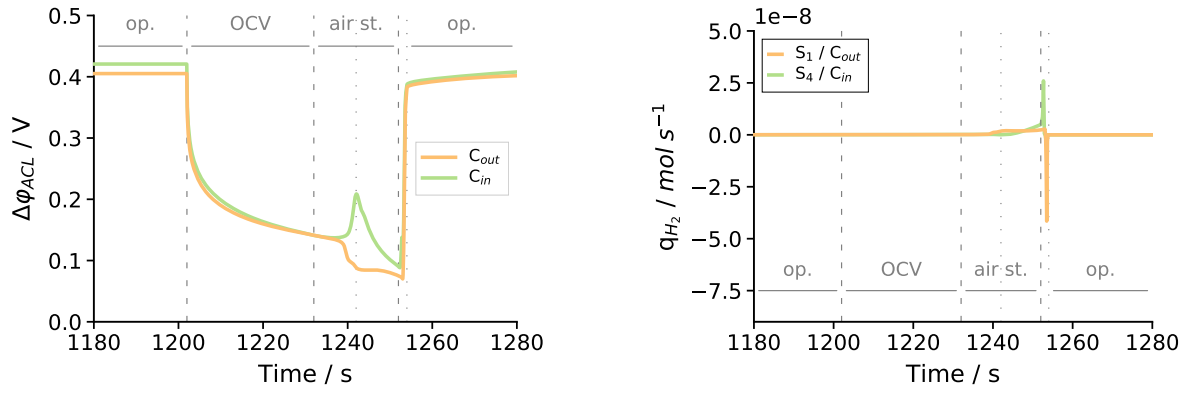


Figure 8.25: Local potential difference $\Delta\varphi_{ACL}$ (left) and hydrogen source q_{H_2} (right) in the ACL in the first (cathode outlet/anode inlet) and last (cathode inlet/anode outlet) segment of the cell during the refresh cycle.

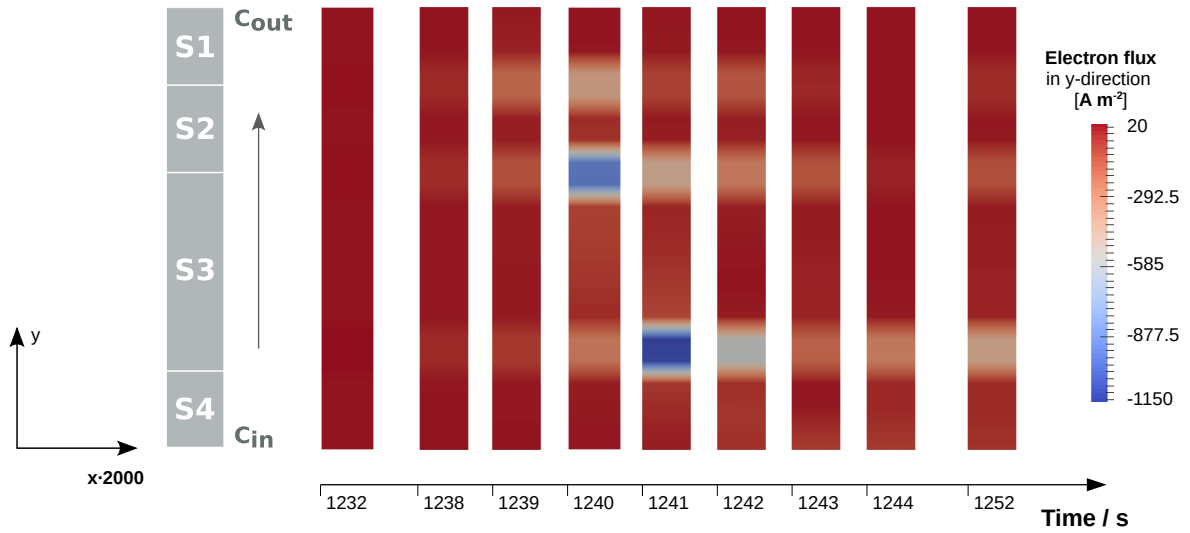


Figure 8.26: *In-plane* electric current in the CCL during the air stop phase of the refresh sequence. The 2D plot shows the CCL magnified by 2000 in x-direction at different time steps.

The electrolyte potential φ_{ion} starts diverging in along the channel as a result of the development of two reaction zones in the cathode catalyst layer during the air stop phase.

The phenomenon can be explained as follows: While the regular ORR as a sink for electrons and protons prevails at cathode inlet, where oxygen is still present, the oxygen-depleted cathode outlet area is dominated by the MOR, which represents a source for H^+ and e^- . The charges in the CCL are mobile in-plane as well as through-plane, which means that in addition to the “regular” current flow across the cell, also a transfer of H^+ and e^- along the channel is possible.

During the air stop sequence, the electrons produced in the “MOR-zone” at cathode outlet migrate in-plane to the “ORR-zone” at cathode inlet. At the same time, the protons produced in the MOR in the cathode outlet area move across the membrane towards the anode. In the anode inlet/cathode outlet area (S1), the current flow across the cell thus reverses, whereas at anode outlet/cathode inlet area (S4), the regular cell behaviour is maintained, with a proton flow from anode to cathode [155, 152].

Figure 8.26 shows the in-plane electron flux in the cathode CL during the air stop phase at different time steps. Negative values indicate an a electron current against the direction of gas flow in the cathode, i. e. from cathode outlet to cathode inlet. While at $t = 1232$ s, the electric current in y-direction is basically zero, at $t = 1239$ s (7 s of air stop), a current flow in y-direction starts evolving with a discrete band, moving from the cathode outlet area towards the cathode inlet area in the catalyst layer. The cathode in-plane current band reaches its peak approximately at $t = 1241$ s near the cathode inlet area, shortly before the highest point in the anode potential difference $\Delta\varphi^{ACL}$ can be observed in S4 (cf. figure 8.25). The narrow and discrete current band formation is a consequence of the segmented BPP set-up of the cell in the model, which will be later discussed in section 8.5.9. The phenomenon itself, i.e. the migration of e^- along the channel from the “MOR-zone” at cathode outlet to the “ORR-zone” at cathode inlet, is independent of the BPP design.

The protons produced in the MOR at cathode outlet during the air stop phase do not migrate in-plane to the cathode inlet area like the electrons. Instead, the protons move across the cell through the membrane to the anode side and lead to a substantial change in the ionic potential, which then leads to the shift in $\Delta\varphi^{ACL}$ and induces the hydrogen evolution in the ACL.

Figure 8.27 shows the development of the local ionic current in the cell and the anode potential $\Delta\varphi^{ACL}$ during the air stop period of the refresh sequence.

The temporary development of multiple reaction zones in the CCL during the air stop sequence with the reaction peak moving from cathode outlet (S1) to cathode inlet (S4) at according to the local reactant availability (cf. sections 8.5.1 and 8.5.2 and section 8.5.3) is visible in the local current density: At approximately $t = 1239$ s the local current density in S1 shows a dip to a negative current, which then successively spreads to the other

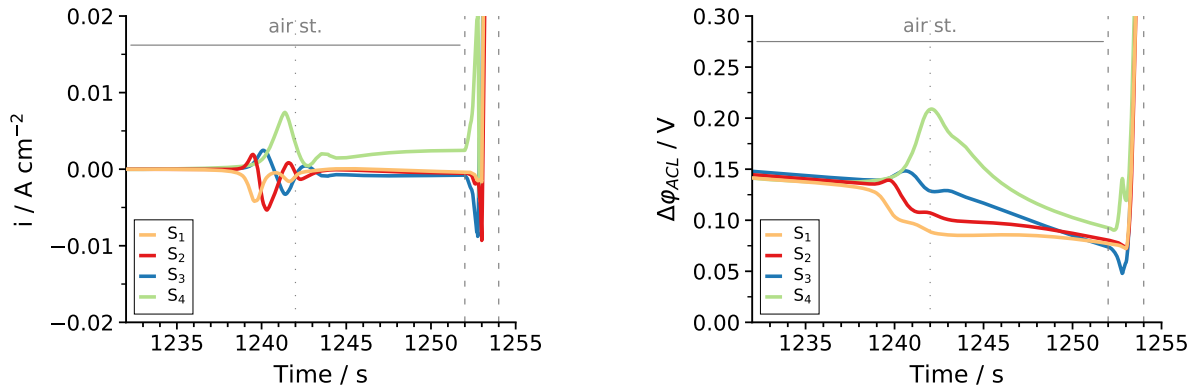


Figure 8.27: Profile of the local ionic current density (left) and the anode potential difference $\Delta\varphi_{ACL}$ (right) in all four segments of the cell (S1-S4) during the air stop period of the refresh cycle.

segments. Only in the cathode inlet segment (S4), where the O_2 -concentration remains high enough to maintain the regular ORR, the local current density shows a peak once the MOR reaction front has moved along the channel at $t \approx 1241$ s. The reaction in this area remains active with for the rest of the air stop period, while the other segments get basically deactivated due to the lack of reactants. Only the secondary, water-activated MOR prevails in S1 to S3, which has a much lower reaction rate than the ORR (cf. figure 8.18).

The anode potential difference in the ACL, which depends on the ionic potential according to $\Delta\varphi = \varphi_{el} - \varphi_{ion}$, develops accordingly. Starting at ≈ 0.15 V at the beginning of the air stop phase, $\Delta\varphi^{ACL}$ sinks below 0.1 V in S1, the anode inlet/cathode outlet area, as a result of the reverse proton flow from cathode to anode induced by the development of the MOR-zone in the CCL. Segments S2 and S3 follow with some time delay, according to the movement MOR-peak in the CCL. The opposite reaction at cathode inlet (S4) manifests in a local peak of $\Delta\varphi^{ACL}$ once the MOR-front reaches the ORR-zone in the cathode inlet segment the CCL.

The profile of the local anode potential $\Delta\varphi^{ACL}$ predicted by the model for the anode inlet and outlet area (figure 8.25) is in good agreement with the experimental study of Rabissi et al. [112], who investigated the local anode potential in the first and last segment of the DMFC during the refresh sequence.

With the local anode potential $\Delta\varphi^{ACL}$ approaching 0 V in the anode inlet/cathode outlet area (S1) during the air stop phase at $\approx t = 1239$ s, hydrogen starts evolving in the ACL. The left image in figure 8.28 shows the development of the hydrogen source q_{H_2} in the ACL during the refresh sequence. The reaction rate is small but existent, predominantly in the anode inlet segment of the cell. During the transition period between air stop and operation between $t = 1252$ s and $t = 1253$ s, when the air flow is resumed in the cathode, a spike in the hydrogen source q_{H_2} can be observed in the ACL in the anode outlet area of S4 and S3 (corresponding to the cathode inlet area). The influence of the shifting reactions can again also be seen in the local current density and anode potential

difference (cf. figure 8.27). As soon as the external current load ramps up at $t = 1253$ s, the hydrogen source in the ACL turns into a sink in all four segments, meaning that the prevalent H_2 in the anode gets consumed.

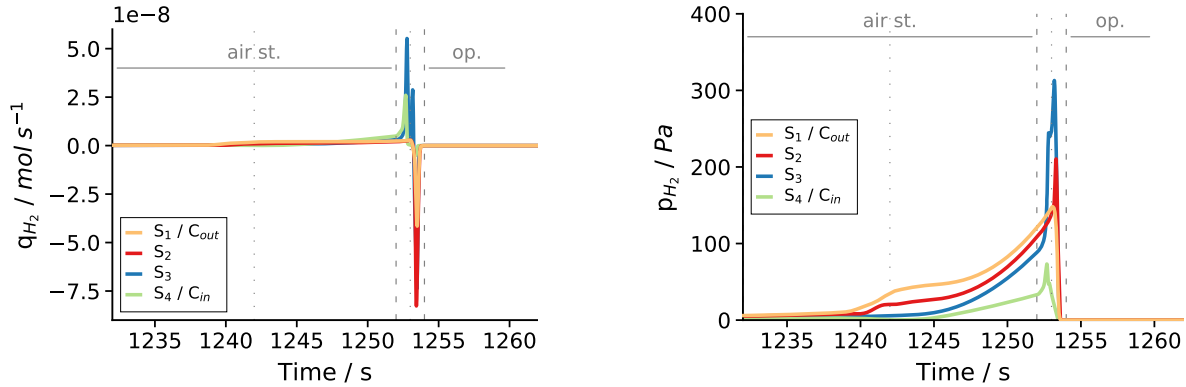


Figure 8.28: Profile of the hydrogen source q_{H_2} (left) and the hydrogen partial pressure p_{H_2} (right) in the ACL in all four segments of the cell (S1-S4) during the air stop period of the refresh cycle.

Figure 8.28 shows the development of the hydrogen partial pressure in the ACL during the air stop period of the refresh cycle. p_{H_2} grows in all segments during the air stop period, with a clear H_2 -concentration gradient from anode inlet (S1) to anode outlet (S4). At the end of the 20 s air stop period in the simulation, the hydrogen partial pressure in the ACL ranges from 120 Pa at anode inlet/cathode outlet to 70 Pa at anode outlet (or rather $x_{H_2}^g|C_{out} \approx 0.11\%$ to $x_{H_2}^g|C_{in} \approx 0.026\%$). When the oxygen flow is resumed in the cathode and the current flow starts, a peak in the hydrogen concentration can be observed in the middle segment S3 with values of almost 320 Pa ($x_{H_2}^g \approx 0.27\%$).

The hydrogen concentrations obtained in the simulation are well within the range of an experimental study on refresh cycles in DMFC by Bresciani et al [20]. The current which is drawn from the cell starting at $t = 1253$ s, leads to a swift consumption of all accumulated hydrogen in the ACL. As soon as the cell is operating under normal conditions again, no more hydrogen is present in the DMFC anode.

8.5.6 Water Activity and Liquid Water Distribution in the CCL

In addition to the electrochemical processes within the catalyst layers, the refresh cycle also influences the local humidity conditions within the DMFC. In the cathode catalyst, water which has accumulated in the outlet area during the operation period, gets removed during the OCV period, as figure 8.29 shows. The cathode inlet area, which is comparably dry during operation, gets almost fully humidified during the air stop period of the refresh cycle.

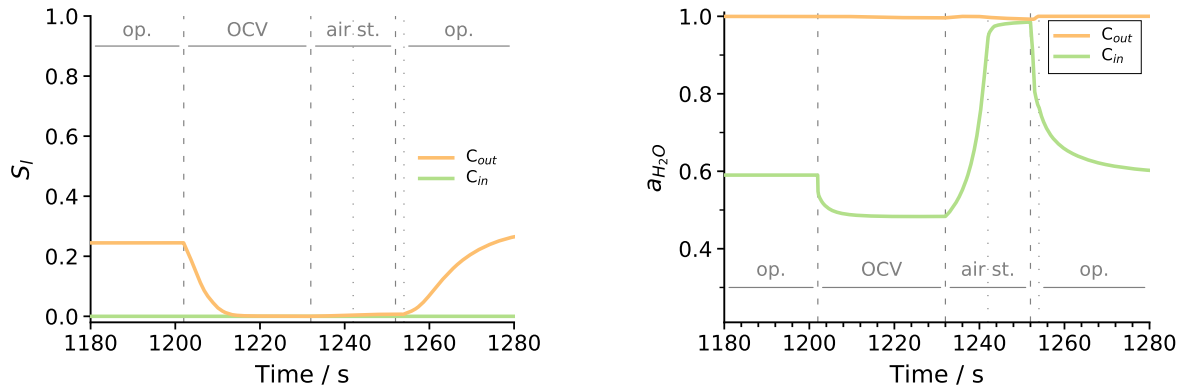


Figure 8.29: Development of the liquid saturation S_l (left) and the water activity a_{H_2O} (right) in the CCL at cathode inlet and cathode outlet during the refresh cycle.

8.5.7 Impact of the Secondary MOR in the CCL

At the Pt-catalyst in the DMFC cathode, two different mechanisms for the reduction of crossover methanol are possible (cf. sec. 6.3.3). The primary MOR mechanism (eq. 6.67), which is predominant under oxygen-rich operating conditions is complemented by a secondary MOR path, which depends on dissociated water on the catalyst surface (eq. 6.70) and gains importance when no oxygen is available there. The validated DMFC model features both reaction mechanisms, therefore the impact of the secondary MOR on the Pt-catalyst during the refresh cycle could be studied.

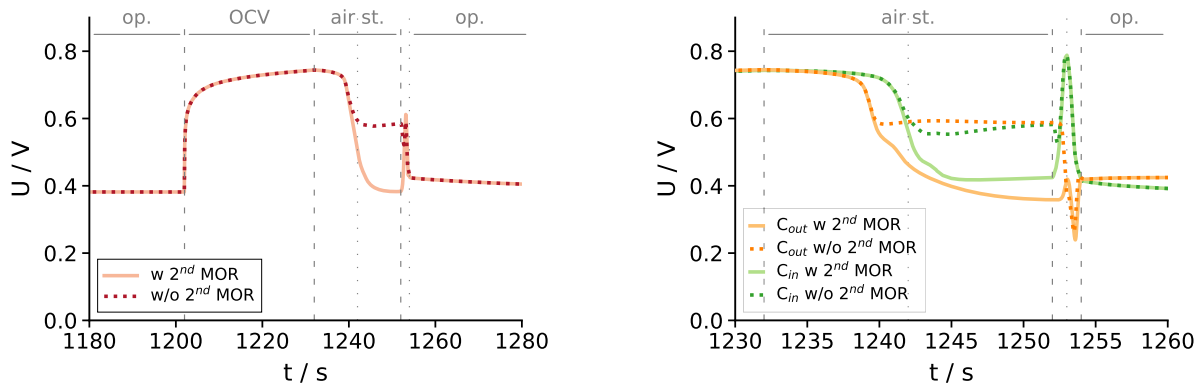


Figure 8.30: Total cell voltage (left) and local cell voltage of the cathode inlet and cathode outlet segment of the cell (right) during the refresh cycle. The plots show the result of the reference simulation including both MOR reactions in the CCL (solid lines) in comparison with the variation *without* the secondary MOR in the model(dashed lines).

A simulation *without* the secondary MOR (eq. 6.70) was performed and compared to the standard refresh simulation. The overall cell voltage as well as the local cell voltage profiles during the refresh cycle are shown in figure 8.30 for both simulations in direct comparison.

While under regular operation with $i = 0.25 \text{ A/cm}^2$ and OCV, the voltage profiles are identical, the simulation without secondary cathode MOR shows a strong deviation from the standard simulation during the air stop phase of the refresh cycle: The cell potential does not sink lower than $\approx 0.575 \text{ V}$.

In figure 8.31, the sinks for oxygen and methanol are shown. Note that the sink for methanol is the sum of the primary and the secondary MOR reaction rate in the CCL. While nothing changes with regard to the oxygen sink, the methanol sink during the air stop phase drops down significantly in case only the oxygen-activated MOR mechanism is enabled in the CCL. In contrast, in case also the secondary water-activated MOR is taken into account, the methanol reaction in the CCL goes on during the air stop period (cf. figure 8.31).

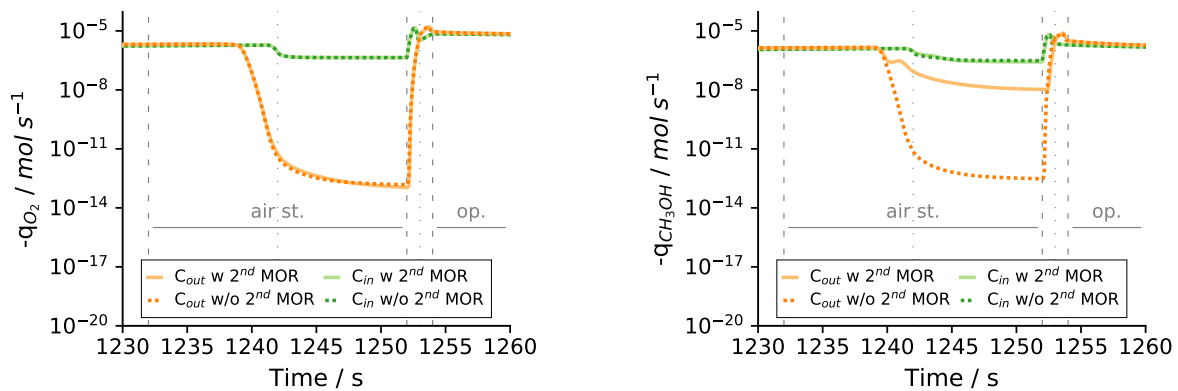


Figure 8.31: Oxygen sink (left) and methanol sink (right) in the cathode inlet and cathode outlet segment of the CCL during the refresh cycle (logarithmic scale). Comparison between reference simulation *with* secondary MOR (solid lines) and variation *without* secondary MOR (dashed lines).

Since both MORs represent a proton source, the missing reaction during the air stop period directly influences the local potential difference in the CCL, as figure 8.32 shows. In case the secondary MOR would not take place, the local potential difference $\Delta\varphi_{\text{CCL}}$ would not sink below 0.7 V at cathode outlet. Instead, the potential difference between electrode and electrolyte would drop lower at cathode inlet, to about 0.65 V . Such a behaviour could not be observed experimentally (cf. Rabissi et al. [113]).

The simulation result highlights that it is essential to consider the two different MOR mechanisms on Pt-catalysts in order to correctly describe the processes within the DMFC cathode under oxygen-depleted conditions.

Interestingly, the simulation predicts the reduction of both PtOx-species also in case the secondary MOR would not take place, due to a swift undershoot in the local potential *after* the air stop period at the point when the air flow is resumed and the current is

ramped up (cf. figure 8.33). However, as previously discussed, the assumption that only the primary MOR takes place in the CCL cannot be justified.

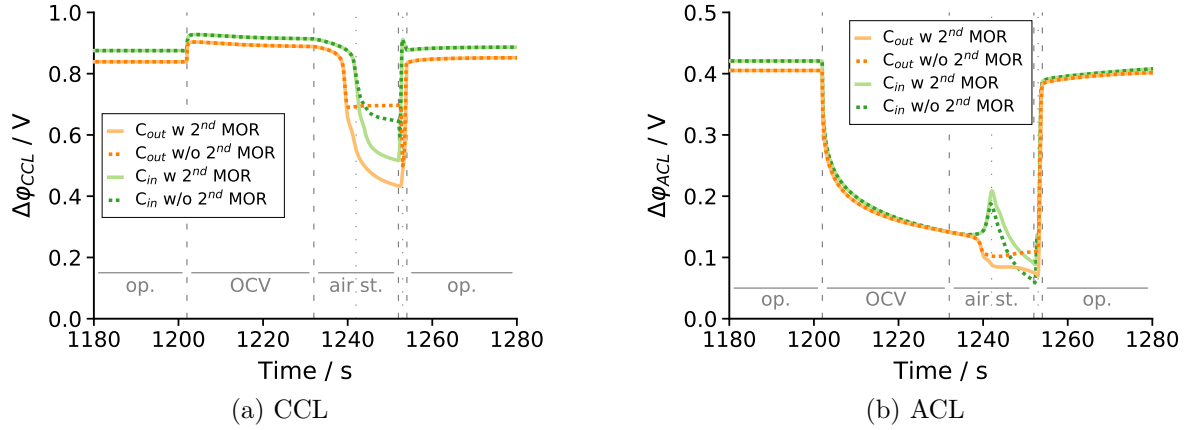


Figure 8.32: Local potential differences $\Delta\phi_{CCL}$ (a) and $\Delta\phi_{ACL}$ (b) in the cathode inlet and cathode outlet segment of the cell during the refresh cycle. Comparison between the reference simulation *with* secondary MOR (solid lines) and the variation *without* secondary MOR (dashed lines).

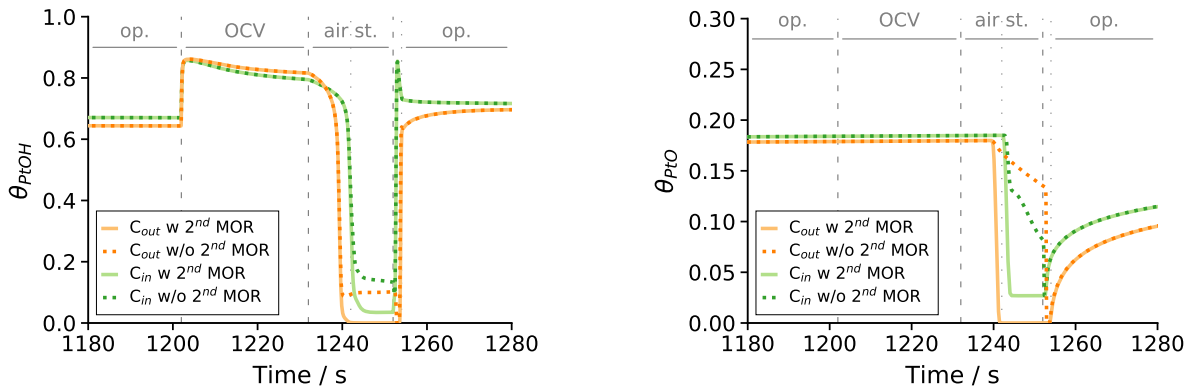


Figure 8.33: Catalyst surface coverage coverage with PtOH (left) and PtO (right) in the cathode inlet and cathode outlet segment of the cell during the refresh cycle. Comparison between the reference simulation *with* secondary MOR (solid lines) and the variation *without* secondary MOR (dashed lines).

8.5.8 Variation: Secondary MOR with increased reaction rate

As mentioned in section 8.3, the parametrisation of the secondary MOR kinetics in the model might correlate with the overestimation of the cell voltage during the air stop phase in the reference simulation compared with the experiments. In order to validate this hypothesis, the refresh simulation was repeated with a somewhat faster kinetics for the secondary MOR: In this simulation, the exchange current density for the H₂O-activated MOR was increased by one order of magnitude from $j_0^{MOR2} = 5 \times 10^{-7} \text{ A/cm}^2$ to $j_0^{MOR2} = 5 \times 10^{-6} \text{ A/cm}^2$.

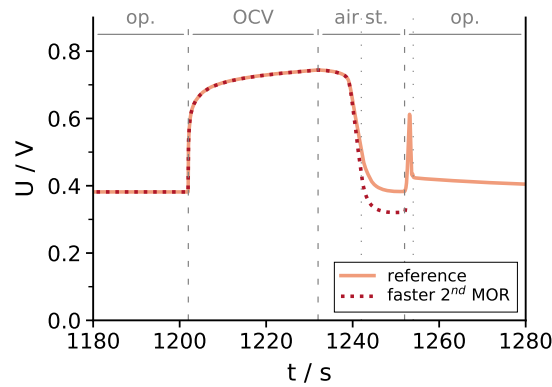


Figure 8.34: Cell voltage during the refresh cycle simulated with the reference model (solid line) compared to the variation with the accelerated secondary MOR kinetics (dashed line).

The simulation result for the cell voltage in comparison with the reference simulation is shown in figure 8.34. With the accelerated secondary MOR in the model description, the resulting cell voltage during the air stop phase is lowered compared to the reference simulation and consequently closer to the experimental results (cf. figure 8.7), which lets conclude that the reference model parametrisation for the MOR kinetics in the CCL is not ideal. The simulation with faster secondary MOR kinetics, however, showed convergence issues when flow and current were resumed at $t = 1252 \text{ s}$ and the simulation could not be completed, that is why the phenomenon was not further studied here.

8.5.9 Impact of the BPP Segmentation

The refresh simulation was performed with the validated DMFC model (cf. sec. 7), which considered a segmented BPP set-up in the cell. Experimental investigations, however, were performed with a continuous BPP (see [112, 113]). In order to evaluate if the segmentation of the BPP had any influence on the local heterogeneities within the DMFC during the refresh cycle, the refresh simulation was repeated with a continuous, non-segmented cathode BPP in the model.

The change from a segmented to a continuous BPP in the simulation only has a minimal affect on the overall cell voltage, as figure 8.35 shows. A minor deviation is visible during the second phase of the air stop period, else the profiles are identical.

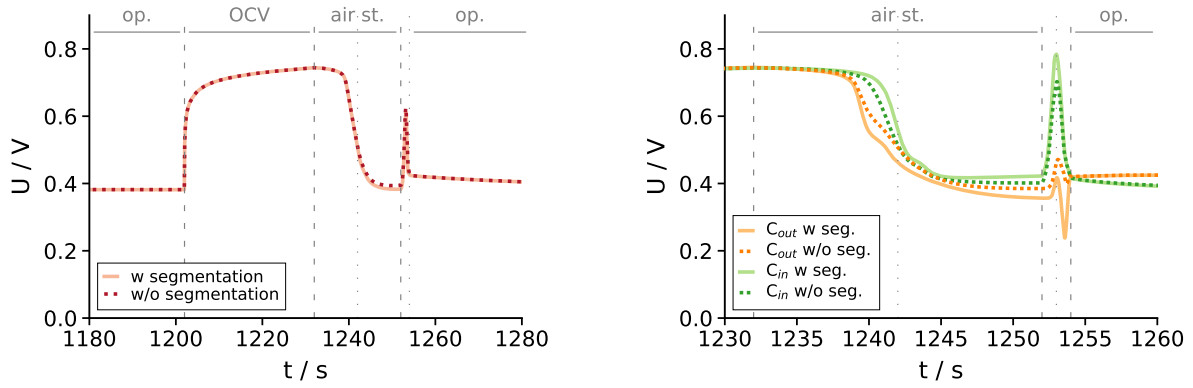


Figure 8.35: Overall cell voltage (left) and local cell voltage of the cathode inlet and cathode outlet segment of the cell (right) during the refresh cycle. Plots show the reference simulation *with* BPP segmentation (solid lines) in comparison with the variation *without* BPP segmentation in the model (dashed lines).

Despite the differences in the local cell voltage, the local potential difference $\Delta\varphi^{CCL}$ in the cathode does *not* change with segmentation (cf. fig. 8.36). In the ACL on the other hand, the divergence in $\Delta\varphi^{ACL}$ between the inlet and outlet segment is much stronger during the air stop period in case of a continuous cathode BPP.

On the local cell voltage during the refresh cycle, however, the segmentation of the cathode BPP has an influence (cf. fig. 8.35): In case of a segmented cathode BPP as in the reference model, the local cell voltage diverges strongly from cathode inlet to cathode outlet during the air stop period and the transition period between air stop and normal operation. *Without* segmentation, the deviation in the local cell voltage from cathode inlet to cathode outlet is less pronounced. The dip in the local cell voltage at cathode outlet between $t = 1253$ s and $t = 1254$ s, when the current is ramped up, is very small in the simulation with a continuous BPP compared to the simulation with the segmented BPP.

Figure 8.37 shows the in-plane electron flux in the cathode CL during the air stop phase

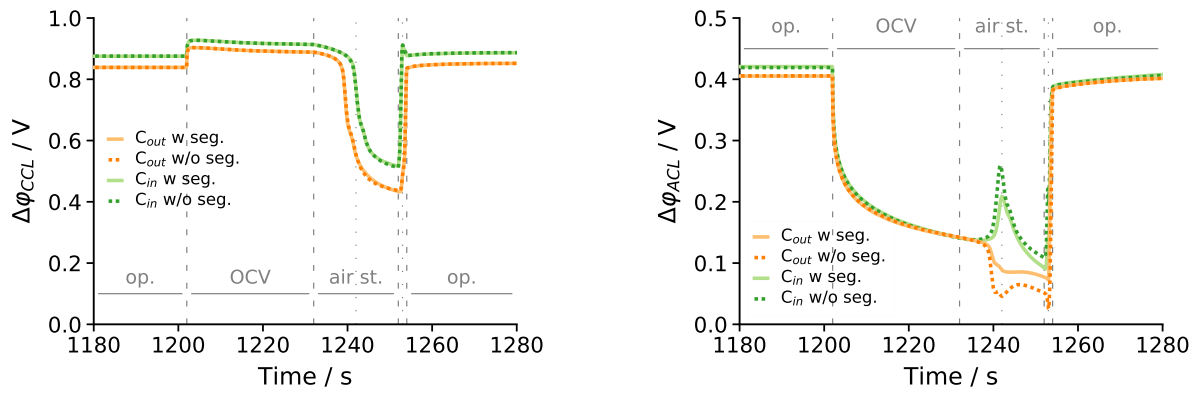


Figure 8.36: Local potential differences $\Delta\varphi_{CCL}$ (left) and $\Delta\varphi_{ACL}$ (right) in the cathode inlet and cathode outlet segment of the cell during the refresh cycle. Comparison between the reference simulation *with* BPP segmentation (solid lines) and the variation *without* BPP segmentation in the model (dashed lines).

at different time steps for the simulation *without* BPP segmentation in the model. Negative values indicate a current against the direction of gas flow in the cathode, i. e. an electron flux from cathode outlet to cathode inlet.

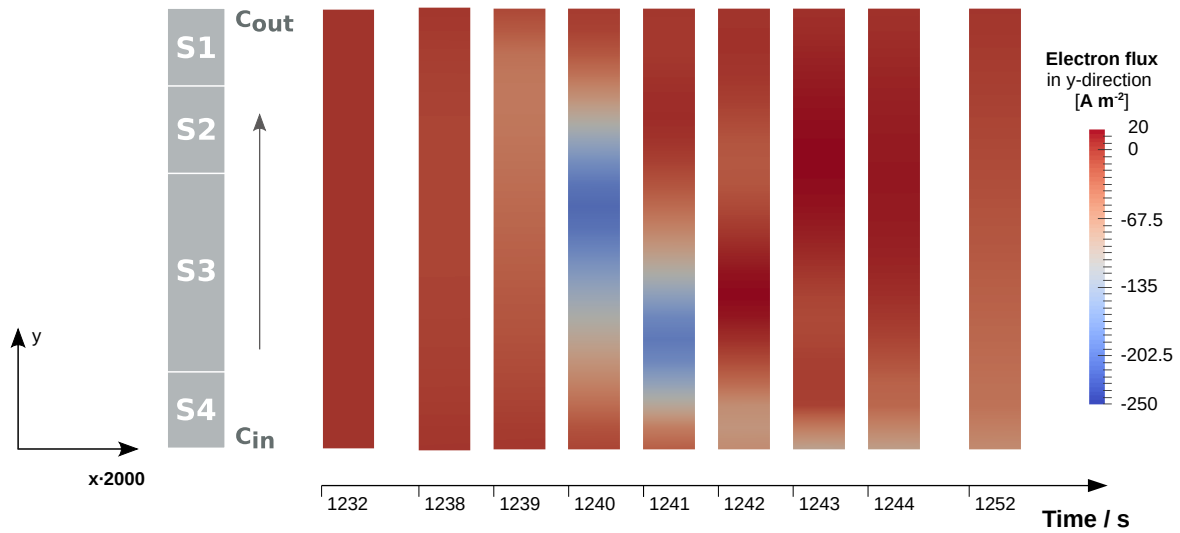


Figure 8.37: Simulation *without* BPP segmentation in the model: *In-plane* electric current in the CCL during the air stop phase of the refresh sequence. The 2D plot shows the CCL magnified by 2000 in x-direction at different time steps.

Just like in the simulation with the segmented BPP (cf. section 8.5.5), at the beginning of the air stop phase $t = 1232$ s where O_2 is still available in the entire CCL, no in-plane current occurs. Between $t = 1239$ s and $t = 1240$ s, when the oxygen-depletion in S1

starts, a negative current in y-direction evolves first at the oxygen-depleted cathode outlet area and the in-plane current front moves towards the cathode inlet area of the CCL over time. In contrast to the simulation with the segmented BPP, where the in-plane current in the CCL occurred as a very discrete band, the negative in-plane current band is smooth along the channel in case the BPP is continuous. The maximum local in-plane current density reached is moderate with a peak value of -250 A m^{-3} for the simulation with a continuous BPP (compare figure 8.26 for the results of the simulation with segmented BPP).

The impact of the BPP segmentation is also visible in the ionic potential and the internal ionic current. Figure 8.38 shows the development of the local current density induced by the formation of the two reaction zones in the CCL during the air stop period for the reference simulation (left) and the variation with a continuous BPP (right) in direct comparison. While qualitatively the evolution of the local current density is the same in both cases, the quantitative result differs, with intensified current values in the simulation with the continuous BPP. The model also predicts a much higher spread of the local anode potential difference $\Delta\varphi_{ACL}$ in case the BPP is continuous, as shown in figure 8.39. The potential values obtained in the variation show a much better quantitative agreement with the experimental results of Rabissi et al. [112], who also performed their measurements with a cell with a continuous cathode BPP.

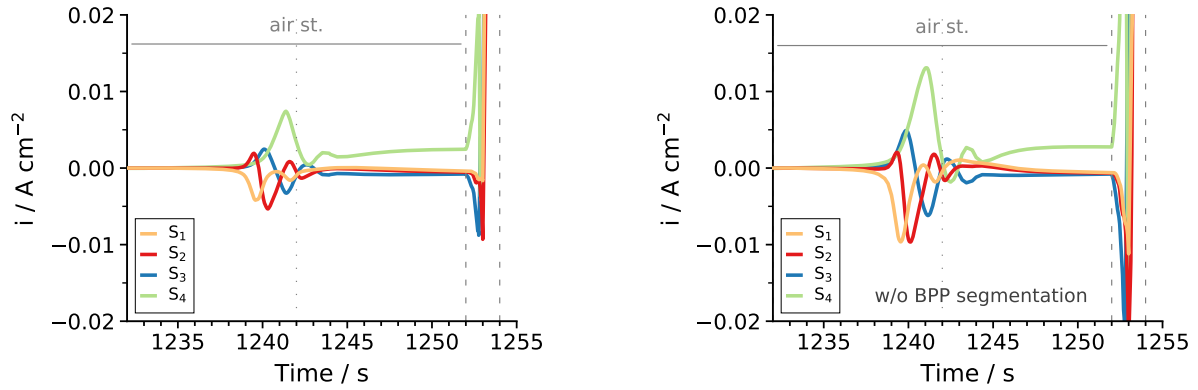


Figure 8.38: Profile of the local ionic current density in all four segments of the cell (S1-S4) during the air stop period of the refresh cycle. Reference simulation *with* BPP segmentation (left) and variation *without* BPP segmentation in the model (right).

The evolution of hydrogen in the DMFC anode is affected by the increased variance in the anode potential difference $\Delta\varphi_{ACL}$: in case of a continuous cathode BPP, the model predicts a much higher production of H_2 in the ACL already in the first phase of the air stop period (cf. fig. 8.40). The profile of q_{H_2} in the ACL in S1 beginning at $t = 1239 \text{ s}$ follows the profile of $\Delta\varphi_{ACL}$ in this segment, which reaches a minimum value of $\approx 0.05 \text{ V}$ in the simulation with the unsegmented cathode BPP (cf. figure 8.39). In the reference

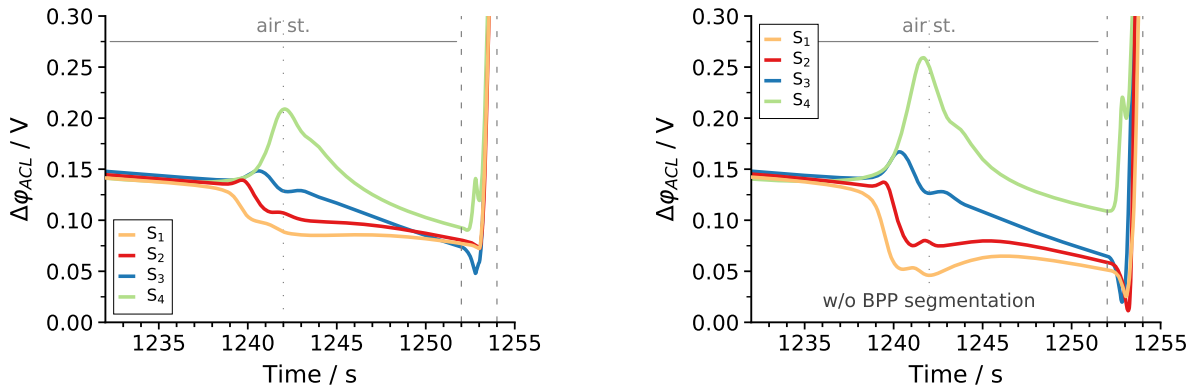


Figure 8.39: Profile of the anode potential difference $\Delta\varphi_{ACL}$ in all four segments of the cell during the air stop period of the refresh cycle. Reference simulation *with* BPP segmentation (left) and variation *without* BPP segmentation in the model (right).

simulation with a segmented BPP, only a minimum value of ca. 0.1 V is reached during the air stop phase, which renders a much lower hydrogen source in the ACL.

Also during the transition period after the air stop, the hydrogen source in the ACL shows a different profile in case of the continuous BPP compared to the segmented BPP. The HER peak in S4 (anode outlet/cathode inlet) at $t = 1252$ s when the air flow ramps up again does not occur in case the cathode BPP is continuous. The consumption of H_2 as soon as the outer current is applied at $t = 1253$ s, on the other hand, is much stronger pronounced than in case of the simulation with the segmented BPP.

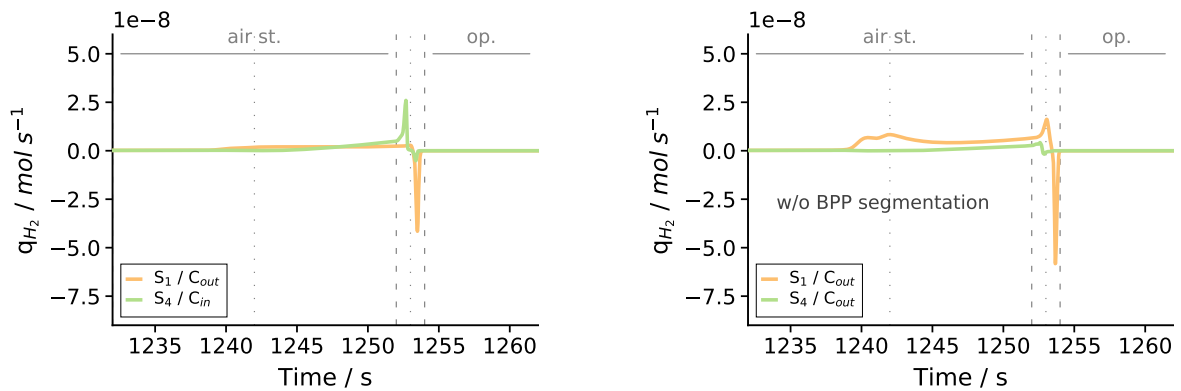


Figure 8.40: Hydrogen source q_{H_2} in the ACL during the air stop period of the refresh cycle S1 (anode inlet/cathode outlet) and S4 (anode outlet/cathode inlet) in the reference simulation *with* BPP segmentation (left) and the variation *without* BPP segmentation in the model (right).

Figure 8.41 shows the resulting differences in the hydrogen partial pressure along the ACL for the two variants. In case of a continuous cathode BPP, the distribution of H_2 shows a stronger gradient along the anode during the air stop period. The overall level of

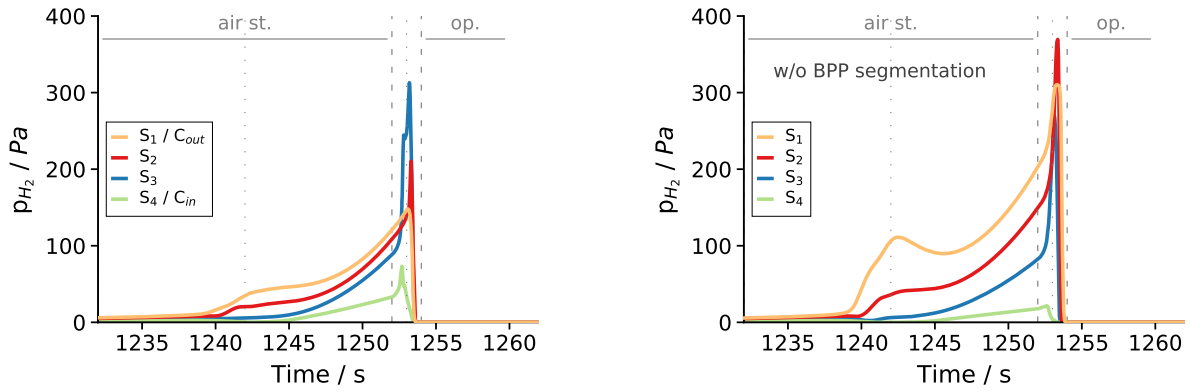


Figure 8.41: Profile of the hydrogen partial pressure p_{H_2} in the ACL in all four segments of the cell (S1-S4) during the air stop period of the refresh cycle in the reference simulation *with* BPP segmentation (left) and the variation *without* BPP segmentation in the model (right).

hydrogen present in the cell is marginally higher in case of the continuous BPP compared to the segmented BPP. Still, the results are in good agreement with the experimental study of Bresciani et al. [20].

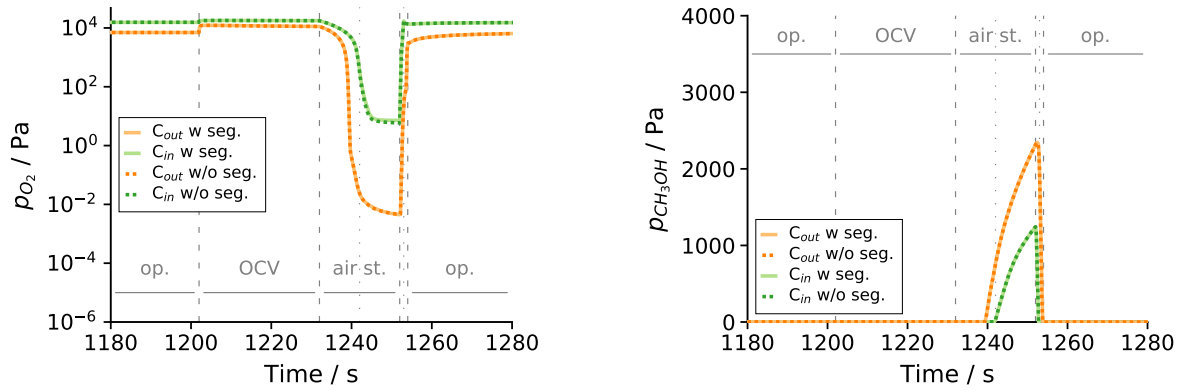


Figure 8.42: Oxygen partial pressure (left) and methanol partial pressure (right) in the CCL at cathode inlet and cathode outlet in the refresh simulation with and *without* cathode BPP segmentation (solid lines vs. dashed lines).

The species distribution in the CCL does not change with segmentation (cf. fig. 8.42). Since consequently, $\Delta\varphi^{CCL}$ remains identical to the case *with* BPP-segmentation, the reduction of the PtOx-species is equally effective in both cases. Figure 8.43 depicts also the profiles of θ_{PtOH} and θ_{PtO} over time for both simulations in direct comparison.

All in all, the simulation results show that the segmentation of the cathode BPP evokes changes in the electrolyte potential and the anode reactions, but has no impact on the species distribution and reaction zones in the DMFC cathode. Qualitative and quantitative findings on the impact of the refresh cycle on the processes in the DMFC cathode are thus transferable from a cell with segmented BPP to a cell with a continuous BPP.

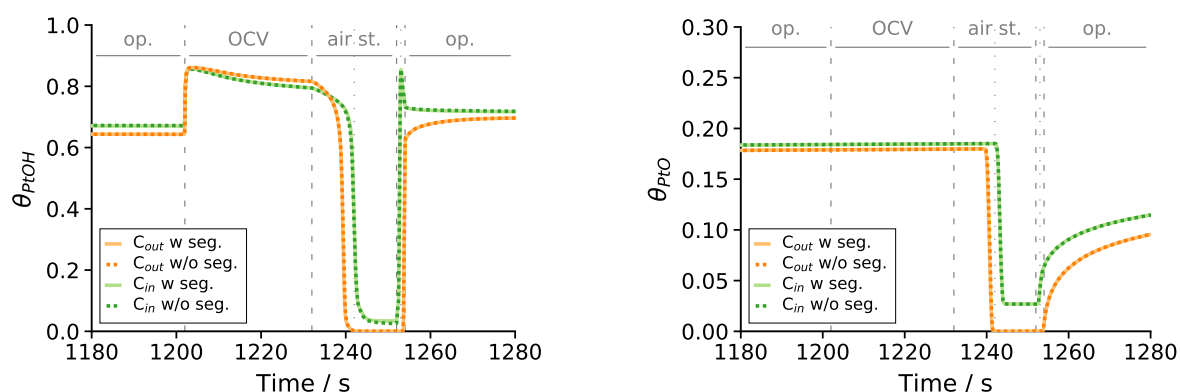


Figure 8.43: Catalyst surface coverage with PtOH (left) and PtO (right) in the CCL at cathode inlet and cathode outlet in the refresh simulation with and *without* cathode BPP segmentation (solid lines vs. dashed lines).

8.5.10 Conclusion: Local Conditions inside the DMFC during the Refresh Cycle

The local processes in the DMFC during a refresh cycle for recovery of temporary performance losses were studied in detail with the transient DMFC model. Apart from quantitative deviations, all relevant effects and their dynamics were predicted with good accuracy by the model, matching the experimental results for the DMFC refresh procedure as described in [20, 112, 113].

During the refresh cycle, the first 10 s of air stop lead to a dramatic decrease of the oxygen partial pressure within the DMFC cathode catalyst layer. The depletion of oxygen starts in the cathode outlet area of the CCL and moves towards the cathode inlet area over time. With the depletion of oxygen, the local potential difference in the CCL drops and the reduction of PtOx-species starts. With the oxygen level in the CCL lowering further, crossover methanol starts accumulating in the CCL during the consecutive 10 s of air stop, starting at the cathode outlet area. The ORR comes to a halt there, and so does the primary oxygen consuming MOR in the CCL. A further potential reduction in the CCL and thus the full reduction of the oxide species on the Pt-catalyst and consequent ECSA recovery results from the reaction of water and methanol via the *secondary* MOR path in the oxygen-depleted areas of the CCL.

When resuming the air flow in the DMFC cathode after the air stop period, the accumulated methanol in the CCL reacts with the incoming oxygen and fades from the catalyst. During this transition period, strong variations in the local species concentration and resulting reactions within the CCL occur along the channel. While soon sufficient oxygen is available at cathode inlet so that fast the ORR becomes dominant there, it takes some time until the amount of methanol present in the cathode outlet area gets oxidised. This spatial separation of oxidation and reduction reaction along the CCL leads to a divergence in the local cell potential when later the current is drawn. The effect fades when the surplus of methanol has vanished and the regular oxygen levels within the CCL are re-established.

Not only the cathode processes during the refresh cycle could be examined with the model, but also the processes in the DMFC anode. In the course of the air stop period, when the different reaction zones in the CCL have formed along the channel, the electrolyte potential starts diverging and approaches 0 V in the anode inlet area. Under these conditions, the evolution of hydrogen is triggered in the ACL, primarily at anode inlet/cathode outlet. The simulation results match with experimental findings on hydrogen evolution and the local potential difference in the ACL of the DMFC [20, 112].

In contrast to the set-up of the experimental studies on the DMFC refresh cycle, the model description included a segmented cathode BPP. The effect of this segmentation on the local processes during the refresh procedure was also studied. In a simulation with a continuous BPP, only an intensification of the effects in the DMFC anode were observed, whereas the processes in the DMFC cathode were not affected by the BPP segmentation.

To sum up, the transient local processes inside the DMFC during the refresh cycle could be well described with the physical 2D model and the simulation results show a considerable agreement with experimental findings.

8.6 Variation of Air Stop Scenarios during the Refresh Cycle

After the processes and influence parameters of the refresh in DMFC were understood, different variations of the refresh procedure were tested with the model with regard to the air stop. The standard refresh simulation presented in section 8.5 is in the following referred to as *reference simulation*.

The following air stop variants were simulated with the DMFC model:

1. extended air stop with a duration of 30 s
2. incomplete refresh
3. optimised air stop boundary conditions
4. nitrogen flush

The boundary conditions for each variation can be found in table 8.2. Figure 8.44 visualises the respective profiles over the refresh cycle.

8.6.1 Variation 1: Extended Air Stop

The reference simulation considered an air stop phase of 20 s, which is shorter than in the experiments. That is why as a first variation, a refresh cycle with an extended air stop duration of 30 s (equivalent to the experimental procedure) was tested with the model. All other boundary conditions in the simulation were identical to the reference (cf. tab. 8.2).

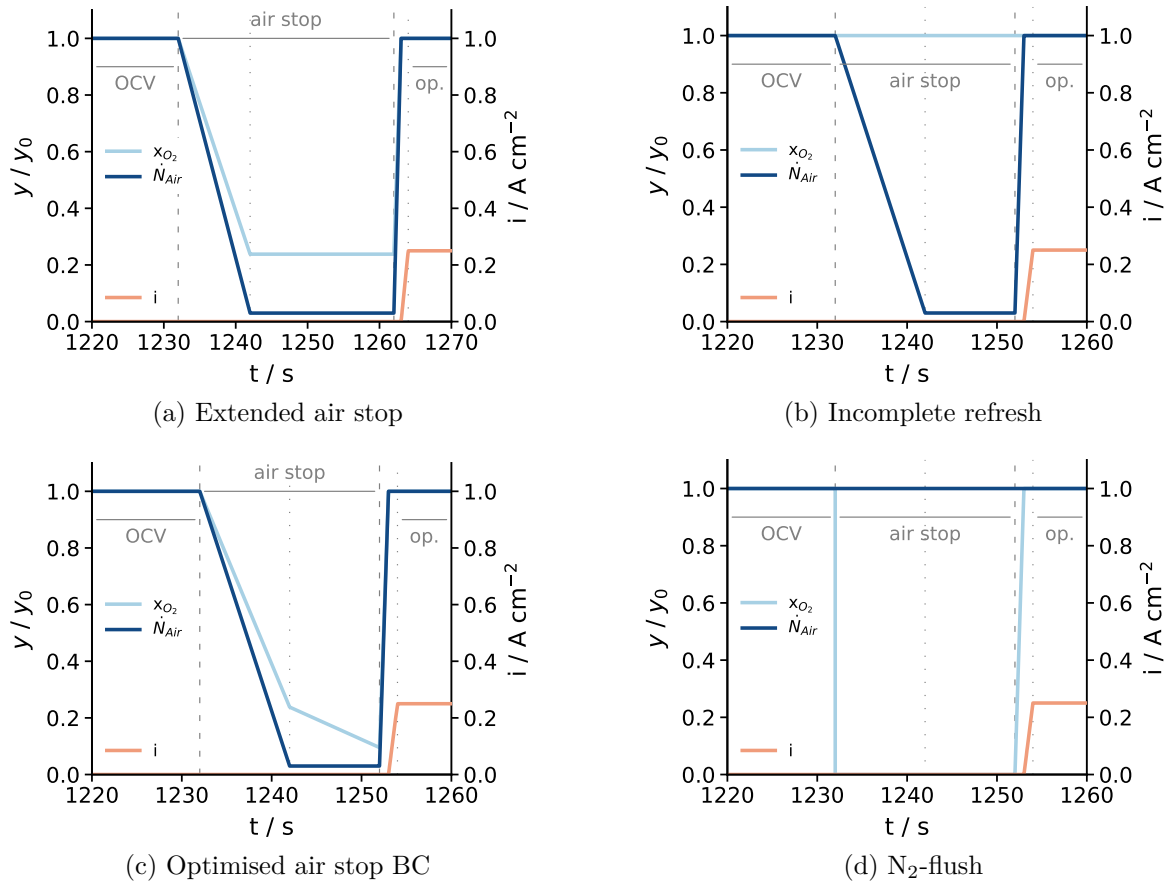


Figure 8.44: Cathode boundary conditions for the oxygen concentration x_{O_2} , the air flow \dot{N}_{Air} and the current density i for the 4 air stop variants in the refresh cycle simulated with the 2D model (cf. tab. 8.2).

Table 8.2: Operating conditions of air stop variations.

Simulation	AS phase	duration	air flow	x_{O_2}
Reference air stop	1	10 s	$N_0 \rightarrow 0.03 \cdot N_0$	$x_0 \rightarrow 0.238 \cdot x_0$
	2	10 s	$0.03 \cdot N_0$	$0.238 \cdot x_0$
Extended air stop	1	10 s	$N_0 \rightarrow 0.03 \cdot N_0$	$x_0 \rightarrow 0.238 \cdot x_0$
	2	20 s	$0.03 \cdot N_0$	$0.238 \cdot x_0$
Incomplete refresh	1	10 s	$N_0 \rightarrow 0.03 \cdot N_0$	x_0
	2	10 s	$0.03 \cdot N_0$	x_0
Optimised BC	1	10 s	$N_0 \rightarrow 0.03 \cdot N_0$	$x_0 \rightarrow 0.238 \cdot x_0$
	2	10 s	$0.03 \cdot N_0$	$0.238 \cdot x_0 \rightarrow 0.0952 \cdot x_0$
N ₂ flush		20 s	N_0	0.0

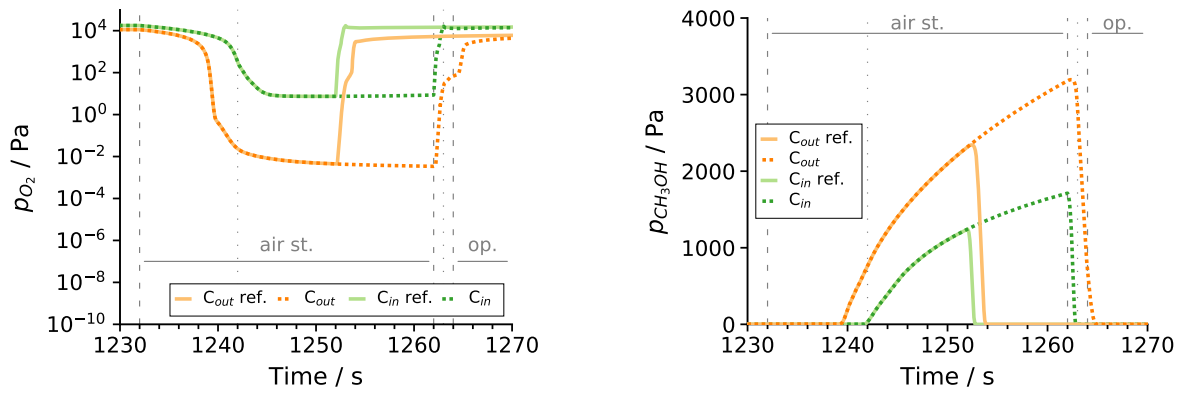


Figure 8.45: Oxygen partial pressure p_{O_2} (left) and methanol partial pressure $p_{\text{CH}_3\text{OH}}$ (right) during the refresh cycle with an extended air stop (dashed lines) compared to the reference (solid lines).

Figure 8.45 shows the profiles of oxygen and methanol along the cell for this variant. Since the boundary conditions for the oxygen concentration at cathode inlet did not change compared to the reference in this simulation, the extended air stop duration does not lead to a further decrease in p_{O_2} in the cathode inlet segment of the CCL. At cathode outlet, the value of p_{O_2} is a little lower after 30 s than after 20 s of air stop. The methanol accumulation in the CCL, on the other hand, is clearly affected by the 10 s longer air stop with an increase in $p_{\text{CH}_3\text{OH}}$ at the cathode inlet segment as well as at the cathode outlet segment.

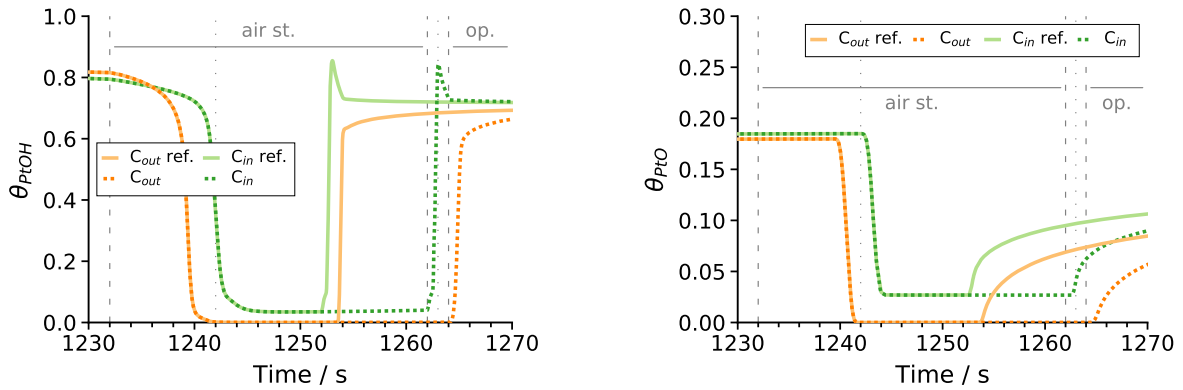


Figure 8.46: Catalyst surface coverage with PtOH (left) and PtO (right) during the refresh cycle simulated with an extended air stop (dashed lines) in comparison with the reference (solid lines).

As the oxygen levels in the CCL remain as high as in the reference simulation, no beneficial effect on the reduction of the PtOx-species can be observed in the simulation with the extended air stop duration, as figure 8.46 shows. The simulation most likely overestimates the available amount of oxygen in the cell during the refresh cycle due to its boundary conditions with a constant oxygen concentration at cathode inlet (cf.

fig. 8.44a). In the experimental set-up, the oxygen concentration at cathode inlet is assumed to sink continuously over the air stop period due to the limited reservoir of oxygen in the tubes. In reality, a longer air stop period could thus presumably improve the recovery of the ECSA in the CCL in case the oxygen level at cathode inlet only sinks slowly.

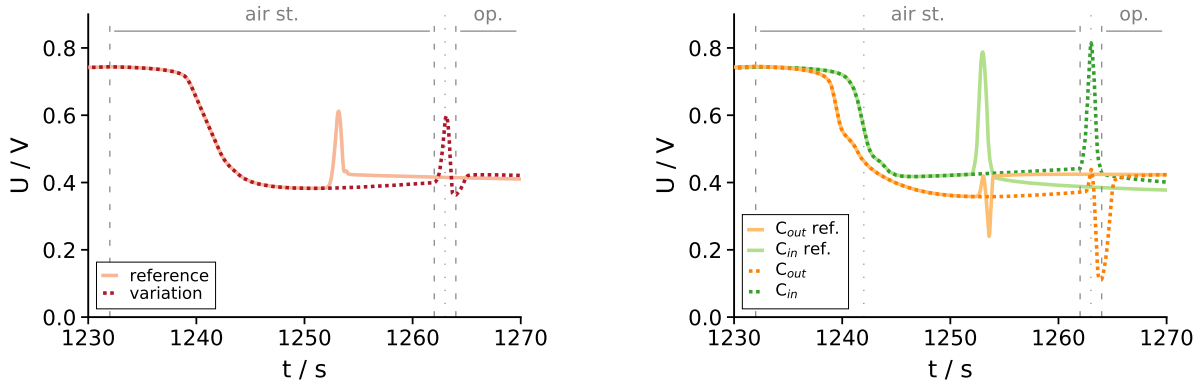


Figure 8.47: Overall cell voltage (left) and local cell voltage at cathode inlet and cathode outlet (right) during the refresh cycle with a 30 s air stop (dashed lines) compared to the reference (solid lines).

In contrast to the predicted oxygen concentration at cathode inlet, the effect of a longer air stop on the methanol accumulation in the DMFC cathode is most likely accurately captured in the simulation. The large amount of methanol in the CCL takes longer to reduce in the transition period between air stop and normal operation, leading to strong divergence in the local potential between cathode inlet and cathode outlet during this phase. As a consequence, a dip in the overall cell voltage is visible after the peak in the transition phase (cf. fig. 8.47). This phenomenon could also be observed experimentally.

8.6.2 Variation 2: Incomplete Refresh

The case of an incomplete refresh was also tested with the model. An incomplete refresh could for example occur when the air flow is stopped, but the valve at cathode inlet remains open, meaning that an “unlimited” reservoir of air is available at cathode inlet. For the simulation this meant that while the flow through the cathode was reduced just as in the reference simulation, the oxygen concentration at cathode inlet, remained at $x_{O_2} = 21\%$ (see tab. 8.2).

The resulting profiles of oxygen and methanol in the CCL are shown in figure 8.48. While at cathode outlet, the oxygen partial pressure sinks with some lag almost as low as in the reference simulation, only a very small reduction of p_{O_2} at cathode inlet can be observed. The prevailing oxygen at cathode inlet inhibits the accumulation of methanol there, while at cathode outlet, the accumulation of CH_3OH is still possible.

The very heterogeneous conditions inside the CCL affect the electrochemical reactions (fig. 8.49), where no drop in the reaction rates for oxygen and methanol is visible at the

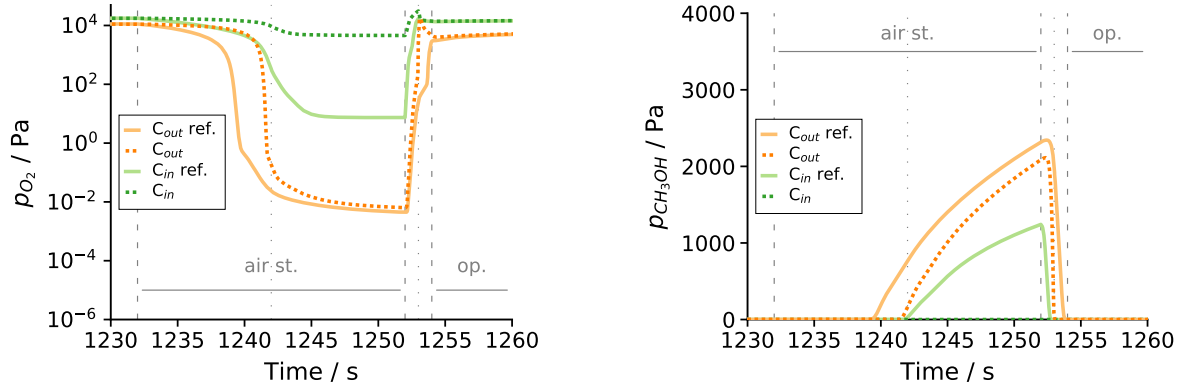


Figure 8.48: Partial pressures of oxygen (left) and methanol (right) in a refresh cycle with an incomplete air stop (dashed lines) compared to the reference (solid lines).

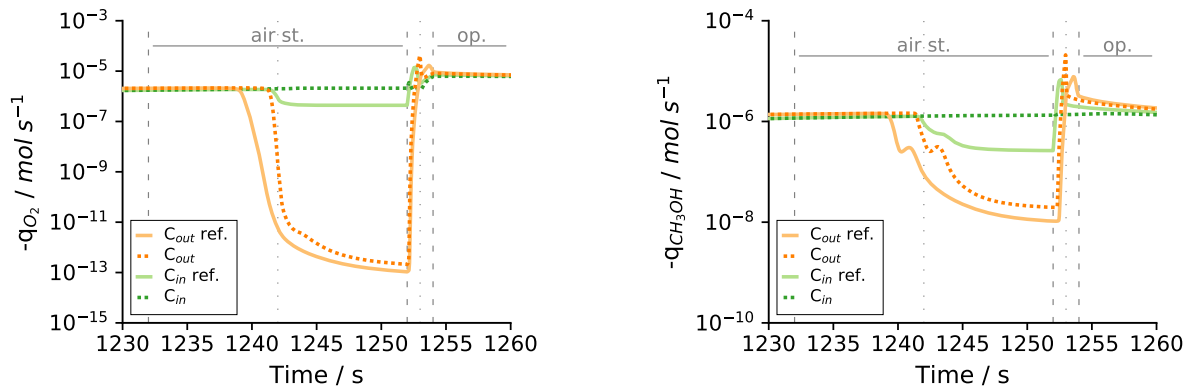


Figure 8.49: Reaction rates for O₂ (left) and CH₃OH (right) in a refresh cycle with an incomplete air stop (dashed lines) compared to the reference (solid lines).

cathode inlet under these circumstances. Consequently, a strong divergence in the local potential differences on anode and cathode (cf. fig. 8.50) can be observed. At cathode inlet, where the oxygen concentration remains high, $\Delta\varphi^{CCL}$ does not sink below 0.8 V, while at cathode outlet a potential of ≈ 0.5 V is reached during the air stop in this simulation. In the anode, the divergence in $\Delta\varphi^{ACL}$ along the channel starts later than in the reference case (after about 10 s), due to the lag in oxygen reduction at cathode outlet. Also in contrast to the reference, the divergence in $\Delta\varphi^{ACL}$ continues over the rest of the air stop period in case of an incomplete air stop. The local anode potential difference at anode inlet/cathode outlet sinks even lower than in the reference case, leading to an increased HER compared to the reference case in this segment.

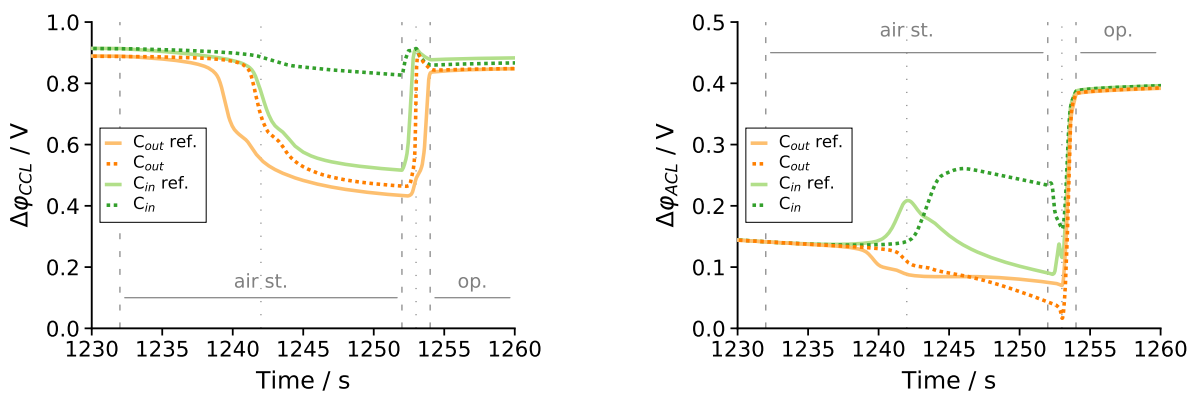


Figure 8.50: Local potential difference $\Delta\varphi$ in CCL (left) and ACL (right) in a refresh cycle with an incomplete air stop (dashed lines) compared to the reference (solid lines).

While at cathode outlet, where with some lag the concentration of O_2 and consequently the local potential difference sinks, both PtOx get reduced during the air stop period for this case. At cathode inlet, however, where the amount of oxygen remains high and the value of $\Delta\varphi^{CCL}$ does not sink below 0.8 V, no reduction of the PtOx-species can be achieved. The value of PtO, which directly affects the ECSA, remains constant at cathode inlet over the entire air stop period. This result confirms that the refresh is incomplete under the conditions described.

In the overall cell voltage, the incomplete refresh can be easily identified: Without oxygen depletion at cathode inlet, the cell voltage drop during air stop appears later and is much less pronounced compared to the normal refresh. The voltage overshoot when flow and current are resumed, on the other hand, shows a higher peak in case of an incomplete refresh.

When looking at the local cell voltage, a strong divergence of ≈ 200 mV between the cathode inlet and cathode outlet segment can be observed during the air stop period of the incomplete air stop (figure 8.52). In the transition phase, when flow and current are resumed, the voltage shoots up in all segments. This is in stark contrast to the ref-

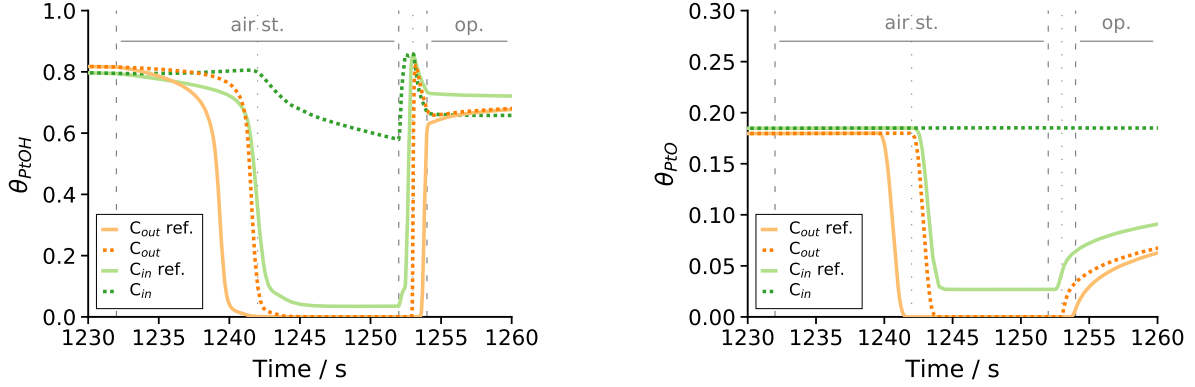


Figure 8.51: Catalyst surface coverage with PtOH (left) and PtO (right) during the refresh cycle simulated with an incomplete air stop (dashed lines) compared to the reference (solid lines).

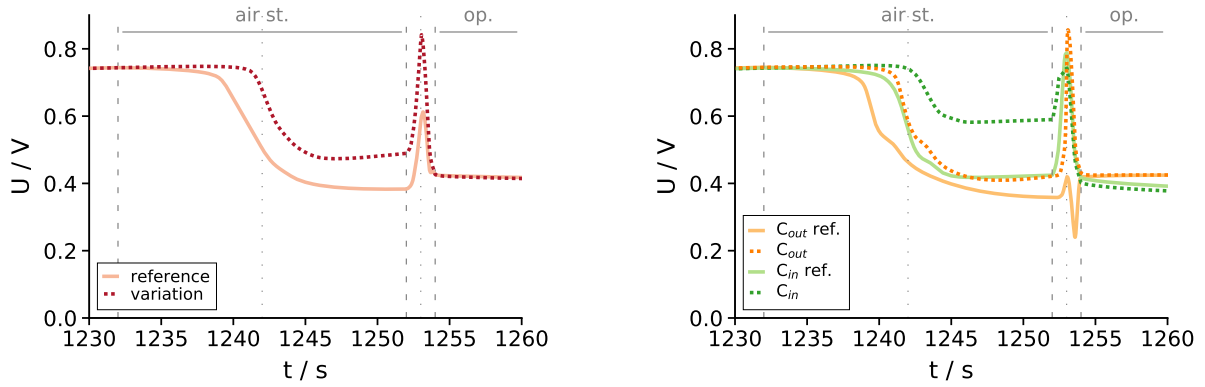


Figure 8.52: Overall cell voltage (left) and local cell voltage at cathode inlet and cathode outlet (right) during the refresh cycle with an incomplete air stop (dashed lines) compared to the the reference (solid lines).

erence simulation, where a dip in the local cell voltage can be observed during this period.

For the incomplete refresh, this behaviour can be explained by the different distribution of methanol and oxygen in the CCL. No methanol is present at cathode inlet after the air stop period, but a high amount of oxygen, and the oxygen concentration in the in-streaming air front is higher than in the reference case. Consequently, the oxidation of the accumulated methanol at cathode outlet happens much faster than in the reference simulation, and the effect of the accumulated methanol is not visible in the local cell voltage (cf. fig. 8.53).

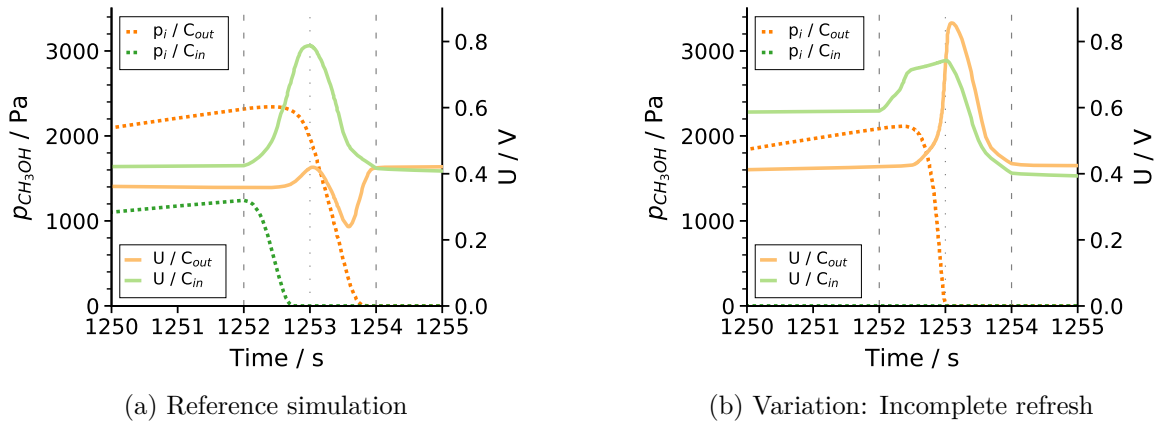


Figure 8.53: Development of p_{CH_3OH} in the CCL (dashed lines) and local cell voltage (solid lines) in the transition period to normal operation after the refresh cycle in (a) the reference simulation and (b) the variation with an incomplete refresh.

8.6.3 Variation 3: Optimised Air Stop Boundary Conditions

In the reference simulation, the oxygen level reached in the cathode inlet segment of the catalyst layer was not low enough to achieve a complete reduction of the PtOx-species during the air stop. That is why the simulation was repeated with an improved set of boundary conditions, where x_{O_2} at cathode inlet was continuously reduced during the entire air stop period (cf. tab. 8.2). This procedure mirrors the experimental conditions better, as the oxygen level at cathode inlet is supposed to sink continuously during air stop due to the limited reservoir of O_2 in the system (cf. Rabissi et al. [113]). The resulting BC-profile over time is shown in figure 8.44c.

These optimised boundary conditions lead to a lower oxygen level in the cathode inlet segment of the CCL during the air stop period in the simulation: a minimum value of $p_{O_2} \approx 1$ Pa is reached in S4 in the variation, compared to $p_{O_2} \approx 7$ Pa in the reference simulation. For methanol, a minor rise in p_{CH_3OH} could be observed under these conditions at cathode inlet (cf. fig 8.54) compared to the reference simulation. The species

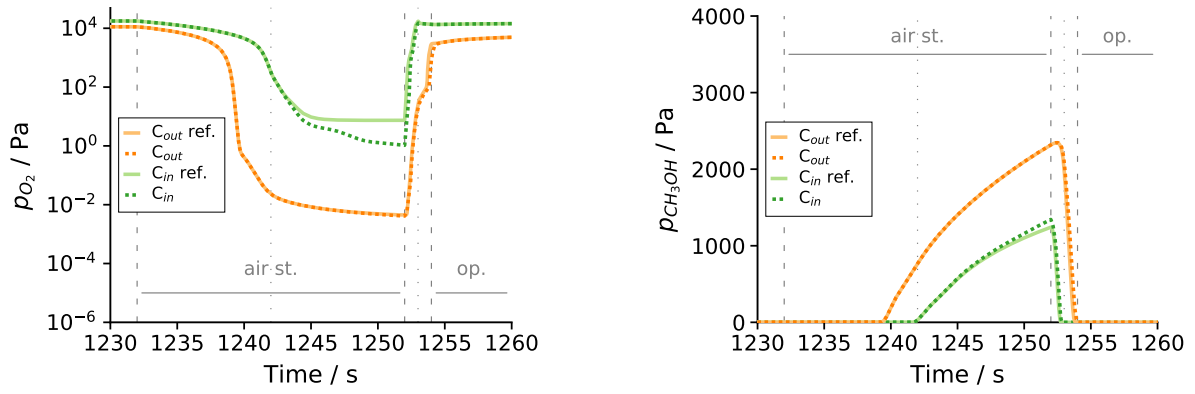


Figure 8.54: Partial pressures of oxygen (left) and methanol (right) during the refresh cycle simulated with optimised air stop boundary conditions (dashed lines) compared to the reference (solid lines).

concentrations at cathode outlet are not affected by the modified simulation BCs.

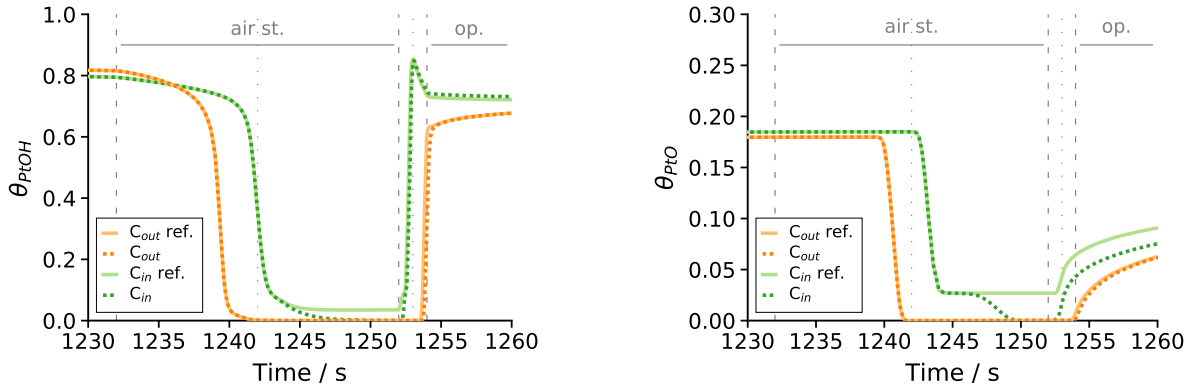


Figure 8.55: Catalyst surface coverage with PtOH (left) and PtO (right) during the refresh cycle simulated with optimised air stop boundary conditions (dashed lines) compared to the reference (solid lines).

With the reduced oxygen level at cathode inlet, a full reduction of both PtOx-species, PtOH and PtO, is achieved in the entire CCL during the refresh cycle (cf. figure 8.55). In the consecutive period of continuous operation, Θ_{PtO} at cathode inlet is lower compared to the reference simulation.

The potential differences $\Delta\varphi$ in anode and cathode obtained in the simulation with the optimised air stop BC are shown in figure 8.56. In the reference simulation, where a residual amount of oxygen remained at cathode inlet during the air stop period, $\Delta\varphi^{ACL}|_{A_{out}}$ was running towards $\Delta\varphi^{ACL}|_{A_{in}}$ in the course of the air stop. In contrast, with the lower amount of O_2 at cathode inlet in the simulation with the optimised air stop BC, the difference in $\Delta\varphi^{ACL}$ from anode inlet to anode outlet remains large until the end of the air stop period. The potential difference in the CCL, on the other hand, gets more

homogeneous along the channel in the course of the air stop simulation in this case.

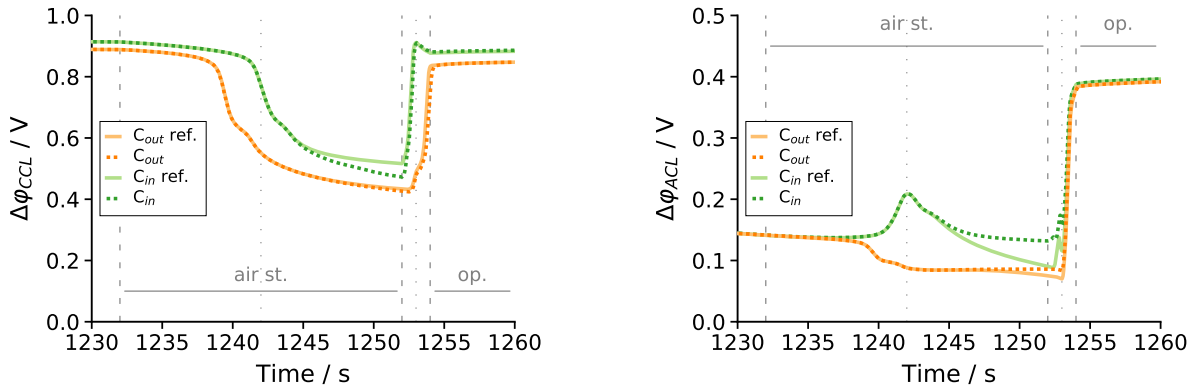


Figure 8.56: Local potential difference $\Delta\varphi$ in CCL (left) and ACL (right) during the refresh cycle simulated with optimised air stop boundary conditions (dashed lines) compared to the reference (solid lines).

The changes in the local conditions within the cell are also reflected by the global cell voltage, which shows a deviation from the reference for the second phase of the air stop period and the transition phase. The global cell voltage reaches a local minimum of $U = 0.34\text{ V}$ at the end of the air stop period. When the air flow is switched on, the rise in the cell voltage is lower compared to the reference simulation, and when the current is applied, a small dip in the cell voltage is visible. This behaviour can be explained when looking at the local processes within the cell.

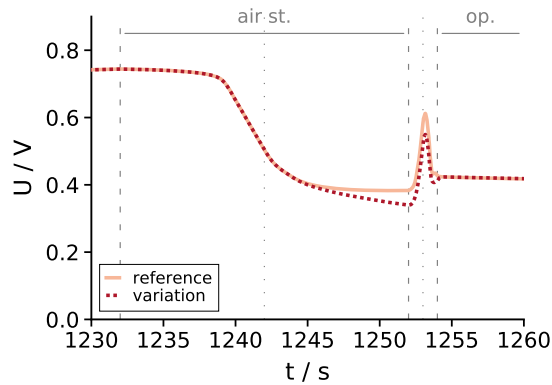


Figure 8.57: Cell voltage during the refresh cycle simulated with optimised air stop boundary conditions (dashed line) compared to the reference (solid line).

As figure 8.58 shows, in the simulation with optimised boundary conditions, the heterogeneities in the local cell voltage along the channel disappear in the second phase of the air stop period. The local cell voltage sinks to $U = 0.34\text{ V}$ in all segments, which is lower than the local potential in S1 (cathode outlet) reached in the reference simulation.

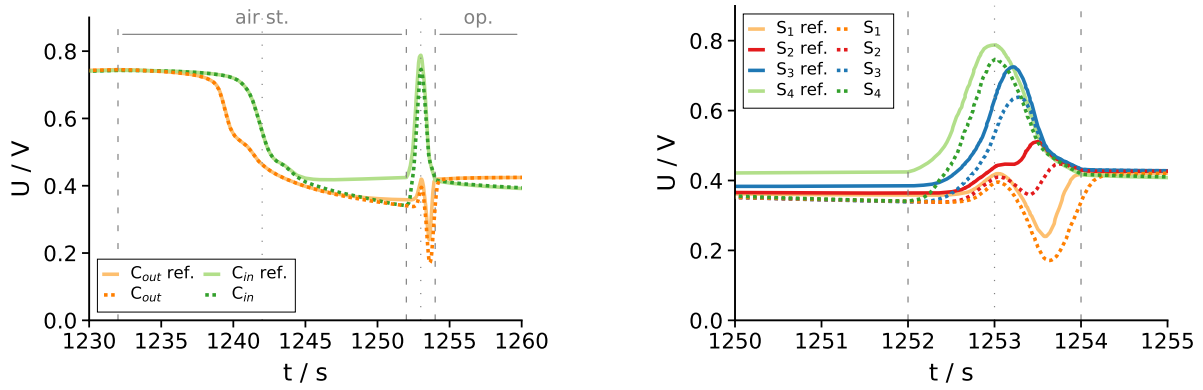


Figure 8.58: Local cell voltage over the full refresh cycle at cathode inlet and cathode outlet (left) and the transition period between air stop and normal operation in all four segments of the DMFC (right) simulated with optimised air stop boundary conditions (dashed lines) compared to the reference (solid lines).

After the air stop, when flow and current are resumed, the rise in the local potential occurs delayed in the simulation with the optimised BCs compared to the reference simulation. Moreover, in comparison to the reference, the peak in the cell voltage is less distinctive in the first two segments of the CCL (S_4 and S_3), whereas in the two cathode outlet segments, S_2 and S_1 , the plunge in the local cell voltage at the end of the transition period is more pronounced (fig. 8.58).

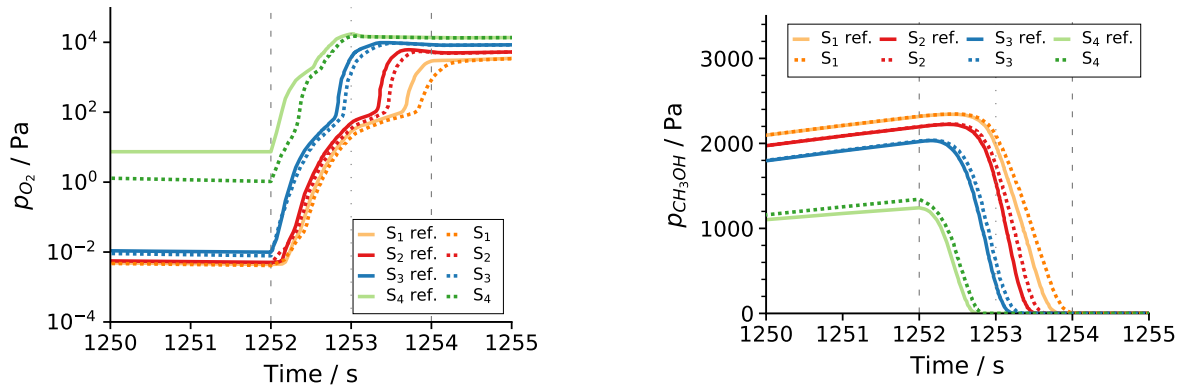


Figure 8.59: Partial pressures of O_2 (left) and CH_3OH (right) in all 4 segments of the CCL during the transition period between air stop and normal operation simulated with optimised air stop boundary conditions (dashed lines) compared to the reference (solid lines).

As described in section 8.5.3, the dip the local cell voltage at cathode outlet results from the reaction of the in-streaming oxygen with the accumulated methanol. In the simulation with optimised BC, it takes longer until the accumulated methanol in the CCL is oxidised by the inflowing air, as the profiles of the local CH_3OH and O_2 partial pressures in figure 8.59 show. Compared to the reference simulation, the methanol concentration

sinks with some delay in all segments in the simulation with the optimised BC. Simultaneously, also the rise in the oxygen concentration is slowed down. This leads to a shift in the reaction front and consequently a lagged and increased voltage spread during the transition period between air stop and normal operation.

The simulation with optimised air stop BCs was also repeated *without* segmentation of the BPP (results not shown here). The differences between the two simulations were just as described for the reference simulation (see section 8.5.9) and thus negligible for the cathode processes, meaning that the results discussed here for the optimised BCs are transferable to a cell without BPP segmentation.

All in all, the simulation results obtained with the optimised air stop boundary conditions are believed to most accurately describe the processes in the DMFC during the refresh cycle.

8.6.4 Variation 4: Nitrogen Flush

Another way to achieve fully oxygen-depleted conditions in the CCL during the refresh cycle is to flush the cathode with nitrogen instead of stopping the air flow. In the model, this is converted by switching the gas composition at the DMFC cathode inlet to $x_{\text{O}_2} = 0\%$. The concentration profiles in the CCL resulting from the simulation of a N_2 -flush during the air stop period are shown in figure 8.60 in comparison with the reference refresh simulation.

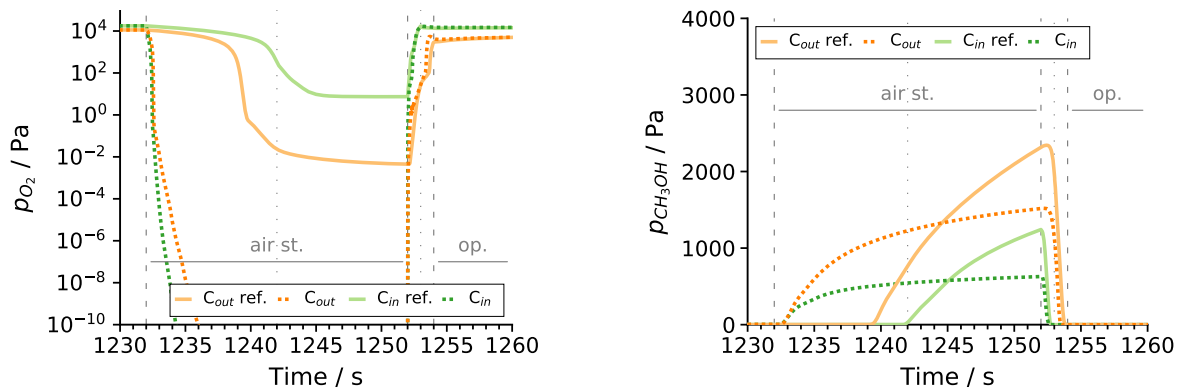


Figure 8.60: Partial pressures of O_2 (left) and CH_3OH (right) during the refresh cycle simulated with a nitrogen flush (dashed lines) compared to the reference (solid lines).

In case of a nitrogen flush, the oxygen in the CCL gets immediately purged in all segments. Already after 1 s, basically no oxygen is present in the catalyst layer any more, neither at cathode inlet nor at cathode outlet. Note that in contrast to all other air stop scenarios, here the oxygen depletion starts at cathode inlet.

The immediate reduction of oxygen also changes the accumulation behaviour of crossover methanol, as can be seen in figure 8.60. Methanol accumulation in the CCL starts already after 1 s, as soon as the oxygen is displaced in the CCL. Despite a continuous rise in the amount of methanol in all segments, $p_{\text{CH}_3\text{OH}}$ remains lower than in case of a regular air stop. This is a consequence of the continuing N_2 -flow in the cathode channel, which leads a dilution of the gas phase with nitrogen.

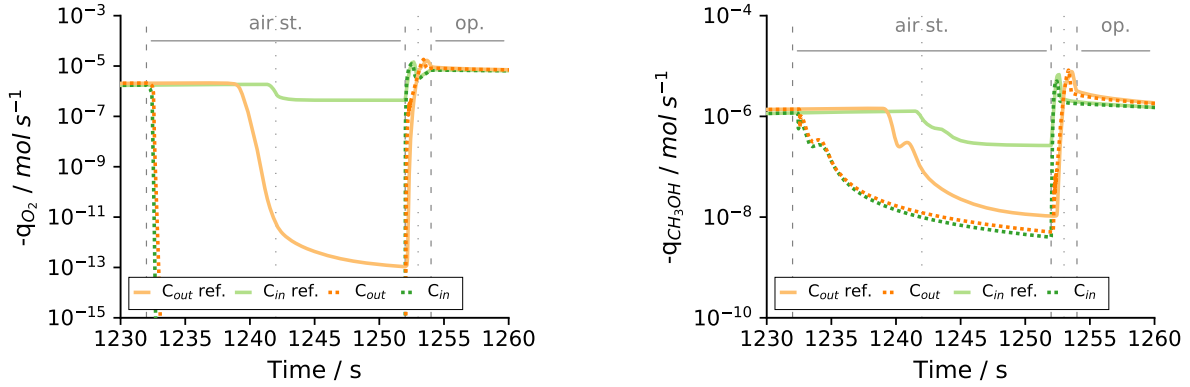


Figure 8.61: Reaction rates for O_2 (left) and CH_3OH (right) during the refresh cycle simulated with a nitrogen flush (dashed lines) compared to the reference (solid lines).

Due to the complete purge of oxygen in the CCL, the ORR and the primary MOR comes to halt in all segments of the CCL (cf. fig. 8.61). Only the secondary MOR goes on during the air stop period, but the reaction rate is low. With basically no electrochemical activity in the CCL, the potential differences $\Delta\varphi^{\text{CCL}}$ and $\Delta\varphi^{\text{ACL}}$ become very homogeneous, as figure 8.62 shows. $\Delta\varphi^{\text{CCL}}$ sinks down much earlier in case of the flush with N_2 compared to the regular air stop with the gradual oxygen depletion. Moreover, slightly lower potentials are reached. The characteristic profile in $\Delta\varphi^{\text{ACL}}$ with the peak at cathode inlet/anode outlet and the dip at cathode outlet/anode inlet disappears in case of the nitrogen flush. As a consequence, no HER is triggered in the DMFC anode.

The platinum oxide species PtOH and PtO get completely reduced in all segments of the CCL under the conditions imposed by the nitrogen flush in DMFC cathode (cf. fig. 8.63). When the cell starts operating under nominal conditions again, ϑ_{PtO} is visibly lower at cathode inlet than in case of the reference simulation, where no full reduction of PtO took place in this segment.

As expected from the local results, the global cell voltage sinks down very quickly during the air stop sequence in case of the N_2 -flush (figure 8.64). The peak in the cell voltage during the transition phase between air stop and normal operation is just as in the reference simulation. Interestingly, the cell voltage is a little lower during the beginning of the next phase of continuous operation compared to the reference simulation, despite the complete reduction of the PtOx -species in case of the N_2 -flush during the air stop period. The difference evens out after a few minutes of operation with $i = 0.25 \text{ A/cm}^2$.

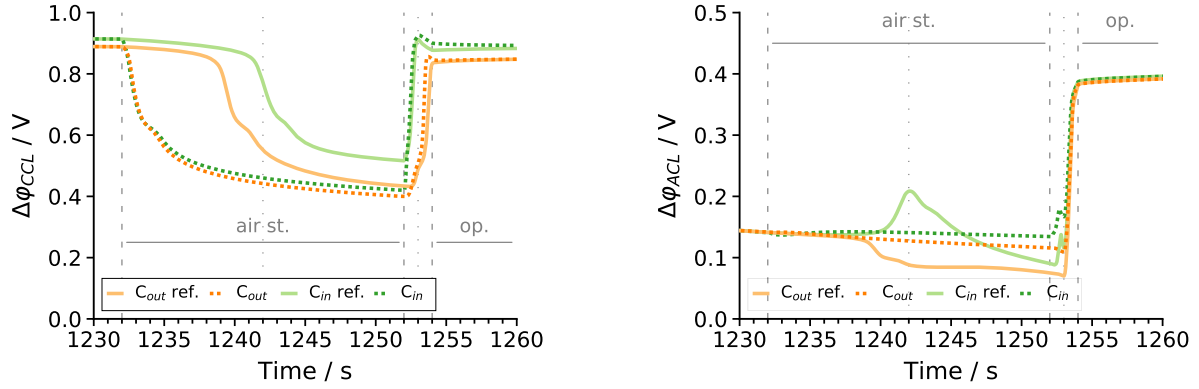


Figure 8.62: Local potential difference $\Delta\varphi$ in CCL (left) and ACL (right) during the refresh cycle simulated with a nitrogen flush (dashed lines) compared to the reference (solid lines).

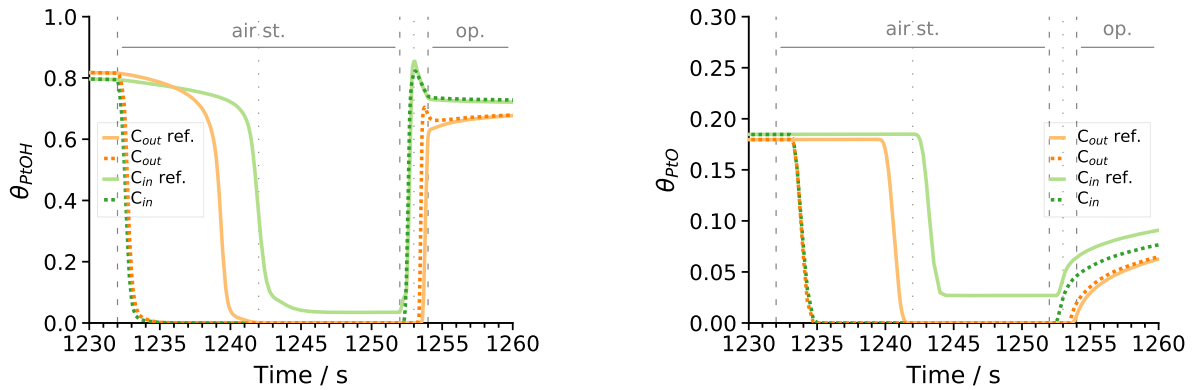


Figure 8.63: Catalyst surface coverage with PtOH (left) and PtO (right) during the refresh cycle simulated with a nitrogen flush (dashed lines) compared to the reference (solid lines).

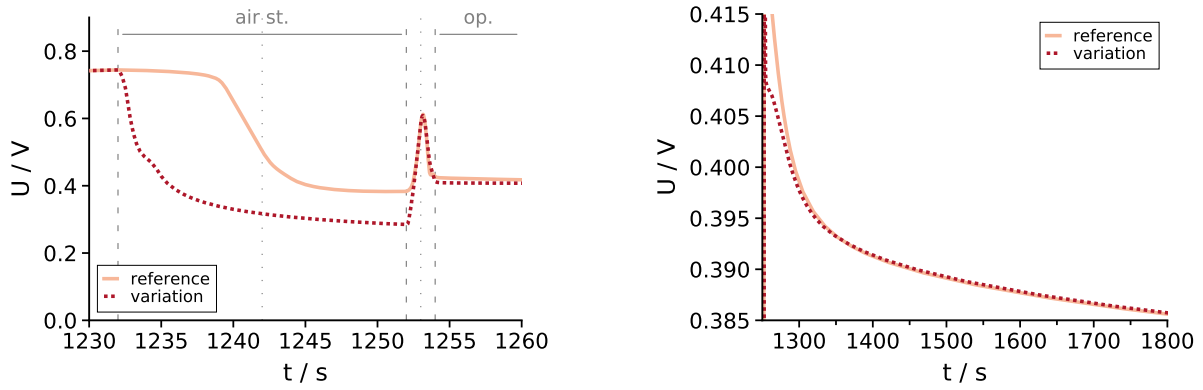


Figure 8.64: Cell voltage during the refresh cycle (left) and *after* the refresh cycle at operation with $i = 0.25 \text{ A/cm}^2$ (right) for the simulation with a nitrogen flush (dashed lines) compared to the reference air stop (solid lines).

This phenomenon can be explained when comparing the local humidity conditions in the CCL, as shown in figure 8.65: In case of the reference simulation with a regular air stop, the water activity in the cathode inlet segment of the CCL rises strongly during the air stop period, until the CCL is almost fully humidified over the cell length. During the next phase of normal operation the level of humidification in S4 sinks down to its steady state value to $a_{\text{H}_2\text{O}} \approx 0.6$.

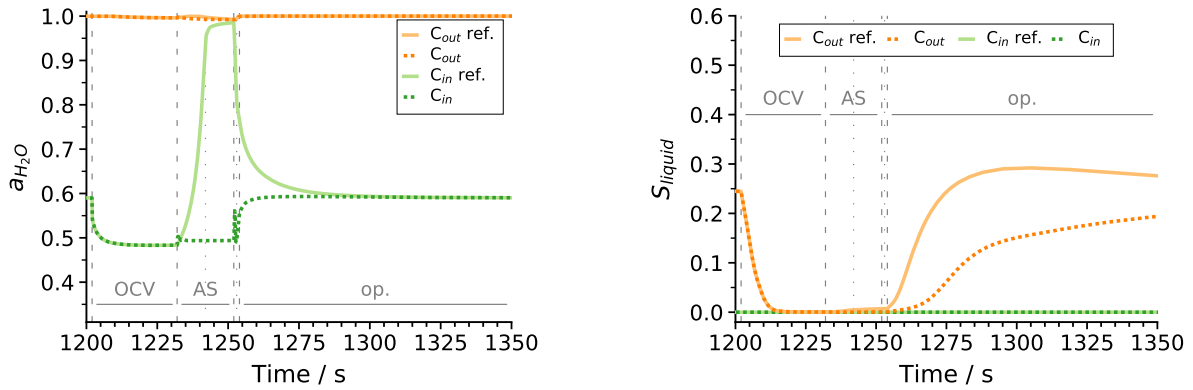


Figure 8.65: Local water activity (left) and liquid saturation in the CCL (right) during the refresh cycle simulated with a nitrogen flush (dashed lines) compared to the reference (solid lines).

In case of the N_2 -flush, however, the CCL in the cathode inlet segment of the DMFC does not get humidified during the air stop period. In addition to the ongoing flow, the missing ORR and MOR, which would produce water, contribute to this behaviour. The relative humidity in the CCL remains low at about 49% at cathode inlet in this case. Also the liquid water saturation in the CCL is strongly affected by the nitrogen flush (cf. fig. 8.64): During the refresh cycle, the liquid water at cathode outlet gets fully purged by the nitrogen stream, while during the regular air stop with no flow through the DMFC cathode, some liquid water forms at cathode outlet at the end of the air stop

period. The N₂-flush not only inhibits the humidification of the CCL, but also keeps the water content of the membrane low.

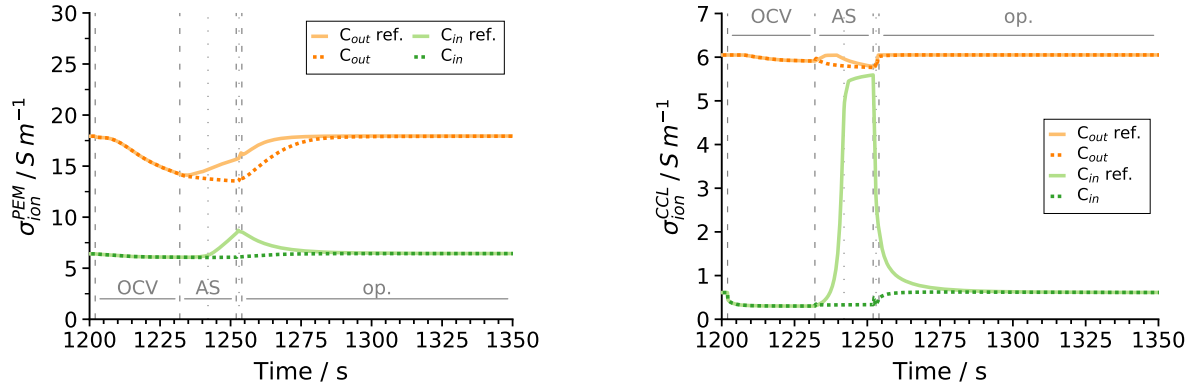


Figure 8.66: Ionic conductivity of PEM (left) and CCL ionomer (right) during the re-fresh cycle simulated with a nitrogen flush (dashed lines) compared to the reference (solid lines).

The ionic conductivity of the ionomer phase in catalyst and membrane are directly affected by the low humidity level in the CCL in case of a nitrogen flush, as figure 8.66 shows. While in a refresh cycle with a regular air stop the ionic conductivity in PEM and CCL ionomer increases, especially at the dry cathode inlet, it remains low in case the cell is flushed with N₂. In the subsequent period of operation at $i = 0.25 \text{ A/cm}^2$, it takes almost 50s until the water content in the cell and as a result the ionic conductivity in the ionomer phases have reached their steady-state values again.

In the first two minutes after the air stop period, the humidity related phenomena outweigh the effect of the fully reduced PtOx-species on the overall cell performance, as the comparison between the voltage profiles of the reference simulation and the simulation with the N₂-flush shows (fig. 8.64). On the long run, however, the cell treated with the nitrogen flush performs slightly better compared to the reference, due to the full reduction of PtO in the entire CCL.

8.6.5 Conclusion: Variation of Air Stop Scenarios

Different air stop scenarios for the DMFC refresh cycle were simulated with the transient DMFC model and analysed in detail: a longer air stop duration, an incomplete air stop, an optimised air stop, and a nitrogen flush.

The first variant, an extension of the air stop duration by 10s, explained the effect of methanol accumulation during the refresh cycle. With the longer duration of the air stop, a larger amount of methanol accumulates in the cathode outlet segment of the CCL. In the transition period between air stop and operation, the inflowing air creates a stronger peak in the methanol oxidation reaction compared to the reference. In addition to that,

it takes longer until the accumulated methanol has reacted. As a result, a stronger divergence in the local potential can be observed along the channel, which is even visible as a dip in the global cell voltage. This voltage dip after the refresh cycle can also be noticed in the experiments.

In case the air stop is incomplete, i. e. the oxygen concentration remains too high in the cathode inlet area of the CCL, methanol does not accumulate in the entire cell, but only at cathode outlet. The different reactant availability leads to strong divergences in the anode and cathode local potential difference. The PtOx-species at the inlet area of the cathode catalyst layer hardly get reduced in this case.

In contrast, with the optimised simulation air stop boundary conditions which resulted in a lower oxygen concentration at cathode inlet it was possible to simulate a refresh cycle where the PtOx-species get fully reduced during the air stop phase. The homogeneous species distribution in the CCL also has an effect on the potential difference between ACL and membrane, which becomes more uniform during the end of the air stop period.

The last variant tested with the model was actively flushing the cell with nitrogen instead of stopping the air flow, which leads to a very different cell behaviour: the continuous stream of nitrogen purges the oxygen from the cathode catalyst layer and leads to an instant potential drop, which occurs homogeneously along the channel. As a result, both PtOx species get fully reduced over the entire length of the catalyst layer. The continuous N₂-flow in the cathode channel results also in a lower amount of methanol accumulating in the CCL and prevents the humidification of the cathode inlet area during the air stop period.

9 Summary

In this work, a transient multiphase DMFC model in 2D has been developed with the aim to describe the physical processes inside a DMFC single cell with a focus on performance heterogeneities along the channel. The model featured the spatial discretisation of the ACL and CCL, which proved essential for the investigation of local inhomogeneities in the cell as well as for understanding transient phenomena during the recovery of reversible cathode degradation.

The model has been thoroughly validated against experimental performance data from a macro-segmented cell, which also included impedance spectra as well as the overall methanol and water crossover. The local resolution of the cell performance helped to verify the modelling of physical processes for mass and charge transport on the global as well as on the local scale. Such a locally resolved model validation can hardly be found in literature.

A very good agreement of the model prediction with the experimental data regarding humidity-related phenomena inside the DMFC cathode as well as general mass transport phenomena and their effect on the cell performance under various operating conditions has been achieved with just one set of model parameters.

The simulation study has highlighted the complex interplay of gas and liquid phase inside the DMFC and its impact on material properties and transport processes inside the cell. Furthermore, the importance of interface processes at the PEM boundaries to the catalyst layers as well as *inside* the catalyst layer on the local cell behaviour could be shown.

For the species transport inside the compositional fuel cell structure, the formation and presence of liquid water plays a dominant role. It could be shown that phase-dependent sorption processes at the DMFC membrane interface fundamentally determine the water transfer from anode to cathode and consequently the distribution of liquid water inside the cell.

The impact of the individual humidity-related transport mechanisms has been evaluated step by step in this work. The ionomer phases in the cell, i.e the bulk membrane as well as the ionomer thin-film in the CL, proved to be highly sensitive to the local water activity and phase conditions and exhibit a strong resistance to proton transport in the areas of the DMFC with poor humidification.

Mass transport resistances in the heterogeneous CL microstructure due to liquid water accumulation could be successfully modelled on the continuum scale by integrating an ionomer-film model.

The validated cell model also proved fit to describe the transient processes within the cell during the recovery of reversible cathode degradation during a refresh cycle. Without any adjustments in the model, the dynamics in the local potential for electrons and ions as well as in the membrane in dependence on the conditions inside the DMFC were predicted with a very good accuracy in anode and cathode.

With its spatial resolution of the CCL, the model rendered a visualisation of the heterogeneous distribution of species and reactions in the course of the refresh sequence. Also the local formation of H_2 in the DMFC anode during the absence of oxygen in the CCL could be successfully described with the model.

The simulation study showed that the methanol crossover through the DMFC membrane and the resulting methanol oxidation reactions in the CCL play an essential role during the refresh cycle. Especially the secondary, H_2O -activated MOR reaction path in the CCL under oxygen-depleted conditions was identified as relevant for the achievement of low local potentials in the DMFC cathode and thus for the full recovery of the cathode ECSA during the air break.

A variation of air stop scenarios was simulated with the model and the impact of the local species distribution on the electrochemical processes within the cell was studied. The variations included settings where the PtOx-surface species in the CCL would get entirely or only partially reduced.

In a simulation of a longer air stop, the effect of methanol accumulation during the air stop period could be visualised and its impact on the heterogeneities in the local cell voltage could be explained. Also the processes during an incomplete air stop, where oxygen is only partially depleted in the cathode catalyst layer, could be shown with the model.

Two air stop variants resulting in a full recovery of the cathode ECSA were identified and examined. The simulation showed that while a flush with pure nitrogen on the one hand swiftly enables a full reduction of the platinum oxides in the CCL, it on the other hand limits the re-humidification of the membrane. By improving the model's refresh boundary conditions, i.e. further limiting the diffusion of oxygen into the cell from external during the air stop period (and thus presumably approximating the experimental conditions more closely), the best results in terms of platinum oxide reduction and ionomer rehydration were achieved.

List of Tables

5.1	Geometrical Parameters	44
5.2	Grid Parameters: Number of cells per layer.	45
5.3	Grading Factors used in NEOPARD-X's grid creator.	46
5.4	Initial Conditions (IC) and Boundary Conditions (BC) in the electrodes.	52
5.5	Initial Conditions (IC) and Coupling Conditions (CC) in the PEM.	52
6.1	Spatial parameters of the porous layers.	55
6.2	Parameters for the $p_c S_w$ -relation.	56
6.3	Water sorption isotherm parameters.	60
6.4	Water sorption kinetic parameters.	61
6.5	Thermodynamic properties of reactants at reference condition	66
6.6	Kinetic parameters for reaction rate calculation.	68
6.7	Parameters for ECSA calculation.	69
6.8	Parameters for ionomer film model.	70
8.1	Operating scheme for standard refresh simulation.	114
8.2	Operating conditions of air stop variations.	144

List of Figures

2.1	Schematic of the DMFC.	17
5.1	The modelling domain.	42
5.2	Model Geometry (not drawn to scale). The layers of the anode sub-domain are shown in red, the layers of the cathode sub-domain in green, and the PEM sub-domain is coloured in blue. The measures for the individual lengths and widths are given in table 5.1. The grid structure can be found in section 5.5.	43
5.3	Grid structure of the 2D DMFC model.	46
5.4	The model boundaries. The boundary conditions applied at the anode boundaries (red dashes) and cathode boundaries (green dashes) are described in section 5.6. No-flow Neumann conditions apply at the boundaries marked with the narrowly dashed lines in grey for all variables. . . .	47
5.5	Coupling interfaces between the model sub-domains. The respective coupling conditions are described in section 5.7.	48
6.1	Capillary pressure-saturation relations for the different porous layers in the DMFC model obtained with eq. 6.10 and the parameters of tab. 6.2. . . .	56
7.1	Segmentation scheme of the modelling domain.	73
7.2	Experimental data: Water flux rate $\dot{N}_{\text{H}_2\text{O}}^{\text{out}}$ measured at the cathode outlet of the cell (given per channel area) for RH 10 % and RH 50 %.	74
7.3	Water crossover fluxes per cell area $\dot{n}_{\text{cross}}^{\text{H}_2\text{O}}$ for RH 10 % and RH 50 %, determined from the experimental data on $\dot{N}_{\text{H}_2\text{O}}^{\text{out}}$	75
7.4	Membrane water content $\lambda_{\text{H}_2\text{O}}$ at operation with RH 10 % at OCV, 0.1 A/cm ² and 0.25 A/cm ² (reference simulation). The 2D plot shows the PEM magnified by 10 ³ in x-direction.	76
7.5	Membrane water content $\lambda_{\text{H}_2\text{O}}$ at operation with RH 50 % at OCV, 0.1 A/cm ² and 0.25 A/cm ² (reference simulation). The 2D plot shows the PEM magnified by 10 ³ in x-direction.	77
7.6	Simulated water crossover flux $\dot{n}_{\text{cross}}^{\text{H}_2\text{O}}$ by diffusion only in comparison to the experimental data (RH 10 %).	77
7.7	Simulated water crossover flux $\dot{n}_{\text{cross}}^{\text{H}_2\text{O}}$ by diffusion and electro-osmotic drag with a drag coefficient of $\kappa_{\text{drag}} = 2.5 \cdot \lambda_{\text{H}_2\text{O}}/22$ in comparison to the experimental data.	78
7.8	Simulated water crossover $\dot{n}_{\text{cross}}^{\text{H}_2\text{O}}$ for RH 10 % and RH 50 % by diffusion and electro-osmotic drag with a drag coefficient of $\kappa_{\text{drag}}^{\text{H}_2\text{O}} = 0.325$ in comparison to the experimental data (reference simulation).	79

7.9	Simulated water crossover flux $\dot{n}_{cross}^{H_2O}$ with and without permeative water transport included in the PEM model in comparison to the experimental data.	80
7.10	Membrane water content λ_{H_2O} in a simulation <i>without</i> sorption kinetics at the PEM/CL interfaces for RH 10 % at OCV, 0.1 A/cm ² and 0.25 A/cm ² (compare with fig. 7.4 for the reference simulation <i>with</i> sorption kinetics). The 2D plot shows the PEM magnified by 10 ³ in x-direction.	81
7.11	Water crossover through the membrane in the simulation <i>without</i> sorption kinetics at the PEM/CL interfaces for RH 10 % and RH 50 % in comparison to the experimental data.	82
7.12	Overall water crossover through the membrane in blue and membrane water content λ_{H_2O} at the PEM/CCL interface in S1 (cathode outlet) in orange in simulation <i>without</i> sorption kinetics (RH 10 %).	83
7.13	Simulation results for water flux at cathode outlet a) <i>without</i> sorption kinetics and b) <i>with</i> sorption kinetics (reference simulation) at the PEM/CL interfaces RH 10 % and RH 50 %) in comparison to the experimental data.	84
7.14	Total water crossover rate $\dot{n}_{cross}^{H_2O}$ for RH 10 % (left) and RH 50 % (right) from experiment and simulation in comparison to the <i>local</i> water crossover rates in the first and last segment of the cell (reference simulation). Note that the local crossover rates are plotted against the local current density.	84
7.15	Total and local water crossover rates $\dot{n}_{cross}^{H_2O}$ of the reference simulation (solid lines) and a variation <i>without</i> electro-osmotic drag (“diffusion only”, dashed lines) in comparison to the experimental data (RH 10 %). Note that the local crossover rates are plotted against the local current density.	85
7.16	Nyquist plots obtained in simulations for $i = 0.1$ A/cm ² at RH 10 % with σ_{ion}^{PEM} described by (a) the Springer model [133] and (b) the Weber model [146] in comparison to the experimental data.	86
7.17	Comparison of the three discussed empirical relations for the membrane’s ionic conductivity σ_{ion} as a function λ_{H_2O} at $T = 348.15$ K.	87
7.18	Nyquist plots obtained from the <i>reference simulation</i> with σ_{ion}^{PEM} described by eq. 6.44 for RH 10 % at 0.1 A/cm ² (left) and 0.25 A/cm ² (right) in comparison to the experimental data.	87
7.19	Nyquist plots obtained from the <i>reference simulation</i> with σ_{ion}^{PEM} described by eq. 6.44 for RH 50 % at 0.1 A/cm ² (left) and 0.25 A/cm ² (right) in comparison to the experimental data.	88
7.20	Methanol molar concentration C_{MeOH}^n in the membrane at operation with RH 10 % for OCV, 0.1 A/cm ² and 0.25 A/cm ² (reference simulation). The 2D plot shows the PEM magnified by 10 ³ in x-direction.	88
7.21	Experimental data: Methanol crossover rates for RH 10 % and RH 50 %.	89
7.22	Simulated methanol crossover rates \dot{n}_{cross}^{MeOH} for RH 10 % and RH 50 % (reference simulation) in comparison to the experimental data.	89

7.23	Total methanol crossover \dot{n}_{cross}^{MeOH} for RH 10 % and RH 50 % from experiment and simulation in comparison to the <i>local</i> methanol crossover rates in the first and last segment of the cell (left) and corresponding local methanol concentrations C_{MeOH}^{ACL} in the ACL (right). Note that the local properties are plotted against the local current density. Reference Simulation.	90
7.24	Experimental data: Total cell voltage and local cell voltage in S1 (cathode outlet/anode inlet) and S4 (cathode inlet/anode outlet) for RH 10 % and RH 50 %. Note that the local cell voltages are plotted against the local current densities in the respective segment.	92
7.25	Simulation result for the total cell voltage (left) and the local cell voltages (right) at the cathode inlet and cathode outlet segment of the DMFC obtained with model including only the membrane-related resistances to charge and species transport as discussed in section 7.1 in comparison to the experimental data (RH 10 %).	93
7.26	Local water activity a_{H_2O} in the cathode inlet and cathode outlet segment of the CCL during operation with RH 10 % and RH 50 % (reference simulation).	94
7.27	Ionic conductivity of Nafion thin-films as presented by Paul et al. [105] (blue symbols) and own empirical relation for σ_{ion}^{CL} (eq. 6.27) (red line).	95
7.28	Simulation result for the local cell voltages at the cathode inlet and cathode outlet segment of the DMFC obtained with model including the membrane-resistances to charge and species transport as discussed in section 7.1 and the resistance to proton transport in the CCL with $\sigma_{ion}^{CL} = f(a_{H_2O})$ (cf. eq. 6.27) for RH 10 % and RH 50 % in comparison to the experimental data.	96
7.29	Liquid saturation in the cathode inlet and cathode outlet segment of the CCL during operation with RH 10 % and RH 50 % (reference simulation).	97
7.30	Liquid saturation in the cathode inlet and cathode outlet segment of the CCL (left) and resulting local cell performances (right) in the simulation in case the ionomer film model (sec. 6.3.10) is deactivated.	98
7.31	Simulation result for the local cell performance of the DMFC's cathode inlet (green) and cathode outlet (orange) segment obtained with the reference model (including the ionomer film model in the ORR kinetics) for RH 10 % and RH 50 % in comparison to the experimental data.	99
7.32	Simulation with the reference model: Cell performance during operation with RH 10 % (left) and RH 50 % (right) in comparison to the experimental data.	100
7.33	Simulation with the reference model: Local cell performance in the DMFC's cathode inlet (green) and cathode outlet (orange) for RH 10 % (left) and RH 50 % (right) in comparison to the experimental data.	100
7.34	Simulation with the reference model: Water flux rate at cathode outlet during operation with RH 10 % (left) and RH 50 % (right) in comparison to the experimental data.	101

7.35	Simulation with the reference model: Methanol crossover rates \dot{n}_{cross}^{MeOH} for RH 10 % (left) and RH 50 % (right) in comparison to the experimental data.	101
7.36	Simulation with the reference model: Water flux at cathode outlet (left) and methanol crossover rate (right) for $\lambda_A = \lambda_C = 3$ at RH 10%.	102
7.37	Simulation with the reference model: Overall cell performance (left) and local cell performance (right) for a stoichiometry of $\lambda_A = \lambda_C = 3$ at RH 10%.	103
7.38	Simulation with the reference model: Overall cell performance (left) and local cell performance (right) for a stoichiometry of $\lambda_A = \lambda_C = 6$ at RH 10%.	103
7.39	Simulation with the reference model: Overall cell performance (left) and local cell performance (right) for a stoichiometry of $\lambda_A = \lambda_C = 6$ at RH 50%.	104
7.40	Simulation with the reference model: Water flux at cathode outlet (left) and methanol crossover rate (right) for $\lambda_A = \lambda_C = 6$ at RH 10%.	104
7.41	Simulation with the reference model: Water flux at cathode outlet (left) and methanol crossover rate (right) for $\lambda_A = \lambda_C = 6$ at RH 50%.	105
7.42	Comparison of the experimental methanol crossover rates for the different stoichiometry combinations for RH 10% (left) and RH 50% (right).	105
7.43	Simulation with the reference model: Impact of the operating mode (galvanostatic/potentiostatic) on the cell performance. Left: Total cell voltage. Right: Local cell voltages.	106
7.44	Simulation with the reference model: Impact of the operating mode (galvanostatic/potentiostatic) on the formation of liquid water in the CCL. .	107
7.45	Simulation with the reference model: Impact of the operating mode (galvanostatic/potentiostatic) on the local cell performances.	107
7.46	Simulation with the reference model: Impact of the BPP segmentation on the local cell performance.	108
8.1	Experimental Data: Voltage profile during a sequence of continuous operation interrupted by a refresh cycle. The figure on the right shows the cell voltage during the different stages of the refresh cycle in detail. . . .	111
8.2	Development of the cathode catalyst surface coverage with PtOH (left) and PtO (right) at cathode inlet and cathode outlet during the period of continuous operation with $i = 0.25 \text{ A/cm}^2$	112
8.3	Distribution of surface coverage with PtOx-species in the CCL after 20 minutes of operation with $i = 0.25 \text{ A/cm}^2$ simulated with the transient DMFC model. The 2D plot shows the CCL magnified by 10^4 in x-direction.	113
8.4	ECSA within the CCL at different stages of the continuous operation with $i = 0.25 \text{ A/cm}^2$ simulated with the transient DMFC model. The 2D plot shows the CCL magnified by 10^4 in x-direction.	113
8.5	Cathode boundary conditions for the oxygen concentration x_{O_2} , the air flow \dot{N}_{Air} and the current density i in the standard refresh simulation (cf. tab. 8.1).	115
8.6	Experimental data (dashed lines) and simulation result (solid lines): Cell voltage profile in the course of a full sequence of continuous operation and refresh cycle	116

8.7	Experimental data (dashed lines, left) and simulation result (solid lines, right): Detailed cell voltage profile during the refresh cycle.	116
8.8	Refresh Simulation: Liquid saturation (left) and oxygen partial pressure (right) in the CCL during the transition from operation at 0.25 A/cm ² to OCV.	117
8.9	Refresh Simulation: Local methanol concentration in the ACL during the transition from operation at 0.25 A/cm ² to OCV with 0.0 A/cm ² (left) and development of the cell voltage (right).	118
8.10	Refresh Simulation: Development of the cell voltage in simulation and experiment during the air stop phase.	118
8.11	Model convergence (left) and corresponding cell voltage profile (right) during the refresh simulation <i>with</i> and <i>without</i> the ionomer film resistances included in the DMFC model (dashed blue line vs. red line).	120
8.12	Oxygen partial pressure p_{O_2} in the CCL at cathode inlet and cathode outlet during the refresh cycle. The profiles are shown in a linear scale (left) and a logarithmic scale (right).	121
8.13	Oxygen partial pressure p_{O_2} within the CCL at different stages of the refresh cycle simulated with the transient DMFC model. The 2D plot shows the CCL magnified in x-direction by 10^4 and p_{O_2} on a logarithmic scale.	121
8.14	Methanol partial pressure p_{CH_3OH} in the CCL at cathode inlet and cathode outlet during the refresh cycle. The profiles are shown in a linear scale (left) and in a logarithmic scale (right).	122
8.15	Methanol partial pressure p_{CH_3OH} within the CCL at different stages of the refresh cycle simulated with the transient DMFC model. The 2D plot shows the CCL magnified by 10^4 in x-direction.	123
8.16	Oxygen reaction rate r_{ORR} within the CCL at different stages of the refresh cycle simulated with the transient DMFC model. The 2D plot shows the CCL magnified in x-direction by 10^4 and r_{ORR} on a logarithmic scale.	123
8.17	Primary methanol oxidation reaction rate r_{MOR} within the CCL at different stages of the refresh cycle simulated with the transient DMFC model. The 2D plot shows the CCL magnified in x-direction by 10^4 and r_{MOR} on a logarithmic scale.	124
8.18	Secondary methanol oxidation reaction rate r_{MOR_2} within the CCL at different stages of the refresh cycle simulated with the transient DMFC model. The 2D plot shows the CCL magnified in x-direction by 10^4 and r_{MOR_2} on a logarithmic scale.	124
8.19	Development of the <i>local</i> cell voltage at cathode inlet and cathode outlet during the refresh cycle in comparison to the total cell voltage. Left: full refresh sequence, right: zoom to air stop and transition phase.	125
8.20	Local potential difference $\Delta\varphi_{CCL}$ in the CCL at cathode inlet and cathode outlet during the refresh cycle.	126
8.21	Cathode catalyst surface coverage with PtOH (left) and PtO (right) at cathode inlet and cathode outlet during the refresh cycle.	127

8.22	Catalyst surface coverage with PtOH in the CCL at different stages of the refresh cycle simulated with the transient DMFC model. The 2D plot shows the CCL magnified by 10^4 in x-direction.	127
8.23	Catalyst surface coverage with PtO in the CCL at different stages of the refresh cycle simulated with the transient DMFC model. The 2D plot shows the CCL by 10^4 magnified in x-direction.	128
8.24	ECSA of the CCL at different stages of the refresh cycle simulated with the transient DMFC model. The 2D plot shows the CCL magnified by 10^4 in x-direction.	128
8.25	Local potential difference $\Delta\varphi_{ACL}$ (left) and hydrogen source q_{H_2} (right) in the ACL in the first (cathode outlet/anode inlet) and last (cathode inlet/anode outlet) segment of the cell during the refresh cycle.	129
8.26	<i>In-plane</i> electric current in the CCL during the air stop phase of the refresh sequence. The 2D plot shows the CCL magnified by 2000 in x-direction at different time steps.	129
8.27	Profile of the local ionic current density (left) and the anode potential difference $\Delta\varphi_{ACL}$ (right) in all four segments of the cell (S1-S4) during the air stop period of the refresh cycle.	131
8.28	Profile of the hydrogen source q_{H_2} (left) and the hydrogen partial pressure p_{H_2} (right) in the ACL in all four segments of the cell (S1-S4) during the air stop period of the refresh cycle.	132
8.29	Development of the liquid saturation S_l (left) and the water activity a_{H_2O} (right) in the CCL at cathode inlet and cathode outlet during the refresh cycle.	133
8.30	Total cell voltage (left) and local cell voltage of the cathode inlet and cathode outlet segment of the cell (right) during the refresh cycle. The plots show the result of the reference simulation including both MOR reactions in the CCL (solid lines) in comparison with the variation <i>without</i> the secondary MOR in the model(dashed lines).	133
8.31	Oxygen sink (left) and methanol sink (right) in the cathode inlet and cathode outlet segment of the CCL during the refresh cycle (logarithmic scale). Comparison between reference simulation <i>with</i> secondary MOR (solid lines) and variation <i>without</i> secondary MOR (dashed lines). . . .	134
8.32	Local potential differences $\Delta\varphi_{CCL}$ (a) and $\Delta\varphi_{ACL}$ (b) in the cathode inlet and cathode outlet segment of the cell during the refresh cycle. Comparison between the reference simulation <i>with</i> secondary MOR (solid lines) and the variation <i>without</i> secondary MOR (dashed lines).	135
8.33	Catalyst surface coverage coverage with PtOH (left) and PtO (right) in the cathode inlet and cathode outlet segment of the cell during the refresh cycle. Comparison between the reference simulation <i>with</i> secondary MOR (solid lines) and the variation <i>without</i> secondary MOR (dashed lines). . .	135
8.34	Cell voltage during the refresh cycle simulated with the reference model (solid line) compared to the variation with the accelerated secondary MOR kinetics (dashed line).	136

8.35	Overall cell voltage (left) and local cell voltage of the cathode inlet and cathode outlet segment of the cell (right) during the refresh cycle. Plots show the reference simulation <i>with</i> BPP segmentation (solid lines) in comparison with the variation <i>without</i> BPP segmentation in the model (dashed lines).	137
8.36	Local potential differences $\Delta\varphi_{CCL}$ (left) and $\Delta\varphi_{ACL}$ (right) in the cathode inlet and cathode outlet segment of the cell during the refresh cycle. Comparison between the reference simulation <i>with</i> BPP segmentation (solid lines) and the variation <i>without</i> BPP segmentation in the model (dashed lines).	138
8.37	Simulation <i>without</i> BPP segmentation in the model: <i>In-plane</i> electric current in the CCL during the air stop phase of the refresh sequence. The 2D plot shows the CCL magnified by 2000 in x-direction at different time steps.	138
8.38	Profile of the local ionic current density in all four segments of the cell (S1-S4) during the air stop period of the refresh cycle. Reference simulation <i>with</i> BPP segmentation (left) and variation <i>without</i> BPP segmentation in the model (right).	139
8.39	Profile of the anode potential difference $\Delta\varphi_{ACL}$ in all four segments of the cell during the air stop period of the refresh cycle. Reference simulation <i>with</i> BPP segmentation (left) and variation <i>without</i> BPP segmentation in the model (right).	140
8.40	Hydrogen source q_{H_2} in the ACL during the air stop period of the refresh cycle S1 (anode inlet/cathode outlet) and S4 (anode outlet/cathode inlet) in the reference simulation <i>with</i> BPP segmentation (left) and the variation <i>without</i> BPP segmentation in the model (right).	140
8.41	Profile of the hydrogen partial pressure p_{H_2} in the ACL in all four segments of the cell (S1-S4) during the air stop period of the refresh cycle in the reference simulation <i>with</i> BPP segmentation (left) and the variation <i>without</i> BPP segmentation in the model (right).	141
8.42	Oxygen partial pressure (left) and methanol partial pressure (right) in the CCL at cathode inlet and cathode outlet in the refresh simulation with and <i>without</i> cathode BPP segmentation (solid lines vs. dashed lines). . .	141
8.43	Catalyst surface coverage with PtOH (left) and PtO (right) in the CCL at cathode inlet and cathode outlet in the refresh simulation with and <i>without</i> cathode BPP segmentation (solid lines vs. dashed lines).	142
8.44	Cathode boundary conditions for the oxygen concentration x_{O_2} , the air flow \dot{N}_{Air} and the current density i for the 4 air stop variants in the refresh cycle simulated with the 2D model (cf. tab. 8.2).	144
8.45	Oxygen partial pressure p_{O_2} (left) and methanol partial pressure p_{CH_3OH} (right) during the refresh cycle with an extended air stop (dashed lines) compared to the reference (solid lines).	145
8.46	Catalyst surface coverage with PtOH (left) and PtO (right) during the refresh cycle simulated with an extended air stop (dashed lines) in comparison with the reference (solid lines).	145

8.47	Overall cell voltage (left) and local cell voltage at cathode inlet and cathode outlet (right) during the refresh cycle with a 30 s air stop (dashed lines) compared to the the reference (solid lines).	146
8.48	Partial pressures of oxygen (left) and methanol (right) in a refresh cycle with an incomplete air stop (dashed lines) compared to the reference (solid lines).	147
8.49	Reaction rates for O_2 (left) and CH_3OH (right) in a refresh cycle with an incomplete air stop (dashed lines) compared to the reference (solid lines).	147
8.50	Local potential difference $\Delta\varphi$ in CCL (left) and ACL (right) in a refresh cycle with an incomplete air stop (dashed lines) compared to the reference (solid lines).	148
8.51	Catalyst surface coverage with PtOH (left) and PtO (right) during the refresh cycle simulated with an incomplete air stop (dashed lines) compared to the reference(solid lines).	149
8.52	Overall cell voltage (left) and local cell voltage at cathode inlet and cathode outlet (right) during the refresh cycle with an incomplete air stop (dashed lines) compared to the the reference (solid lines).	149
8.53	Development of p_{CH_3OH} in the CCL (dashed lines) and local cell voltage (solid lines) in the transition period to normal operation after the refresh cycle in (a) the reference simulation and (b) the variation with an incomplete refresh.	150
8.54	Partial pressures of oxygen (left) and methanol (right) during the refresh cycle simulated with optimised air stop boundary conditions (dashed lines) compared to the reference (solid lines).	151
8.55	Catalyst surface coverage with PtOH (left) and PtO (right) during the refresh cycle simulated with optimised air stop boundary conditions (dashed lines) compared to the reference (solid lines).	151
8.56	Local potential difference $\Delta\varphi$ in CCL (left) and ACL (right) during the refresh cycle simulated with optimised air stop boundary conditions (dashed lines) compared to the reference (solid lines).	152
8.57	Cell voltage during the refresh cycle simulated with optimised air stop boundary conditions (dashed line) compared to the reference (solid line).	152
8.58	Local cell voltage over the full refresh cycle at cathode inlet and cathode outlet (left) and the transition period between air stop and normal operation in all four segments of the DMFC (right) simulated with optimised air stop boundary conditions (dashed lines) compared to the reference (solid lines).	153
8.59	Partial pressures of O_2 (left) and CH_3OH (right) in all 4 segments of the CCL during the transition period between air stop and normal operation simulated with optimised air stop boundary conditions (dashed lines) compared to the reference (solid lines).	153
8.60	Partial pressures of O_2 (left) and CH_3OH (right) during the refresh cycle simulated with a nitrogen flush (dashed lines) compared to the reference (solid lines).	154

8.61	Reaction rates for O ₂ (left) and CH ₃ OH (right) during the refresh cycle simulated with a nitrogen flush (dashed lines) compared to the reference (solid lines).	155
8.62	Local potential difference $\Delta\varphi$ in CCL (left) and ACL (right) during the refresh cycle simulated with a nitrogen flush (dashed lines) compared to the reference (solid lines).	156
8.63	Catalyst surface coverage with PtOH (left) and PtO (right) during the refresh cycle simulated with a nitrogen flush (dashed lines) compared to the reference (solid lines).	156
8.64	Cell voltage during the refresh cycle (left) and <i>after</i> the refresh cycle at operation with $i = 0.25 \text{ A/cm}^2$ (right) for the simulation with a nitrogen flush (dashed lines) compared to the reference air stop (solid lines). . . .	157
8.65	Local water activity (left) and liquid saturation in the CCL (right) during the refresh cycle simulated with a nitrogen flush (dashed lines) compared to the reference (solid lines).	157
8.66	Ionic conductivity of PEM (left) and CCL ionomer (right) during the refresh cycle simulated with a nitrogen flush (dashed lines) compared to the reference (solid lines).	158

Bibliography

- [1] Mehdi Andisheh-Tadbir, Francesco P. Orfino, and Erik Kjeang. “Three-dimensional phase segregation of micro-porous layers for fuel cells by nano-scale X-ray computed tomography”. In: *Journal of Power Sources* 310 (2016), pp. 61–69. ISSN: 0378-7753. DOI: [10.1016/j.jpowsour.2016.02.001](https://doi.org/10.1016/j.jpowsour.2016.02.001).
- [2] Ermete Antolini. “The problem of Ru dissolution from Pt–Ru catalysts during fuel cell operation: analysis and solutions”. In: *Journal of Solid State Electrochemistry* 15.3 (2011), pp. 455–472. DOI: [10.1007/s10008-010-1124-7](https://doi.org/10.1007/s10008-010-1124-7).
- [3] P. Argyropoulos, K. Scott, and W.M. Taama. “One-dimensional thermal model for direct methanol fuel cell stacks: Part I. Model development”. In: *Journal of Power Sources* 79.2 (1999), pp. 169–183. ISSN: 0378-7753. DOI: [10.1016/S0378-7753\(99\)00181-0](https://doi.org/10.1016/S0378-7753(99)00181-0).
- [4] Antonino Salvatore Aricò, Vincenzo Baglio, and Vincenzo Antonucci. “Direct Methanol Fuel Cells: History, Status and Perspectives”. In: *Electrocatalysis of Direct Methanol Fuel Cells*. John Wiley & Sons, Ltd, 2009. Chap. 1, pp. 1–78. ISBN: 9783527627707. DOI: [10.1002/9783527627707.ch1](https://doi.org/10.1002/9783527627707.ch1).
- [5] T. Arlt et al. “In-operando investigation of the humidity condition and the swelling of a Nafion-based membrane in a DMFC with synchrotron X-ray imaging”. In: *Journal of Power Sources* 297 (2015), pp. 83–89. ISSN: 0378-7753. DOI: [10.1016/j.jpowsour.2015.07.064](https://doi.org/10.1016/j.jpowsour.2015.07.064).
- [6] Katherina Baber et al. “Numerical scheme for coupling two-phase compositional porous-media flow and one-phase compositional free flow”. In: *IMA Journal of Applied Mathematics* 77.6 (2012), pp. 887–909. ISSN: 0272-4960. DOI: [10.1093/imamat/hxs048](https://doi.org/10.1093/imamat/hxs048).
- [7] Yehuda Bachmat and Jacob Bear. “Macroscopic modelling of transport phenomena in porous media. 1: The continuum approach”. In: *Transport in Porous Media* 1.3 (1986), pp. 213–240. ISSN: 1573-1634. DOI: [10.1007/BF00238181](https://doi.org/10.1007/BF00238181).
- [8] Hafez Bahrami and Amir Faghri. “Review and advances of direct methanol fuel cells: Part II: Modeling and numerical simulation”. In: *Journal of Power Sources* 230 (2013), pp. 303–320. ISSN: 0378-7753. DOI: [10.1016/j.jpowsour.2012.12.009](https://doi.org/10.1016/j.jpowsour.2012.12.009).
- [9] BASF. *BASF develops process for climate-friendly methanol*. <https://www.basf.com/global/en/media/news-releases/2019/05/p-19-218.html>. 2019.
- [10] P. Bastian et al. “A generic grid interface for parallel and adaptive scientific computing. Part I: abstract framework”. In: *Computing* 82.2 (2008), pp. 103–119. ISSN: 1436-5057. DOI: [10.1007/s00607-008-0003-x](https://doi.org/10.1007/s00607-008-0003-x).

- [11] P. Bastian et al. “A generic grid interface for parallel and adaptive scientific computing. Part II: implementation and tests in DUNE”. In: *Computing* 82.2 (2008), pp. 121–138. ISSN: 1436-5057. DOI: [10.1007/s00607-008-0004-9](https://doi.org/10.1007/s00607-008-0004-9).
- [12] P. Bastian et al. “UG – A flexible software toolbox for solving partial differential equations”. In: *Computing and Visualization in Science* 1.1 (1997), pp. 27–40. ISSN: 1432-9360. DOI: [10.1007/s007910050003](https://doi.org/10.1007/s007910050003).
- [13] Peter Bastian, Felix Heimann, and Sven Marnach. “Generic implementation of finite element methods in the distributed and unified numerics environment (DUNE)”. In: *Kybernetika* 46.2 (2010), pp. 294–315. ISSN: 0023-5954.
- [14] S. F. Baxter, V. S. Battaglia, and R. E. White. “Methanol Fuel Cell Model: Anode”. In: *Journal of The Electrochemical Society* 146.2 (1999), pp. 437–447. DOI: [10.1149/1.1391626](https://doi.org/10.1149/1.1391626).
- [15] Tomasz Bednarek and Georgios Tsotridis. “Calculation of effective transport properties of partially saturated gas diffusion layers”. In: *Journal of Power Sources* 340 (2017), pp. 111–120. ISSN: 0378-7753. DOI: [10.1016/j.jpowsour.2016.10.098](https://doi.org/10.1016/j.jpowsour.2016.10.098).
- [16] Michael Bowker. “Methanol Synthesis from CO₂ Hydrogenation”. In: *ChemCatChem* 11.17 (2019), pp. 4238–4246. DOI: [10.1002/cctc.201900401](https://doi.org/10.1002/cctc.201900401).
- [17] F. Bresciani et al. “A combined in-situ and post-mortem investigation on local permanent degradation in a direct methanol fuel cell”. In: *Journal of Power Sources* 306 (2016), pp. 49–61. ISSN: 0378-7753. DOI: [10.1016/j.jpowsour.2015.11.105](https://doi.org/10.1016/j.jpowsour.2015.11.105).
- [18] F. Bresciani et al. “A comparison of operating strategies to reduce DMFC degradation”. In: *International Journal of Energy Research* 38.1 (2014), pp. 117–124. DOI: [10.1002/er.3115](https://doi.org/10.1002/er.3115).
- [19] F. Bresciani et al. “A Parametric Analysis on DMFC Anode Degradation”. In: *Fuel Cells* 14.3 (2014), pp. 386–394. DOI: [10.1002/fuce.201300132](https://doi.org/10.1002/fuce.201300132).
- [20] F. Bresciani et al. “Experimental investigation on DMFC temporary degradation”. In: *International Journal of Hydrogen Energy* 39.36 (2014), pp. 21647–21656. ISSN: 0360-3199. DOI: [10.1016/j.ijhydene.2014.09.072](https://doi.org/10.1016/j.ijhydene.2014.09.072).
- [21] O. Burheim et al. “Ex situ measurements of through-plane thermal conductivities in a polymer electrolyte fuel cell”. In: *Journal of Power Sources* 195.1 (2010), pp. 249–256. ISSN: 03787753. DOI: [10.1016/j.jpowsour.2009.06.077](https://doi.org/10.1016/j.jpowsour.2009.06.077).
- [22] A. Casalegno and R. Marchesi. “DMFC performance and methanol cross-over: Experimental analysis and model validation”. In: *Journal of Power Sources* 185.1 (2008), pp. 318–330. ISSN: 0378-7753. DOI: [10.1016/j.jpowsour.2008.06.071](https://doi.org/10.1016/j.jpowsour.2008.06.071).
- [23] A. Casalegno, R. Marchesi, and D. Parenti. “Two-Phase 1D+1D Model of a DMFC: Development and Validation on Extensive Operating Conditions Range”. In: *Fuel Cells* 8.1 (2008), pp. 37–44. DOI: [10.1002/fuce.200700030](https://doi.org/10.1002/fuce.200700030).
- [24] Hou-Chin Cha, Charn-Ying Chen, and Jr-Yuan Shiu. “Investigation on the durability of direct methanol fuel cells”. In: *Journal of Power Sources* 192.2 (2009), pp. 451–456. ISSN: 0378-7753. DOI: [10.1016/j.jpowsour.2009.03.028](https://doi.org/10.1016/j.jpowsour.2009.03.028).

-
- [25] L. Chaabane et al. "Swelling and permeability of Nafion®117 in water-methanol solutions: An experimental and modelling investigation". In: *Journal of Membrane Science* 377.1 (2011), pp. 54–64. ISSN: 0376-7388. DOI: [10.1016/j.memsci.2011.03.037](https://doi.org/10.1016/j.memsci.2011.03.037).
- [26] Charn-Ying Chen and Hou-Chin Cha. "Strategy to optimize cathode operating conditions to improve the durability of a Direct Methanol Fuel Cell". In: *Journal of Power Sources* 200 (2012), pp. 21–28. ISSN: 0378-7753. DOI: [10.1016/j.jpowsour.2011.10.100](https://doi.org/10.1016/j.jpowsour.2011.10.100).
- [27] Weimin Chen et al. "Test on the degradation of direct methanol fuel cell". In: *Electrochimica Acta* 51.12 (2006), pp. 2391–2399. ISSN: 0013-4686. DOI: [10.1016/j.electacta.2005.07.016](https://doi.org/10.1016/j.electacta.2005.07.016).
- [28] Xuan Cheng et al. "Characterization of catalysts and membrane in DMFC lifetime testing". In: *Electrochimica Acta* 51.22 (2006), pp. 4620–4625. ISSN: 0013-4686. DOI: [10.1016/j.electacta.2005.12.043](https://doi.org/10.1016/j.electacta.2005.12.043).
- [29] Hiroshi Chizawa et al. "Impacts of Carbon Corrosion on Cell Performance Decay". In: *ECS Transactions* 11.1 (2007), pp. 981–992. DOI: [10.1149/1.2781011](https://doi.org/10.1149/1.2781011).
- [30] Dong Young Chung, Kyung-Jae Lee, and Yung-Eun Sung. "Methanol Electro-Oxidation on the Pt Surface: Revisiting the Cyclic Voltammetry Interpretation". In: *The Journal of Physical Chemistry C* 120.17 (2016), pp. 9028–9035. DOI: [10.1021/acs.jpcc.5b12303](https://doi.org/10.1021/acs.jpcc.5b12303).
- [31] Youngsu Chung et al. "Understanding a Degradation Mechanism of Direct Methanol Fuel Cell Using TOF-SIMS and XPS". In: *The Journal of Physical Chemistry C* 112.1 (2007), pp. 313–318. DOI: [10.1021/jp0759372](https://doi.org/10.1021/jp0759372).
- [32] John Cruickshank and Keith Scott. "The degree and effect of methanol crossover in the direct methanol fuel cell". In: *Journal of Power Sources* 70.1 (1998), pp. 40–47. ISSN: 0378-7753. DOI: [10.1016/S0378-7753\(97\)02626-8](https://doi.org/10.1016/S0378-7753(97)02626-8).
- [33] Robert M. Darling and Jeremy P. Meyers. "Kinetic Model of Platinum Dissolution in PEMFCs". In: *Journal of The Electrochemical Society* 150.11 (2003), A1523. DOI: [10.1149/1.1613669](https://doi.org/10.1149/1.1613669).
- [34] James W. Demmel et al. "A Supernodal Approach to Sparse Partial Pivoting". In: *SIAM Journal on Matrix Analysis and Applications* 20.3 (1999), pp. 720–755. DOI: [10.1137/S0895479895291765](https://doi.org/10.1137/S0895479895291765).
- [35] Jiri Divisek et al. "Performance Modeling of a Direct Methanol Fuel Cell". In: *Journal of The Electrochemical Society* 150.6 (2003), A811. DOI: [10.1149/1.1572150](https://doi.org/10.1149/1.1572150).
- [36] D. Dixon et al. "Degradation effects at the methanol inlet, outlet and center region of a stack MEA operated in DMFC". In: *Journal of Power Sources* 196.13 (2011), pp. 5538–5545. ISSN: 0378-7753. DOI: [10.1016/j.jpowsour.2011.02.007](https://doi.org/10.1016/j.jpowsour.2011.02.007).
- [37] H. Dohle, J. Divisek, and R. Jung. "Process engineering of the direct methanol fuel cell". In: *Journal of Power Sources* 86.1 (2000), pp. 469–477. ISSN: 0378-7753. DOI: [10.1016/S0378-7753\(99\)00456-5](https://doi.org/10.1016/S0378-7753(99)00456-5).

- [38] *Dumux Handbook Version 2.7*. <https://dumux.org/docs/>. 2015.
- [39] Christian Eickes et al. “Recoverable Cathode Performance Loss in Direct Methanol Fuel Cells”. In: *Journal of The Electrochemical Society* 153.1 (2006), A171. DOI: [10.1149/1.2136073](https://doi.org/10.1149/1.2136073).
- [40] M. Eikerling. “Water Management in Cathode Catalyst Layers of PEM Fuel Cells”. In: *Journal of The Electrochemical Society* 153.3 (2006), E58–E70. ISSN: 00134651. DOI: [10.1149/1.2160435](https://doi.org/10.1149/1.2160435).
- [41] R. Escudero-Cid et al. “Degradation of DMFC using a New Long-Term Stability Cycle”. In: *International Journal of Green Energy* 12.6 (2015), pp. 641–653. DOI: [10.1080/15435075.2013.867269](https://doi.org/10.1080/15435075.2013.867269).
- [42] B. Flemisch et al. “DuMux: DUNE for multi-phase,component,scale,physics,... flow and transport in porous media”. In: *Advances in Water Resources* 34.9 (2011), pp. 1102–1112. ISSN: 0309-1708. DOI: [10.1016/j.advwatres.2011.03.007](https://doi.org/10.1016/j.advwatres.2011.03.007).
- [43] Georg Futter. “Physical modeling of PEMFC performance and chemical membrane degradation”. PhD thesis. University of Stuttgart, 2019. DOI: [10.18419/opus-10261](https://doi.org/10.18419/opus-10261).
- [44] Georg A. Futter et al. “Physical modeling of polymer-electrolyte membrane fuel cells: Understanding water management and impedance spectra”. In: *Journal of Power Sources* 391 (2018), pp. 148–161. ISSN: 0378-7753. DOI: [10.1016/j.jpowsour.2018.04.070](https://doi.org/10.1016/j.jpowsour.2018.04.070).
- [45] Lajos Gancs et al. “The Impact of Ru Contamination of a Pt/C Electrocatalyst on Its Oxygen-Reducing Activity”. In: *Electrochemical and Solid-State Letters* 10.9 (2007), B150. DOI: [10.1149/1.2754382](https://doi.org/10.1149/1.2754382).
- [46] *Gaoncell*. <https://www.gaoncell.com/technology/tec-fc/dmfc>. 2021.
- [47] Pablo A. García-Salaberri and Marcos Vera. “On the effect of operating conditions in liquid-feed direct methanol fuel cells: A multiphysics modeling approach”. In: *Energy* 113 (2016), pp. 1265–1287. ISSN: 0360-5442. DOI: [10.1016/j.energy.2016.07.074](https://doi.org/10.1016/j.energy.2016.07.074).
- [48] Pablo A. García-Salaberri, Marcos Vera, and Immaculada Iglesias. “Modeling of the anode of a liquid-feed DMFC: Inhomogeneous compression effects and two-phase transport phenomena”. In: *Journal of Power Sources* 246 (2014), pp. 239–252. ISSN: 0378-7753. DOI: [10.1016/j.jpowsour.2013.06.166](https://doi.org/10.1016/j.jpowsour.2013.06.166).
- [49] Hubert A. Gasteiger et al. “Methanol electrooxidation on well-characterized platinum-ruthenium bulk alloys”. In: *The Journal of Physical Chemistry* 97.46 (1993), pp. 12020–12029. DOI: [10.1021/j100148a030](https://doi.org/10.1021/j100148a030).
- [50] Hubert A. Gasteiger et al. “Temperature-Dependent Methanol Electro-Oxidation on Well-Characterized Pt-Ru Alloys”. In: *Journal of The Electrochemical Society* 141.7 (1994), pp. 1795–1803. DOI: [10.1149/1.2055007](https://doi.org/10.1149/1.2055007).
- [51] Jiabin Ge and Hongtan Liu. “A three-dimensional mathematical model for liquid-fed direct methanol fuel cells”. In: *Journal of Power Sources* 160.1 (2006), pp. 413–421. ISSN: 0378-7753. DOI: [10.1016/j.jpowsour.2006.02.001](https://doi.org/10.1016/j.jpowsour.2006.02.001).

-
- [52] Shanhai Ge et al. “Absorption, Desorption, and Transport of Water in Polymer Electrolyte Membranes for Fuel Cells”. In: *Journal of The Electrochemical Society* 152.6 (2005), A1149–A1157. DOI: [10.1149/1.1899263](https://doi.org/10.1149/1.1899263).
- [53] M. Th. van Genuchten. “A Closed-form Equation for Predicting the Hydraulic Conductivity of Unsaturated Soils”. In: *Soil Science Society of America Journal* 44.5 (1980), pp. 892–898. DOI: [10.2136/sssaj1980.03615995004400050002x](https://doi.org/10.2136/sssaj1980.03615995004400050002x).
- [54] Dietmar Gerteisen. “Transient and steady-state analysis of catalyst poisoning and mixed potential formation in direct methanol fuel cells”. In: *Journal of Power Sources* 195.19 (2010), pp. 6719–6731. ISSN: 0378-7753. DOI: [10.1016/j.jpowsour.2010.04.004](https://doi.org/10.1016/j.jpowsour.2010.04.004).
- [55] Jeff T. Gostick et al. “Wettability and capillary behavior of fibrous gas diffusion media for polymer electrolyte membrane fuel cells”. In: *Journal of Power Sources* 194.1 (2009), pp. 433–444. ISSN: 0378-7753. DOI: [10.1016/j.jpowsour.2009.04.052](https://doi.org/10.1016/j.jpowsour.2009.04.052).
- [56] Jeffrey T. Gostick et al. “Capillary pressure and hydrophilic porosity in gas diffusion layers for polymer electrolyte fuel cells”. In: *Journal of Power Sources* 156.2 (2006), pp. 375–387. ISSN: 0378-7753. DOI: [10.1016/j.jpowsour.2005.05.086](https://doi.org/10.1016/j.jpowsour.2005.05.086).
- [57] A. Hamnett. “Mechanism and electrocatalysis in the direct methanol fuel cell”. In: *Catalysis Today* 38.4 (1997). Fuel Cells and Catalysis, pp. 445–457. ISSN: 0920-5861. DOI: [10.1016/S0920-5861\(97\)00054-0](https://doi.org/10.1016/S0920-5861(97)00054-0).
- [58] Liang Hao et al. “Modeling and Experimental Validation of Pt Loading and Electrode Composition Effects in PEM Fuel Cells”. In: *Journal of The Electrochemical Society* 162.8 (2015), F854–F867. DOI: [10.1149/2.0221508jes](https://doi.org/10.1149/2.0221508jes).
- [59] D. Harvey, J.G. Pharoah, and K. Karan. “A comparison of different approaches to modelling the PEMFC catalyst layer”. In: *Journal of Power Sources* 179.1 (2008), pp. 209–219. ISSN: 0378-7753. DOI: [10.1016/j.jpowsour.2007.12.077](https://doi.org/10.1016/j.jpowsour.2007.12.077).
- [60] Rainer Helmig. *Multiphase flow and transport processes in the subsurface: a contribution to the modeling of hydrosystems*. Springer-Verlag Berlin Heidelberg, 1997. ISBN: 9783642645457.
- [61] Harry Hoster et al. “Pt–Ru model catalysts for anodic methanol oxidation: Influence of structure and composition on the reactivity”. In: *Physical Chemistry Chemical Physics* 3.3 (2001), pp. 337–346.
- [62] H Hoster et al. “Current-time behavior of smooth and porous PtRu surfaces for methanol oxidation”. In: *Journal of the Electrochemical Society* 148.5 (2001), A496.
- [63] Ralf Huber and Rainer Helmig. “Node-centered finite volume discretizations for the numerical simulation of multiphase flow in heterogeneous porous media”. In: *Computational Geosciences* 4.2 (2000), pp. 141–164. DOI: [10.1023/A:1011559916309](https://doi.org/10.1023/A:1011559916309).

- [64] Fraunhofer ISE. *A Glimpse into Real-Time Methanol Synthesis: Dynamic Operation of a Miniplant at Fraunhofer ISE*. <https://www.ise.fraunhofer.de/en/press-media/press-releases/2020/a-glimpse-inot-real-time-methanol-synthesis-dynamic-operation-of-a-miniplant-at-fraunhofer-ise.html>. 2020.
- [65] T. Iwasita. “Electrocatalysis of methanol oxidation”. In: *Electrochimica Acta* 47.22 (2002), pp. 3663–3674. ISSN: 0013-4686. DOI: [10.1016/S0013-4686\(02\)00336-5](https://doi.org/10.1016/S0013-4686(02)00336-5).
- [66] T. Jahnke et al. “A transient multi-scale model for direct methanol fuel cells”. In: *Electrochimica Acta* 232 (2017), pp. 215–225. ISSN: 0013-4686. DOI: [10.1016/j.electacta.2017.02.116](https://doi.org/10.1016/j.electacta.2017.02.116).
- [67] Thomas Jahnke et al. “Physical Modeling of Catalyst Degradation in Low Temperature Fuel Cells: Platinum Oxidation, Dissolution, Particle Growth and Platinum Band Formation”. In: *Journal of The Electrochemical Society* 167.1 (2019), p. 013523. DOI: [10.1149/2.0232001jes](https://doi.org/10.1149/2.0232001jes).
- [68] Min Ku Jeon et al. “Performance degradation study of a direct methanol fuel cell by electrochemical impedance spectroscopy”. In: *Electrochimica Acta* 53.2 (2007), pp. 447–452. ISSN: 0013-4686. DOI: [10.1016/j.electacta.2007.06.063](https://doi.org/10.1016/j.electacta.2007.06.063).
- [69] Prabhuram Joghee et al. “A review on direct methanol fuel cells–In the perspective of energy and sustainability”. In: *MRS Energy & Sustainability* 2.3 (2015). DOI: [10.1557/mre.2015.4](https://doi.org/10.1557/mre.2015.4).
- [70] Shinji Jomori et al. “An Experimental Study of the Effects of Operational History on Activity Changes in a PEMFC”. In: *Journal of The Electrochemical Society* 160.9 (2013), F1067–F1073. DOI: [10.1149/2.103309jes](https://doi.org/10.1149/2.103309jes).
- [71] Primož Jovanovič et al. “Potentiodynamic dissolution study of PtRu/C electrocatalyst in the presence of methanol”. In: *Electrochimica Acta* 211 (2016), pp. 851–859. ISSN: 0013-4686. DOI: [10.1016/j.electacta.2016.06.109](https://doi.org/10.1016/j.electacta.2016.06.109).
- [72] Seunghun Jung. “Non-isothermal multi-dimensional direct methanol fuel cell model with micro-porous layers mitigating water/methanol crossover”. In: *Journal of Power Sources* 231 (2013), pp. 60–81. ISSN: 0378-7753. DOI: [10.1016/j.jpowsour.2012.12.086](https://doi.org/10.1016/j.jpowsour.2012.12.086).
- [73] Seunghun Jung, Yongjun Leng, and Chao-Yang Wang. “Role of CO₂ in Methanol and Water Transport in Direct Methanol Fuel Cells”. In: *Electrochimica Acta* 134 (2014), pp. 35–48. ISSN: 0013-4686. DOI: [10.1016/j.electacta.2014.04.087](https://doi.org/10.1016/j.electacta.2014.04.087).
- [74] P.S. Kauranen, E. Skou, and J. Munk. “Kinetics of methanol oxidation on carbon-supported Pt and Pt + Ru catalysts”. In: *Journal of Electroanalytical Chemistry* 404.1 (1996), pp. 1–13. ISSN: 1572-6657. DOI: [10.1016/0022-0728\(95\)04298-9](https://doi.org/10.1016/0022-0728(95)04298-9).
- [75] Ahmad El-kharouf et al. “Ex-situ characterisation of gas diffusion layers for proton exchange membrane fuel cells”. In: *Journal of Power Sources* 218 (2012), pp. 393–404. ISSN: 0378-7753. DOI: [10.1016/j.jpowsour.2012.06.099](https://doi.org/10.1016/j.jpowsour.2012.06.099).

-
- [76] Johan Ko et al. “Comparison of numerical simulation results with experimental current density and methanol-crossover data for direct methanol fuel cells”. In: *Journal of Power Sources* 196.3 (2011), pp. 935–945. ISSN: 0378-7753. DOI: [10.1016/j.jpowsour.2010.08.102](https://doi.org/10.1016/j.jpowsour.2010.08.102).
- [77] Klaus-Dieter Kreuer. “The role of internal pressure for the hydration and transport properties of ionomers and polyelectrolytes”. In: *Solid State Ionics* 252 (2013), pp. 93–101. ISSN: 0167-2738. DOI: [10.1016/j.ssi.2013.04.018](https://doi.org/10.1016/j.ssi.2013.04.018).
- [78] Klaus-Dieter Kreuer et al. “Transport in Proton Conductors for Fuel-Cell Applications: Simulations, Elementary Reactions, and Phenomenology”. In: *Chemical Reviews* 104.10 (2004), pp. 4637–4678. DOI: [10.1021/cr020715f](https://doi.org/10.1021/cr020715f).
- [79] R. Krishna and J.A. Wesselingh. “The Maxwell-Stefan approach to mass transfer”. In: *Chemical Engineering Science* 52.6 (1997), pp. 861–911. ISSN: 0009-2509. DOI: [10.1016/S0009-2509\(96\)00458-7](https://doi.org/10.1016/S0009-2509(96)00458-7).
- [80] A.A. Kulikovskiy et al. “DMFC: Galvanic or electrolytic cell?” In: *Electrochemistry Communications* 8.5 (2006), pp. 754–760. ISSN: 1388-2481. DOI: [10.1016/j.elecom.2006.03.011](https://doi.org/10.1016/j.elecom.2006.03.011).
- [81] Peter Kurzweil. *Brennstoffzellentechnik: Grundlagen, Materialien, Anwendungen, Gaserzeugung*. 3. Auflage. Wiesbaden: Springer Vieweg, 2016, XII, 260 pages. ISBN: 978-3-658-14935-2. DOI: [10.1007/978-3-658-14935-2](https://doi.org/10.1007/978-3-658-14935-2).
- [82] Ahmet Kusoglu and Adam Z. Weber. “New Insights into Perfluorinated Sulfonic-Acid Ionomers”. In: *Chemical Reviews* 117.3 (2017), pp. 987–1104. DOI: [10.1021/acs.chemrev.6b00159](https://doi.org/10.1021/acs.chemrev.6b00159).
- [83] Ahmet Kusoglu et al. “Water Uptake of Fuel-Cell Catalyst Layers”. In: *Journal of The Electrochemical Society* 159.9 (2012), F530–F535. DOI: [10.1149/2.031209jes](https://doi.org/10.1149/2.031209jes).
- [84] Markku J. Lampinen and Marina Fomino. “Analysis of Free Energy and Entropy Changes for Half-Cell Reactions”. In: *Journal of The Electrochemical Society* 140.12 (1993), pp. 3537–3546. DOI: [10.1149/1.2221123](https://doi.org/10.1149/1.2221123).
- [85] A. Lauser et al. “A new approach for phase transitions in miscible multi-phase flow in porous media”. In: *Advances in Water Resources* 34.8 (2011), pp. 957–966. ISSN: 0309-1708. DOI: [10.1016/j.advwatres.2011.04.021](https://doi.org/10.1016/j.advwatres.2011.04.021).
- [86] Xianglin Li and Amir Faghri. “Review and advances of direct methanol fuel cells (DMFCs) part I: Design, fabrication, and testing with high concentration methanol solutions”. In: *Journal of Power Sources* 226 (2013), pp. 223–240. ISSN: 0378-7753. DOI: [10.1016/j.jpowsour.2012.10.061](https://doi.org/10.1016/j.jpowsour.2012.10.061).
- [87] Fuqiang Liu and Chao-Yang Wang. “Mixed Potential in a Direct Methanol Fuel Cell”. In: *Journal of The Electrochemical Society* 154.6 (2007), B514. DOI: [10.1149/1.2718404](https://doi.org/10.1149/1.2718404).
- [88] Qingye Lu et al. “Anodic activation of PtRu/C catalysts for methanol oxidation”. In: *The Journal of Physical Chemistry B* 109.5 (2005), pp. 1715–1722.

- [89] Paul W. Majsztrik et al. “Water sorption, desorption and transport in Nafion membranes”. In: *Journal of Membrane Science* 301.1 (2007), pp. 93–106. ISSN: 0376-7388. DOI: [10.1016/j.memsci.2007.06.022](https://doi.org/10.1016/j.memsci.2007.06.022).
- [90] Libeth Maldonado et al. “Characterization of polymer electrolyte Nafion membranes: Influence of temperature, heat treatment and drying protocol on sorption and transport properties”. In: *Journal of Membrane Science* 389 (2012), pp. 43–56. ISSN: 0376-7388. DOI: [10.1016/j.memsci.2011.10.014](https://doi.org/10.1016/j.memsci.2011.10.014).
- [91] Nenad M. Marković et al. “Electro-oxidation mechanisms of methanol and formic acid on Pt-Ru alloy surfaces”. In: *Electrochimica Acta* 40.1 (1995), pp. 91–98. ISSN: 0013-4686. DOI: [10.1016/0013-4686\(94\)00241-R](https://doi.org/10.1016/0013-4686(94)00241-R).
- [92] Asad Mehmood et al. “A review on durability issues and restoration techniques in long-term operations of direct methanol fuel cells”. In: *Journal of Power Sources* 297 (2015), pp. 224–241. ISSN: 0378-7753. DOI: [10.1016/j.jpowsour.2015.07.094](https://doi.org/10.1016/j.jpowsour.2015.07.094).
- [93] Frank Meier and Gerhart Eigenberger. “Transport parameters for the modelling of water transport in ionomer membranes for PEM-fuel cells”. In: *Electrochimica Acta* 49.11 (2004), pp. 1731–1742. ISSN: 0013-4686. DOI: [10.1016/j.electacta.2003.12.004](https://doi.org/10.1016/j.electacta.2003.12.004).
- [94] Jeremy P. Meyers and John Newman. “Simulation of the Direct Methanol Fuel Cell: I. Thermodynamic Framework for a Multicomponent Membrane”. In: *Journal of The Electrochemical Society* 149.6 (2002), A710. DOI: [10.1149/1.1473188](https://doi.org/10.1149/1.1473188).
- [95] Jeremy P. Meyers and John Newman. “Simulation of the Direct Methanol Fuel Cell: II. Modeling and Data Analysis of Transport and Kinetic Phenomena”. In: *Journal of The Electrochemical Society* 149.6 (2002), A718. DOI: [10.1149/1.1473189](https://doi.org/10.1149/1.1473189).
- [96] Jeremy P. Meyers and John Newman. “Simulation of the Direct Methanol Fuel Cell: III. Design and Optimization”. In: *Journal of The Electrochemical Society* 149.6 (2002), A729. DOI: [10.1149/1.1473190](https://doi.org/10.1149/1.1473190).
- [97] Tobias Morawietz et al. “Quantitative in Situ Analysis of Ionomer Structure in Fuel Cell Catalytic Layers”. In: *ACS Applied Materials & Interfaces* 8.40 (2016), pp. 27044–27054. DOI: [10.1021/acsami.6b07188](https://doi.org/10.1021/acsami.6b07188).
- [98] Steffen Müthing. “A Flexible Framework for Multi Physics and Multi Domain PDE Simulations”. PhD thesis. University of Stuttgart, 2015. DOI: [10.18419/opus-3620](https://doi.org/10.18419/opus-3620).
- [99] Steffen Müthing and Peter Bastian. “Dune-Multidomaingrid: A Metagrid Approach to Subdomain Modeling”. In: *Advances in DUNE*. Ed. by Andreas Dedner, Bernd Flemisch, and Robert Klöforn. Berlin, Heidelberg: Springer Berlin Heidelberg, 2012, pp. 59–73. ISBN: 978-3-642-28589-9.
- [100] Ryan P. O’Hayre, ed. *Fuel cell fundamentals*. 2. ed. Hoboken, NJ: Wiley, 2009, XXV, 546 pages. ISBN: 978-0-470-25843-9.

-
- [101] Hwanyeong Oh et al. “Experimental dissection of oxygen transport resistance in the components of a polymer electrolyte membrane fuel cell”. In: *Journal of Power Sources* 345 (2017), pp. 67–77. ISSN: 0378-7753. DOI: [10.1016/j.jpowsour.2017.01.087](https://doi.org/10.1016/j.jpowsour.2017.01.087).
- [102] J.-Y. Park et al. “Operating Temperature Dependency on Performance Degradation of Direct Methanol Fuel Cells”. In: *Fuel Cells* 12.3 (2012), pp. 426–438. DOI: [10.1002/fuce.201100184](https://doi.org/10.1002/fuce.201100184).
- [103] Jun-Young Park et al. “The operating mode dependence on electrochemical performance degradation of direct methanol fuel cells”. In: *International Journal of Hydrogen Energy* 33.18 (2008), pp. 4833–4843. ISSN: 0360-3199. DOI: [10.1016/j.ijhydene.2008.04.060](https://doi.org/10.1016/j.ijhydene.2008.04.060).
- [104] Ji-Yeon Park et al. “Investigations of performance degradation and mitigation strategies in direct methanol fuel cells”. In: *International Journal of Hydrogen Energy* 34.4 (2009), pp. 2043–2051. ISSN: 0360-3199. DOI: [10.1016/j.ijhydene.2008.10.092](https://doi.org/10.1016/j.ijhydene.2008.10.092).
- [105] Devproshad K. Paul, Richard McCreery, and Kunal Karan. “Proton Transport Property in Supported Nafion Nanothin Films by Electrochemical Impedance Spectroscopy”. In: *Journal of The Electrochemical Society* 161.14 (2014), F1395–F1402. DOI: [10.1149/2.0571414jes](https://doi.org/10.1149/2.0571414jes).
- [106] Zhe Peng et al. “In-Situ Measurement of Electroosmotic Drag Coefficient in Nafion Membrane for the PEMFC”. In: *The Journal of Physical Chemistry B* 115.44 (2011), pp. 12835–12844. DOI: [10.1021/jp205291f](https://doi.org/10.1021/jp205291f).
- [107] Piotr Piela et al. “Ruthenium Crossover in Direct Methanol Fuel Cell with Pt-Ru Black Anode”. In: *Journal of The Electrochemical Society* 151.12 (2004), A2053. DOI: [10.1149/1.1814472](https://doi.org/10.1149/1.1814472).
- [108] Bruce E. Poling, John M. Prausnitz, and John P. O’Connell, eds. *Properties of Gases and Liquids, Fifth Edition*. 5. ed. New York: McGraw-Hill Education, 2001. ISBN: 978-0-07-011682-5.
- [109] J. Prabhuram, T.S. Zhao, and H. Yang. “Methanol adsorbates on the DMFC cathode and their effect on the cell performance”. In: *Journal of Electroanalytical Chemistry* 578.1 (2005), pp. 105–112. ISSN: 1572-6657. DOI: [10.1016/j.jelechem.2004.12.025](https://doi.org/10.1016/j.jelechem.2004.12.025).
- [110] C. Rabissi et al. “A locally resolved investigation on direct methanol fuel cell uneven components fading: Local cathode catalyst layer tuning for homogeneous operation and reduced degradation rate”. In: *Journal of Power Sources* 404 (2018), pp. 135–148. DOI: [10.1016/j.jpowsour.2018.09.094](https://doi.org/10.1016/j.jpowsour.2018.09.094).
- [111] C. Rabissi et al. “A locally resolved investigation on direct methanol fuel cell uneven components fading: Steady state and degradation local analysis”. In: *Journal of Power Sources* 397 (2018), pp. 361–373. ISSN: 0378-7753. DOI: [10.1016/j.jpowsour.2018.07.034](https://doi.org/10.1016/j.jpowsour.2018.07.034).

- [112] C. Rabissi et al. “In operando investigation of anode overpotential dynamics in direct methanol fuel cells”. In: *International Journal of Hydrogen Energy* 41.40 (2016), pp. 18221–18225. ISSN: 0360-3199. DOI: [10.1016/j.ijhydene.2016.08.140](https://doi.org/10.1016/j.ijhydene.2016.08.140).
- [113] C. Rabissi et al. “In operando measurement of localised cathode potential to mitigate DMFC temporary degradation”. In: *International Journal of Hydrogen Energy* 43.20 (2018), pp. 9797–9802. ISSN: 0360-3199. DOI: [10.1016/j.ijhydene.2018.04.043](https://doi.org/10.1016/j.ijhydene.2018.04.043).
- [114] Claudio Rabissi. “DMFC Local Performance Investigation For Optimized Durability”. PhD thesis. Politecnico di Milano, 2018.
- [115] Rinat R. Rashapov and Jeff T. Gostick. “In-Plane Effective Diffusivity in PEMFC Gas Diffusion Layers”. In: *Transport in Porous Media* 115.3 (2016), pp. 411–433. ISSN: 1573-1634. DOI: [10.1007/s11242-016-0648-4](https://doi.org/10.1007/s11242-016-0648-4).
- [116] Rinat R. Rashapov, Jonathan Unno, and Jeff T. Gostick. “Characterization of PEMFC Gas Diffusion Layer Porosity”. In: *Journal of The Electrochemical Society* 162.6 (2015), F603–F612. DOI: [10.1149/2.0921506jes](https://doi.org/10.1149/2.0921506jes).
- [117] D. Rivin et al. “Solubility and transport behavior of water and alcohols in NafionTM”. In: *Polymer* 42.2 (2001), pp. 623–635. ISSN: 0032-3861. DOI: [10.1016/S0032-3861\(00\)00350-5](https://doi.org/10.1016/S0032-3861(00)00350-5).
- [118] L. M. Roen, C. H. Paik, and T. D. Jarvi. “Electrocatalytic Corrosion of Carbon Support in PEMFC Cathodes”. In: *Electrochemical and Solid-State Letters* 7.1 (2004), A19. DOI: [10.1149/1.1630412](https://doi.org/10.1149/1.1630412).
- [119] Debra R Rolison et al. “Role of hydrous ruthenium oxide in Pt- Ru direct methanol fuel cell anode electrocatalysts: the importance of mixed electron/proton conductivity”. In: *Langmuir* 15.3 (1999), pp. 774–779.
- [120] Quirina I. Roode-Gutzmer, Doreen Kaiser, and Martin Bertau. “Renewable Methanol Synthesis”. In: *ChemBioEng Reviews* 6.6 (2019), pp. 209–236. DOI: [10.1002/cben.201900012](https://doi.org/10.1002/cben.201900012).
- [121] Loka Subramanyam Sarma et al. “Investigations of direct methanol fuel cell (DMFC) fading mechanisms”. In: *Journal of Power Sources* 167.2 (2007), pp. 358–365. ISSN: 0378-7753. DOI: [10.1016/j.jpowsour.2007.02.020](https://doi.org/10.1016/j.jpowsour.2007.02.020).
- [122] Dirk Uwe Sauer et al. “Measurement of the current distribution in a direct methanol fuel cell—Confirmation of parallel galvanic and electrolytic operation within one cell”. In: *Journal of Power Sources* 176.2 (2008), pp. 477–483. ISSN: 0378-7753. DOI: [10.1016/j.jpowsour.2007.08.056](https://doi.org/10.1016/j.jpowsour.2007.08.056).
- [123] Alexander Schröder et al. “Combined local current distribution measurements and high resolution neutron radiography of operating Direct Methanol Fuel Cells”. In: *Electrochemistry Communications* 11.8 (2009), pp. 1606–1609. DOI: [10.1016/j.elecom.2009.06.008](https://doi.org/10.1016/j.elecom.2009.06.008).

-
- [124] Alexander Schröder et al. “The influence of gas diffusion layer wettability on direct methanol fuel cell performance: A combined local current distribution and high resolution neutron radiography study”. In: *Journal of Power Sources* 195.15 (2010), pp. 4765–4771. ISSN: 0378-7753. DOI: [10.1016/j.jpowsour.2010.02.057](https://doi.org/10.1016/j.jpowsour.2010.02.057).
 - [125] Paul von Schroeder. “Über Erstarrungs- und Quellungserscheinungen von Gelatine”. In: *Zeitschrift für Physikalische Chemie* 45U.1 (1903), pp. 75–117. DOI: [doi:10.1515/zpch-1903-4503](https://doi.org/10.1515/zpch-1903-4503).
 - [126] Thorsten Schultz, Ulrike Krewer, and Kai Sundmacher. “Impact of electrode kinetics on the dynamic response of a DMFC to change of methanol feed concentration”. In: *Journal of Power Sources* 165.1 (2007), pp. 138–151. ISSN: 0378-7753. DOI: [10.1016/j.jpowsour.2006.11.021](https://doi.org/10.1016/j.jpowsour.2006.11.021).
 - [127] Thorsten Schultz and Kai Sundmacher. “Rigorous dynamic model of a direct methanol fuel cell based on Maxwell–Stefan mass transport equations and a Flory–Huggins activity model: Formulation and experimental validation”. In: *Journal of Power Sources* 145.2 (2005). Selected papers presented at the Fuel Cells Science and Technology Meeting, pp. 435–462. ISSN: 0378-7753. DOI: [10.1016/j.jpowsour.2005.02.036](https://doi.org/10.1016/j.jpowsour.2005.02.036).
 - [128] K. Scott, P. Argyropoulos, and K. Sundmacher. “A model for the liquid feed direct methanol fuel cell”. In: *Journal of Electroanalytical Chemistry* 477.2 (1999), pp. 97–110. ISSN: 1572-6657. DOI: [10.1016/S0022-0728\(99\)00359-9](https://doi.org/10.1016/S0022-0728(99)00359-9).
 - [129] K. Scott, W. Taama, and J. Cruickshank. “Performance and modelling of a direct methanol solid polymer electrolyte fuel cell”. In: *Journal of Power Sources* 65.1 (1997). The 20th International Power Sources Symposium, pp. 159–171. ISSN: 0378-7753. DOI: [10.1016/S0378-7753\(97\)02485-3](https://doi.org/10.1016/S0378-7753(97)02485-3).
 - [130] *SFC Energy*. <https://www.my-efoy.com/en/efoy-fuell-cells>. 2021.
 - [131] Y. Shao-Horn et al. “Instability of Supported Platinum Nanoparticles in Low-Temperature Fuel Cells”. In: *Topics in Catalysis* 46.3-4 (2007), pp. 285–305. DOI: [10.1007/s11244-007-9000-0](https://doi.org/10.1007/s11244-007-9000-0).
 - [132] A. Siebke et al. “Investigation of the Limiting Processes of a DMFC by Mathematical Modeling”. In: *Fuel Cells* 3.1 - 2 (2003), pp. 37–47. DOI: [10.1002/fuce.200320210](https://doi.org/10.1002/fuce.200320210).
 - [133] T. E. Springer, T. A. Zawodzinski, and S. Gottesfeld. “Polymer Electrolyte Fuel Cell Model”. In: *Journal of The Electrochemical Society* 138.8 (1991), pp. 2334–2342. DOI: [10.1149/1.2085971](https://doi.org/10.1149/1.2085971).
 - [134] Wei Sun, Brant A. Peppley, and Kunal Karan. “An improved two-dimensional agglomerate cathode model to study the influence of catalyst layer structural parameters”. In: *Electrochimica Acta* 50.16-17 (2005), pp. 3359–3374. ISSN: 00134686. DOI: [10.1016/j.electacta.2004.12.009](https://doi.org/10.1016/j.electacta.2004.12.009).

- [135] K. Sundmacher et al. “Dynamics of the direct methanol fuel cell (DMFC): experiments and model-based analysis”. In: *Chemical Engineering Science* 56.2 (2001). 16th International Conference on Chemical Reactor Engineering, pp. 333–341. ISSN: 0009-2509. DOI: [10.1016/S0009-2509\(00\)00233-5](https://doi.org/10.1016/S0009-2509(00)00233-5).
- [136] Kai Sundmacher and Keith Scott. “Direct methanol polymer electrolyte fuel cell: Analysis of charge and mass transfer in the vapour–liquid–solid system”. In: *Chemical Engineering Science* 54.13 (1999), pp. 2927–2936. ISSN: 0009-2509. DOI: [10.1016/S0009-2509\(98\)00344-3](https://doi.org/10.1016/S0009-2509(98)00344-3).
- [137] thyssenkrupp. *Smart, sustainable, one-stop solution: Renewable methanol to mitigate greenhouse gases*. <https://www.thyssenkrupp-industrial-solutions.com/power-to-x/en/green-methanol>. 2020.
- [138] Nicolò S. Vasile, Alessandro H.A. Monteverde Videla, and Stefania Specchia. “Effects of the current density distribution on a single-cell DMFC by tuning the anode catalyst in layers of gradual loadings: Modelling and experimental approach”. In: *Chemical Engineering Journal* 322 (2017), pp. 722–741. ISSN: 1385-8947. DOI: [10.1016/j.cej.2017.04.060](https://doi.org/10.1016/j.cej.2017.04.060).
- [139] Nicolò S. Vasile et al. “Influence of membrane-type and flow field design on methanol crossover on a single-cell DMFC: An experimental and multi-physics modeling study”. In: *International Journal of Hydrogen Energy* 42.46 (2017), pp. 27995–28010. ISSN: 0360-3199. DOI: [10.1016/j.ijhydene.2017.06.214](https://doi.org/10.1016/j.ijhydene.2017.06.214).
- [140] Marcos Vera. “A single-phase model for liquid-feed DMFCs with non-Tafel kinetics”. In: *Journal of Power Sources* 171.2 (2007), pp. 763–777. ISSN: 0378-7753. DOI: [10.1016/j.jpowsour.2007.05.098](https://doi.org/10.1016/j.jpowsour.2007.05.098).
- [141] Anil V. Virkar and Yingke Zhou. “Mechanism of Catalyst Degradation in Proton Exchange Membrane Fuel Cells”. In: *Journal of The Electrochemical Society* 154.6 (2007), B540. DOI: [10.1149/1.2722563](https://doi.org/10.1149/1.2722563).
- [142] Y. Wang and D.U. Sauer. “Optimization of DMFC regulation based on spatial modeling”. In: *International Journal of Hydrogen Energy* 40.35 (2015), pp. 12023–12033. ISSN: 0360-3199. DOI: [10.1016/j.ijhydene.2015.06.030](https://doi.org/10.1016/j.ijhydene.2015.06.030).
- [143] Z. H. Wang and C. Y. Wang. “Mathematical Modeling of Liquid-Feed Direct Methanol Fuel Cells”. In: *Journal of The Electrochemical Society* 150.4 (2003), A508. DOI: [10.1149/1.1559061](https://doi.org/10.1149/1.1559061).
- [144] S. Wasmus and A. Küver. “Methanol oxidation and direct methanol fuel cells: a selective review”. In: *Journal of Electroanalytical Chemistry* 461.1 (1999), pp. 14–31. ISSN: 1572-6657. DOI: [10.1016/S0022-0728\(98\)00197-1](https://doi.org/10.1016/S0022-0728(98)00197-1).
- [145] M. Watanabe and S. Motoo. “Electrocatalysis by ad-atoms: Part II. Enhancement of the oxidation of methanol on platinum by ruthenium ad-atoms”. In: *Journal of Electroanalytical Chemistry and Interfacial Electrochemistry* 60.3 (1975), pp. 267–273. ISSN: 0022-0728. DOI: [10.1016/S0022-0728\(75\)80261-0](https://doi.org/10.1016/S0022-0728(75)80261-0).

-
- [146] Adam Z. Weber and John Newman. “Transport in Polymer-Electrolyte Membranes: II. Mathematical Model”. In: *Journal of The Electrochemical Society* 151.2 (2004), A311–A325. DOI: [10.1149/1.1639157](https://doi.org/10.1149/1.1639157).
- [147] Adam Z. Weber et al. “A Critical Review of Modeling Transport Phenomena in Polymer-Electrolyte Fuel Cells”. In: *Journal of The Electrochemical Society* 161.12 (2014), F1254–F1299. DOI: [10.1149/2.0751412jes](https://doi.org/10.1149/2.0751412jes).
- [148] Hui Xu, Russell Kunz, and James M. Fenton. “Investigation of Platinum Oxidation in PEM Fuel Cells at Various Relative Humidities”. In: *Electrochemical and Solid-State Letters* 10.1 (2007), B1. DOI: [10.1149/1.2372230](https://doi.org/10.1149/1.2372230).
- [149] T.Z. Yan and Tien-Chien Jen. “Two-phase flow modeling of liquid-feed direct methanol fuel cell”. In: *International Journal of Heat and Mass Transfer* 51.5 (2008), pp. 1192–1204. ISSN: 0017-9310. DOI: [10.1016/j.ijheatmasstransfer.2007.03.007](https://doi.org/10.1016/j.ijheatmasstransfer.2007.03.007).
- [150] H. Yang, T.S. Zhao, and Q. Ye. “In situ visualization study of CO₂ gas bubble behavior in DMFC anode flow fields”. In: *Journal of Power Sources* 139.1 (2005), pp. 79–90. ISSN: 0378-7753. DOI: [10.1016/j.jpowsour.2004.05.033](https://doi.org/10.1016/j.jpowsour.2004.05.033).
- [151] W.W. Yang and T.S. Zhao. “A two-dimensional, two-phase mass transport model for liquid-feed DMFCs”. In: *Electrochimica Acta* 52.20 (2007), pp. 6125–6140. ISSN: 0013-4686. DOI: [10.1016/j.electacta.2007.03.069](https://doi.org/10.1016/j.electacta.2007.03.069).
- [152] Xiao-Guang Yang, Qiang Ye, and Ping Cheng. “Oxygen starvation induced cell potential decline and corresponding operating state transitions of a direct methanol fuel cell in galvanostatic regime”. In: *Electrochimica Acta* 117 (2014), pp. 179–191. ISSN: 0013-4686. DOI: [10.1016/j.electacta.2013.11.112](https://doi.org/10.1016/j.electacta.2013.11.112).
- [153] Q. Ye and T. S. Zhao. “Abrupt Decline in the Open-Circuit Voltage of Direct Methanol Fuel Cells at Critical Oxygen Feed Rate”. In: *Journal of The Electrochemical Society* 152.11 (2005), A2238. DOI: [10.1149/1.2047350](https://doi.org/10.1149/1.2047350).
- [154] Q. Ye et al. “Electrochemical Reactions in a DMFC under Open-Circuit Conditions”. In: *Electrochemical and Solid-State Letters* 8.1 (2005), A52. DOI: [10.1149/1.1836111](https://doi.org/10.1149/1.1836111).
- [155] Qiang Ye, Xiao-Guang Yang, and Ping Cheng. “Modeling of spontaneous hydrogen evolution in a direct methanol fuel cell”. In: *Electrochimica Acta* 69 (2012), pp. 230–238. ISSN: 0013-4686. DOI: [10.1016/j.electacta.2012.02.108](https://doi.org/10.1016/j.electacta.2012.02.108).
- [156] Wei Yuan et al. “Visualization of two-phase flow and temperature characteristics of an active liquid-feed direct methanol fuel cell with diverse flow fields”. In: *Applied Energy* 179 (2016), pp. 85–98. ISSN: 0306-2619. DOI: [10.1016/j.apenergy.2016.06.127](https://doi.org/10.1016/j.apenergy.2016.06.127).
- [157] M. Zago et al. “Effect of anode MPL on water and methanol transport in DMFC: Experimental and modeling analyses”. In: *International Journal of Hydrogen Energy* 39.36 (2014), pp. 21620–21630. ISSN: 0360-3199. DOI: [10.1016/j.ijhydene.2014.03.147](https://doi.org/10.1016/j.ijhydene.2014.03.147).

- [158] M. Zago et al. “On the actual cathode mixed potential in direct methanol fuel cells”. In: *Journal of Power Sources* 325 (2016), pp. 714–722. ISSN: 0378-7753. DOI: [10.1016/j.jpowsour.2016.06.093](https://doi.org/10.1016/j.jpowsour.2016.06.093).
- [159] M. Zago et al. “Water transport and flooding in DMFC: Experimental and modeling analyses”. In: *Journal of Power Sources* 217 (2012), pp. 381–391. ISSN: 0378-7753. DOI: [10.1016/j.jpowsour.2012.06.022](https://doi.org/10.1016/j.jpowsour.2012.06.022).
- [160] Nada Zamel et al. “Effect of liquid water on transport properties of the gas diffusion layer of polymer electrolyte membrane fuel cells”. In: *International Journal of Hydrogen Energy* 36.9 (2011), pp. 5466–5478. ISSN: 0360-3199. DOI: [10.1016/j.ijhydene.2011.01.146](https://doi.org/10.1016/j.ijhydene.2011.01.146).
- [161] Qiao Zhao, Paul Majsztrik, and Jay Benziger. “Diffusion and Interfacial Transport of Water in Nafion”. In: *The Journal of Physical Chemistry B* 115.12 (2011), pp. 2717–2727. DOI: [10.1021/jp1112125](https://doi.org/10.1021/jp1112125).
- [162] Su Zhou et al. “Analysis of the nonlinear dynamics of a direct methanol fuel cell”. In: *Phys. Chem. Chem. Phys.* 3 (3 2001), pp. 347–355. DOI: [10.1039/B0072830](https://doi.org/10.1039/B0072830).